Summary of the Bulletin of the International Seismological Centre

2011

January – June

Volume 48 Issue 1-6

www.isc.ac.uk

isc-mirror.iris.washington.edu

ISSN 2309-236X

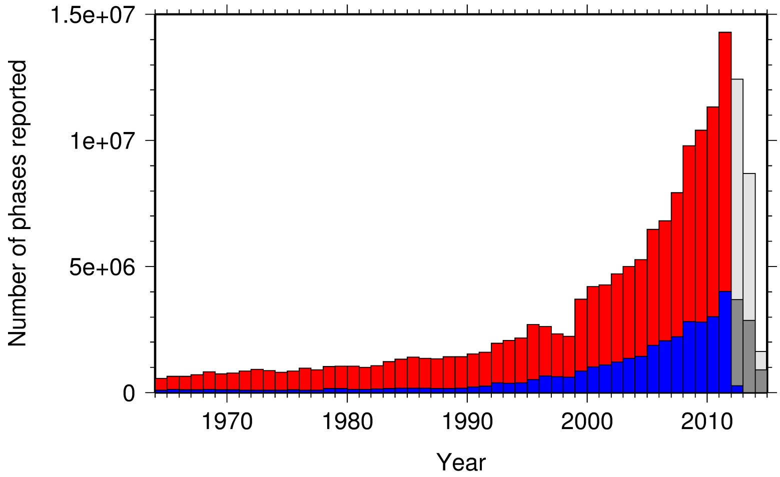

The number of phases (red) and number of amplitudes (blue) collected by the ISC for events each year since 1964. The data in grey covers the current period where data are still being collected before the ISC review takes place and are accurate at the time of publication. See Section 9.3.

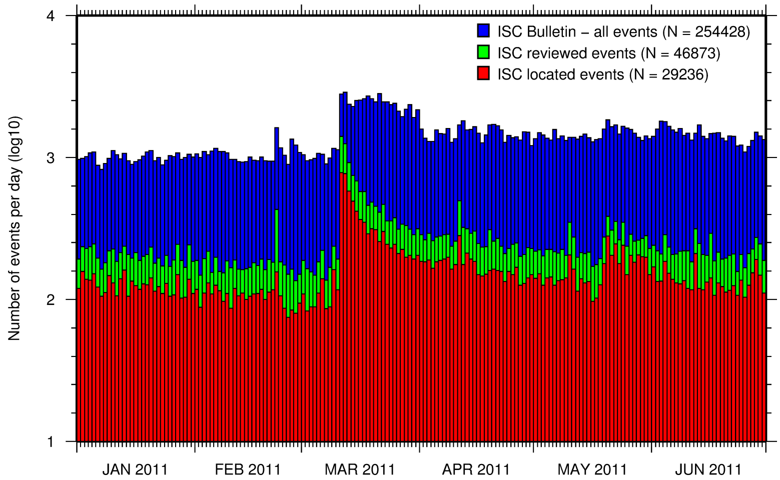

The number of events within the Bulletin for the current summary period. The vertical scale is logarithmic. See Section 10.1.

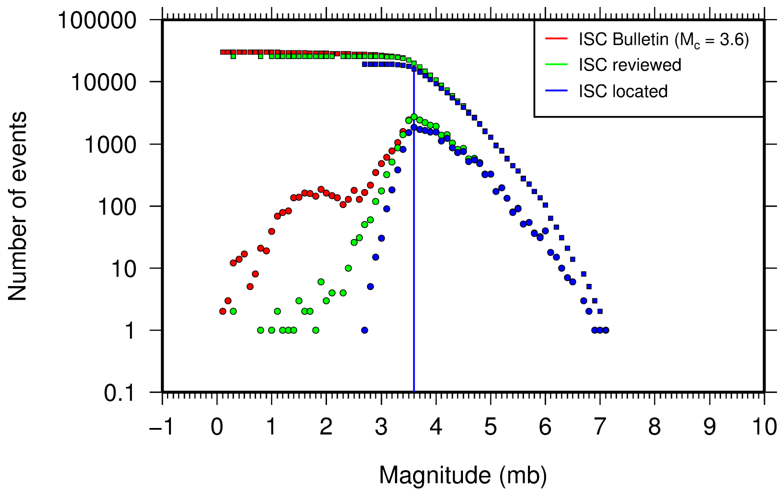

Frequency and cumulative frequency magnitude distribution for all events in the ISC Bulletin, ISC reviewed events and events located by the ISC. The magnitude of completeness (M_C) is shown for the ISC Bulletin. Note: only events with values of m_b are represented in the figure. See Section 10.4.

Contents

1 Preface **1**

2 The International Seismological Centre **2**

2.1 The ISC Mandate . . . 2
2.2 Brief History of the ISC . . . 3
2.3 Former Directors of the ISC and its U.K. Predecessors . . . 4
2.4 Member Institutions of the ISC . . . 5
2.5 Sponsoring Organisations . . . 11
2.6 Data Contributing Agencies . . . 11
2.7 ISC Staff . . . 20

3 ISC Operational Procedures **25**

3.1 Introduction . . . 25
3.2 Data Collection . . . 25
3.3 ISC Automatic Procedures . . . 26
3.3.1 Grouping . . . 26
3.3.2 Association . . . 28
3.3.3 Thresholding . . . 29
3.3.4 Location by the ISC . . . 29
3.4 ISC Location Algorithm . . . 30
3.4.1 Seismic Phases . . . 31
3.4.2 Correlated travel-time prediction error structure . . . 32
3.4.3 Depth resolution . . . 34
3.4.4 Depth-phase stack . . . 34
3.4.5 Initial hypocentre . . . 35
3.4.6 Iterative linearised location algorithm . . . 35
3.4.7 Validation tests . . . 36
3.4.8 Magnitude calculation . . . 36
3.4.9 Body-wave magnitudes . . . 38
3.4.10 Surface-wave magnitudes . . . 39
3.5 Review Process . . . 40
3.6 History of Operational Changes . . . 41

4 Availability of the ISC Bulletin **43**

5 **Citing the International Seismological Centre** **44**

6 **IASPEI Standards** **46**

6.1 Standard Nomenclature of Seismic Phases 46

6.2 Flinn-Engdahl Regions 53

6.3 IASPEI Magnitudes 60

6.4 The IASPEI Seismic Format (ISF) 64

6.5 Ground Truth (GT) Events 66

6.6 Nomenclature of Event Types 68

7 **Summary of Seismicity, January - June 2011** **70**

8 **Notable Events** **75**

8.1 The Canterbury, New Zealand Earthquake Sequence II: The M_W 6.2 Christchurch Earthquake of 21 February 2011 and Continuing Aftershock Sequence 75

8.1.1 Introduction 75

8.1.2 The M_W 6.2 Christchurch Earthquake 77

8.1.3 Effects on the built environment 84

8.1.4 Aftershock Sequence 89

8.1.5 Stress Studies and Aftershock Forecasts 91

8.1.6 Discussion 91

8.1.7 Conclusions 94

8.1.8 Acknowledgements 95

8.1.9 References 95

8.2 An overview of the M_W 9, 11 March 2011, Tohoku earthquake 100

8.2.1 Introduction 100

8.2.2 Rupture process of the Tohoku earthquake 102

8.2.3 Seismicity and slow slip along the plate boundary before the Tohoku earthquake 107

8.2.4 Aftershock activity and postseismic deformation 110

8.2.5 Shallow crustal seismicity induced by the Tohoku earthquake 114

8.2.6 Discussion 116

8.2.7 Summary 118

8.2.8 Acknowledgements 118

8.2.9 References 119

9 **Statistics of Collected Data** **133**

9.1 Introduction 133

9.2 Summary of Agency Reports to the ISC 133

9.3 Arrival Observations 138

9.4 Hypocentres Collected 145

9.5 Collection of Network Magnitude Data 147

9.6 Moment Tensor Solutions . . . 152
9.7 Timing of Data Collection . . . 155

10 Overview of the ISC Bulletin 157

10.1 Events . . . 157
10.2 Seismic Phases and Travel-Time Residuals . . . 166
10.3 Seismic Wave Amplitudes and Periods . . . 172
10.4 Completeness of the ISC Bulletin . . . 175
10.5 Magnitude Comparisons . . . 176

11 The Leading Data Contributors 181

11.1 The Largest Data Contributors . . . 181
11.2 Contributors Reporting the Most Valuable Parameters . . . 183
11.3 The Most Consistent and Punctual Contributors . . . 189

12 Appendix 190

13 Glossary of ISC Terminology 207

14 Acknowledgements 211

References 212

1

Preface

Dear Colleague,

This is the first 2011 issue of the Summary of the ISC Bulletin which remains the most fundamental reason for the ISC continued operations. This issue covers the period of January-June 2011.

This publication presents a description of the ISC data available on the attached DVD-ROM and from the ISC website. It contains information on the ISC, its Members, Sponsors and Data providers. It offers analysis of the data contributed to the ISC by many seismological agencies worldwide as well as analysis of the data in the ISC Bulletin itself.

This issue also includes important seismological standards and procedures used by the ISC in its operations. In particular, the description of the IASPEI Standard Seismic Phase List has been updated to reflect the amplitude naming guidelines developed by the CoSOI/IASPEI magnitude working group.

This issue also contains two invited articles on the notable March 2011 Great Tohoku earthquake and February 2011 Christchurch earthquake and related aftershock sequence.

We hope that you find this publication useful in your work. If your home-institution or company is unable, for one reason or another, to support the long-term international operations of the ISC in full by becoming a Member, then, please, consider subscribing to this publication by contacting us at admin@isc.ac.uk.

With kind regards to our Data Contributors, Members, Sponsors and users,

Dr Dmitry A. Storchak
Director
International Seismological Centre (ISC)

2

The International Seismological Centre

2.1 The ISC Mandate

The International Seismological Centre (ISC) was set up in 1964 with the assistance of UNESCO as a successor to the International Seismological Summary (ISS) to carry forward the pioneering work of Prof. John Milne, Sir Harold Jeffreys and other British scientists in collecting, archiving and processing seismic station and network bulletins and preparing and distributing the definitive summary of world seismicity.

Under the umbrella of the International Association of Seismology and Physics of the Earth Interior (IASPEI/IUGG), the ISC has played an important role in setting international standards such as the International Seismic Bulletin Format (ISF), the IASPEI Standard Seismic Phase List (SSPL) and both the old and New IASPEI Manual of the Seismological Observatory Practice (NMSOP-2) (www.iaspei.org/projects/NMSOP.html).

The ISC has contributed to scientific research and prominent scientists such as John Hodgson, Eugine Herrin, Hal Thirlaway, Jack Oliver, Anton Hales, Ola Dahlman, Shigeji Suehiro, Nadia Kondorskaya, Vit Karnik, Stephan Müller, David Denham, Bob Engdahl, Adam Dziewonski, John Woodhouse and Guy Masters all considered it an important duty to serve on the ISC Executive Committee and the Governing Council.

The current mission of the ISC is to maintain:

- the ISC **Bulletin** – the longest continuous definitive summary of World seismicity (collaborating with 130 seismic networks and data centres around the world). (www.isc.ac.uk/iscbulletin/)
- the **International** Seismographic Station Registry (**IR**, jointly with the World Data Center for Seismology, Denver). (www.isc.ac.uk/registries/)
- the IASPEI Reference Event List (Ground Truth, **GT**, jointly with IASPEI). (www.isc.ac.uk/gtevents/)

These are fundamentally important tasks. Bulletin data produced, archived and distributed by the ISC for almost 50 years are the definitive source of such information and are used by thousands of seismologists worldwide for seismic hazard estimation, for tectonic studies and for regional and global imaging of the Earth's structure. Key information in global tomographic imaging is derived from the analysis of ISC data. The ISC Bulletin served as a major source of data for such well known products as the ak135 global 1-D velocity model and the EHB (*Engdahl et al.*, 1998) and Centennial (*Engdahl and Villaseñor*, 2002) catalogues. It presents an important quality-control benchmark for the Comprehensive Nuclear-Test-Ban Treaty Organization (CTBTO). Hypocentre parameters from the ISC Bulletin are used by the Data Management Center of the Incorporated Research Institutions for Seismology (IRIS DMC) to serve event-oriented user-requests for waveform data. The ISC-GEM Bulletin is a cornerstone of the ISC-GEM Global Instrumental Reference Earthquake Catalogue for Global Earthquake risk Model (GEM).

The ISC relational database currently holds approximately 90 Gb of unique data. The ISC Bulletin contains over 5 million seismic events: earthquakes, chemical and nuclear explosions, mine blasts and mining induced events. At least 1.5 million of them are regional and teleseismically recorded events that have been reviewed by the ISC analysts. The ISC Bulletin contains approximately 150 million individual seismic station readings of arrival times, amplitudes, periods, SNR, slowness and azimuth, reported by approximately 17,000 seismic stations currently registered in the IR. Over 6,000 stations have contributed to the ISC Bulletin in recent years. This number includes the numerous sites of the USArray. The IASPEI GT List currently contains 7802 events for which latitude, longitude and depth of origin are known with high confidence (to 5 km or better) and seismic signals were recorded at regional and/or teleseismic distances.

2.2 Brief History of the ISC

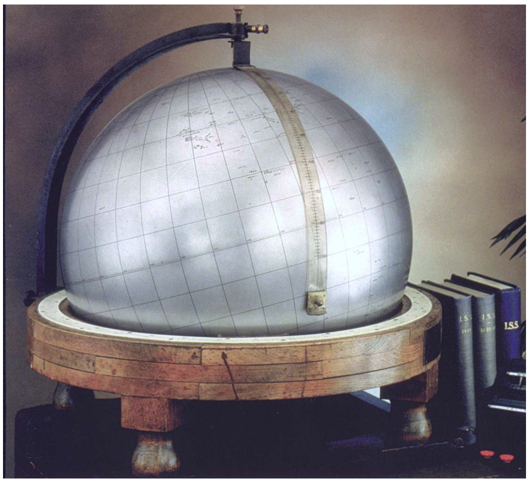

Figure 2.1: *The steel globe bearing positions of early seismic stations was used for locating positions of earthquakes for the International Seismological Summaries.*

Earthquake effects have been noted and documented from the earliest times, but it is only since the development of earthquake recording instruments in the latter half of the 19th century that a proper study of their occurrence has been possible. After the first teleseismic observation of an earthquake in 1889, the need for international exchange of readings was recognised in 1895 by Prof. John Milne and by Ernst von Rebeur Paschwitz together with Georg Gerland, resulting in the publication of the first international seismic bulletins. Milne's "Shide Circulars" were issued under the auspices of the Seismological Committee of the British Association for the Advancement of Science (BAAS), while co-workers of Gerland at the Central Bureau of the International Association of Seismology worked independently in Strasbourg (BCIS).

Following Milne's death in 1913, Seismological Bulletins of the BAAS were continued under Prof. H.H. Turner, later based at Oxford University. Upon formal post-war dissolution of the International Association of Seismology in 1922 the newly founded Seismological Section of the International Union of Geodesy and Geophysics (IUGG) set up the International Seismological Summary (ISS) to continue at Oxford under Turner, to produce the definitive global catalogues from the 1918 data-year onwards, under the auspices of IUGG and with the support of the BAAS.

ISS production, led by several professors at Oxford University, and Sir Harold Jeffreys at Cambridge University, continued until it was superseded by the ISC Bulletin, after the ISC was formed in Edinburgh in 1964 with Dr P.L. Willmore as its first director.

During the period 1964 to 1970, with the help of UNESCO and other international scientific bodies, the ISC was reconstituted as an international non-governmental body, funded by interested institutions from various countries. Initially there were supporting members from seven countries, now there are almost 60, and member institutions include national academies, research foundations, government departments and research institutes, national observatories and universities. Each member, contributing a minimum unit of subscription or more, appoints a representative to the ISC's Governing Council, which meets every two years to decide the ISC's policy and operational programme. Representatives from the International Association of Seismology and Physics of the Earth's Interior also attend these meetings. The Governing Council appoints the Director and a small Executive Committee to oversee the ISC's operations.

Figure 2.2: ISC building in Thatcham, Berkshire, UK.

In 1975, the ISC moved to Newbury in southern England to make use of better computing facilities there. The ISC subsequently acquired its own computer and in 1986 moved to its own building at Pipers Lane, Thatcham, near Newbury. The internal layout of the new premises was designed for the ISC and includes not only office space but provision for the storage of extensive stocks of ISS and ISC publications and a library of seismological observatory bulletins, journals and books collected over many tens of years.

In 1997 the first set of the ISC Bulletin CD-ROMs was produced (not counting an earlier effort at USGS). The first ISC website appeared in 1998 and the first ISC database was put in day-to-day operations from 2001.

Throughout 2009-2011 a major internal reconstruction of the ISC building was undertaken to allow for more members of staff working in mainstream ISC operations as well as major development projects such as the CTBTO Link, ISC-GEM Catalogue and the ISC Bulletin Rebuild.

2.3 Former Directors of the ISC and its U.K. Predecessors

John Milne
Publisher of the Shide Cicular Reports on Earthquakes
1899-1913

Herbert Hall Turner

Seismological Bulletins of the BAAS

1913-1922
Director of the ISS
1922-1930

Harry Hemley Plaskett
Director of the ISS
1931-1946

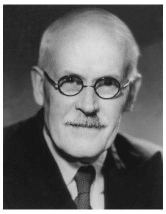

Harold Jeffreys
Director of the ISS
1946-1957

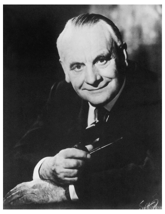

Robert Stoneley
Director of the ISS
1957-1963

P.L. (Pat) Willmore
Director of the ISS
1963-1970
Director of the ISC
1964-1970

Edouard P. Arnold
Director of the ISC
1970-1977

Anthony A. Hughes
Director of the ISC
1977-1997

Raymond J. Willemann
Director of the ISC
1998-2003

Avi Shapira
Director of the ISC
2004-2007

2.4 Member Institutions of the ISC

Article IV(a-b) of the ISC Working Statutes stipulates that any national academy, agency, scientific institution or other non-profit organisation may become a Member of the ISC on payment to the ISC of a sum equal to at least one unit of subscription and the nomination of a voting representative to serve on the ISC's governing body. Membership shall be effective for one year from the date of receipt at the ISC of the annual contribution of the Member and is thereafter renewable for periods of one year.

The ISC is currently supported with funding from its 62 Member Institutions and a four-year Grant Award EAR-0949072 from the US National Science Foundation.

Figures 2.3 and 2.4 show major sectors to which the ISC Member Institutions belong and proportional financial contributions that each of these sectors make towards the ISC's annual budget.

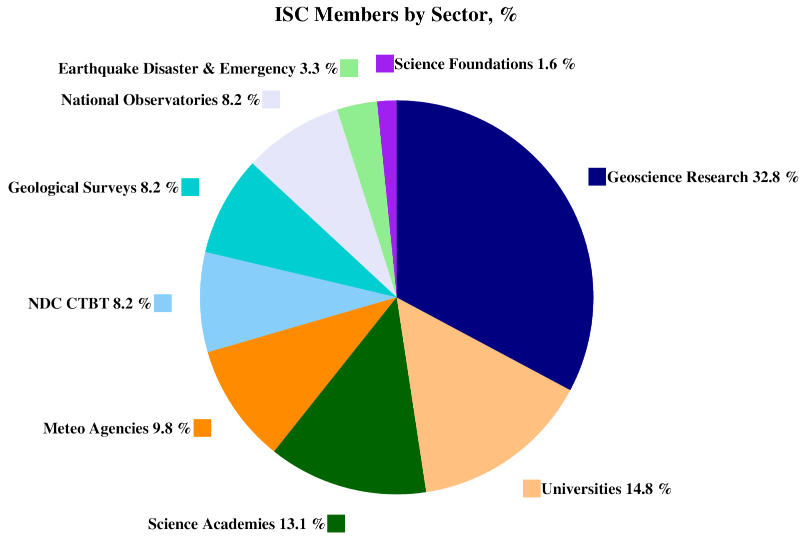

Figure 2.3: *Distribution of the ISC Member Institutions by sector in year 2013 as a percentage of total number of Members.*

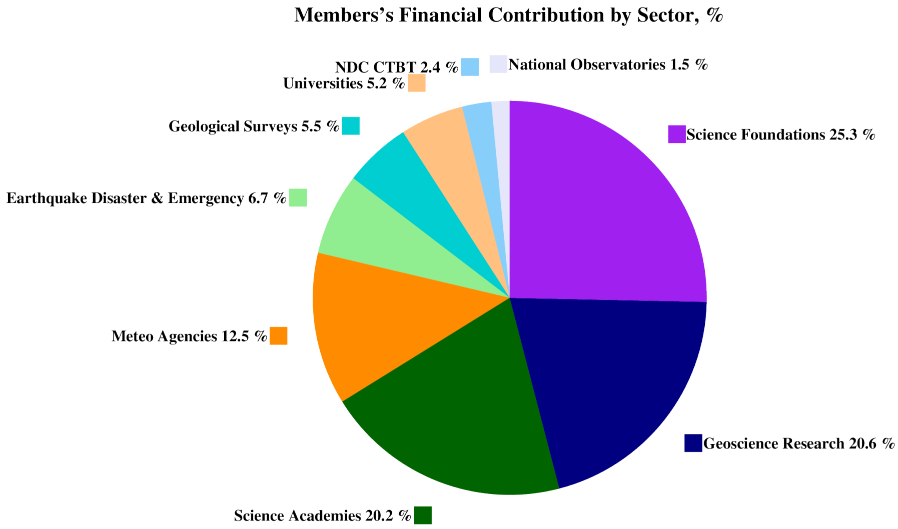

Figure 2.4: *Distribution of Member's financial contributions to the ISC by sector in year 2013 as a percentage of total annual Member contributions.*

There follows a list of all current Member Institutions with a category (1 through 9) assigned according to the ISC Working Statutes. Each category relates to the number of membership units contributed.

Centre de Recherche en Astronomie, Astrophysique et Géophysique (CRAAG)
Algeria
www.craag.dz
Category: 1

Instituto Nacional de Prevención Sísmica (INPRES)
Argentina
www.inpres.gov.ar
Category: 1

Seismology Research Centre
Australia
www.seis.com.au
Category: 1

The University of Melbourne
Australia
www.unimelb.edu.au
Category: 1

Geoscience Australia
Australia
www.ga.gov.au
Category: 3

Bundesministerium für Wissenschaft und Forschung
Austria
www.bmbwk.gv.at
Category: 2

Centre of Geophysical Monitoring (CGM) of the National Academy of Sciences of Belarus
Belarus
www.cgm.org.by
Category: 1

Observatoire Royal de Belgique
Belgium
www.astro.oma.be
Category: 1

The Geological Survey of Canada
Canada
gsc.nrcan.gc.ca
Category: 4

China Earthquake Administration
China
www.gov.cn
Category: 5

Institute of Earth Sciences, Academia Sinica
Chinese Taipei
www.earth.sinica.edu.tw
Category: 1

Geological Survey Department
Cyprus
www.moa.gov.cy
Category: 1

Academy of Sciences of the Czech Republic
Czech Republic
www.cas.cz
Category: 2

Geological Survey of Denmark and Greenland - GEUS
Denmark
www.geus.dk
Category: 2

National Research Institute for Astronomy and Geophysics (NRIAG), Cairo
Egypt
www.nriag.sci.eg
Category: 1

The University of Helsinki
Finland
www.helsinki.fi
Category: 2

Laboratoire de Détection et de Géophysique/CEA
France
www-dase.cea.fr
Category: 2

Institute National des Sciences de l'Univers
France
www.insu.cnrs.fr
Category: 4

Bundesanstalt für Geowissenschaften und Rohstoffe
Germany
www.bgr.bund.de
Category: 4

GeoForschungsZentrum Potsdam
Germany
www.gfz-potsdam.de
Category: 2

The Seismological Institute, National Observatory of Athens
Greece
www.noa.gr
Category: 1

The Hungarian Academy of Sciences
Hungary
www.mta.hu
Category: 1

The Icelandic Meteorological Office
Iceland
www.vedur.is
Category: 1

India Meteorological Department
India
www.imd.ernet.in
Category: 4

Iraqi Seismic Network
Iraq
www.imos-tm.com
Category: 1

Dublin Institute for Advanced Studies
Ireland
www.dias.ie
Category: 1

Soreq Nuclear Research Centre (SNRC)
Israel
www.soreq.gov.il
Category: 1

The Geophysical Institute of Israel
Israel
www.gii.co.il
Category: 1

Istituto Nazionale di Geofisica e Vulcanologia
Italy
www.ingv.it
Category: 3

Istituto Nazionale di Oceanografia e di Geofisica Sperimentale
Italy
www.ogs.trieste.it
Category: 1

University of the West Indies
Jamaica
www.mona.uwi.edu
Category: 1

The Japan Meteorological Agency (JMA)
Japan
www.jma.go.jp
Category: 5

Japan Agency for Marine-Earth Science and Technology (JAMSTEC)
Japan
www.jamstec.go.jp
Category: 3

Earthquake Research Institute, University of Tokyo
Japan
www.eri.u-tokyo.ac.jp
Category: 3

Natural Resources Authority, Amman
Jordan
www.nra.gov.jo
Category: 1

Institute of Geophysics, National University of Mexico
Mexico
www.igeofcu.unam.mx
Category: 1

The Royal Netherlands Meteorological Institute
Netherlands
www.knmi.nl
Category: 2

Institute of Geological and Nuclear Sciences
New Zealand
www.gns.cri.nz
Category: 3

The University of Bergen
Norway
www.uib.no
Category: 2

Stiftelsen NORSAR
Norway
www.norsar.no
Category: 2

Institute of Geophysics, Polish Academy of Sciences
Poland
www.igf.edu.pl
Category: 1

Instituto Português do Mar e da Atmosfera
Portugal
www.ipma.pt
Category: 2

Red Sísmica de Puerto Rico
Puerto Rico
redsismica.uprm.edu
Category: 1

Korean Meterological Administration
Republic of Korea
www.kma.go.kr
Category: 1

National Institute for Earth Physics
Romania
www.infp.ro
Category: 1

Russian Academy of Sciences
Russia
www.ras.ru
Category: 5

Environmental Agency of Slovenia
Slovenia
www.arso.gov.si
Category: 1

Council for Geoscience
South Africa
www.geoscience.org.za
Category: 1

Instituto Geográfico Nacional
Spain
www.ign.es
Category: 3

Uppsala Universitet
Sweden
www.uu.se
Category: 2

National Defence Research Establishment
Sweden
www.foi.se
Category: 1

The Swiss Academy of Sciences
Switzerland
www.scnat.ch
Category: 2

University of the West Indies
Trinidad and Tobago
sta.uwi.edu
Category: 1

Kandilli Observatory and Earthquake Research Institute
Turkey
www.koeri.boun.edu.tr
Category: 1

Disaster and Emergency Management Presidency
Turkey
www.deprem.gov.tr
Category: 2

AWE Blacknest
United Kingdom
www.blacknest.gov.uk
Category: 1

British Geological Survey
United Kingdom
www.bgs.ac.uk
Category: 2

The Royal Society of London
United Kingdom
www.royalsociety.org
Category: 6

National Earthquake Information Center, U.S. Geological Survey
U.S.A.
www.neic.usgs.gov
Category: 2

Incorporated Research Institutions for Seismology
U.S.A.
www.iris.edu
Category: 1

The National Science Foundation of the United States. (Grant No. EAR-0949072)
U.S.A.
www.nsf.gov
Category: 9

University of Texas at Austin
U.S.A.
www.utexas.edu
Category: 1

In addition the ISC is currently in receipt of grants from the International Data Centre (IDC) of the Preparatory Commission of the Comprehensive Nuclear-Test-Ban Treaty Organization (CTBTO), the Global Earthquake risk Model Foundation (GEM) and the International Union of Geodesy and Geophysics (IUGG).

2.5 Sponsoring Organisations

Article IV(c) of the ISC Working Statutes stipulates any commercial organisation with an interest in the objectives and/or output of the ISC may become an Associate Member of the ISC on payment of an Associate membership fee, but without entitlement to representation with a vote on the ISC's governing body.

REF TEK
A DIVISION OF TRIMBLE
www.reftek.com

REF TEK designs and manufactures application specific, high-performance, battery-operated, field-portable geophysical data acquisition devices for the global market. With over 35 years of experience, REF TEK provides customers with complete turnkey solutions that include high resolution recorders, broadband sensors, state-of-the-art communications (V-SAT, GPRS, etc), installation, training, and continued customer support. Over 7,000 REF TEK instruments are currently being used globally for multiple applications. From portable earthquake monitoring to telemetry earthquake monitoring, earthquake aftershock recording to structural monitoring and more, REF TEK equipment is suitable for a wide variety of application needs.

2.6 Data Contributing Agencies

In addition to its Members and Sponsors, the ISC owes its existence and successful long-term operations to its 131 seismic bulletin data contributors. These include government agencies responsible for national seismic networks, geoscience research institutions, geological surveys, meteorological agencies, universities, national data centres for monitoring the CTBT and individual observatories. There would be no ISC Bulletin available without the regular stream of data that are unselfishly and generously contributed to the ISC on a free basis.

The Institute of Seismology, Academy of Sciences of Albania
Albania
TIR

Centre de Recherche en Astronomie, Astrophysique et Géophysique
Algeria
CRAAG

Universidad Nacional de La Plata
Argentina
LPA

Instituto Nacional de Prevención Sísmica
Argentina
SJA

National Survey of Seismic Protection
Armenia
NSSP

Geoscience Australia
Australia
AUST

International Data Centre, CTBTO
Austria
IDC

Österreichischer Geophysikalischer Dienst
Austria
VIE

Republic Center of Seismic Survey
Azerbaijan
AZER

Centre of Geophysical Monitoring
Belarus
BELR

Royal Observatory of Belgium
Belgium
UCC

Observatorio San Calixto
Bolivia
SCB

Instituto Astronomico e Geofísico
Brazil
VAO

Geophysical Institute, Bulgarian Academy of Sciences
Bulgaria
SOF

Canadian Hazards Information Service, Natural Resources Canada
Canada
OTT

Departamento de Geofísica, Universidad de Chile
Chile
GUC

China Earthquake Networks Center
China
BJI

Institute of Earth Sciences, Academia Sinica
Chinese Taipei
ASIES

Red Sismológica Nacional de Colombia
Colombia
RSNC

Central American Seismic Center
Costa Rica
CASC

Seismological Survey of the Republic of Croatia
Croatia
ZAG

Servicio Sismológico Nacional Cubano
Cuba
SSNC

Cyprus Geological Survey Department
Cyprus
NIC

Geophysical Institute, Academy of Sciences of the Czech Republic
Czech Republic
PRU

West Bohemia Seismic Network
Czech Republic
WBNET

Geological Survey of Denmark and Greenland
Denmark
DNK

Observatoire Géophysique d'Arta
Djibouti
ARO

Servicio Nacional de Sismología y Vulcanología
Ecuador
IGQ

National Research Institute of Astronomy and Geophysics
Egypt
HLW

University of Addis Ababa
Ethiopia
AAE

Institute of Seismology, University of Helsinki
Finland
HEL

Laboratoire de Détection et de Géophysique/CEA
France
LDG

Institut de Physique du Globe
France
STR

Centre Sismologique Euro-Méditerranéen (CSEM/EMSC)
France
CSEM

Laboratoire de Géophysique/CEA
French Polynesia
PPT

Seismological Observatory Skopje
FYR Macedonia
SKO

Seismic Monitoring Centre of Georgia
Georgia
TIF

Seismological Observatory Berggießhübel, TU Bergakademie Freiberg
Germany
BRG

Bundesanstalt für Geowissenschaften und Rohstoffe
Germany
BGR

Geophysikalisches Observatorium Collm
Germany
CLL

Alfred Wegener Institute for Polar and Marine Research
Germany
AWI

Department of Geophysics, Aristotle University of Thessaloniki
Greece
THE

National Observatory of Athens
Greece
ATH

Hong Kong Observatory
Hong Kong
HKC

Geodetic and Geophysical Research Institute
Hungary
BUD

Icelandic Meteorological Office
Iceland
REY

National Geophysical Research Institute
India
HYB

India Meteorological Department
India
NDI

Badan Meteorologi, Klimatologi dan Geofisika
Indonesia
DJA

International Institute of Earthquake Engineering and Seismology (IIEES)
Iran
THR

Tehran University
Iran
TEH

Iraqi Meteorological and Seismology Organisation
Iraq
ISN

Dublin Institute for Advanced Studies
Ireland
DIAS

The Geophysical Institute of Israel
Israel
GII

Istituto Nazionale di Geofisica e Vulcanologia
Italy
ROM

Istituto Nazionale di Oceanografia e di Geofisica Sperimentale (OGS)
Italy
TRI

Station Géophysique de Lamto
Ivory Coast
LIC

Jamaica Seismic Network
Jamaica
JSN

National Institute of Polar Research
Japan
SYO

National Research Institute for Earth Science and Disaster Prevention
Japan
NIED

Japan Meteorological Agency
Japan
JMA

The Matsushiro Seismological Observatory
Japan
MAT

Jordan Seismological Observatory
Jordan
JSO

Seismological Experimental Methodological Expedition
Kazakhstan
SOME

National Nuclear Center
Kazakhstan
NNC

Kyrgyz Seismic Network
Kyrgyzstan
KNET

Institute of Seismology, Academy of Sciences of Kyrgyz Republic
Kyrgyzstan
KRNET

National Council for Scientific Research
Lebanon
GRAL

Geological Survey of Lithuania
Lithuania
LIT

Macao Meteorological and Geophysical Bureau
Macao, China
MCO

Malaysian Meteorological Service
Malaysia
KLM

Red Sismica del Noroeste de Mexico (RESOM)
Mexico
ECX

Instituto de Geofísica de la UNAM
Mexico
MEX

Institute of Geophysics and Geology
Moldova
MOLD

Research Centre of Astronomy and Geophysics
Mongolia
OBM

Seismological Institute of Montenegro
Montenegro
PDG

The Geological Survey of Namibia
Namibia
NAM

Department of Mines and Geology, Ministry of Industry of Nepal
Nepal
DMN

Koninklijk Nederlands Meteorologisch Instituut
Netherlands
DBN

Institute of Geological and Nuclear Sciences
New Zealand
WEL

Stiftelsen NORSAR
Norway
NAO

University of Bergen
Norway
BER

Sultan Qaboos University
Oman
OMAN

Micro Seismic Studies Programme, PINSTECH
Pakistan
MSSP

Philippine Institute of Volcanology and Seismology
Philippines
MAN

Manila Observatory
Philippines
QCP

Institute of Geophysics, Polish Academy of Sciences
Poland
WAR

Instituto Geofisico do Infante Dom Luiz
Portugal
IGIL

Sistema de Vigilância Sismológica dos Açores
Portugal
SVSA

Instituto Português do Mar e da Atmosfera, I.P.
Portugal
INMG

Korea Meteorological Administration
Republic of Korea
KMA

National Institute for Earth Physics
Romania
BUC

Sakhalin Experimental and Methodological Seismological Expedition, GS RAS
Russia
SKHL

Yakutiya Regional Seismological Center, GS SB RAS
Russia
YARS

Kola Regional Seismic Centre, GS RAS
Russia
KOLA

North Eastern Regional Seismological Centre, GS RAS
Russia
NERS

Kamchatkan Experimental and Methodological Seismological Department, GS RAS
Russia
KRSC

Altai-Sayan Seismological Centre, GS SB RAS
Russia
ASRS

Geophysical Survey of Russian Academy of Sciences
Russia
MOS

Baykal Regional Seismological Centre, GS SB RAS
Russia
BYKL

Saudi Geological Survey
Saudi Arabia
SGS

Seismological Survey of Serbia
Serbia
BEO

Geophysical Institute, Slovak Academy of Sciences
Slovakia
BRA

Environmental Agency of the Republic of Slovenia
Slovenia
LJU

Ministry of Mines, Energy and Rural Electrification
Solomon Islands
HNR

Council for Geoscience
South Africa
PRE

Instituto Geográfico Nacional
Spain
MDD

University of Uppsala
Sweden
UPP

Swiss Seismological Sevice (SED)
Switzerland
ZUR

National Syrian Seismological Center
Syria
NSSC

Thai Meteorological Department
Thailand
BKK

University of the West Indies
Trinidad and Tobago
TRN

Disaster and Emergency Management Presidency
Turkey
DDA

Kandilli Observatory and Research Institute
Turkey
ISK

Subbotin Institute of Geophysics, National Academy of Sciences
Ukraine
SIGU

Dubai Seismic Network
United Arab Emirates
DSN

British Geological Survey
United Kingdom
BGS

IRIS Data Management Center
U.S.A.
IRIS

IASPEI Working Group on Reference Events
U.S.A.
IASPEI

United States Geological Survey
U.S.A.
USGS

National Earthquake Information Center
U.S.A.
NEIC

Scripps Institution of Oceanography
U.S.A.
SIO

The Global CMT Project
U.S.A.
GCMT

Red Sísmica de Puerto Rico
U.S.A.
RSPR

Pacific Northwest Seismic Network
U.S.A.
PNSN

Fundación Venezolana de Investigaciones Sismológicas
Venezuela
FUNV

National Center for Scientific Research
Vietnam
PLV

Yemen National Seismological Center
Yemen
DHMR

Geological Survey Department of Zambia
Zambia
LSZ

Goetz Observatory
Zimbabwe
BUL

CWB
Chinese Taipei
TAP

2.7 ISC Staff

Listed below are the staff (and their country of origin) who were employed at the ISC at the time of this ISC Bulletin Summary.

- Dmitry Storchak
- Director
- Russia/United Kingdom

- Maureen Aspinwall
- Administration Officer
- United Kingdom

- James Harris
- System and Database Administrator
- United Kingdom

- John Eve
- Data Collection Officer
- United Kingdom

- Emily Delahaye
- Seismologist/Lead Analyst
- Canada

- Blessing Shumba
- Seismologist/Analyst
- Zimbabwe

- Ivana Jukić
- Seismologist/Analyst
- Croatia

- Rosemary Wylie
- Trainee Analyst
- United Kingdom

- Rebecca Verney
- Trainee Analyst
- United Kingdom

- István Bondár
- Senior Seismologist
- Hungary

- Wayne Richardson
- Senior Seismologist
- New Zealand

- Domenico Di Giacomo
- Seismologist
- Italy

- Sepideh Rastin
- Seismologist/Developer
- Iran

- Konstantinos Lentas
- Seismologist/Developer
- Greece

- Przemek Ozgo
- Junior System Administrator
- Poland

- Natalia Safronova
- Historical Data Entry Officer
- Russia

- Elizabeth Ball
- Historical Data Entry Officer
- United Kingdom

- Daniela Catanescu
- Historical Data Entry Officer
- Romania

3

ISC Operational Procedures

3.1 Introduction

The relational database at the ISC is the primary source for the ISC Bulletin. This database is also the source for the ISC web-based search, the ISC CD-ROMs and this printed Summary. The ISC database is also mirrored at several institutions such as the Data Management Center of the Incorporated Research Institutions for Seismology (IRIS DMC), Earthquake Research Institute (ERI) of the University of Tokyo and a few others.

The database holds information about ISC events, both natural and anthropogenic. Information on each event may include hypocentre estimates, moment tensors, event type, felt and damaging reports and associated station observations reported by different agencies and grouped together per physical event.

The majority of the ISC events (∼80%) are small and are not reviewed by the ISC analysts. Those that are reviewed (∼20%, usually magnitude greater than 3.5) may or may not include an ISC hypocentre solution and magnitude estimates. The decision depends on whether the wealth of combined information from several agencies as compared to the data of each single agency alone warrants the ISC location. The events are called ISC events regardless of whether they have been reviewed or located by the ISC or not.

All events located by the ISC are reviewed by the ISC analysts but not the other way round. Analyst review involves an examination of the integrity of all reported parametric information. It does not involve review of waveforms. Even if waveforms from all of the ∼6,000 stations included in a typical recent month of the ISC Bulletin were freely available, it would be an unmanageable task to inspect them all.

We shall now describe briefly current processes and procedures involved in producing the Bulletin of the International Seismological Centre. These have been developed from former practices described in the Introduction to earlier issues of the ISC Bulletin to account for modern methods and technologies of data collection and analysis.

3.2 Data Collection

Parametric data, mainly comprising seismic event hypocentre solutions, phase arrival observations and associated magnitude data, are now mostly emailed to the ISC (seismo@isc.ac.uk) by agencies around the world. Other macroseismic and source information associated with seismic events may also be incorporated in accordance with modern standards. The process of data collection at the ISC involves the automatic parsing of these data into the ISC relational database. The ISC now has over 200 individual parsers to account for legacy and current bulletin data formats used by data reporters.

Figure 3.1 shows the 313 agencies that have reported bulletin data to the ISC, directly or via regional data centres, during the entire period of the ISC existence: these agencies are also listed in Table 12.1 of the Appendix. In Figure 3.1, corresponding countries are shown shaded in red. Please note that the continent of Antarctica appears white on the map despite a steady stream of bulletin data from Antarctic stations: the agencies that run these stations are based elsewhere.

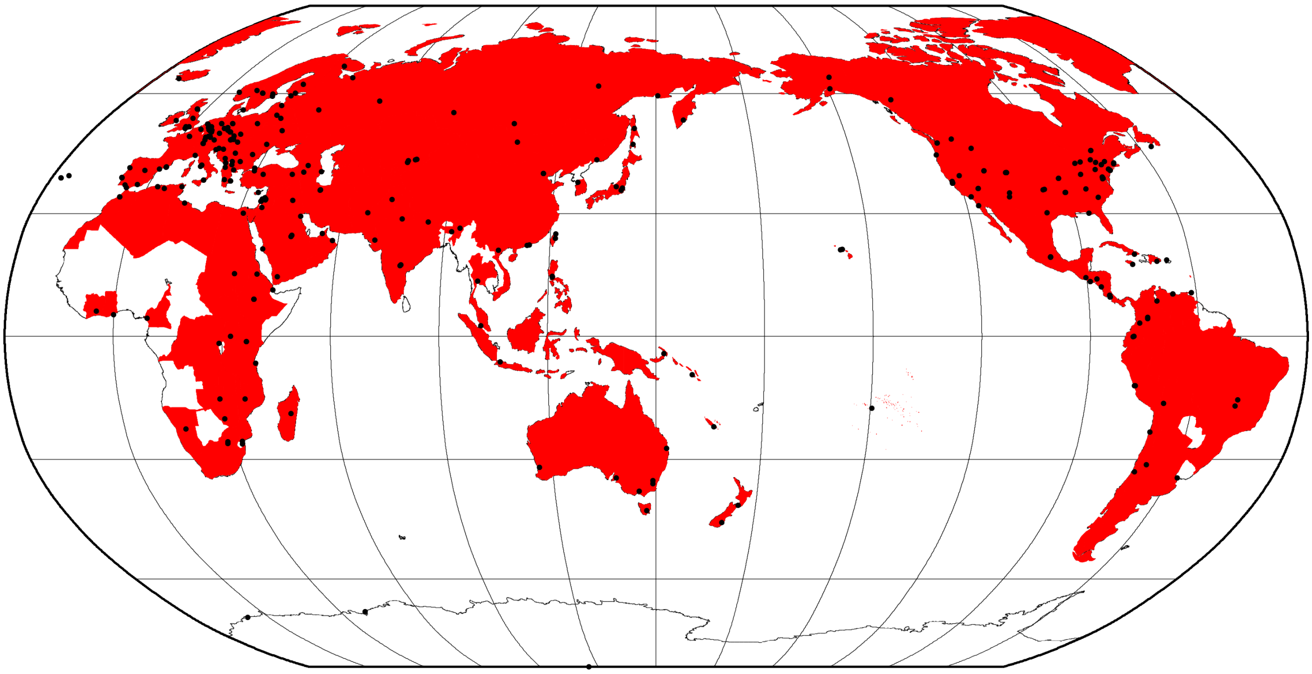

Figure 3.1: *Map of 313 agencies and corresponding countries that have reported seismic bulletin data to the ISC at least once during the entire period of the ISC operations, either directly or via regional data centres. Corresponding countries are shaded in red.*

3.3 ISC Automatic Procedures

3.3.1 Grouping

Grouping is the automatic process by which the many hypocentre solutions sent by the agencies reporting to the ISC for the same physical event are merged together into a single ISC event. This process possibly begins with an alert message and ends before a final review by ISC analysts. The process periodically runs through a set time interval of the input data stream, typically one day, looking for hypocentres in newly received data that are not yet grouped into an ISC event. Thus it considers only data more recent than the last data month reviewed by the ISC analysts. Immediately after grouping the seismic arrival associator is run on the same time interval, dealing with new phase arrival data not associated with any hypocentre.

The first stage of grouping gets a score where possible for each hypocentre to determine whether the reported hypocentre will be considered to be the primary estimate, or prime, for an ISC event. This score is based on the station arrival times reported in association with the hypocentre in four epicentral distance zones that characterise the networks of stations reporting:

1. Whole network
2. Local, 0 - 150 km
3. Near-regional, 3° - 10°
4. Teleseismic, 28° - 180°

For each distance zone, the azimuthal gap, the secondary azimuthal gap (the largest azimuthal gap filled by a single station), the minimum and maximum epicentral distance and number of stations are all used to calculate the value of dU, the normalised absolute deviation from best fitting uniformly distributed stations (*Bondár and McLaughlin*, 2009a). Clearly, this procedure can only use:

1. Bulletin data with hypocentres and sufficient associated seismic arrivals
2. Data for stations that are in the International Registry (IR)
3. Station data that are actually reported to ISC: CENC (China), for example, reports at most 24 stations, whilst many more may have been used to determine the hypocentre.

The hypocentres are then each considered in turn for grouping using one of two methods, the first by searching for a similar hypocentre, and the second by searching for the best fit of the reported phase arrival data that are associated with the candidate hypocentre. The method chosen for a reporter is based on feedback gained from ISC analysts.

For finding similar hypocentres, three sets of limits for origin-time difference and epicentral separation are used according to the type of bulletin data, be it alert, provisional or final: these limits are, respectively:

- ± 2 minutes and 10°
- ± 2 minutes and 4°
- ± 1 minutes and 2°

If there is no overlap with the hypocentre of an existing ISC event, a new event is formed. For each candidate hypocentre, a proximity score is otherwise calculated based on differences in time, t, and distance, s, between the candidate hypocentre and a hypocentre in an event with which it could potentially be grouped.

Proximity score $= 2 - (dt/dt_{max}) - (ds/ds_{max})$

where ds_{max} is the maximum distance between hypocentres and dt_{max} the maximum difference in origin time.

As long as there is no duplication of hypocentre (with the same author, origin time and location within tight limits) the candidate hypocentre together with the associated phase data is grouped with the prime hypocentre of the event and the initial dU score is used to reassess the prime hypocentre designation. Apparent duplicated hypocentre estimations, including preliminary solutions relayed by other agencies, need to be assessed to determine whether they should really be split between different events. Should there be two or more equally valid events, these can be assessed in turn and may eventually be merged together.

Grouping by fit of the associated phase arrival data is simpler. The residuals of the arrival data are calculated using ak135 travel times for all suitable prime hypocentres within the widest proximity limits given above for similar hypocentres. The hypocentre and associated phase arrival data is then grouped with the event with the best fitting prime hypocentre, which may similarly be re-designated according to the dU scores. Associations of phase arrival data are updated to be with the prime hypocentre estimate of each ISC event.

It follows that a hypocentre and associated phase arrival data submitted by a reporter will have the reported hypocentre set as the prime hypocentre in the ISC event if no other submitted hypocentre estimate is a closer match. It follows also that a hypocentre submitted without phase data can only be grouped with a similar hypocentre. Generally, early arriving data may be superseded by later arriving data: the data will still be in the ISC database but be deprecated, that is, marked as being no longer useful for further processes.

3.3.2 Association

Association is the automatic procedure, run routinely after grouping, that links reported phase arrivals at IR stations with the prime hypocentres of ISC events. As grouping took care of those phases associated with reported hypocentres, by associating the phases to the respective prime hypocentres of the ISC events without further checks, this procedure is only required for phase arrival observations that were sent without any association of event made for them by the reporter. Currently only 5% of arrival data is sent unassociated compared with 25% ten years ago.

If a phase arrival is found to be very similar to another already reported, it is placed in the same event, otherwise the procedure below is followed.

For associating a phase arrival, suitable events are sought with prime hypocentre origin-times in the window 40 minutes before and 100 s after the arrival time. For each phase arrival and prime hypocentre an ak135 travel-time residual is calculated for either the reported arrival phase name or an alternative from a default list if appropriate. Possible timing errors that are multiples of 60 s (a minute) are considered if the phase arrival is at a station not known to be digitally recording. A reporting likelihood is then determined based on the reported event magnitude: a magnitude default of 3.0 is used if no magnitude is given.

A final score is calculated from the residuals, from the likelihood of the phase observations for the magnitude of the event and from the S-P misfit. A phase arrival along with all other phase arrivals in that reading for the station is then associated with the prime hypocentre with the best score. If no suitable match is found, the reading remains unassociated but may be used at some later stage.

3.3.3 Thresholding

Thresholding is the process determining which events are to be reviewed by the ISC analysts. In former times, before email transmission of data was convenient, all events were reviewed, with magnitudes nearly always 3.5 or above. Nowadays, data contributors are encouraged to send all their data, which are stored in the ISC database. The overwhelming amount of data, including that for many more smaller events and from many more seismograph stations, led to the advent of ISC Comprehensive Bulletin, for all events, and the ISC Reviewed Bulletin, for selected events reviewed by ISC analysts. Thresholding has been under constant review since the start of the 1999 data year.

Several criteria are considered to decide which events merit review. Once a decision is made, whether or not an event is to be reviewed, further criteria are not considered.

In this section, M is the maximum magnitude reported by any agency for the event. The sequence of tests in the automatic decision process for reviewing events is currently:

- All events reported by the International Data Centre (IDC) of the Comprehensive Nuclear-Test-Ban Treaty Organization (CTBTO) are reviewed.
- If M is greater than or equal to 3.5, the event is reviewed.
- If M is less than 2.5, the event is not reviewed.
- If M is unknown, the number of data sources of hypocentres and phase arrivals is used. Care is taken here to avoid counting indirect reports arriving via agencies such as NEIC, CSEM and CASC, which compile regional and global data:
  - If the number of hypocentre authors is greater than two and the maximum epicentral distance of arrival data is greater than 10°, the event is reviewed.
  - If the number of arrival authors is greater than two and the maximum epicentral distance of arrival data is greater than 10°, the event is reviewed.
  - Otherwise the event is not reviewed.
- If M is between 2.5 and 3.5:
  - If the number of hypocentre and seismic arrival authors is less than two, the event is not reviewed.
  - If any bulletin contributing to the event has at least ten stations within 3° and the secondary azimuthal gap (the largest azimuthal gap filled by a single station) is less than 135°, the event is not reviewed.

3.3.4 Location by the ISC

The automatic processes group and associate incoming data into ISC events as indicated above. These data are available to users before review by the ISC analysts but there will be no ISC hypocentre solutions for any of the events. The candidate events due for review by the ISC analysts are determined by the thresholding process, which is why many smaller events remain without an ISC hypocentre solution even after the analyst review.

Several further checks of the data are made in preparation for the analyst review, and initial trial estimates for ISC hypocentres are then generated using the accumulated data. If sufficiently robust, the ISC hypocentre estimation will be retained and be made the prime solution for the event, but this, of course, will itself be subject to the analyst review.

It is important to note that not all reviewed events will have an ISC hypocentre. For the reviewed events certain criteria must be met for an initial ISC location of an event to be made. These criteria are shown below:

- All events with an IDC hypocentre, unless IDC is the only hypocentre author and there are less than six associated phases.
- Two or more reporters of data
- Phase data at epicentral distance $\geq 20°$

The ISC locator also needs an intial seed location; in all events except those with eight or more reporters of data where the existing prime is used, this is calculated using a Neighbourhood Algorithm (NA) (*Sambridge*, 1999; *Sambridge and Kennett*, 2001). More information about the ISC location algorithm and initial seed is given in the next section.

3.4 ISC Location Algorithm

The new ISC location algorithm is described in detail in *Bondár and Storchak* (2011) (doi: 10.1111/j.1365-246X.2011.05107.x, Manual www.isc.ac.uk/iscbulletin/iscloc/); here we give a short summary of the major features. Ever since the ISC came into existence in 1964, it has been committed to providing a homogeneous bulletin that benefits scientific research. Hence the location algorithm used by the ISC, except for some minor modifications, has remained largely unchanged for the past 40 years (*Adams et al.*, 1982; *Bolt*, 1960). While the ISC location procedures have served the scientific community well in the past, they can certainly be improved.

Linearised location algorithms are very sensitive to the initial starting point for the location. The old procedures made the assumption that a good initial hypocentre is available among the reported hypocentres. However, there is no guarantee that any of the reported hypocentres are close to the global minimum in the search space. Furthermore, attempting to find a free-depth solution was futile when the data had no resolving power for depth (e.g. when the first arrival is not within the inflection point of the P travel-time curve). When there was no depth resolution, the algorithm would simply pick a point on the origin time – depth trade-off curve. The old ISC locator assumed that the observational errors are independent. The recent years have seen a phenomenal growth both in the number of reported events and phases, owing to the ever-increasing number of stations worldwide. Similar ray paths will produce correlated travel-time prediction errors due to unmodelled heterogeneities in the Earth, resulting in underestimated location uncertainties and for unfavourable network geometries, location bias. Hence, accounting for correlated travel-time prediction errors becomes imperative if we want to improve (or simply maintain) location accuracy as station networks become progressively denser. Finally, publishing network magnitudes that may have been derived from a single station measurement was rather prone to producing erroneous event magnitude estimates.

To meet the challenge imposed by the ever-increasing data volume from heavily unbalanced networks we introduced a new ISC location algorithm to ensure the efficient handling of data and to further improve the location accuracy of events reviewed by the ISC. The new ISC location algorithm

- Uses all ak135 (*Kennett et al.*, 1995) predicted phases (including depth phases) in the location;
- Obtains the initial hypocentre guess via the Neighbourhood Algorithm (NA) (*Sambridge*, 1999; *Sambridge and Kennett*, 2001);
- Performs iterative linearised inversion using an *a priori* estimate of the full data covariance matrix to account for correlated model errors (*Bondár and McLaughlin*, 2009b);
- Attempts a free-depth solution if and only if there is depth resolution, otherwise it fixes the depth to a region-dependent default depth;
- Scales uncertainties to 90% confidence level and calculates location quality metrics for various distance ranges;
- Obtains a depth-phase depth estimate based on reported surface reflections via depth-phase stacking (*Murphy and Barker*, 2006);
- Provides robust network magnitude estimates with uncertainties.

3.4.1 Seismic Phases

One of the major advantages of using the ak135 travel-time predictions (*Kennett et al.*, 1995) is that they do not suffer from the baseline difference between P, S and PKP phases compared with the Jeffreys-Bullen tables (*Jeffreys and Bullen*, 1940). Furthermore, ak135 offers an abundance of phases from the IASPEI Standard Seismic List (*Storchak et al.*, 2003; 2011) that can be used in the location, most notably the PKP branches and depth-sensitive phases. Elevation and ellipticity corrections (*Dziewonski and Gilbert*, 1976; *Engdahl et al.*, 1998; *Kennett et al.*, 1996), using the WG84 ellipsoid parameters, are added to the ak135 predictions. For depth phases, bounce point (elevation correction at the surface reflection point) and water depth (for pwP) corrections are calculated using the algorithm of *Engdahl et al.* (1998). We use the ETOPO1 global relief model (*Amante and Eakins*, 2009) to obtain the elevation or the water depth at the bounce point.

Phase picking errors are described by *a priori* measurement error estimates derived from the inspection of the distribution of ground truth residuals (residuals calculated with respect to the ground truth location) from the IASPEI Reference Event List (*Bondár and McLaughlin*, 2009a). For phases that do not have a sufficient number of observations in the ground truth database we establish *a priori* measurement errors so that the consistency of the relative weighting schema is maintained. First-arriving P-type phases (P, Pn, Pb, Pg) are picked more accurately than later phases, so their measurement error estimates are the smallest, 0.8 s. The measurement error for first-arriving S-phases (S, Sn, Sb, Sg) is set to 1.5 s. Phases traversing through or reflecting from the inner/outer core of the Earth have somewhat larger (1.3 s for PKP, PKS, PKKP, PKKS and P'P' branches as well as PKiKP, PcP and PcS, and 1.8 s for SKP, SKS, SKKP, SKKS and S'S' branches as well as SKiKP, ScP and ScS) measurement error estimates to account for possible identification errors among the various branches. Free-surface reflections and conversions (PnPn, PbPb, PgPg, PS, PnS, PgS and SnSn, SbSb, SgSg, SP, SPn, SPg) are observed less frequently and with larger uncertainty, and therefore suffer from large, 2.5 s, measurement errors. Similarly, a measurement error of 2.8 s is assigned to the longer period and typically emergent diffracted phases (Pdif, Sdif, PKPdif). The *a priori* measurement error for the commonly observed depth phases (pP, sP, pS, sS and pwP) is set to 1.3 s, while the remaining depth phases (pPKP, sPKP, pSKS, sSKS branches and pPb, sPb, sSb, pPn, sPn, sSn) have the measurement error estimate set to 1.8 s. We set the measurement error estimate to 2.5 s for the less reliable depth phases (pPg, sPg, sSg, pPdif, pSdif, sPdif and sSdif). Note that we also allow for distance-dependent measurement errors. For instance, to account for possible phase identification errors at far-regional distances the *a priori* measurement error for Pn and P is increased from 0.8 s to 1.2 s and for Sn and S from 1.5 s to 1.8 s between 15° and 28°. The measurement errors between 40° and 180° are set to 1.3 s and 1.8 s for the prominent PP and SS arrivals respectively, but they are increased to 1.8 s and 2.5 s between 25° and 40°.

The relative weighting scheme (Figure 3.2) described above ensures that arrivals picked less reliably or prone to phase identification errors are down-weighted in the location algorithm. Since the ISC works with reported parametric data with wildly varying quality, we opted for a rather conservative set of *a priori* measurement error estimates.

3.4.2 Correlated travel-time prediction error structure

Most location algorithms, either linearised or non-linear, assume that all observational errors are independent. This assumption is violated when the separation between stations is less than the scale length of local velocity heterogeneities. When correlated travel-time prediction errors are present, the data covariance matrix is no longer diagonal, and the redundancy in the observations reduces the effective number of degrees of freedom. Thus, ignoring the correlated error structure inevitably results in underestimated location uncertainty estimates. For events located by an unbalanced seismic network this may also lead to a biased location estimate. *Chang et al.* (1983) demonstrated that accounting for correlated error structure in a linearised location algorithm is relatively straightforward once an estimate of the non-diagonal data covariance matrix is available. To determine the data covariance matrix we follow the approach described by *Bondár and McLaughlin* (2009b). They assume that the similarity between ray paths is well approximated by the station separation. This simplifying assumption allows for the estimation of covariances between station pairs from a generic P variogram model derived from ground truth residuals. Because the overwhelming number of phases in the ISC Bulletin is teleseismic P, we expect that the generic variogram model will perform reasonably well anywhere on the globe.

Since in this representation the covariances depend only on station separations, the covariance matrix (and its inverse) needs to be calculated only once. We assume that different phases owing to the different ray paths they travel along as well as station pairs with a separation larger than 1000 km are uncorrelated. Hence, the data covariance matrix is a sparse, block-diagonal matrix. Furthermore, if the stations in

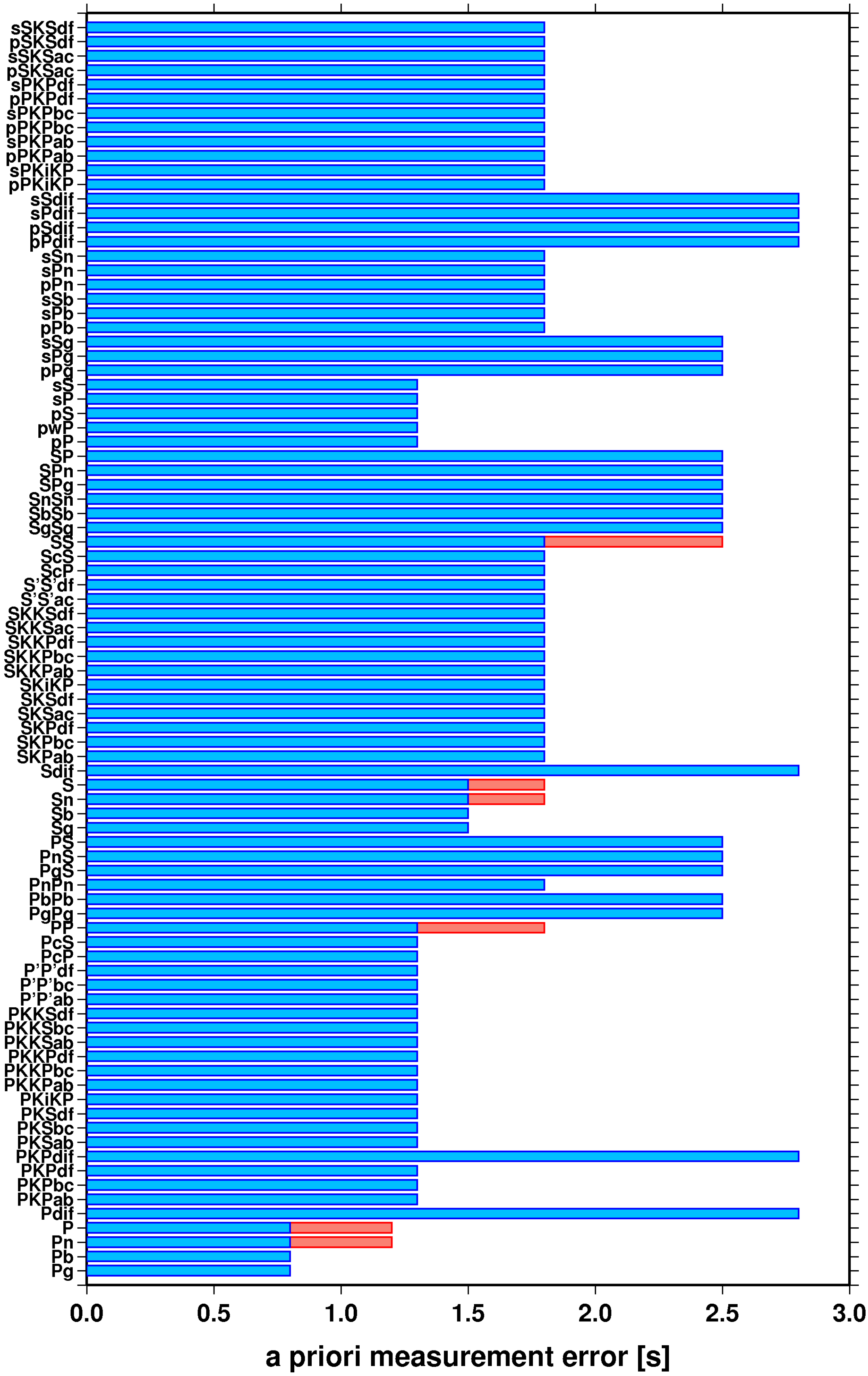

Figure 3.2: A priori *measurement error estimates for phases used in the location algorithm. The red coloured errors are distance-dependent, which are applied for distances when phase identification errors may occur (see text).*

each phase block are ordered by their nearest neighbour distance, the phase blocks themselves become block-diagonal. To reduce the computational time of inverting large matrices we exploit the inherent block-diagonal structure by inverting the covariance matrix block-by-block. The *a priori* measurement error variances are added to the diagonal of the data covariance matrix.

3.4.3 Depth resolution

In principle, depth can be resolved if there is a mixture of upgoing and downgoing waves emanating from the source, that is, if there are stations covering the distance range where the vertical partial derivative of the travel-time of the first-arriving phase changes sign (local networks), or if there are phases with vertical slowness of opposite sign (depth phases). Core reflections, such as PcP, and to a lesser extent, secondary phases (S in particular) could also help in resolving the depth.

We developed a number of criteria to test whether the reported data for an event have sufficient depth resolution:

- local network: one or more stations within 0.2° with time-defining phases
- depth phases: five or more time-defining depth phases reported by at least two agencies (to reduce a chance of misinterpretation by a single inexperienced analyst)
- core reflections: five or more time-defining core reflections (PcP, ScS) reported by at least two agencies
- local/near regional S: five or more time-defining S and P pairs within 3°

We attempt a free-depth solution if any of the above criteria are satisfied; otherwise we fix the depth to a default depth dependent on the epicentre location. The default depth grid was derived from the EHB (*Engdahl et al.*, 1998) free-depth solutions, including the fixed-depth EHB earthquakes that were flagged as having reliable depth estimate (personal communication with Bob Engdahl), as well as from free-depth solutions obtained by the new locator when locating the entire ISC Bulletin data-set. As Figure 3.3 indicates, the default depth grid provides a reasonable depth estimate where seismicity is well established. Note that the depths of known anthropogenic events and landslides are fixed to the surface.

3.4.4 Depth-phase stack

While we use depth phases directly in the location, the depth-phase stacking method (*Murphy and Barker*, 2006) provides an independent means to obtain robust depth estimates. Because the depth obtained from the depth-phase stacking method implicitly depends on the epicentre itself, we perform the depth-phase stack only twice: first, with respect to the initial location in order to obtain a reasonable starting point for the depth in the grid search described in the following section; second, with respect to the final location to obtain the final estimate for the depth-phase constrained depth.

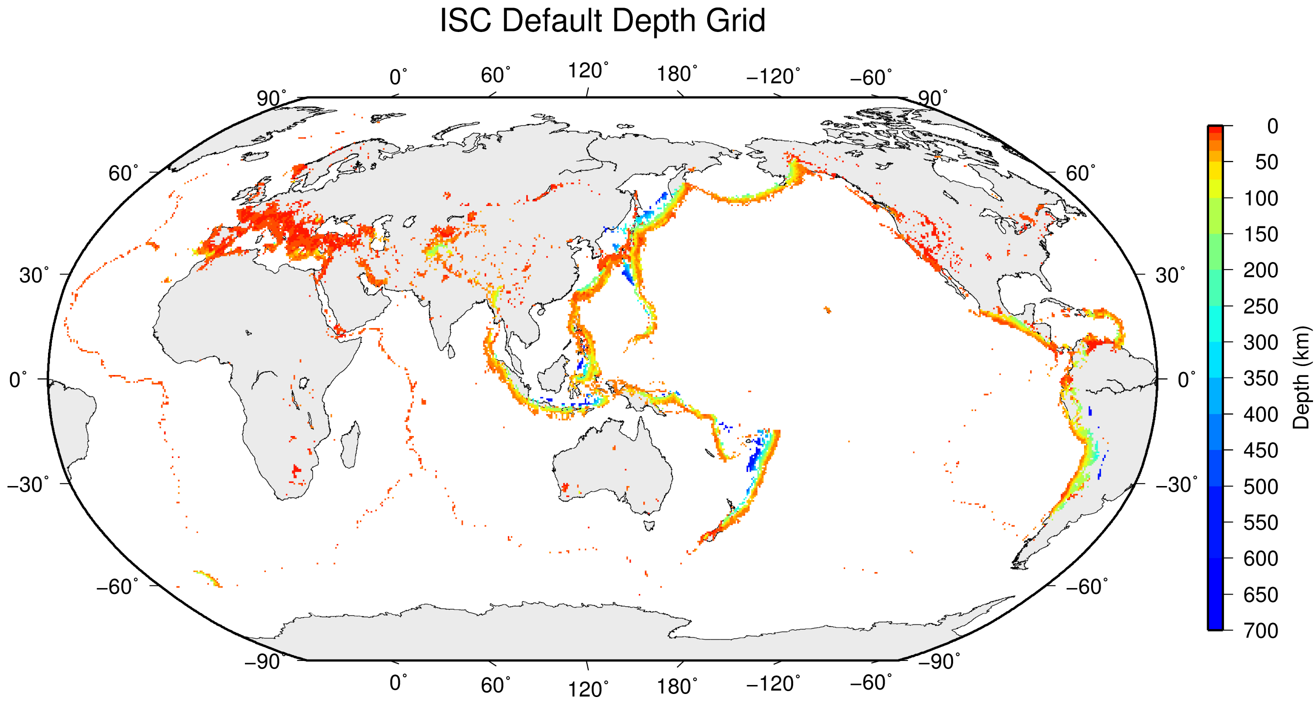

Figure 3.3: *Default depths on a 0.5×0.5 degree grid derived from EHB free-depth solutions and EHB events flagged as reliable depth, as well as free-depth solutions from the entire ISC Bulletin located with the new locator.*

3.4.5 Initial hypocentre

For poorly recorded events the reported hypocentres may exhibit a large scatter and they could suffer from large location errors, especially if they are only recorded teleseismically. In order to obtain a good initial hypocentre guess for the linearised location algorithm we employ the Neighbourhood Algorithm (NA) (*Sambridge*, 1999; *Sambridge and Kennett*, 2001). NA is a nonlinear grid search method capable of exploring a large search space and rapidly closing in on the global optimum. *Kennett* (2006) discusses in detail the NA algorithm and its use for locating earthquakes.

We perform a search around the median of reported hypocentre parameters with a generously defined search region – within a 2° radius circle around the median epicentre, 10 s around the median origin time and 150 km around the median reported depth. These default search parameters were obtained by trial-and-error runs to achieve a compromise between execution time and allowance for gross errors in the median reported hypocentre parameters. Note that if our test for depth resolution fails, we fix the depth to the region-dependent default depth. The initial hypocentre estimate will be the one with the smallest L1-norm misfit among the NA trial hypocentres. Once close to the global optimum, we proceed with the linearised location algorithm to obtain the final solution and corresponding formal uncertainties.

3.4.6 Iterative linearised location algorithm

We adopt the location algorithm described in detail in *Bondár and McLaughlin* (2009b). Recall that in the presence of correlated travel-time prediction errors the data covariance matrix is no longer diagonal. Using the singular value decomposition of the data covariance matrix we construct a projection matrix that orthogonalises the data set and projects redundant observations into the null space. In other words, we solve the inversion problem in the eigen coordinate system in which the transformed observations are independent.

The model covariance matrix yields the four-dimensional error ellipsoid whose projections provide the two-dimensional error ellipse and one-dimensional errors for depth and origin time. These uncertainties are scaled to the 90% confidence level. Note that since we projected the system of equations into the eigen coordinate system, the number of independent observations is less than the total number of observations. Hence, the estimated location error ellipses necessarily become larger, providing a more realistic representation of the location uncertainties. The major advantage of this approach is that the projection matrix is calculated only once for each event location.

3.4.7 Validation tests

To demonstrate improvements due to the new location procedures, we located some 7,200 GT0-5 events in the IASPEI Reference Event List (*Bondár and McLaughlin*, 2009a) both with the old ISC locator (which constitutes the baseline) and with the new location algorithm. We also located the entire (1960-2010) ISC Bulletin, including four years of the International Seismological Summary (ISS, the predecessor of the ISC) catalogue (*Villaseñor and Engdahl*, 2005; 2007).

The location of GT events demonstrated that the new ISC location algorithm provides small but consistent location improvements, considerable improvements in depth determination and significantly more accurate formal uncertainty estimates. Even using a 1-D model and a variogram model that fits teleseismic observations we could achieve realistic uncertainty estimates, as the 90% confidence error ellipses cover the true locations 80-85% of the time. The default depth grid provides reasonable depth estimates where there is seismicity. We have shown that the location and depth accuracy obtained by the new algorithm matches or surpasses the EHB accuracy.

We noted above that the location improvements for the ground truth events are consistent, but minor. This is not surprising as most of the events in the IASPEI Reference Event List are very well-recorded with a small azimuthal gap and dominated by P-type phases. In these circumstances we could expect significant location improvements only for heavily unbalanced networks where large numbers of correlated ray paths conspire to introduce location bias. On the other hand, the ISC Bulletin represents a plethora of station configurations ranging from reasonable to the most unfavourable network geometries. Hence, we could expect more dramatic location improvements when locating the entire ISC Bulletin. Although in this case we cannot measure the improvement in location accuracy due to the lack of ground truth information, we show that with the new locator we obtain significantly better clustering of event locations (Figure 3.4), thus providing an improved view of the seismicity of the Earth.

3.4.8 Magnitude calculation

Currently the ISC locator calculates body and surface wave magnitudes. MS is calculated for shallow events (depth $<$ 60 km) only. At least three station magnitudes are required for a network (mb or MS) magnitude. The network magnitude is defined as the median of the station magnitudes, and its

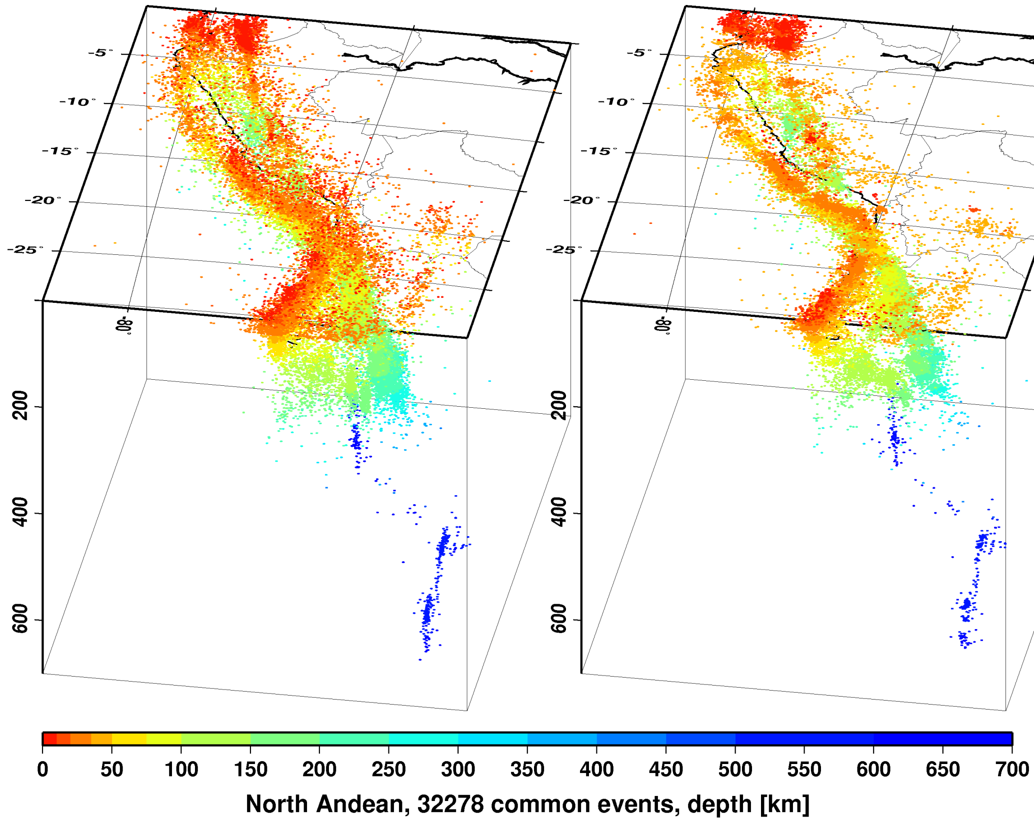

(a)

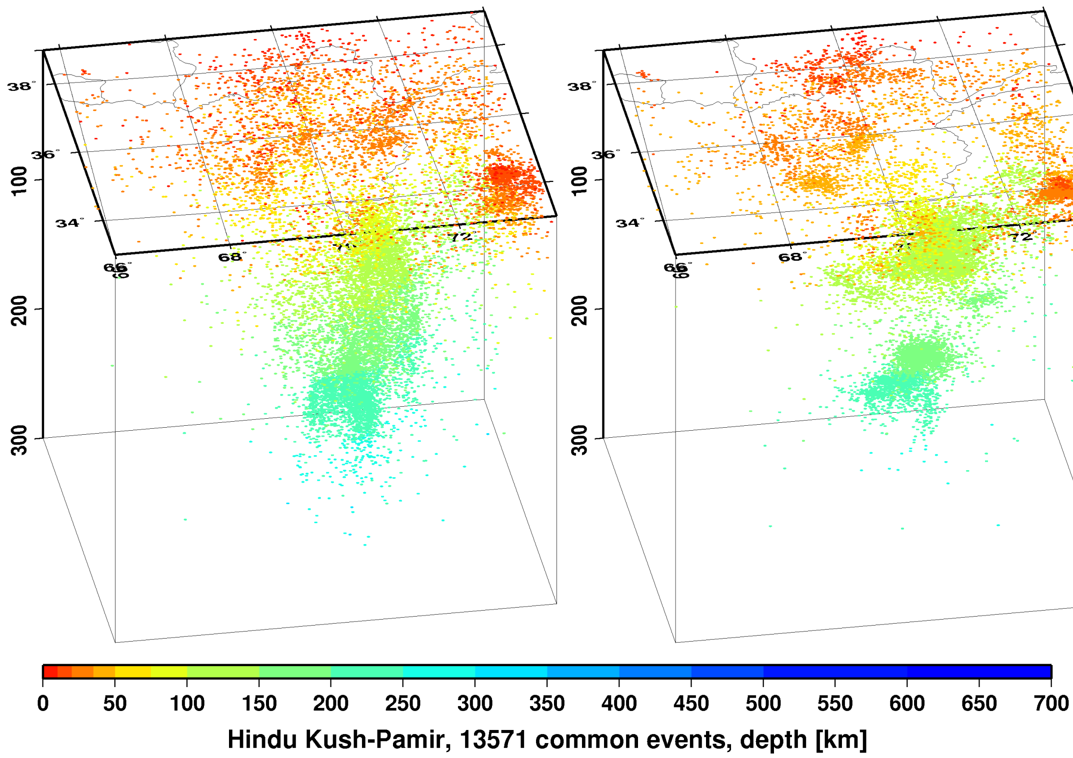

(b)

Figure 3.4: *Comparison of seismicity maps for common events in the reviewed ISC Bulletin (old locator, left) and the located ISC Bulletin (new locator, right) for the North Andean (a) and Hindu Kush - Pamir regions (b). The events are better clustered when located with the new locator.*

uncertainty is defined as the standard median absolute deviation (SMAD) of the alpha-trimmed (*alpha* = 20%) station magnitudes.

The station magnitude is defined as the median of reading magnitudes for a station. The reading magnitude is defined as the magnitude computed from the maximal log(A/T) in a reading. Amplitude magnitudes are calculated for each reported amplitude-period pair.

3.4.9 Body-wave magnitudes

Body-wave magnitudes are calculated for each reported amplitude-period pair, provided that the phase is in the list of phases that can contribute to *mb* (P, pP, sP, AMB, IAmb, pmax), the station is between the epicentral distances $21 - 100°$ and the period is less than 3 s.

A reading contains all parametric data reported by a single agency for an event at a station, and it may have several reported amplitude and periods. The amplitudes are measured as zero-to-peak values in nanometres. For each pair an amplitude *mb* is calculated.

$$mb_{amp} = log(A/T) + Q(\Delta, h) - 3 \tag{3.1}$$

If no amplitude-period pairs are reported for a reading, the body-wave magnitude is calculated using the reported logat values for $log(A/T)$.

$$mb_{amp} = logat + Q(\Delta, h) - 3 \tag{3.2}$$

where the magnitude attenuation $Q(\Delta, h)$ value is calculated using the Gutenberg-Richter tables (*Gutenberg and Richter*, 1956).

For each reading the ISC locator finds the reported amplitude-period pair for which A/T is maximal:

$$mb_{rd} = log(max(A/T)) + Q(\Delta, h) - 3 \tag{3.3}$$

Or, if no amplitude-period pairs were reported for the reading:

$$mb_{rd} = max(logat) + Q(\Delta, h) - 3 \tag{3.4}$$

Several agencies may report data from the same station. The station magnitude is defined as the median of the reading magnitudes for a station.

$$mb_{sta} = median(mb_{rd}) \tag{3.5}$$

Once all station *mb* values are determined, the station magnitudes are sorted and the lower and upper alpha percentiles are made non-defining. The network *mb* and its uncertainty are then calculated as the median and the standard median absolute deviation (SMAD) of the alpha-trimmed station magnitudes, respectively.

3.4.10 Surface-wave magnitudes

Surface-wave magnitudes are calculated for each reported amplitude-period pair, provided that the phase is in the list of phases that can contribute to MS (*AMS, IAMs_20, LR, MLR, M, L*), the station is between the epicentral distances 20 – 160° and the period is between 10 – 60 s.

For each reported amplitude-period pair MS is calculated using the Prague formula (*Vaněk et al.*, 1962). Amplitude MS is calculated for each component (Z, E, N) separately.

$$MS_{amp} = log(A/T) + 1.66 * log(\Delta) + 0.3 \tag{3.6}$$

To calculate the reading MS, the ISC locator first finds the reported amplitude-period pair for which A/T is maximal on the vertical component.

$$MS_Z = log(max(A_Z/T_Z)) + 1.66 * log(\Delta) + 0.3 \tag{3.7}$$

Then it finds the max(A/T) for the E and N components for which the period measured on the horizontal components is within ±5s from the period measured on the vertical component.

$$MS_E = log(max(A_E/T_E)) + 1.66 * log(\Delta) + 0.3 \tag{3.8}$$

$$MS_N = log(max(A_N/T_N)) + 1.66 * log(\Delta) + 0.3 \tag{3.9}$$

The horizontal MS is calculated as

$$max(A/T)h = \begin{cases} \sqrt{2(max(A_E/T_E))^2} & \text{if } MS_N \text{ does not exist} \\ \sqrt{(max(A_E/T_E))^2 + (max(A_N/T_N))^2} & \text{if } MS_E \text{ and } MS_N \text{ exist} \\ \sqrt{2(max(A_N/T_N))^2} & \text{if } MS_E \text{ does not exist} \end{cases} \tag{3.10}$$

$$MS_H = log(max(A/T)_H) + 1.66 * log(\Delta) + 0.3 \tag{3.11}$$

The reading MS is defined as

$$MS = \begin{cases} (MS_Z + MS_H)/2 & \text{if } MS_Z \text{ and } MS_H \text{ exist} \\ MS_H & \text{if } MS_Z \text{ does not exist} \\ MS_Z & \text{if } MS_H \text{ does not exist} \end{cases} \tag{3.12}$$

Several agencies may report data from the same station. The station magnitude is defined as the median of the reading magnitudes for a station.

$$MS_{sta} = median(MS_{rd}) \tag{3.13}$$

Once all station MS values are determined, the station magnitudes are sorted and the lower and upper alpha percentiles are made non-defining. The network MS and its uncertainty are calculated as the median and the standard median absolute deviation (SMAD) of the alpha-trimmed station magnitudes, respectively.

3.5 Review Process

Typically, for each month, the ISC analysts now review approximately 20% of the events in the ISC database, currently 3,500-5,000 per data month. This review is done about 24 months behind real time to allow for the comprehensive collection of data from networks and data centres worldwide.

Users of the ISC Bulletin can be assured that all ISC Bulletin events with an ISC hypocentre solution have been reviewed by the ISC analysts. Not all reviewed events will end up having an ISC hypocentre solution, but events that have not been reviewed are flagged accordingly.

An automatic process creates a monthly listing of the events for the analysts to review. The analysis is performed in batches: thus, events are generally not finalised one at a time, and a completed month of events is published after all the analysis is finished.

The first batch of editing involves careful examination of all events selected for review for the month. The entire month is then reprocessed incorporating the editing changes deemed necessary by the analysts. The analysts next review the same events again in a second pass through the data, checking for each event where there is a change that the result was as could be expected by comparing the revised solution against the initial solution. When the analysts are satisfied with an event, it is no longer revised in a subsequent pass but analysis continues in several passes until all events are considered satisfactory.

The analysts initially print the entire monthly listing, which is split into sections each with about 150 events. Each event, uniquely identified in the monthly printout, shows the reported hypocentres, magnitudes and phase arrivals grouped and associated for the event, as well as an ISC solution of hypocentre, if there is one, along with quality metrics, error estimates, redetermined magnitudes and phase arrival-time residuals. Ancillary information including the geographic region and reported macroseismic observations is also present in the listing for each pass.

The analysts have the capability to execute a variety of commands that can be used to merge or split events, to move phase arrivals or hypocentres from one event to another or to modify the reported phase names. Each of these changes initiates a new revision of the relevant events and ISC hypocentre solutions. There are also several commands to change the starting depth or location in the location algorithm.

The main tasks in reviewing the ISC Bulletin are to:

1. Check that the grouping of hypocentres and association of phase arrivals is appropriate.
2. Check that the depth and location is appropriate for the region and reported phase arrivals.
3. Check that no data are missing for an event, given the region and magnitude, and that included data are appropriate.

4. Examine the phase arrival-time residuals to check that the ISC hypocentre solution is appropriate.
5. Look for outliers in the observations and for misassociated phases.

As well as examining each event closely, it is also important to scan the hypocentres and phase arrivals of adjacent events, close in time and space, to ensure that there is uniformity in the composition of the events. In some cases, two events should be merged into one event, as apparent in some other case. In other cases, one apparent event needs to be split into two events, when the automatic grouping has erroneously created one event with more than one reported hypocentre out of the observations for two real events that are distinct but closely occurring.

Misassociated phase arrivals are returned to the unassociated data stream, if not immediately placed by the analyst in another event where they belong, These unassociated phases are then available to be associated with some other event if the time and location is appropriate. The analysts also check that no phase is associated to more than one event.

Towards the end of the monthly analysis, the ISC 'Search' procedure runs, attempting to build events from the remaining set of unassociated phase arrivals. The algorithm is based on the methodology of *Engdahl and Gunst* (1966). Candidate events are validated or rejected by attempting to find ISC hypocentres for them using the ISC locator. The surviving events are then reviewed. Those events with phase arrival observations reported by stations from at least two networks are added to the ISC Bulletin if the solutions meet the standards set by the ISC analysts. These events have only an ISC determination of hypocentre.

At the end of analysis for a data month, a set of final checks is run for quality control, with the results reviewed by an analyst and the defects rectified. These are checks for inconsistencies and errors to ensure the general integrity of the ISC Bulletin.

3.6 History of Operational Changes

- From data-month January 2001 onwards, both P and S groups of arrival times are used in location.
- From data-month September 2002 onwards, the printed ISC Bulletins have been generated directly from the ISC Relational Database.
- From data-month October 2002, a new location program ISCloc has been used in operations. Also, the IASPEI standard phase list has now been adopted by the ISC. Please see Section 6.1 for details.
- From data-month January 2003 onwards, an updated regionalisation scheme has been adopted (*Young et al.*, 1996).
- From data-month January 2006 the ISC hypocentres are computed using the *ak135* earth velocity model (*Kennett et al.*, 1995) and then reviewed by ISC seismologists. The ISC still produces the hypocentre solutions based on Jeffreys-Bullen travel time tables (agency code ISCJB), yet these solutions are no longer reviewed.

  The ISC is planning to re-compute the entire ISC dataset using *ak135* once new procedures for the rebuild are designed, tested, discussed and approved by the ISC Governing Council. Until that time the automatic ISCJB locations will continue to be produced alongside the *ak135* solutions to maintain the long-time continuity of the ISC Bulletin.

- From data-month January 2009, a new location program (*Bondár and Storchak*, 2011) has been used in operations. The new program uses all predicted *ak135* phases and accounts for correlated model errors. An overview of the location algorithm is provided in this volume (Section 3.4).

4

Availability of the ISC Bulletin

The ISC Bulletin is available from the following sources:

- Web searches
  The entire ISC Bulletin is available directly from the ISC website via tailored searches.
  (www.isc.ac.uk/iscbulletin/search)
  (isc-mirror.iris.washington.edu/iscbulletin/search)
  - Bulletin search - provides the most verbose output of the ISC Bulletin in ISF or QuakeML.
  - Event catalogue - only outputs the prime hypocentre for each event, producing a simple list of events, locations and magnitudes.
  - Arrivals - search for arrivals in the ISC Bulletin. Users can search for specific phases for selected stations and events.
- CD-ROMs/DVD-ROMs

  CDs/DVDs can be ordered from the ISC for any published volume (one per year), or for all back issues of the Bulletin (not including the latest volume). The data discs contain the Bulletin as a PDF, in IASPEI Seismic Format (ISF), and in Fixed Format Bulletin (FFB) format. An event catalogue is also included, together with the International Registry of seismic station codes.
- FTP site

  The ISC Bulletin is also available to download from the ISC ftp site, which contains the Bulletin in PDF, ISF and FFB formats. (ftp://www.isc.ac.uk)
  (ftp://isc-mirror.iris.washington.edu)

Mirror service

A mirror of the ISC database, website and ftp site is available at IRIS DMC (isc-mirror.iris.washington.edu), which benefits from their high-speed internet connection, providing an alternative method of accessing the ISC Bulletin.

5

Citing the International Seismological Centre

Data from the ISC should always be cited. This includes use by academic or commercial organisations, as well as individuals. A citation should show how the data were retrieved and may be in one of these suggested forms:

Data retrieved from the ISC web site:

- International Seismological Centre, On-line Bulletin, http://www.isc.ac.uk, Internatl. Seis. Cent., Thatcham, United Kingdom, 2013.

Data transcribed from the IASPEI reference event bulletin:

- International Seismological Centre, Reference Event Bulletin, http://www.isc.ac.uk, Internatl. Seis. Cent., Thatcham, United Kingdom, 2013.

Data transcribed from the EHB bulletin:

- International Seismological Centre, EHB Bulletin, http://www.isc.ac.uk, Internatl. Seis. Cent., Thatcham, United Kingdom, 2013.

Data copied from ISC CD-ROMs/DVD-ROMs:

- International Seismological Centre, Bulletin Disks 1-22 [CD-ROM], Internatl. Seis. Cent., Thatcham, United Kingdom, 2013.

Data transcribed from the printed Bulletin:

- International Seismological Centre, Bull. Internatl. Seis. Cent., 48(1), Thatcham, United Kingdom, 2013.

The ISC is named as a valid data centre for citations within American Geophysical Union (AGU) publications. As such, please follow the AGU guidelines when referencing ISC data in one of their journals. The ISC may be cited as both the institutional author of the Bulletin and the source from which the data were retrieved.

BibTex entry example:

@manual{ISCcitation2013,
author = "International Seismological Centre",

title = "On-line Bulletin",
organization = "Int. Seis. Cent.",
note = "http://www.isc.ac.uk",
address = "Thatcham, United Kingdom",
year = "2013"
}

6

IASPEI Standards

6.1 Standard Nomenclature of Seismic Phases

The following list of seismic phases was approved by the IASPEI Commission on Seismological Observation and Interpretation (CoSOI) and adopted by IASPEI on 9th July 2003. More details can be found in *Storchak et al.* (2003) and *Storchak et al.* (2011). Ray paths for some of these phases are shown in Figures 6.1–6.6.

Crustal Phases

Pg	At short distances, either an upgoing P wave from a source in the upper crust or a P wave bottoming in the upper crust. At larger distances also, arrivals caused by multiple P-wave reverberations inside the whole crust with a group velocity around 5.8 km/s.
Pb	Either an upgoing P wave from a source in the lower crust or a P wave bottoming in the lower crust (alt: P*)
Pn	Any P wave bottoming in the uppermost mantle or an upgoing P wave from a source in the uppermost mantle
PnPn	Pn free-surface reflection
PgPg	Pg free-surface reflection
PmP	P reflection from the outer side of the Moho
PmPN	PmP multiple free surface reflection; N is a positive integer. For example, PmP2 is PmPPmP.
PmS	P to S reflection/conversion from the outer side of the Moho
Sg	At short distances, either an upgoing S wave from a source in the upper crust or an S wave bottoming in the upper crust. At larger distances also, arrivals caused by superposition of multiple S-wave reverberations and SV to P and/or P to SV conversions inside the whole crust.
Sb	Either an upgoing S wave from a source in the lower crust or an S wave bottoming in the lower crust (alt: S*)
Sn	Any S wave bottoming in the uppermost mantle or an upgoing S wave from a source in the uppermost mantle
SnSn	Sn free-surface reflection
SgSg	Sg free-surface reflection
SmS	S reflection from the outer side of the Moho
SmSN	SmS multiple free-surface reflection; N is a positive integer. For example, SmS2 is SmSSmS.
SmP	S to P reflection/conversion from the outer side of the Moho
Lg	A wave group observed at larger regional distances and caused by superposition of multiple S-wave reverberations and SV to P and/or P to SV conversions inside the whole crust. The maximum energy travels with a group velocity of approximately 3.5 km/s
Rg	Short-period crustal Rayleigh wave

Mantle Phases

P	A longitudinal wave, bottoming below the uppermost mantle; also an upgoing longitudinal wave from a source below the uppermost mantle
PP	Free-surface reflection of P wave leaving a source downward
PS	P, leaving a source downward, reflected as an S at the free surface. At shorter distances the first leg is represented by a crustal P wave.
PPP	Analogous to PP
PPS	PP which is converted to S at the second reflection point on the free surface; travel time matches that of PSP
PSS	PS reflected at the free surface
PcP	P reflection from the core-mantle boundary (CMB)
PcS	P converted to S when reflected from the CMB
PcPN	PcP reflected from the free surface N - 1 times; N is a positive integer. For example PcP2 is PcPPcP.
Pz+P	(alt: PzP) P reflection from outer side of a discontinuity at depth z; z may be a positive numerical value in km. For example, P660+P is a P reflection from the top of the 660 km discontinuity.
Pz-P	P reflection from inner side of a discontinuity at depth z. For example, P660-P is a P reflection from below the 660 km discontinuity, which means it is precursory to PP.
Pz+S	(alt:PzS) P converted to S when reflected from outer side of discontinuity at depth z
Pz-S	P converted to S when reflected from inner side of discontinuity at depth z
PScS	P (leaving a source downward) to ScS reflection at the free surface
Pdif	P diffracted along the CMB in the mantle (old: Pdiff)
S	Shear wave, bottoming below the uppermost mantle; also an upgoing shear wave from a source below the uppermost mantle
SS	Free-surface reflection of an S wave leaving a source downward
SP	S, leaving a source downward, reflected as P at the free surface. At shorter distances the second leg is represented by a crustal P wave.
SSS	Analogous to SS
SSP	SS converted to P when reflected from the free surface; travel time matches that of SPS
SPP	SP reflected at the free surface
ScS	S reflection from the CMB
ScP	S converted to P when reflected from the CMB
ScSN	ScS multiple free-surface reflection; N is a positive integer. For example ScS2 is ScSScS.
Sz+S	S reflection from outer side of a discontinuity at depth z; z may be a positive numerical value in km. For example S660+S is an S reflection from the top of the 660 km discontinuity. (alt: SzS)
Sz-S	S reflection from inner side of discontinuity at depth z. For example, S660-S is an S reflection from below the 660 km discontinuity, which means it is precursory to SS.
Sz+P	(alt: SzP) S converted to P when reflected from outer side of discontinuity at depth z
Sz-P	S converted to P when reflected from inner side of discontinuity at depth z
ScSP	ScS to P reflection at the free surface
Sdif	S diffracted along the CMB in the mantle (old: Sdiff)

Core Phases

PKP	Unspecified P wave bottoming in the core (alt: P')
PKPab	P wave bottoming in the upper outer core; ab indicates the retrograde branch of the PKP caustic (old: PKP2)
PKPbc	P wave bottoming in the lower outer core; bc indicates the prograde branch of the PKP caustic (old: PKP1)
PKPdf	P wave bottoming in the inner core (alt: PKIKP)

PKPpre	A precursor to PKPdf due to scattering near or at the CMB (old: PKhKP)
PKPdif	P wave diffracted at the inner core boundary (ICB) in the outer core
PKS	Unspecified P wave bottoming in the core and converting to S at the CMB
PKSab	PKS bottoming in the upper outer core
PKSbc	PKS bottoming in the lower outer core
PKSdf	PKS bottoming in the inner core
P'P'	Free-surface reflection of PKP (alt: PKPPKP)
P'N	PKP reflected at the free surface N - 1 times; N is a positive integer. For example, P'3 is P'P'P'. (alt: PKPN)
P'z-P'	PKP reflected from inner side of a discontinuity at depth z outside the core, which means it is precursory to P'P'; z may be a positive numerical value in km
P'S'	(alt: PKPSKS) PKP converted to SKS when reflected from the free surface; other examples are P'PKS, P'SKP
PS'	P (leaving a source downward) to SKS reflection at the free surface (alt: PSKS)
PKKP	Unspecified P wave reflected once from the inner side of the CMB
PKKPab	PKKP bottoming in the upper outer core
PKKPbc	PKKP bottoming in the lower outer core
PKKPdf	PKKP bottoming in the inner core
PNKP	P wave reflected N - 1 times from inner side of the CMB; N is a positive integer.
PKKPpre	A precursor to PKKP due to scattering near the CMB
PKiKP	P wave reflected from the inner core boundary (ICB)
PKNIKP	P wave reflected N - 1 times from the inner side of the ICB
PKJKP	P wave traversing the outer core as P and the inner core as S
PKKS	P wave reflected once from inner side of the CMB and converted to S at the CMB
PKKSab	PKKS bottoming in the upper outer core
PKKSbc	PKKS bottoming in the lower outer core
PKKSdf	PKKS bottoming in the inner core
PcPP'	PcP to PKP reflection at the free surface; other examples are PcPS', PcSP', PcSS', PcPSKP, PcSSKP. (alt: PcPPKP)
SKS	unspecified S wave traversing the core as P (alt: S')
SKSac	SKS bottoming in the outer core
SKSdf	SKS bottoming in the inner core (alt: SKIKS)
SPdifKS	SKS wave with a segment of mantleside Pdif at the source and/or the receiver side of the ray path (alt: SKPdifS)
SKP	Unspecified S wave traversing the core and then the mantle as P
SKPab	SKP bottoming in the upper outer core
SKPbc	SKP bottoming in the lower outer core
SKPdf	SKP bottoming in the inner core
S'S'	Free-surface reflection of SKS (alt: SKSSKS)
S'N	SKS reflected at the free surface N - 1 times; N is a positive integer
S'z-S'	SKS reflected from inner side of discontinuity at depth z outside the core, which means it is precursory to S'S'; z may be a positive numerical value in km.
S'P'	(alt: SKSPKP) SKS converted to PKP when reflected from the free surface; other examples are S'SKP, S'PKS.
S'P	(alt: SKSP) SKS to P reflection at the free surface
SKKS	Unspecified S wave reflected once from inner side of the CMB
SKKSac	SKKS bottoming in the outer core
SKKSdf	SKKS bottoming in the inner core
SNKS	S wave reflected N - 1 times from inner side of the CMB; N is a positive integer.
SKiKS	S wave traversing the outer core as P and reflected from the ICB
SKJKS	S wave traversing the outer core as P and the inner core as S
SKKP	S wave traversing the core as P with one reflection from the inner side of the CMB and then continuing as P in the mantle

SKKPab	SKKP bottoming in the upper outer core
SKKPbc	SKKP bottoming in the lower outer core
SKKPdf	SKKP bottoming in the inner core
ScSS'	ScS to SKS reflection at the free surface; other examples are ScPS', ScSP', ScPP', ScSSKP, ScPSKP. (alt: ScSSKS)

Near-source Surface reflections (Depth Phases)

pP*y*	All P-type onsets (P*y*), as defined above, which resulted from reflection of an upgoing P wave at the free surface or an ocean bottom. WARNING: The character *y* is only a wild card for any seismic phase, which could be generated at the free surface. Examples are pP, pPKP, pPP, pPcP, etc.
sP*y*	All P*y* resulting from reflection of an upgoing S wave at the free surface or an ocean bottom; for example, sP, sPKP, sPP, sPcP, etc.
pS*y*	All S-type onsets (S*y*), as defined above, which resulted from reflection of an upgoing P wave at the free surface or an ocean bottom; for example, pS, pSKS, pSS, pScP, etc.
sS*y*	All S*y* resulting from reflection of an upgoing S wave at the free surface or an ocean bottom; for example, sSn, sSS, sScS, sSdif, etc.
pwP*y*	All P*y* resulting from reflection of an upgoing P wave at the ocean's free surface
pmP*y*	All P*y* resulting from reflection of an upgoing P wave from the inner side of the Moho

Surface Waves

L	Unspecified long-period surface wave
LQ	Love wave
LR	Rayleigh wave
G	Mantle wave of Love type
G*N*	Mantle wave of Love type; *N* is integer and indicates wave packets traveling along the minor arcs (odd numbers) or major arc (even numbers) of the great circle
R	Mantle wave of Rayleigh type
R*N*	Mantle wave of Rayleigh type; *N* is integer and indicates wave packets traveling along the minor arcs (odd numbers) or major arc (even numbers) of the great circle
PL	Fundamental leaking mode following P onsets generated by coupling of P energy into the waveguide formed by the crust and upper mantle SPL S wave coupling into the PL waveguide; other examples are SSPL, SSSPL.

Acoustic Phases

H	A hydroacoustic wave from a source in the water, which couples in the ground
HPg	H phase converted to Pg at the receiver side
HSg	H phase converted to Sg at the receiver side
HRg	H phase converted to Rg at the receiver side
I	An atmospheric sound arrival which couples in the ground
IPg	I phase converted to Pg at the receiver side
ISg	I phase converted to Sg at the receiver side
IRg	I phase converted to Rg at the receiver side
T	A tertiary wave. This is an acoustic wave from a source in the solid earth, usually trapped in a low-velocity oceanic water layer called the SOFAR channel (SOund Fixing And Ranging).
TPg	T phase converted to Pg at the receiver side
TSg	T phase converted to Sg at the receiver side
TRg	T phase converted to Rg at the receiver side

Amplitude Measurement Phases

The following set of amplitude measurement names refers to the IASPEI Magnitude Standard (see www.iaspei.org/commissions/CSOI/Summary_of_WG_recommendations.pdf) compliance to which is indicated by the presence of leading letter I. The absence of leading letter I indicates that a measurement is non-standard. Letter A indicates a measurement in nm made on a displacement seismogram, whereas letter V indicates a measurement in nm/s made on a velocity seismogram.

IAML	Displacement amplitude measured according to the IASPEI standard for local magnitude ML
IAMs_20	Displacement amplitude measured according to IASPEI standard for surface-wave magnitude $MS(20)$
IVMs_BB	Velocity amplitude measured according to IASPEI standard for broadband surface-wave magnitude $MS(BB)$
IAmb	Displacement amplitude measured according to IASPEI standard for short-period teleseismic body-wave magnitude mb
IVmB_BB	Velocity amplitude measured according to IASPEI standard for broadband teleseismic body-wave magnitude $mB(BB)$
AX_IN	Displacement amplitude of phase of type X (e.g., PP, S, etc), measured on an instrument of type IN (e.g., SP - short-period, LP - long-period, BB - broadband)
VX_IN	Velocity amplitude of phase of type X and instrument of type IN (as above)
A	Unspecified displacement amplitude measurement
V	Unspecified velocity amplitude measurement
AML	Displacement amplitude measurement for nonstandard local magnitude
AMs	Displacement amplitude measurement for nonstandard surface-wave magnitude
Amb	Displacement amplitude measurement for nonstandard short-period body-wave magnitude
AmB	Displacement amplitude measurement for nonstandard medium to long-period body-wave magnitude
END	Time of visible end of record for duration magnitude

Unidentified Arrivals

x	unidentified arrival (old: i, e, NULL)
rx	unidentified regional arrival (old: i, e, NULL)
tx	unidentified teleseismic arrival (old: i, e, NULL)
Px	unidentified arrival of P type (old: i, e, NULL, (P), P?)
Sx	unidentified arrival of S type (old: i, e, NULL, (S), S?)

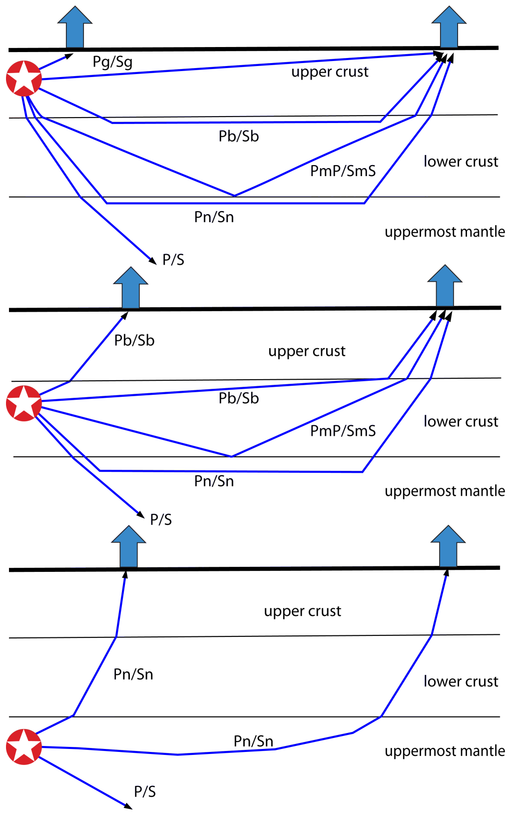

Figure 6.1: *Seismic 'crustal phases' observed in the case of a two-layer crust in local and regional distance ranges (0°<D< about 20°) from the seismic source in the: upper crust (top); lower crust (middle); and uppermost mantle (bottom).*

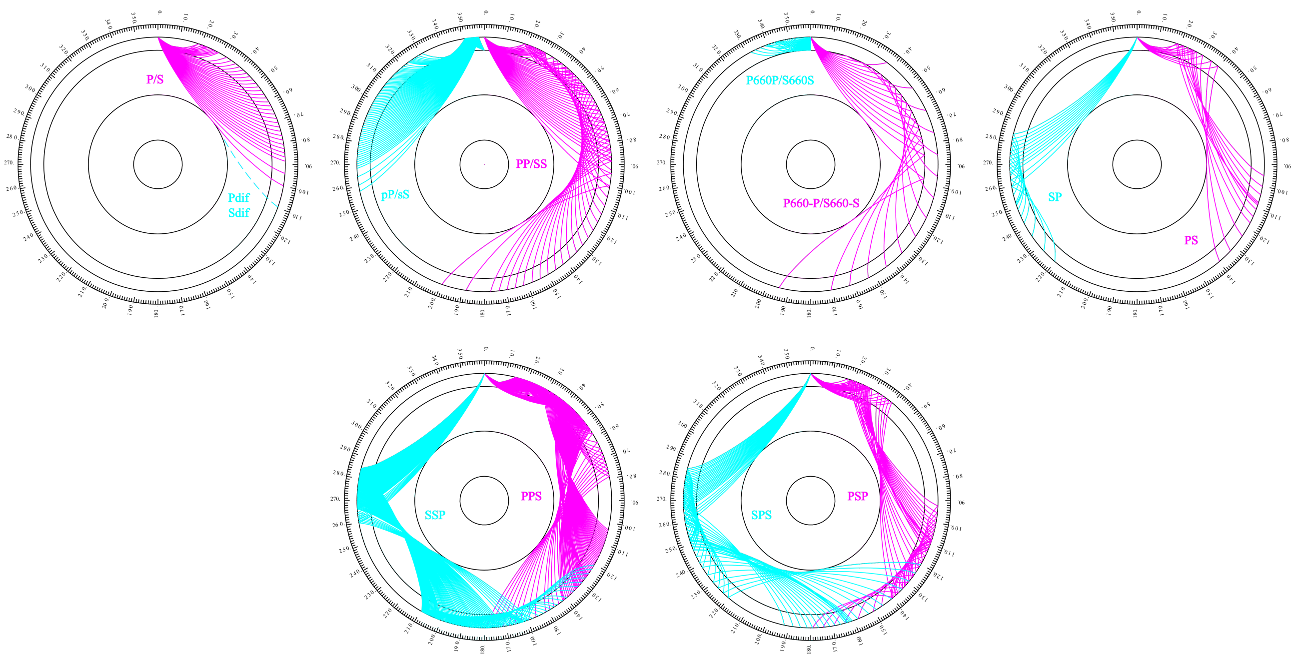

Figure 6.2: *Mantle phases observed at the teleseismic distance range D > about 20°.*

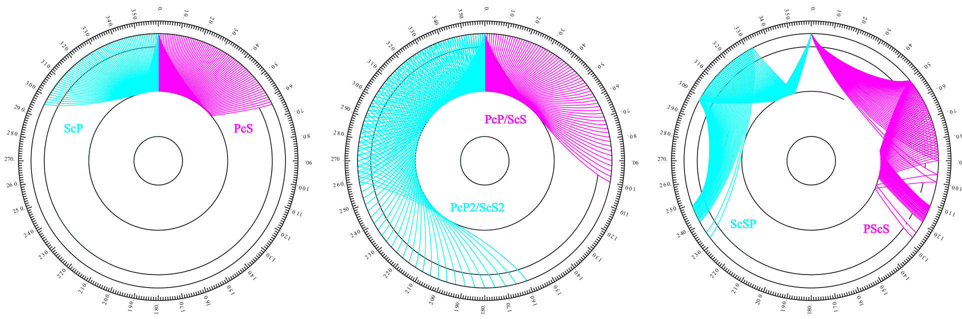

Figure 6.3: *Reflections from the Earth's core.*

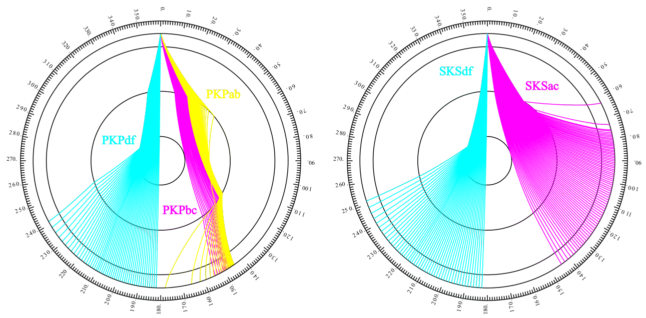

Figure 6.4: *Seismic rays of direct core phases.*

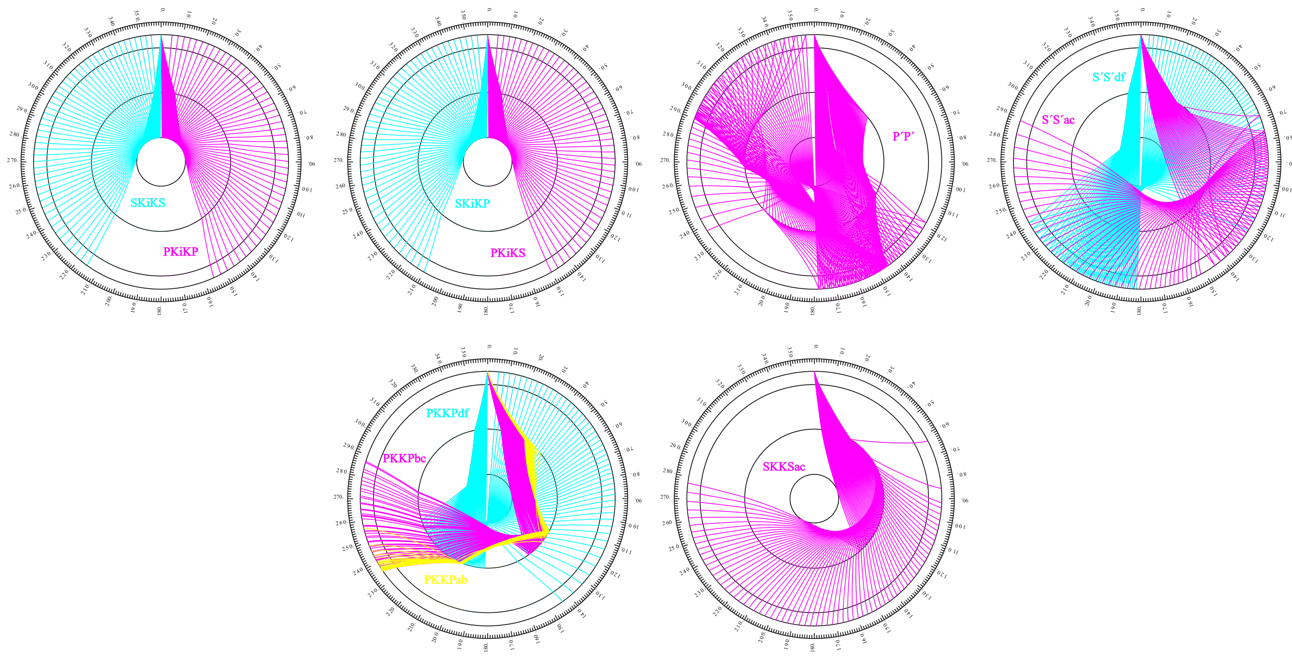

Figure 6.5: *Seismic rays of single-reflected core phases.*

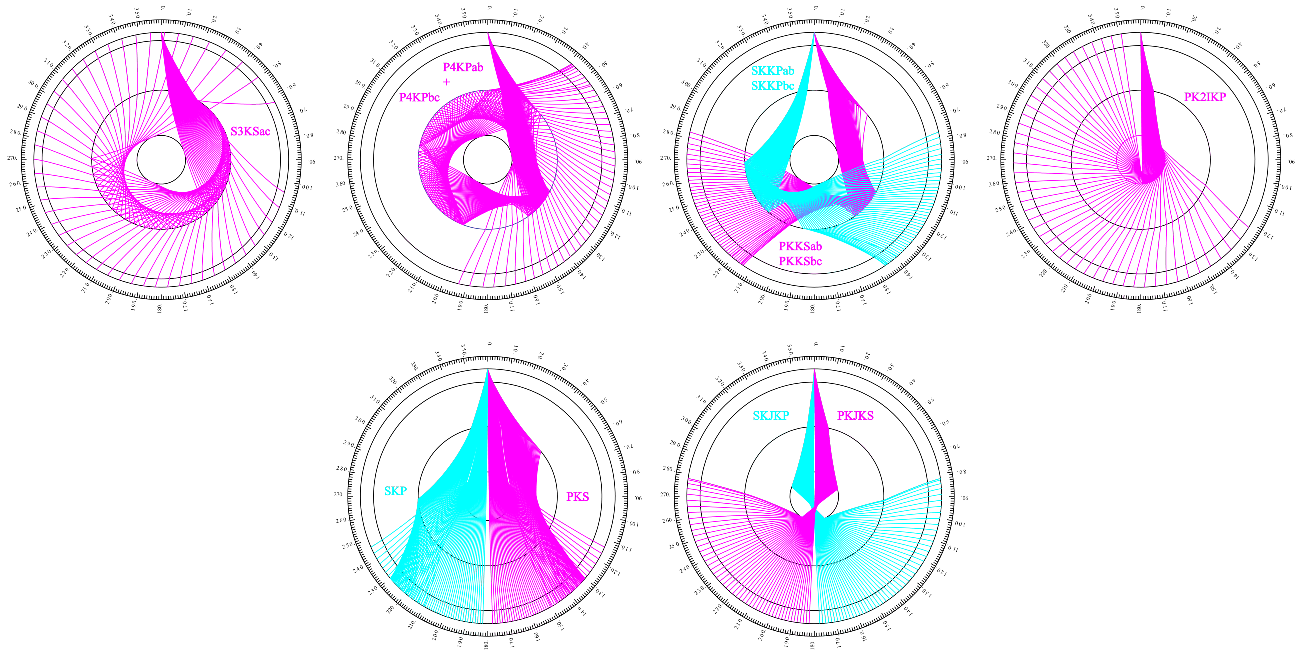

Figure 6.6: *Seismic rays of multiple-reflected and converted core phases.*

6.2 Flinn-Engdahl Regions

The Flinn-Engdahl regions were first proposed by *Flinn and Engdahl* (1965), with the standard defined by *Flinn et al.* (1974). The latest version of the schema, published by *Young et al.* (1996), divides the Earth into 50 seismic regions (Figure 6.7), which are further subdivided producing a total of 754 geographical regions (listed below). The geographic regions are numbered 1 to 757 with regions 172, 299 and 550 no longer in use. The boundaries of these regions are defined at one-degree intervals.

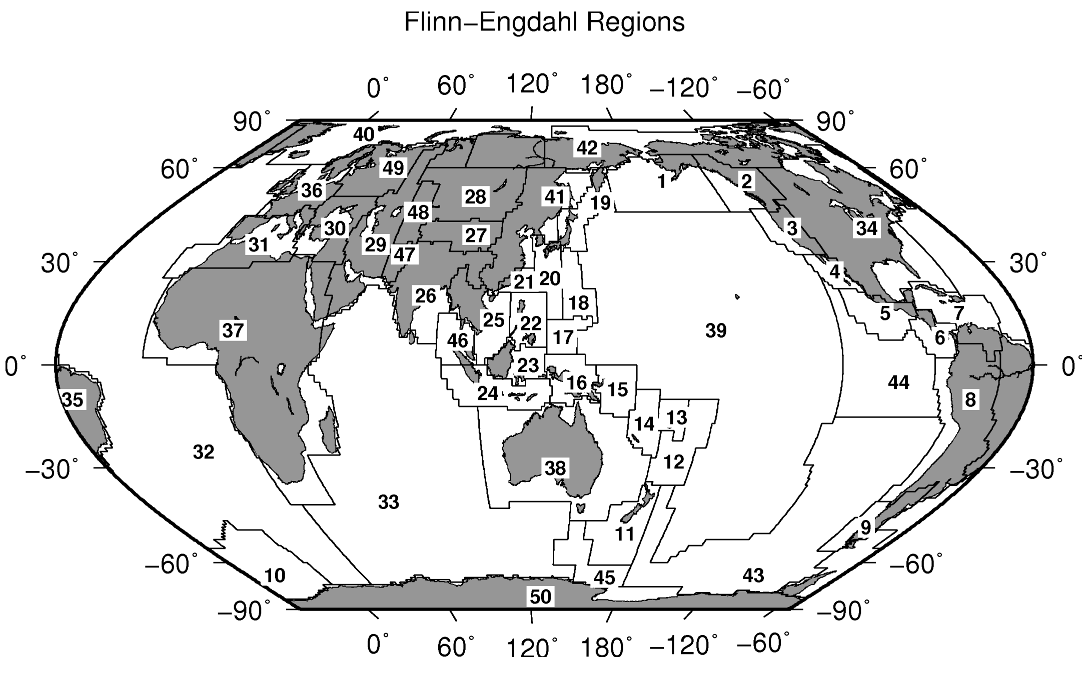

Figure 6.7: *Map of all Flinn-Engdahl seismic regions.*

Seismic Region 1
Alaska-Aleutian Arc
1. Central Alaska
2. Southern Alaska
3. Bering Sea
4. Komandorsky Islands region
5. Near Islands
6. Rat Islands
7. Andreanof Islands
8. Pribilof Islands
9. Fox Islands
10. Unimak Island region
11. Bristol Bay
12. Alaska Peninsula
13. Kodiak Island region
14. Kenai Peninsula
15. Gulf of Alaska
16. South of Aleutian Islands
17. South of Alaska

Seismic Region 2
Eastern Alaska to Vancouver Island
18. Southern Yukon Territory
19. Southeastern Alaska
20. Off coast of southeastern Alaska
21. West of Vancouver Island
22. Queen Charlotte Islands region
23. British Columbia
24. Alberta
25. Vancouver Island region
26. Off coast of Washington
27. Near coast of Washington
28. Washington-Oregon border region
29. Washington

Seismic Region 3
California-Nevada Region
30. Off coast of Oregon
31. Near coast of Oregon
32. Oregon
33. Western Idaho
34. Off coast of northern California
35. Near coast of northern California
36. Northern California
37. Nevada
38. Off coast of California
39. Central California
40. California-Nevada border region
41. Southern Nevada
42. Western Arizona
43. Southern California
44. California-Arizona border region
45. California-Baja California border region
46. Western Arizona-Sonora border region

Seismic Region 4
Lower California and Gulf of California
47. Off west coast of Baja California
48. Baja California
49. Gulf of California
50. Sonora
51. Off coast of central Mexico
52. Near coast of central Mexico

Seismic Region 5
Mexico-Guatemala Area
53. Revilla Gigedo Islands region
54. Off coast of Jalisco
55. Near coast of Jalisco
56. Near coast of Michoacan
57. Michoacan
58. Near coast of Guerrero
59. Guerrero
60. Oaxaca
61. Chiapas
62. Mexico-Guatemala border region
63. Off coast of Mexico
64. Off coast of Michoacan
65. Off coast of Guerrero
66. Near coast of Oaxaca
67. Off coast of Oaxaca
68. Off coast of Chiapas
69. Near coast of Chiapas
70. Guatemala
71. Near coast of Guatemala
730. Northern East Pacific Rise

Seismic Region 6
Central America
72. Honduras
73. El Salvador
74. Near coast of Nicaragua
75. Nicaragua
76. Off coast of central America
77. Off coast of Costa Rica
78. Costa Rica
79. North of Panama
80. Panama-Costa Rica border region
81. Panama
82. Panama-Colombia border region
83. South of Panama

Seismic Region 7
Caribbean Loop
84. Yucatan Peninsula
85. Cuba region
86. Jamaica region
87. Haiti region
88. Dominican Republic region
89. Mona Passage
90. Puerto Rico region
91. Virgin Islands
92. Leeward Islands
93. Belize
94. Caribbean Sea
95. Windward Islands
96. Near north coast of Colombia
97. Near coast of Venezuela
98. Trinidad
99. Northern Colombia
100. Lake Maracaibo
101. Venezuela
731. North of Honduras

Seismic Region 8
Andean South America
102. Near west coast of Colombia
103. Colombia
104. Off coast of Ecuador
105. Near coast of Ecuador
106. Colombia-Ecuador border region
107. Ecuador
108. Off coast of northern Peru
109. Near coast of northern Peru
110. Peru-Ecuador border region
111. Northern Peru
112. Peru-Brazil border region
113. Western Brazil
114. Off coast of Peru
115. Near coast of Peru
116. Central Peru
117. Southern Peru
118. Peru-Bolivia border region
119. Northern Bolivia
120. Central Bolivia
121. Off coast of northern Chile
122. Near coast of northern Chile
123. Northern Chile
124. Chile-Bolivia border region
125. Southern Bolivia
126. Paraguay
127. Chile-Argentina border region
128. Jujuy Province
129. Salta Province
130. Catamarca Province
131. Tucuman Province
132. Santiago del Estero Province
133. Northeastern Argentina
134. Off coast of central Chile
135. Near coast of central Chile
136. Central Chile
137. San Juan Province
138. La Rioja Province
139. Mendoza Province

140. San Luis Province
141. Cordoba Province
142. Uruguay

Seismic Region 9
Extreme South America
143. Off coast of southern Chile
144. Southern Chile
145. Southern Chile-Argentina border region
146. Southern Argentina

Seismic Region 10
Southern Antilles
147. Tierra del Fuego
148. Falkland Islands region
149. Drake Passage
150. Scotia Sea
151. South Georgia Island region
152. South Georgia Rise
153. South Sandwich Islands region
154. South Shetland Islands
155. Antarctic Peninsula
156. Southwestern Atlantic Ocean
157. Weddell Sea
732. East of South Sandwich Islands

Seismic Region 11
New Zealand Region
158. Off west coast of North Island
159. North Island
160. Off east coast of North Island
161. Off west coast of South Island
162. South Island
163. Cook Strait
164. Off east coast of South Island
165. North of Macquarie Island
166. Auckland Islands region
167. Macquarie Island region
168. South of New Zealand

Seismic Region 12
Kermadec-Tonga-Samoa Area
169. Samoa Islands region
170. Samoa Islands
171. South of Fiji Islands
172. West of Tonga Islands (REGION NOT IN USE)
173. Tonga Islands
174. Tonga Islands region
175. South of Tonga Islands
176. North of New Zealand
177. Kermadec Islands region
178. Kermadec Islands
179. South of Kermadec Islands

Seismic Region 13
Fiji Area
180. North of Fiji Islands
181. Fiji Islands region
182. Fiji Islands

Seismic Region 14
Vanuatu (New Hebrides)
183. Santa Cruz Islands region
184. Santa Cruz Islands
185. Vanuatu Islands region
186. Vanuatu Islands
187. New Caledonia
188. Loyalty Islands
189. Southeast of Loyalty Islands

Seismic Region 15
Bismarck and Solomon Islands
190. New Ireland region
191. North of Solomon Islands
192. New Britain region
193. Bougainville-Solomon Islands region
194. D'Entrecasteaux Islands region
195. South of Solomon Islands

Seismic Region 16
New Guinea
196. Irian Jaya region
197. Near north coast of Irian Jaya
198. Ninigo Islands region
199. Admiralty Islands region
200. Near north coast of New Guinea
201. Irian Jaya
202. New Guinea
203. Bismarck Sea
204. Aru Islands region
205. Near south coast of Irian Jaya
206. Near south coast of New Guinea
207. Eastern New Guinea region
208. Arafura Sea

Seismic Region 17
Caroline Islands to Guam
209. Western Caroline Islands
210. South of Mariana Islands

Seismic Region 18
Guam to Japan
211. Southeast of Honshu
212. Bonin Islands region
213. Volcano Islands region
214. West of Mariana Islands
215. Mariana Islands region
216. Mariana Islands

Seismic Region 19
Japan-Kurils-Kamchatka
217. Kamchatka Peninsula
218. Near east coast of Kamchatka Peninsula
219. Off east coast of Kamchatka Peninsula
220. Northwest of Kuril Islands
221. Kuril Islands
222. East of Kuril Islands
223. Eastern Sea of Japan
224. Hokkaido region
225. Off southeast coast of Hokkaido
226. Near west coast of eastern Honshu
227. Eastern Honshu
228. Near east coast of eastern Honshu
229. Off east coast of Honshu
230. Near south coast of eastern Honshu

Seismic Region 20
Southwestern Japan and Ryukyu Islands
231. South Korea
232. Western Honshu
233. Near south coast of western Honshu
234. Northwest of Ryukyu Islands
235. Kyushu
236. Shikoku
237. Southeast of Shikoku
238. Ryukyu Islands
239. Southeast of Ryukyu Islands
240. West of Bonin Islands
241. Philippine Sea

Seismic Region 21
Taiwan
242. Near coast of southeastern China
243. Taiwan region
244. Taiwan
245. Northeast of Taiwan
246. Southwestern Ryukyu Islands
247. Southeast of Taiwan

Seismic Region 22
Philippines
248. Philippine Islands region
249. Luzon
250. Mindoro
251. Samar
252. Palawan
253. Sulu Sea
254. Panay

255. Cebu
256. Leyte
257. Negros
258. Sulu Archipelago
259. Mindanao
260. East of Philippine Islands

Seismic Region 23
Borneo-Sulawesi
261. Borneo
262. Celebes Sea
263. Talaud Islands
264. North of Halmahera
265. Minahassa Peninsula, Sulawesi
266. Northern Molucca Sea
267. Halmahera
268. Sulawesi
269. Southern Molucca Sea
270. Ceram Sea
271. Buru
272. Seram

Seismic Region 24
Sunda Arc
273. Southwest of Sumatera
274. Southern Sumatera
275. Java Sea
276. Sunda Strait
277. Jawa
278. Bali Sea
279. Flores Sea
280. Banda Sea
281. Tanimbar Islands region
282. South of Jawa
283. Bali region
284. South of Bali
285. Sumbawa region
286. Flores region
287. Sumba region
288. Savu Sea
289. Timor region
290. Timor Sea
291. South of Sumbawa
292. South of Sumba
293. South of Timor

Seismic Region 25
Myanmar and Southeast Asia
294. Myanmar-India border region
295. Myanmar-Bangladesh border region
296. Myanmar
297. Myanmar-China border region
298. Near south coast of Myanmar
299. Southeast Asia (REGION NOT IN USE)
300. Hainan Island
301. South China Sea
733. Thailand
734. Laos
735. Kampuchea
736. Vietnam
737. Gulf of Tongking

Seismic Region 26
India-Xizang-Szechwan-Yunnan
302. Eastern Kashmir
303. Kashmir-India border region
304. Kashmir-Xizang border region
305. Western Xizang-India border region
306. Xizang
307. Sichuan
308. Northern India
309. Nepal-India border region
310. Nepal
311. Sikkim
312. Bhutan
313. Eastern Xizang-India border region
314. Southern India
315. India-Bangladesh border region
316. Bangladesh
317. Northeastern India
318. Yunnan
319. Bay of Bengal

Seismic Region 27
Southern Xinjiang to Gansu
320. Kyrgyzstan-Xinjiang border region
321. Southern Xinjiang
322. Gansu
323. Western Nei Mongol
324. Kashmir-Xinjiang border region
325. Qinghai

Seismic Region 28
Alma-Ata to Lake Baikal
326. Southwestern Siberia
327. Lake Baykal region
328. East of Lake Baykal
329. Eastern Kazakhstan
330. Lake Issyk-Kul region
331. Kazakhstan-Xinjiang border region
332. Northern Xinjiang
333. Tuva-Buryatia-Mongolia border region
334. Mongolia

Seismic Region 29
Western Asia
335. Ural Mountains region
336. Western Kazakhstan
337. Eastern Caucasus
338. Caspian Sea
339. Northwestern Uzbekistan
340. Turkmenistan
341. Iran-Turkmenistan border region
342. Turkmenistan-Afghanistan border region
343. Turkey-Iran border region
344. Iran-Armenia-Azerbaijan border region
345. Northwestern Iran
346. Iran-Iraq border region
347. Western Iran
348. Northern and central Iran
349. Northwestern Afghanistan
350. Southwestern Afghanistan
351. Eastern Arabian Peninsula
352. Persian Gulf
353. Southern Iran
354. Southwestern Pakistan
355. Gulf of Oman
356. Off coast of Pakistan

Seismic Region 30
Middle East-Crimea-Eastern Balkans
357. Ukraine-Moldova-Southwestern Russia region
358. Romania
359. Bulgaria
360. Black Sea
361. Crimea region
362. Western Caucasus
363. Greece-Bulgaria border region
364. Greece
365. Aegean Sea
366. Turkey
367. Turkey-Georgia-Armenia border region
368. Southern Greece
369. Dodecanese Islands
370. Crete
371. Eastern Mediterranean Sea
372. Cyprus region
373. Dead Sea region
374. Jordan-Syria region
375. Iraq

Seismic Region 31
Western Mediterranean Area
376. Portugal
377. Spain

378. Pyrenees
379. Near south coast of France
380. Corsica
381. Central Italy
382. Adriatic Sea
383. Northwestern Balkan Peninsula
384. West of Gibraltar
385. Strait of Gibraltar
386. Balearic Islands
387. Western Mediterranean Sea
388. Sardinia
389. Tyrrhenian Sea
390. Southern Italy
391. Albania
392. Greece-Albania border region
393. Madeira Islands region
394. Canary Islands region
395. Morocco
396. Northern Algeria
397. Tunisia
398. Sicily
399. Ionian Sea
400. Central Mediterranean Sea
401. Near coast of Libya

Seismic Region 32
Atlantic Ocean

402. North Atlantic Ocean
403. Northern Mid-Atlantic Ridge
404. Azores Islands region
405. Azores Islands
406. Central Mid-Atlantic Ridge
407. North of Ascension Island
408. Ascension Island region
409. South Atlantic Ocean
410. Southern Mid-Atlantic Ridge
411. Tristan da Cunha region
412. Bouvet Island region
413. Southwest of Africa
414. Southeastern Atlantic Ocean
738. Reykjanes Ridge
739. Azores-Cape St. Vincent Ridge

Seismic Region 33
Indian Ocean

415. Eastern Gulf of Aden
416. Socotra region
417. Arabian Sea
418. Lakshadweep region
419. Northeastern Somalia
420. North Indian Ocean
421. Carlsberg Ridge
422. Maldive Islands region
423. Laccadive Sea
424. Sri Lanka
425. South Indian Ocean
426. Chagos Archipelago region
427. Mauritius-Reunion region
428. Southwest Indian Ridge
429. Mid-Indian Ridge
430. South of Africa
431. Prince Edward Islands region
432. Crozet Islands region
433. Kerguelen Islands region
434. Broken Ridge
435. Southeast Indian Ridge
436. Southern Kerguelen Plateau
437. South of Australia
740. Owen Fracture Zone region
741. Indian Ocean Triple Junction
742. Western Indian-Antarctic Ridge

Seismic Region 34
Eastern North America

438. Saskatchewan
439. Manitoba
440. Hudson Bay
441. Ontario
442. Hudson Strait region
443. Northern Quebec
444. Davis Strait
445. Labrador
446. Labrador Sea
447. Southern Quebec
448. Gaspe Peninsula
449. Eastern Quebec
450. Anticosti Island
451. New Brunswick
452. Nova Scotia
453. Prince Edward Island
454. Gulf of St. Lawrence
455. Newfoundland
456. Montana
457. Eastern Idaho
458. Hebgen Lake region, Montana
459. Yellowstone region
460. Wyoming
461. North Dakota
462. South Dakota
463. Nebraska
464. Minnesota
465. Iowa
466. Wisconsin
467. Illinois
468. Michigan
469. Indiana
470. Southern Ontario
471. Ohio
472. New York
473. Pennsylvania
474. Vermont-New Hampshire region
475. Maine
476. Southern New England
477. Gulf of Maine
478. Utah
479. Colorado
480. Kansas
481. Iowa-Missouri border region
482. Missouri-Kansas border region
483. Missouri
484. Missouri-Arkansas border region
485. Missouri-Illinois border region
486. New Madrid region, Missouri
487. Cape Girardeau region, Missouri
488. Southern Illinois
489. Southern Indiana
490. Kentucky
491. West Virginia
492. Virginia
493. Chesapeake Bay region
494. New Jersey
495. Eastern Arizona
496. New Mexico
497. Northwestern Texas-Oklahoma border region
498. Western Texas
499. Oklahoma
500. Central Texas
501. Arkansas-Oklahoma border region
502. Arkansas
503. Louisiana-Texas border region
504. Louisiana
505. Mississippi
506. Tennessee
507. Alabama
508. Western Florida
509. Georgia
510. Florida-Georgia border region
511. South Carolina
512. North Carolina
513. Off east coast of United States
514. Florida Peninsula
515. Bahama Islands
516. Eastern Arizona-Sonora border region
517. New Mexico-Chihuahua border region
518. Texas-Mexico border region
519. Southern Texas
520. Near coast of Texas
521. Chihuahua
522. Northern Mexico
523. Central Mexico
524. Jalisco
525. Veracruz
526. Gulf of Mexico
527. Bay of Campeche

Seismic Region 35
Eastern South America
528. Brazil
529. Guyana
530. Suriname
531. French Guiana

Seismic Region 36
Northwestern Europe
532. Eire
533. United Kingdom
534. North Sea
535. Southern Norway
536. Sweden
537. Baltic Sea
538. France
539. Bay of Biscay
540. The Netherlands
541. Belgium
542. Denmark
543. Germany
544. Switzerland
545. Northern Italy
546. Austria
547. Czech and Slovak Republics
548. Poland
549. Hungary

Seismic Region 37
Africa
550. Northwest Africa (REGION NOT IN USE)
551. Southern Algeria
552. Libya
553. Egypt
554. Red Sea
555. Western Arabian Peninsula
556. Chad region
557. Sudan
558. Ethiopia
559. Western Gulf of Aden
560. Northwestern Somalia
561. Off south coast of northwest Africa
562. Cameroon
563. Equatorial Guinea
564. Central African Republic
565. Gabon
566. Congo
567. Zaire
568. Uganda
569. Lake Victoria region
570. Kenya
571. Southern Somalia
572. Lake Tanganyika region
573. Tanzania
574. Northwest of Madagascar
575. Angola
576. Zambia
577. Malawi
578. Namibia
579. Botswana
580. Zimbabwe
581. Mozambique
582. Mozambique Channel
583. Madagascar
584. South Africa
585. Lesotho
586. Swaziland
587. Off coast of South Africa
743. Western Sahara
744. Mauritania
745. Mali
746. Senegal-Gambia region
747. Guinea region
748. Sierra Leone
749. Liberia region
750. Cote d'Ivoire
751. Burkina Faso
752. Ghana
753. Benin-Togo region
754. Niger
755. Nigeria

Seismic Region 38
Australia
588. Northwest of Australia
589. West of Australia
590. Western Australia
591. Northern Territory
592. South Australia
593. Gulf of Carpentaria
594. Queensland
595. Coral Sea
596. Northwest of New Caledonia
597. New Caledonia region
598. Southwest of Australia
599. Off south coast of Australia
600. Near coast of South Australia
601. New South Wales
602. Victoria
603. Near southeast coast of Australia
604. Near east coast of Australia
605. East of Australia
606. Norfolk Island region
607. Northwest of New Zealand
608. Bass Strait
609. Tasmania region
610. Southeast of Australia

Seismic Region 39
Pacific Basin
611. North Pacific Ocean
612. Hawaiian Islands region
613. Hawaiian Islands
614. Eastern Caroline Islands region
615. Marshall Islands region
616. Enewetak Atoll region
617. Bikini Atoll region
618. Gilbert Islands region
619. Johnston Island region
620. Line Islands region
621. Palmyra Island region
622. Kiritimati region
623. Tuvalu region
624. Phoenix Islands region
625. Tokelau Islands region
626. Northern Cook Islands
627. Cook Islands region
628. Society Islands region
629. Tubuai Islands region
630. Marquesas Islands region
631. Tuamotu Archipelago region
632. South Pacific Ocean

Seismic Region 40
Arctic Zone
633. Lomonosov Ridge
634. Arctic Ocean
635. Near north coast of Kalaallit Nunaat
636. Eastern Kalaallit Nunaat
637. Iceland region
638. Iceland
639. Jan Mayen Island region
640. Greenland Sea
641. North of Svalbard
642. Norwegian Sea
643. Svalbard region
644. North of Franz Josef Land
645. Franz Josef Land
646. Northern Norway
647. Barents Sea
648. Novaya Zemlya
649. Kara Sea
650. Near coast of northwestern Siberia
651. North of Severnaya Zemlya
652. Severnaya Zemlya
653. Near coast of northern Siberia
654. East of Severnaya Zemlya
655. Laptev Sea

Seismic Region 41
Eastern Asia
656. Southeastern Siberia
657. Priamurye-Northeastern China border region
658. Northeastern China
659. North Korea

660. Sea of Japan
661. Primorye
662. Sakhalin Island
663. Sea of Okhotsk
664. Southeastern China
665. Yellow Sea
666. Off east coast of southeastern China

Seismic Region 42
Northeastern Asia, Northern Alaska to Greenland

667. North of New Siberian Islands
668. New Siberian Islands
669. Eastern Siberian Sea
670. Near north coast of eastern Siberia
671. Eastern Siberia
672. Chukchi Sea
673. Bering Strait
674. St. Lawrence Island region
675. Beaufort Sea
676. Northern Alaska
677. Northern Yukon Territory
678. Queen Elizabeth Islands
679. Northwest Territories
680. Western Kalaallit Nunaat
681. Baffin Bay
682. Baffin Island region

Seismic Region 43
Southeastern and Antarctic Pacific Ocean

683. Southeastcentral Pacific Ocean
684. Southern East Pacific Rise
685. Easter Island region
686. West Chile Rise
687. Juan Fernandez Islands region
688. East of North Island
689. Chatham Islands region
690. South of Chatham Islands
691. Pacific-Antarctic Ridge
692. Southern Pacific Ocean
756. Southeast of Easter Island

Seismic Region 44
Galapagos Area

693. Eastcentral Pacific Ocean
694. Central East Pacific Rise
695. West of Galapagos Islands
696. Galapagos Islands region
697. Galapagos Islands
698. Southwest of Galapagos Islands
699. Southeast of Galapagos Islands
757. Galapagos Triple Junction region

Seismic Region 45
Macquarie Loop

700. South of Tasmania
701. West of Macquarie Island
702. Balleny Islands region

Seismic Region 46
Andaman Islands to Sumatera

703. Andaman Islands region
704. Nicobar Islands region
705. Off west coast of northern Sumatera
706. Northern Sumatera
707. Malay Peninsula
708. Gulf of Thailand

Seismic Region 47
Baluchistan

709. Southeastern Afghanistan
710. Pakistan
711. Southwestern Kashmir
712. India-Pakistan border region

Seismic Region 48
Hindu Kush and Pamir

713. Central Kazakhstan
714. Southeastern Uzbekistan
715. Tajikistan
716. Kyrgyzstan
717. Afghanistan-Tajikistan border region
718. Hindu Kush region
719. Tajikistan-Xinjiang border region
720. Northwestern Kashmir

Seismic Region 49
Northern Eurasia

721. Finland
722. Norway-Murmansk border region
723. Finland-Karelia border region
724. Baltic States-Belarus-Northwestern Russia
725. Northwestern Siberia
726. Northern and central Siberia

Seismic Region 50
Antarctica

727. Victoria Land
728. Ross Sea
729. Antarctica

6.3 IASPEI Magnitudes

The ISC publishes a diversity of magnitude data. Although trying to be as complete and specific as possible, preference is now given to magnitudes determined according to standard procedures recommended by the Working Group on Magnitude Measurements of the IASPEI Commission on Seismological Observation and Interpretation (CoSOI). So far, such standards have been agreed upon for the local magnitude ML, the local-regional mb_Lg, and for two types each of body-wave (mb and mB_BB) and surface-wave magnitudes (Ms_20 and Ms_BB). With the exception of ML, all other standard magnitudes are measured on vertical-component records only. BB stands for direct measurement on unfiltered velocity broadband records in a wide range of periods, provided that their passband covers at least the period range within which mB_BB and Ms_BB are supposed to be measured. Otherwise, a deconvolution has to be applied prior to the amplitude and period measurement so as to assure that this specification is met. In contrast, mb_Lg, mb and Ms_20 are based on narrowband amplitude measurements around periods of 1 s and 20 s, respectively.

ML is consistent with the original definition of the local magnitude by *Richter* (1935) and mB_BB in close agreement with the original definition of medium-period body-wave magnitude mB measured in a wide range of periods between some 2 to 20 s and calibrated with the *Gutenberg and Richter* (1956) Q-function for vertical-component P waves. Similarly, Ms_BB is best tuned to the unbiased use of the IASPEI (1967) recommended standard magnitude formula for surface-wave amplitudes in a wide range of periods and distances, as proposed by its authors *Vaněk et al.* (1962). In contrast, mb and Ms_20 are chiefly based on measurement standards defined by US agencies in the 1960s in conjunction with the global deployment of the World-Wide Standard Seismograph Network (WWSSN), which did not include medium or broadband recordings. Some modifications were made in the 1970s to account for IASPEI recommendations on extended measurement time windows for mb. Although not optimal for calibrating narrow-band spectral amplitudes measured around 1 s and 20 s only, mb and Ms_20 use the same original calibrations functions as mB_BB and Ms_BB. But mb and Ms_20 data constitute by far the largest available magnitude data sets. Therefore they continue to be used, with appreciation for their advantages (e.g., mb is by far the most frequently measured teleseismic magnitude and often the only available and reasonably good magnitude estimator for small earthquakes) and their shortcomings (see section 3.2.5.2 of Chapter 3 in NMSOP-2).

Abbreviated descriptions of the standard procedures for ML, mb_Lg, mb, mB_BB and Ms_BB are summarised below. For more details, including also the transfer functions of the simulation filters to be used, see www.iaspei.org/commissions/CSOI/Summary_WG-Recommendations_20130327.pdf.

All amplitudes used in the magnitude formulas below are in most circumstances to be measured as one-half the maximum deflection of the seismogram trace, peak-to-adjacent-trough or trough-to-adjacent-peak, where the peak and trough are separated by one crossing of the zero-line: this measurement is sometimes described as "one-half peak-to-peak amplitude." The periods are to be measured as twice the time-intervals separating the peak and adjacent-trough from which the amplitudes are measured. The amplitude-phase arrival-times are to be measured and reported too as the time of the zero-crossing between the peak and adjacent-trough from which the amplitudes are measured. The issue of amplitude and period measuring procedures, and circumstances under which alternative procedures are acceptable or preferable, is discussed further in Section 5 of IS 3.3 and in section 3.2.3.3 of Chapter 3 of NMSOP-2.

Amplitudes measured according to recommended IASPEI standard procedures should be reported with the following ISF amplitude "phase names": IAML, IAmb_Lg, IAmb, IAMs_20, IVmB_BB and IVMs_BB. "I" stands for "International" or "IASPEI", "A" for displacement amplitude, measured in nm, and "V" for velocity amplitude, measured in nm/s. Although the ISC will calculate standard surface-wave magnitudes only for earthquakes shallower than 60 km, contributing agencies or stations are encouraged to report standard amplitude measurements of IAMs_20 and IVMs_BB for deeper earthquakes as well.

Note that the commonly known classical calibration relationships have been modified in the following to be consistent with displacements measured in nm, and velocities in nm/s, which is now common with high-resolution digital data and analysis tools. With these general definitions of the measurement parameters, where R is hypocentral distance in km (typically less than 1000 km), Δ is epicentral distance in degrees and h is hypocentre depth in km, the standard formulas and procedures read as follows:

ML:

$$ML = \log_{10}(A) + 1.11\log_{10}R + 0.00189R - 2.09 \tag{6.1}$$

for crustal earthquakes in regions with attenuative properties similar to those of southern California, and with A being the maximum trace amplitude in nm that is measured on output from a horizontal-component instrument that is filtered so that the response of the seismograph/filter system replicates that of a Wood-Anderson standard seismograph (but with a static magnification of 1). For the normalised simulated response curve and related poles and zeros see Figure 1 and Table 1 in IS 3.3 of NMSOP-2.

Equation (6.1) is an expansion of that of *Hutton and Boore* (1987). The constant term in equation (6.1), −2.09, is based on an experimentally determined static magnification of the Wood-Anderson of 2080 (see *Uhrhammer and Collins* (1990)), rather than the theoretical magnification of 2800 that was specified by the seismograph´s manufacturer. The formulation of equation (6.1) assures that reported ML amplitude data are not affected by uncertainty in the static magnification of the Wood-Anderson seismograph.

For seismographic stations containing two horizontal components, amplitudes are measured independently from each horizontal component and each amplitude is treated as a single datum. There is no effort to measure the two observations at the same time, and there is no attempt to compute a vector average. For crustal earthquakes in regions with attenuative properties that are different from those of coastal California and for measuring magnitudes with vertical-component seismographs the constants in the above equation have to be re-determined to adjust for the different regional attenuation and travel paths as well as for systematic differences between amplitudes measured on horizontal and vertical seismographs.

mb_Lg:

$$mb\_Lg = \log_{10}(A) + 0.833\log_{10}R + 0.434\gamma(R - 10) - 0.87 \tag{6.2}$$

where A = "sustained ground-motion amplitude" in nm, defined as the third largest amplitude in the time window corresponding to group velocities of 3.6 to 3.2 km/s, in the period (T) range 0.7 s to 1.3 s; R = epicentral distance in km, γ = coefficient of attenuation in km^{-1}. γ is related to the quality factor Q through the equation $\gamma = \pi/(QUT)$, where U is group velocity and T is the wave period of the L_g wave. γ is a strong function of crustal structure and should be determined specifically for the region in which the mb_Lg is to be used. A and T are measured on output from a vertical-component instrument that is filtered so that the frequency response of the seismograph/filter system replicates that of a WWSSN short-period seismograph (see Figure 1 and Table 1 in IS 3.3 of NMSOP-2). Arrival times with respect to the origin of the seismic disturbance are used, along with epicentral distance, to compute group velocity U.

mb:

$$mb = \log_{10}(A/T) + Q(\Delta, h) - 3.0 \tag{6.3}$$

where A = vertical component P-wave ground amplitude in nm measured at distances $20° \le \Delta \le 100°$ and calculated from the maximum trace-amplitude with $T < 3$ s in the entire P-phase train (time spanned by P, pP, sP, and possibly PcP and their codas, and ending preferably before PP). A and T are measured on output from an instrument that is filtered so that the frequency response of the seismograph/filter system replicates that of a WWSSN short-period seismograph (see Figure 1 and Table 1 in IS 3.3 of NMSOP-2). A is determined by dividing the maximum trace amplitude by the magnification of the simulated WWSSN-SP response at period T.

$Q(\Delta, h)$ = attenuation function for PZ (P-waves recorded on vertical component seismographs) established by *Gutenberg and Richter* (1956) in the tabulated or algorithmic form as used by the U.S. Geological Survey/National Earthquake Information Center (USGS/NEIC) (see Table 2 in IS 3.3 and program description PD 3.1 in NMSOP-2);

mB_BB:

$$mB\_BB = \log_{10}(Vmax/2\pi) + Q(\Delta, h) - 3.0 \tag{6.4}$$

where $Vmax$ = vertical component ground velocity in nm/s at periods between 0.2 s $< T <$ 30 s, measured in the range $20° \le \Delta \le 100°$. $Vmax$ is calculated from the maximum trace-amplitude in the entire P-phase train (see mb), as recorded on a seismogram that is proportional to velocity at least in the period range of measurements. $Q(\Delta, h)$ = attenuation function for PZ established by *Gutenberg and Richter* (1956) (see 6.3). Equation (6.3) differs from the equation for mB of *Gutenberg and Richter* (1956) by virtue of the $log_{10}(Vmax/2\pi)$ term, which replaces the classical $\log_{10}(A/T)_{max}$ term. Contributors should continue to send observations of A and T to ISC.

Ms_20:

$$Ms\_20 = \log_{10}(A/T) + 1.66\log_{10}\Delta + 0.3 \tag{6.5}$$

where A = vertical-component ground displacement in nm at $20° \le \Delta \le 160°$ epicentral distance measured from the maximum trace amplitude of a surface-wave phase having a period T between 18 s and 22 s on a waveform that has been filtered so that the frequency response of the seismograph/filter replicates that of a WWSSN long-period seismograph (see Figure 1 and Table 1 in IS 3.3 of NMSOP-2). A is determined by dividing the maximum trace amplitude by the magnification of the simulated WWSSN-LP response at period T. Equation (6.5) is formally equivalent to the Ms equation proposed by *Vaněk et al.* (1962) but is here applied to vertical motion measurements in a narrow range of periods.

Ms_BB:

$$Ms\_BB = \log_{10}(Vmax/2\pi) + 1.66\log_{10}\Delta + 0.3 \tag{6.6}$$

where $Vmax$ = vertical-component ground velocity in nm/s associated with the maximum trace-amplitude in the surface-wave train at periods between 3 s $< T <$ 60 s as recorded at distances $2^\circ \leq \Delta \leq 160^\circ$ on a seismogram that is proportional to velocity in that range of considered periods. Equation (6.6) is based on the Ms equation proposed by *Vaněk et al.* (1962), but is here applied to vertical motion measurements and is used with the $\log_{10}(Vmax/2\pi)$ term replacing the $\log_{10}(A/T)_{max}$ term of the original. As for mB_BB, observations of A and T should be reported to ISC.

Mw:

$$Mw = (\log_{10} M_0 - 9.1)/1.5 \tag{6.7}$$

Moment magnitude Mw is calculated from data of the scalar seismic moment M_0 (when given in Nm), or

$$Mw = (\log_{10} M_0 - 16.1)/1.5 \tag{6.8}$$

its CGS equivalent when M_0 is in dyne·cm.

Please note that the magnitude nomenclature used in this Section uses the IASPEI standards as the reference. However, the magnitude type is typically written in plain text in most typical data reports and so it is in this document. Moreover, writing magnitude types in plain text allows us to reproduce the magnitude type as stored in the database and provides a more direct identification of the magnitude type reported by different agencies. A short description of the common magnitude types available in this Summary is reported in 9.6.

6.4 The IASPEI Seismic Format (ISF)

The ISF is the IASPEI approved standard format for the exchange of parametric seismological data (hypocentres, magnitudes, phase arrivals, moment tensors etc.) and is one of the formats used by the ISC. It was adopted as standard in August 2001 and is an extension of the International Monitoring System 1.0 (IMS1.0) standard, which was developed for exchanging data used to monitor the Comprehensive Nuclear-Test-Ban Treaty. An example of the ISF is shown in Listing 6.1.

Bulletins which use the ISF are comprised of origin and arrival information, provided in a series of data blocks. These include: a bulletin title block; an event title block; an origin block; a magnitude sub-block; an effect block; a reference block; and a phase block.

Within these blocks an important extension of the IMS1.0 standard is the ability to add additional comments and thus provide further parametric information. The ISF comments are distinguishable within the open parentheses required for IMS1.0 comments by beginning with a hash mark (#) followed by a keyword identifying the type of formatted comment. Each additional line required in the ISF comment begins with the hash (within the comment parentheses) followed by blank spaces at least as long as the keyword. Optional lines within the comment are signified with a plus sign (+) instead of a hash mark. The keywords include `PRIME` (to designate a prime origin of a hypocentre); `CENTROID` (to indicate the centroid origin); `MOMTENS` (moment tensor solution); `FAULT_PLANE` (fault plane solution); `PRINAX` (principal axes); `PARAM` (an origin parameter e.g. hypocentre depth given by a depth phase).

The full documentation for the ISF is maintained at the ISC and can be downloaded from:
www.isc.ac.uk/doc/code/isf/isf.pdf

The documentation for the IMS1.0 standard can be downloaded from:
www.isc.ac.uk/doc/code/isf/ims1_0.pdf

Listing 6.1: Example of an ISF formatted event

```
Event 15146084 Near east coast of eastern Honshu
   Date       Time        Err   RMS Latitude Longitude  Smaj  Smin  Az Depth   Err Ndef Nsta Gap  mdist  Mdist Qual   Author      OrigID
2010/09/01 07:32:00                 37.9000  141.9000f                  44.0                                          NIED        17047453
 (#MOMTENS sc    M0 fCLVD    MRR    MTT    MPP    MRT    MTP    MPR NST1 NST2 Author   )
 (#             eM0 eCLVD    eRR    eTT    ePP    eRT    eTP    ePR NCO1 NCO2 Duration )
 (#        16 5.760                                                 NIED     )
 (#                                                                          )
 (#FAULT_PLANE Typ Strike   Dip    Rake  NP  NS Plane Author    )
 (#            BDC 199.00 19.00   86.00                NIED     )
 (+                 23.00 71.00   91.00                         )
 (Epicenter information from JMA Focal Mechanism Solution Determined Manually Variance reduction = 96.98%)
2010/09/01 07:32:47.50        1.470  37.8300  142.2400                  37.0          71       281  11.00  51.10     uk BJI         15275482
2010/09/01 07:32:52.20   0.92         38.0320  141.8090   6.7   4.5 110  44.0         114                                  MOS         16741494
2010/09/01 07:32:52.53   0.35 0.889  37.9202  141.8229 4.090 2.740 145  49.7  2.76  490  478 122   0.65  92.01 m i fe ISCJB       01631732
 (#PARAM pP_DEPTH=41.11021)
2010/09/01 07:32:52.60   0.10         37.9100  141.8700   1.1   0.9  -1  43.0   1.0                                     fe JMA         16271222
 (Felt I=III-III J1)
2010/09/01 07:32:53.66   0.42 0.770  37.9250  141.7880   5.1   3.4 140  44.4   3.9  102       127   3.17 127.67     fe NEIC        01134459
 (#MOMTENS sc    M0 fCLVD    MRR    MTT    MPP    MRT    MTP    MPR NST1 NST2 Author   )
 (#             eM0 eCLVD    eRR    eTT    ePP    eRT    eTP    ePR NCO1 NCO2 Duration )
 (#        16 5.800        3.600 -0.550 -3.040  1.850 -1.140  4.150            NIED     )
 (#                                                                          )
 (#FAULT_PLANE Typ Strike   Dip    Rake  NP  NS Plane Author    )
 (#            BDC 199.00 19.00   86.00                NIED     )
 (+                 23.00 71.00   91.00                         )
 (Recorded [3 JMA] in Miyagi; [2 JMA] in Fukushima and Iwate; [1 JMA] in Akita, Aomori, Ibaraki, Tochigi and Yamagata.)
2010/09/01 07:32:53.70   0.20         37.9300  142.0600 2.224 1.112  -1  50.3   1.0  262   89                               GCMT        00124877
 (#CENTROID)
 (#MOMTENS sc    M0 fCLVD    MRR    MTT    MPP    MRT    MTP    MPR NST1 NST2 Author   )
 (#             eM0 eCLVD    eRR    eTT    ePP    eRT    eTP    ePR NCO1 NCO2 Duration )
 (#        16 6.891        5.430 -0.440 -4.990  1.500 -2.070  3.710   64   89 GCMT     )
 (#                        0.173  0.118  0.120  0.100  0.094  0.110  102  160     0.90 )
 (#FAULT_PLANE Typ Strike   Dip    Rake  NP  NS Plane Author    )
 (#            BDC  22.00 63.00   91.00                GCMT     )
 (+                201.00 27.00   89.00                         )
 (#PRINAX sc  T_val T_azim  T_pl  B_val B_azim  B_pl  P_val P_azim  P_pl Author   )
 (#       16  6.711 293.00 72.00  0.360 201.00  0.00 -7.072 111.00 18.00 GCMT     )
 (nsta1 refers to body waves, cutoff=40s. nsta2 refers to surface waves, cutoff=50s.)
2010/09/01 07:32:55.05   1.77 1.070  37.8692  141.9450  12.9  10.4 100  63.6  16.8   36       127   3.24 117.04     uk IDC         16680924
2010/09/01 07:32:52.23   0.30 1.333  37.8836  141.9148 5.558 4.001 142  38.9  2.33  542  478  61   0.72 141.68 m i se ISC         01237353
 (#PRIME)
 (#PARAM pP_DEPTH=39.00000)

Magnitude  Err Nsta Author      OrigID
Mw     5.1          NIED      17047453
Ms     4.8       61 BJI       15275482
Ms7    4.6       58 BJI       15275482
mB     5.1       48 BJI       15275482
mb     5.0       63 BJI       15275482
MS     4.7       19 MOS       16741494
mb     5.2       49 MOS       16741494
MS     4.6       43 ISCJB     01631732
mb     4.9      138 ISCJB     01631732
       5.0          JMA       16271222
mb     5.0       55 NEIC      01134459
MW     5.1          NIED      01134459
MW     5.2       89 GCMT      00124877
MS     4.4 0.1   28 IDC       16680924
Ms1    4.4 0.1   28 IDC       16680924
mb     4.4 0.1   27 IDC       16680924
mb1    4.5 0.0   33 IDC       16680924
mb1mx  4.4 0.0   37 IDC       16680924
mbtmp  4.7 0.1   33 IDC       16680924
ms1mx  4.3 0.1   31 IDC       16680924
MS     4.7 0.2   43 ISC       01237353
mb     4.9 0.2  145 ISC       01237353

Sta     Dist  EvAz Phase        Time      TRes  Azim AzRes   Slow   SRes Def   SNR       Amp   Per Qual Magnitude    ArrID
JIO     0.72 322.1 Pn       07:33:05.9   -0.06                           T__                        d_             49540510
JIO     0.72 322.1 Sn       07:33:15.0   -0.82                           T__                        __             49540511
JMM     0.89 269.2 Pn       07:33:08.4    0.2                            T__                        d_             49540512
JMM     0.89 269.2 Sn       07:33:19.2   -0.68                           T__                        __             49540513
JFK     0.97 238.3 Pn       07:33:09.5    0.1                            T__                        d_             49540514
JFK     0.97 238.3 Sn       07:33:21.5   -0.54                           T__                        __             49540515
JOU     1.10 296.4 Pn       07:33:11.5    0.4                            T__                        d_             49540516
JOU     1.10 296.4 Sn       07:33:25.4    0.3                            T__                        _e             49540517
ONAJ    1.18 229.0 Pn       07:33:12.4    0.1                            T__                        d_             49540530
JMK     1.20 333.1 Pn       07:33:12.5    0.0                            T__                        d_             49540518
JMK     1.20 333.1 Sn       07:33:27.1   -0.39                           T__                        _e             49540519
OFUJ    1.21 350.9 Pn       07:33:12.3   -0.34                           T__                        d_             49540531
.
.
.
532A   91.05  49.8 P        07:45:52.799 -0.00  90.9                     T__                        __             05504129
334A   91.18  47.9 P        07:45:54.012  0.7   91.0                     T__                        __             05504128
H06N1  91.36  64.9 T        09:27:33.559                                 ___   6.0                  __             58438458
MIAR   91.43  42.9 P        07:45:54.85   0.5   91.2                     T__                        __             05504179
Y39A   91.60  43.6 P        07:45:55.543  0.4   91.4                     T__                        __             05504214
534A   91.98  49.0 P        07:45:57.308  0.2   91.8                     T__                        __             05504130
KEST   94.59 323.1 LR       08:33:52.432       320.5         38.70       ___           466.5 18.65  __             58438480
ESDC   96.70 334.2 LR       08:34:40.011       345.0         38.30       ___           375.8 20.18  __             58438449
TORD  117.01 315.6 PKPdf    07:51:32.55  -0.82  17.7          2.30       T__   5.1       0.4  0.70  __             58438504
TORD  117.01 315.6 PP       07:52:39.3   -2.90  31.2          6.30       T__   6.5       1.3  0.68  __             58438505
QSPA  127.62 180.0 PKPdf    07:51:52.02  -0.16                           T__                        _e             23535420
SNAA  141.68 197.1 PKPdf    07:52:13.751 -4.52                           T__                        __             20375340
VNA2  143.24 196.3 PKPbc    07:52:18.562  0.4  122.0          2.31       ___                        __             20375338
VNA1  143.64 196.2 PKPbc    07:52:19.77   0.6                            ___                        __             20375339
```

6.5 Ground Truth (GT) Events

Accurate locations are crucial in testing Earth models derived from body and surface wave tomography as well as in location calibration studies. 'Ground Truth' (GT) events are well-established source locations and origin times. A database of IASPEI reference events (GT earthquakes and explosions) is hosted at the ISC (www.isc.ac.uk). A full description of GT selection criteria can be found in *Bondár and McLaughlin* (2009a).

The events are coded by category GT0, GT1, GT2 or GT5, where the epicentre of a GTX event is known to within X km to a 95% confidence level. A map of all IASPEI reference events is shown in Figure 6.8 and the types of event are categorised in Figure 6.9. GT0 are explosions with announced locations and origin times. GT1 and GT2 are typically explosions, mine blasts or rock bursts either associated to explosion phenomenology located upon overhead imagery with seismically determined origin times, or precisely located by in-mine seismic networks. GT1-2 events are assumed to be shallow, but depth is unknown.

The database consists of nuclear explosions of GT0–5 quality, adopted from the Nuclear Explosion Database (*Bennett et al.*, 2010); GT0–5 chemical explosions, rock bursts, mine-induced events, as well as a few earthquakes, inherited from the reference event set by *Bondár et al.* (2004); GT5 events (typically earthquakes with crustal depths) which have been identified using either the method of *Bondár et al.* (2008) (2,275 events) or *Bondár and McLaughlin* (2009a) (updated regularly from the EHB catalogue (*Engdahl et al.*, 1998)), which uses the following criteria:

- 10 or more stations within 150 km from the epicentre
- one or more stations within 10 km
- $\Delta U \leq 0.35$
- a secondary azimuthal gap $\leq 160°$

where ΔU is the network quality metric defined as the mean absolute deviation between the best-fitting uniformly distributed network of stations and the actual network:

$$\Delta U = \frac{4\sum |esaz_i - (unif_i + b)|}{360N}, 0 \leq \Delta U \leq 1 \tag{6.9}$$

where N is the number of stations, $esaz_i$ is the ith event-to-station azimuth, $unif_i = 360i/N$ for $i = 0$, ..., $N-1$, and $b = avg\,(esaz_i) - avg\,(unif_i)$. ΔU is normalised so that it is 0 when the stations are uniformly distributed in azimuth and 1 when all the stations are at the same azimuth.

The seismological community is invited to participate in this project by nominating seismic events for the reference event database. Submitters may be contacted for further confirmation and for arrival time data. The IASPEI Reference Event List will be periodically published both in written and electronic form with proper acknowledgement of all submitters.

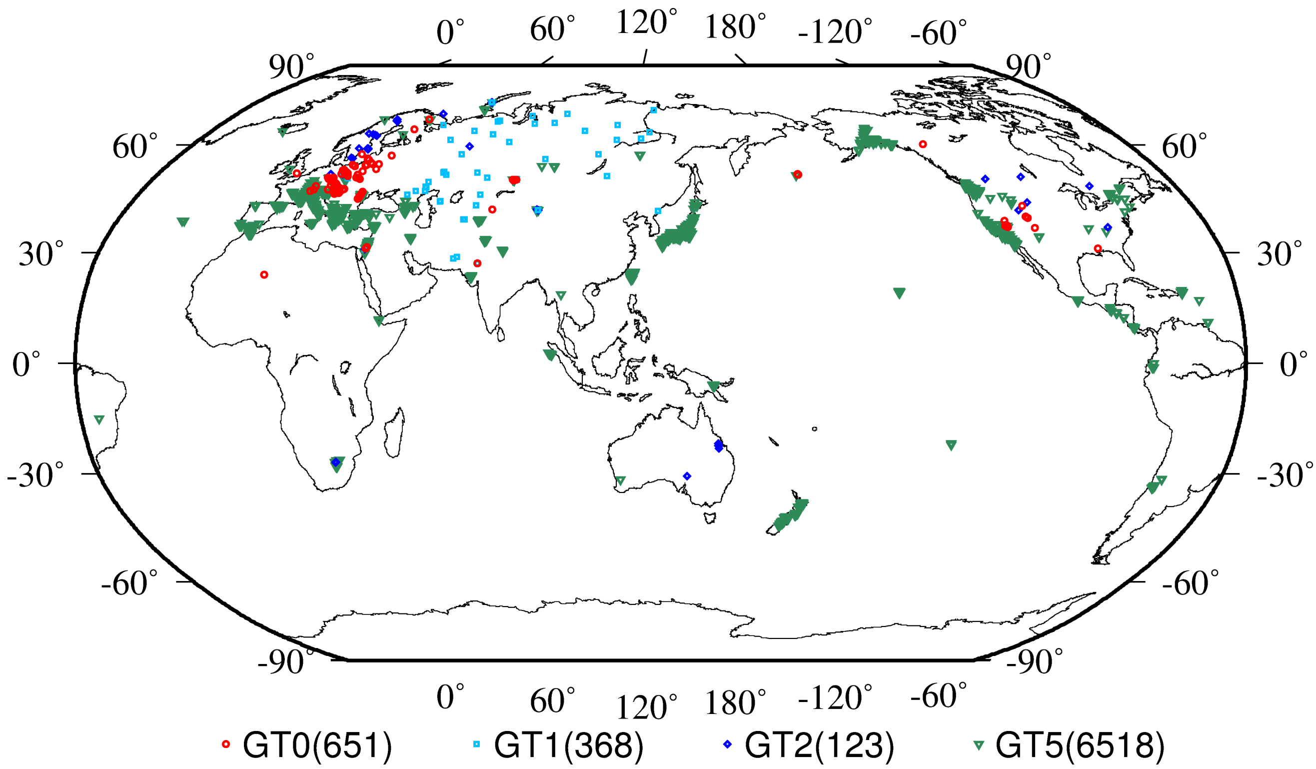

Figure 6.8: *Map of all IASPEI Reference Events as of September 2012.*

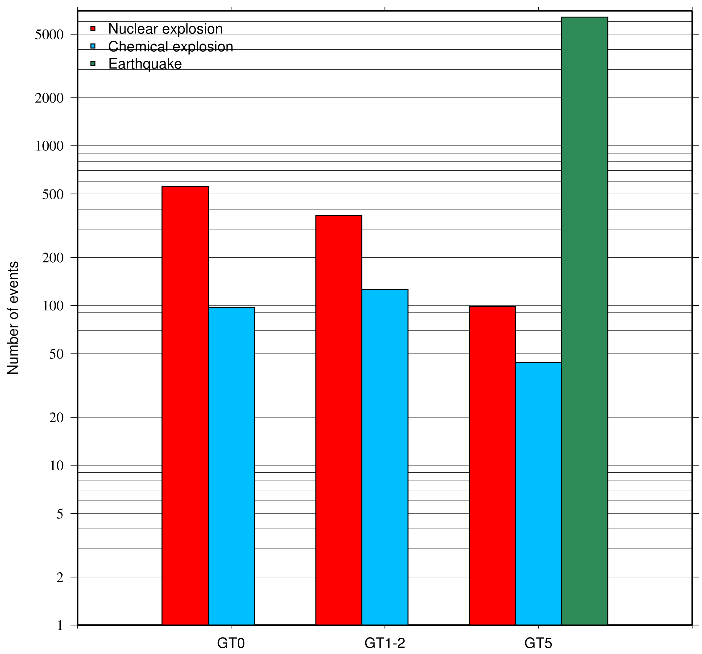

Figure 6.9: *Histogram showing the event types within the IASPEI Reference Event list as of September 2012.*

6.6 Nomenclature of Event Types

The nomenclature of event types currently used in the ISC Bulletin takes its origin from the IASPEI International Seismic Format (ISF).

Event type codes are composed of a leading character that generally indicates the confidence with which the type of the event is asserted and a trailing character that generally gives the type of the event. The leading and trailing characters may be used in any combination.

The **leading** characters are:

- s = suspected
- k = known
- f = felt (implies known)
- d = damaging (implies felt and known)

The **trailing** characters are:

- c = meteoritic event
- e = earthquake
- h = chemical explosion
- i = induced event
- l = landslide
- m = mining explosion
- n = nuclear explosion
- r = rock burst
- x = experimental explosion

A chemical explosion might be for mining or experimental purposes, and it is conceivable that other types of event might be assigned two or more different event type codes. This is deliberate, and matches the ambiguous identification of events in existing databases.

In addition, the code `uk` is used for events of unknown type and `ls` is used for known landslides.

The frequency of the different event types designated in the ISC Bulletin since 1964 is indicated in Figure 6.10.

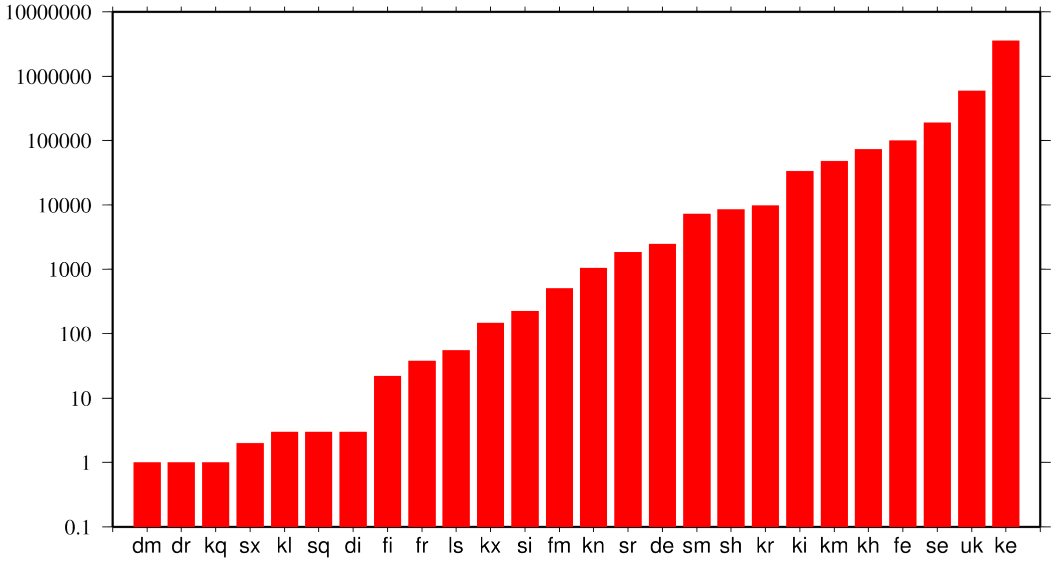

Figure 6.10: *Event types in the ISC Bulletin*

There are currently plans to revise this nomenclature as part of the coordination process between the National Earthquake Information Center (NEIC/USGS), European-Mediterranean Seismological Centre (CSEM) and the ISC.

7

Summary of Seismicity, January - June 2011

The first six months of 2011 saw the occurence of the great M_W 9.1 tsunamigenic earthquake centred off the Pacific coast of Tohoku, Japan. There were at least 15703 deaths and much devastation and disruption along the Japanese coastal regions, including damage to a nuclear power plant resulting from the tsunami that had a maximum run-up height of 37.88m. The sequence included a M_W 7.3 foreshock and three aftershocks greater than M_W 7 before the end of June, with the largest aftershock (M_W 7.9) centred well to the south of the mainshock. The M_W 7.1 aftershock occurring closer to shore resulted in two more deaths and further damage and disruption.

This large sequence, extending into subsequent months, caused an increased workload for ISC analysts, who often had to reconcile local and teleseimic arrivals reported for near-simultaneous events dispersed over a broad region while maintaining a consistency of analysis and depth assignment.

Of the other earthquakes of M_W 7 or more for this summary period, there were three associated deaths for the shallow event in southwestern Pakistan. Although widely felt, the deep earthquake beneath northern Argentina was not damaging. However, among smaller events, there were at least 181 deaths amd considerable damage in and near the city of Christchurch, New Zealand, resulting from the February M_W 6.1 earthquake in a sequence that followed the less devastating M_W 7.0 Darfield earthquake further west in September 2010.

Elsewhere, there were 25 deaths in March following an earthquake in the Myanmar-China border region, and at least 74 more deaths later that month after a strong earthquake in Myanmar. In May, there were at least 10 deaths in the wake of a moderate-magnitude earthquake in the Lorca area of Spain.

The number of events in this Bulletin Summary categorised by type are given in Table 7.1.

The period between January and June 2011 produced 10 earthquakes with $M_W \geq 7$; these are listed in Table 7.2.

Figure 7.1 shows the number of moderate and large earthquakes in the first half of 2011. The distribution of the number of earthquakes should follow the Gutenberg-Richter law.

Figures 7.2 to 7.6 show the geographical distribution of moderate and large earthquakes in various magnitude ranges.

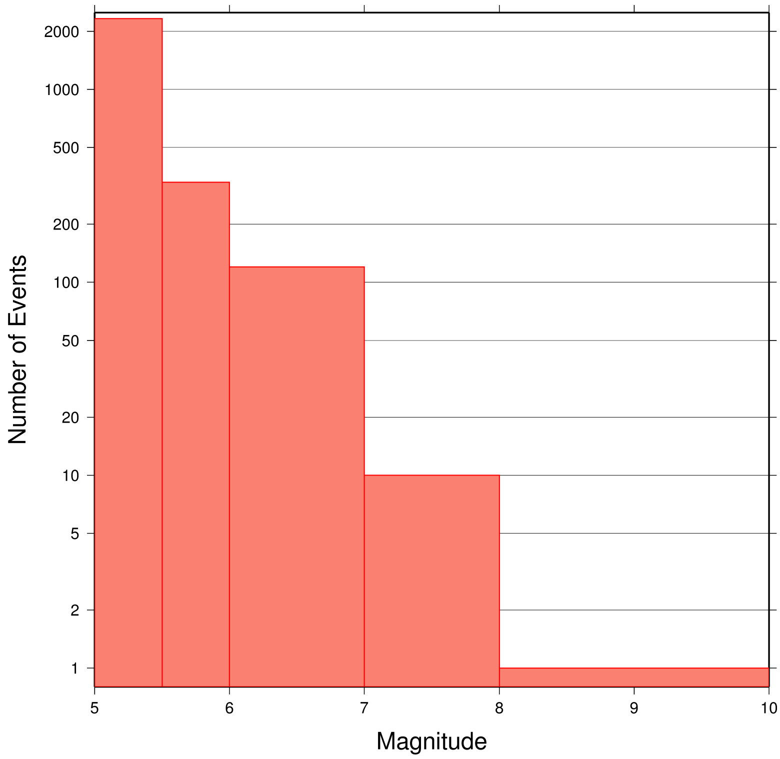

Figure 7.1: *Number of moderate and large earthquakes between January and June 2011. The non-uniform magnitude bias here correspond with the magnitude intervals used in Figures 7.2 to 7.6.*

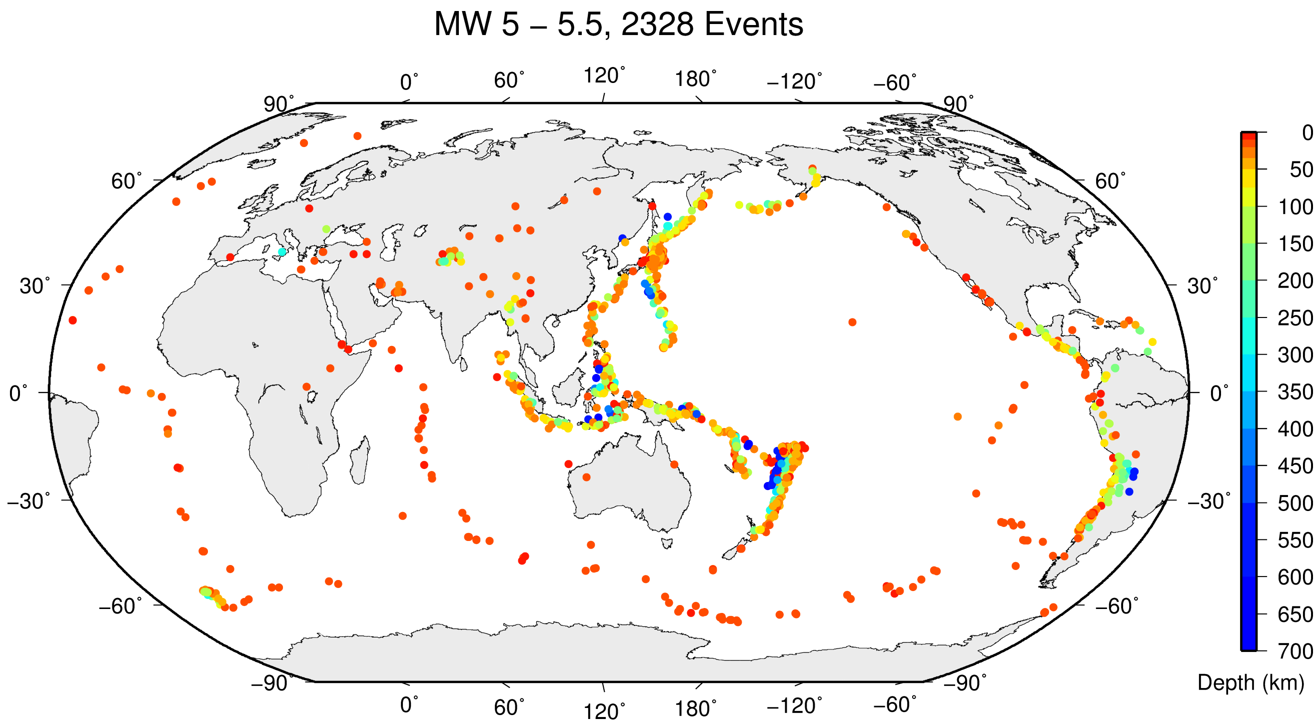

Figure 7.2: *Geographic distribution of magnitude 5-5.5 earthquakes between January and June 2011.*

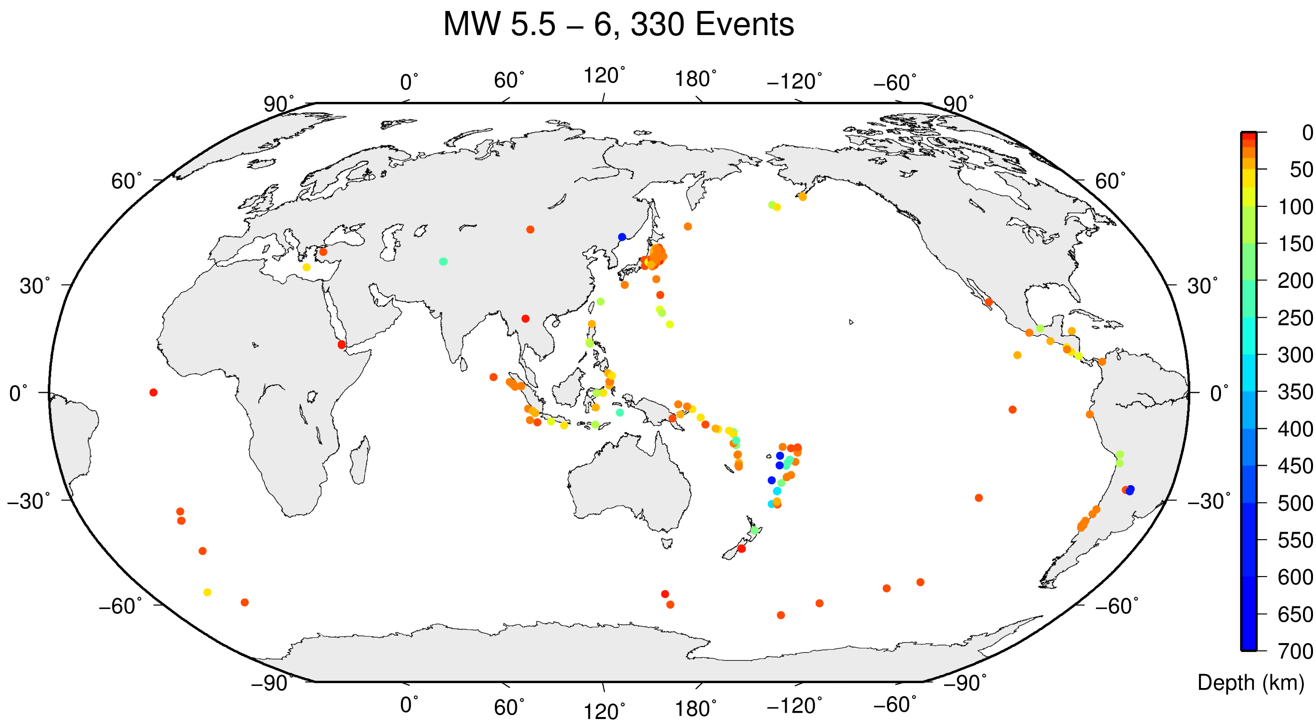

Figure 7.3: *Geographic distribution of magnitude 5.5-6 earthquakes between January and June 2011.*

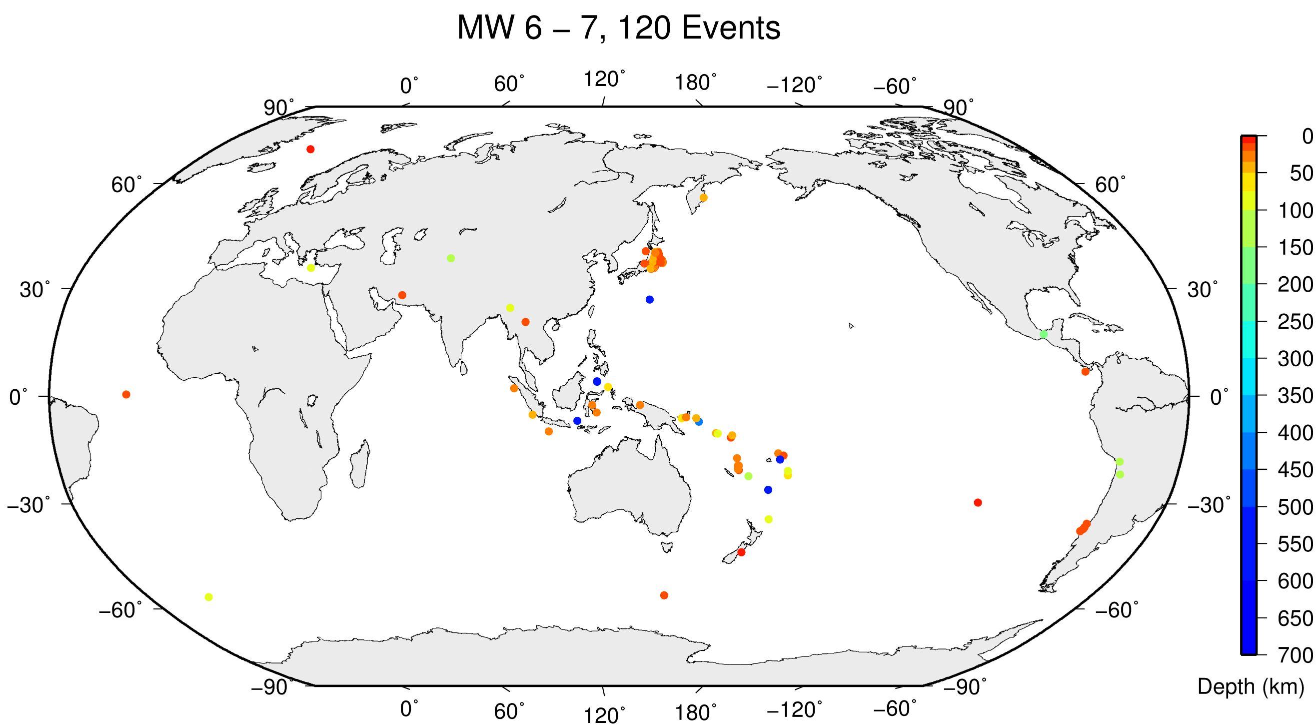

Figure 7.4: *Geographic distribution of magnitude 6-7 earthquakes between January and June 2011.*

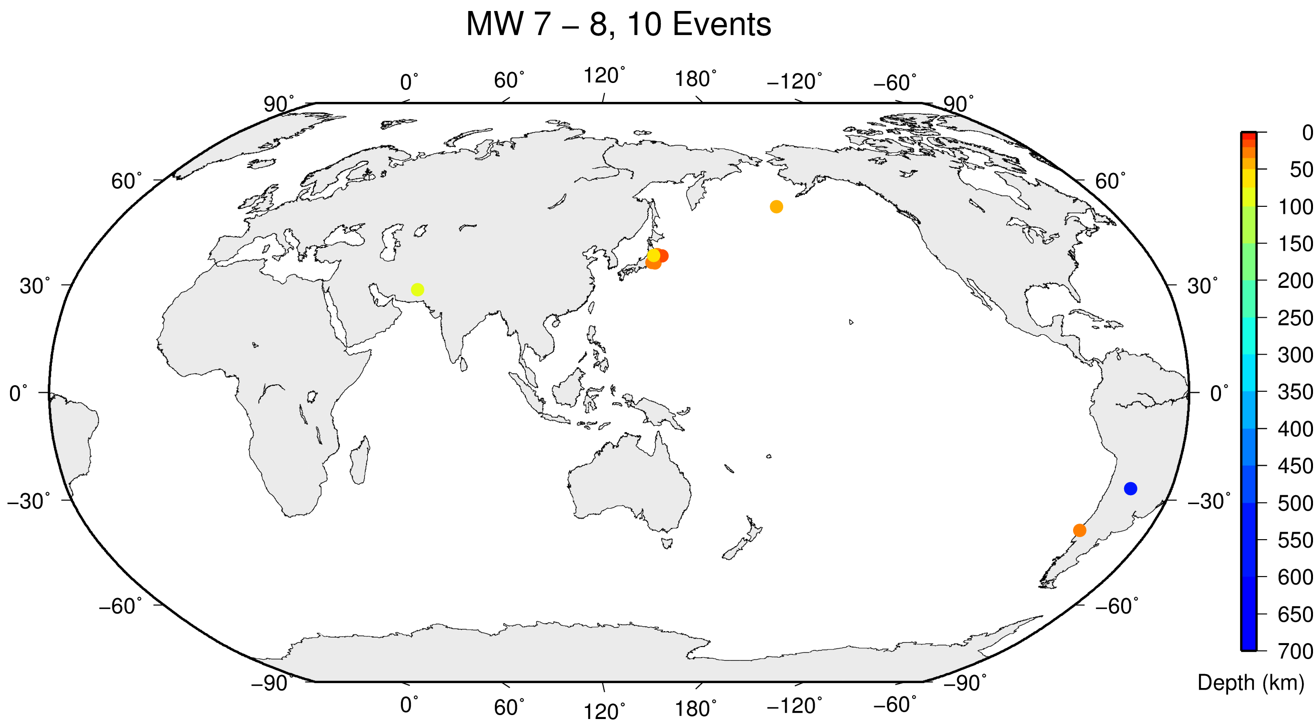

Figure 7.5: *Geographic distribution of magnitude 7-8 earthquakes between January and June 2011.*

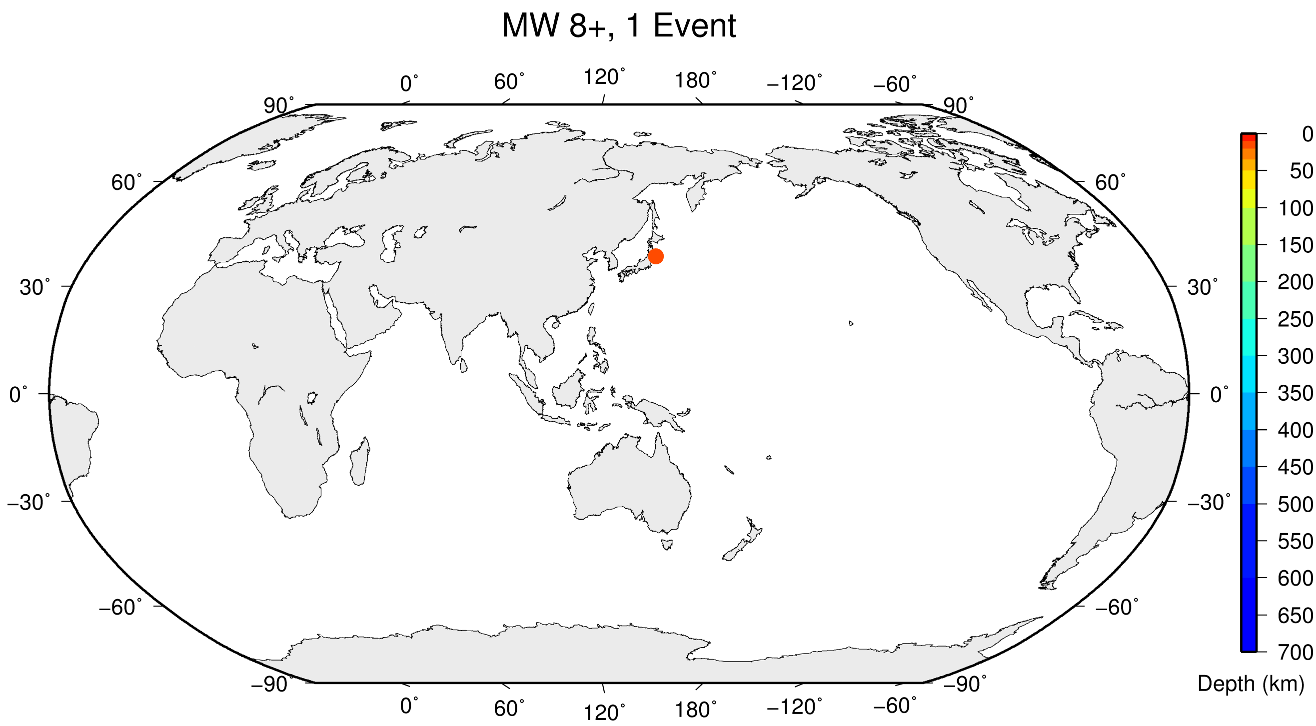

Figure 7.6: *Geographic distribution of magnitude 8+ earthquakes between January and June 2011.*

Table 7.1: *Summary of events by type between January and June 2011.*

damaging earthquake	16
damaging rockburst	1
felt earthquake	2220
felt induced event	1
known earthquake	189783
known chemical explosion	3029
known induced event	2563
known mine explosion	7972
known rockburst	49
known experimental explosion	57
suspected earthquake	13039
suspected chemical explosion	36
suspected induced event	3
suspected mine explosion	3682
suspected rockburst	236
unknown	33589
total	256276

Table 7.2: *Summary of the earthquakes of magnitude $M_W \geq 7$ between January and June 2011.*

Date	lat	lon	depth	M_W	Flinn-Engdahl Region
2011-03-11 05:46:23	38.30	142.50	19	9.1	Near east coast of eastern Honshu
2011-03-11 06:15:37	36.23	141.09	25	7.9	Near east coast of eastern Honshu
2011-03-11 06:25:50	38.05	144.63	19	7.7	Off east coast of Honshu
2011-03-09 02:45:19	38.44	142.98	26	7.3	Near east coast of eastern Honshu
2011-06-24 03:09:38	51.98	-171.82	49	7.3	Fox Islands
2011-01-18 20:23:25	28.68	63.99	79	7.2	Southwestern Pakistan
2011-01-02 20:20:18	-38.39	-73.40	24	7.2	Near coast of central Chile
2011-04-07 14:32:44	38.25	141.73	53	7.1	Near east coast of eastern Honshu
2011-01-01 09:56:58	-26.85	-63.24	584	7.0	Santiago del Estero Province
2011-01-13 16:16:42	-20.60	168.59	14	7.0	Loyalty Islands

8

Notable Events

8.1 The Canterbury, New Zealand Earthquake Sequence II: The M_W 6.2 Christchurch Earthquake of 21 February 2011 and Continuing Aftershock Sequence

John Ristau
GNS Science
Lower Hutt
New Zealand

8.1.1 Introduction

The moment magnitude (M_W) 6.2 Christchurch earthquake of 21 February 2011 UTC (22 February 2011 NZST) was an aftershock to the 3 September 2010 UTC M_W 7.1 Darfield earthquake that occurred 40 km west of Christchurch (Figure 8.1) (Kaiser *et al.* 2012). Although much smaller than the Darfield earthquake, the Christchurch earthquake was far more devastating to the city of Christchurch, New Zealand's second largest city (population *c.* 377 000). The Christchurch earthquake occurred at shallow depth, ∽6 km SE of the city centre beneath the outer suburbs of Christchurch. The impact of the earthquake was severe, most notably 185 fatalities. The Darfield earthquake occurred at 04:35 on a Saturday morning (NZST) when streets were largely deserted. In contrast, the Christchurch earthquake struck at 12:51 NZST on a weekday when the city centre was highly populated. Building damage, including collapse of some office buildings and widespread damage to heritage structures, was severe. Liquefaction was widespread, and numerous rockfalls and slope failures caused further damage. This was the deadliest earthquake to occur in New Zealand since the 3 February 1931 Hawkes Bay earthquake (M_W 7.4 – 7.6).

The Christchurch earthquake was well recorded (Figure 8.1) by the national GeoNet broadband and strong-motion networks (Petersen *et al.* 2011) and the regional Canterbury CanNet strong-motion network (Avery *et al.* 2004). In addition, more than 180 low-cost micro-electro-mechanical accelerometers were deployed alongside a network of volunteer-owned, internet-connected computers as part of the Quake-Catcher Network (QCN) (Lawrence *et al.* 2014; Cochran *et al.* 2011; Cochran *et al.* 2009). Many of the temporary seismometers and accelerometers installed by GNS Science to record Darfield aftershocks were still operating when the Christchurch event occurred, supplementing the CanNet instruments that provided some of the best near-field ground-shaking measurements.

New Zealand straddles the boundary of the Pacific and Australian plates, and the Canterbury region, where the Darfield and Christchurch earthquakes occurred, is a region of continental convergence across

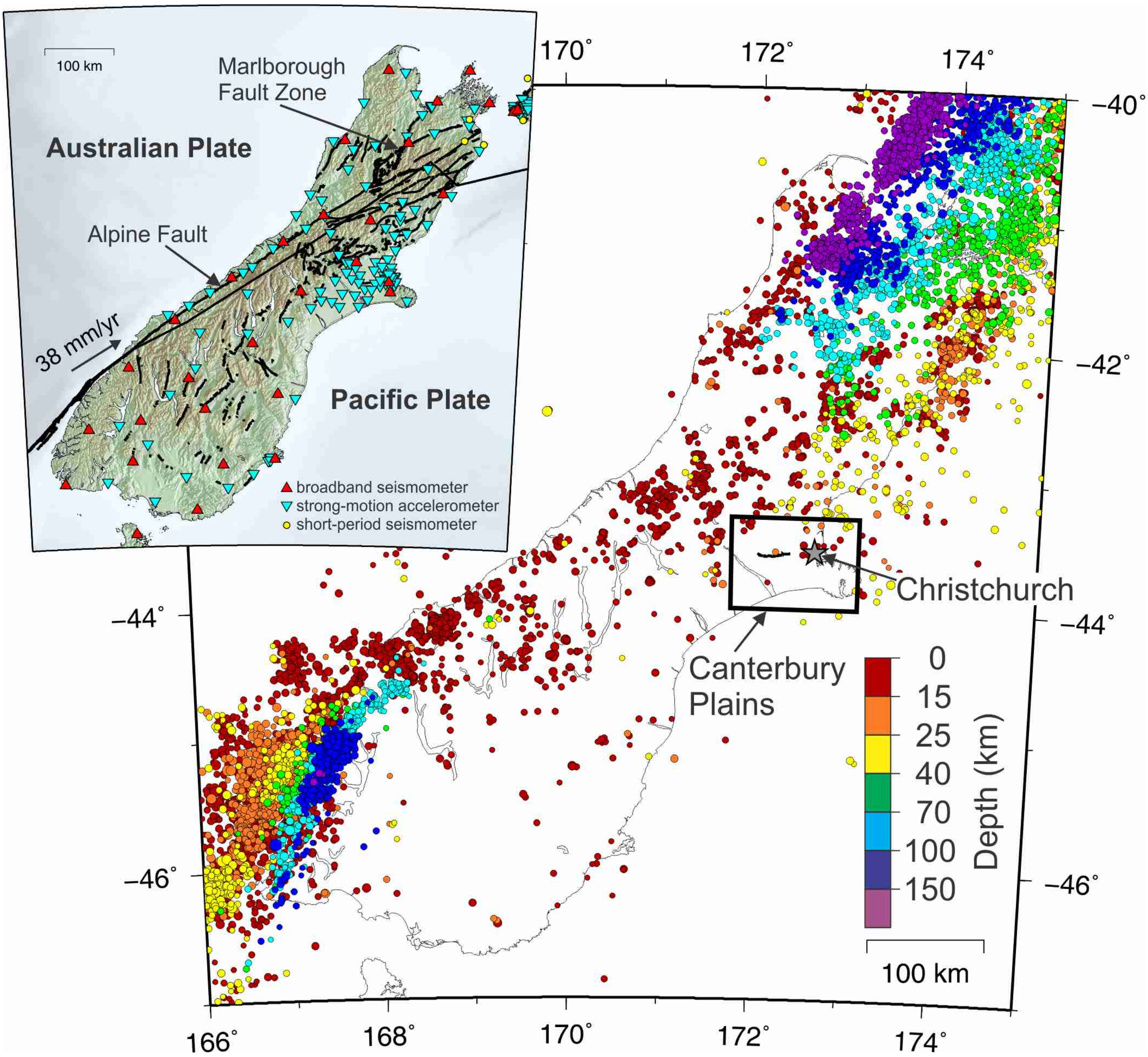

Figure 8.1: *Tectonic setting of the South Island of New Zealand, and recorded seismicity (M $\geq$ 3) for the 10-year period until 2 September 2010. Major active faults, including the Alpine Fault and Marlborough Fault Zone, are shown by the black lines. Also shown is the seismograph network of broadband seismometers, strong-motion accelerometers, and short-period seismometers operated by GeoNet. Note the low rate of seismicity in the Canterbury Plains region before September 2010.*

the Pacific/Australia plate boundary (Figure 8.1). In the South Island, the Alpine Fault runs along the west coast and accommodates the vast majority of the relative plate motion. Palaeoseismic evidence suggests that the Alpine Fault ruptures in major earthquakes ($M > 7.5$) with recurrence intervals of ∽200 – 300 years, with the most recent event in 1717 (e.g. Cooper and Norris 1990; Yetton *et al.* 1998; Rhoades and Van Dissen 2003; Sutherland *et al.* 2007; Berryman *et al.* 2012). Several $M > 6$ - 7 earthquakes have occurred in the foothills of the Southern Alps east of the Alpine Fault and west of Christchurch in the past 150 years. These include 1888 North Canterbury M_W 7.1 (Cowan 1991), 1929 Arthur's Pass M_W 7.0 (Doser *et al.* 1999), 1994 Arthur's Pass M_W 6.7 (Abercrombie *et al.* 2000) and 1995 Cass M_W 6.2 (Gledhill *et al.* 2000). The Darfield earthquake demonstrated that the zone of active deformation in the eastern South Island extends beyond the visible range front. There are many mapped active faults in the eastern foothills of the Southern Alps (e.g. Stirling *et al.* 2008); however, no active faults had been previously mapped in the Canterbury plains, including the Christchurch region. Dorn *et al.* (2010) carried out high-resolution reflection seismic studies in the western part of the Canterbury Plains. Unfortunately none of the seismic lines crossed the Greendale Fault.

In this paper I present an overview of the Christchurch earthquake and the continuing aftershock sequence since 21 February 2011. I will discuss the source properties of the Christchurch earthquake, characteristics of the aftershock sequence, and the effect of the earthquake on the city of Christchurch.

8.1.2 The M_W 6.2 Christchurch Earthquake

Before the M_W 7.1 Darfield earthquake the Canterbury Plains region had a historically low level of seismic activity compared with many other parts of New Zealand (e.g. Anderson and Webb, 1994) (Figure 8.1). Typically the largest aftershock in a sequence is about one magnitude unit smaller than the mainshock. For the M_W 7.1 Darfield earthquake the largest aftershock expected was ∽M_W 6.0, but the largest aftershock was only of M_W 5.0 during the first $5\frac{1}{2}$ months. On 22 February 2011 at 12:51 NZST the M_W 6.2 Christchurch earthquake struck ∽6 km SE of the city centre as an aftershock to the Darfield earthquake.

The Christchurch earthquake occurred on a previously unmapped NE-SW striking fault in the Port Hills area of the outer suburbs of Christchurch (Figure 8.2 a), where there were temporary instruments already installed (Figure 8.2 b). Figure 8.2 c and Table 8.1 show the focal mechanisms from the USGS centroid moment tensor solution (http://earthquake.usgs.gov/regional/neic/), the Global CMT Project solution (http://www.globalcmt.org/) and the GeoNet regional moment tensor solution, all indicating primarily reverse faulting with a strike-slip component. The Christchurch earthquake was far more devastating to Christchurch than the Darfield earthquake due to several factors that will be discussed later, and triggered an extensive aftershock sequence centred around Christchurch and into Pegasus Bay east of Christchurch, mostly notably a M_W 6.0 aftershock on 13 June 2011 UTC.

In the $5\frac{1}{2}$ months following the M_W 7.1 Darfield earthquake much of the aftershock activity had been focused in the Canterbury Plains west of Christchurch. Aftershock activity also extended east of the Greendale Fault towards Christchurch, most notably the 26 December 2010 NZST (25 December 2010 UTC) cluster of aftershocks that occurred near the city centre (Ristau 2011). The Christchurch earthquake occurred east of the main aftershock zone in an area of small positive stress resulting from the

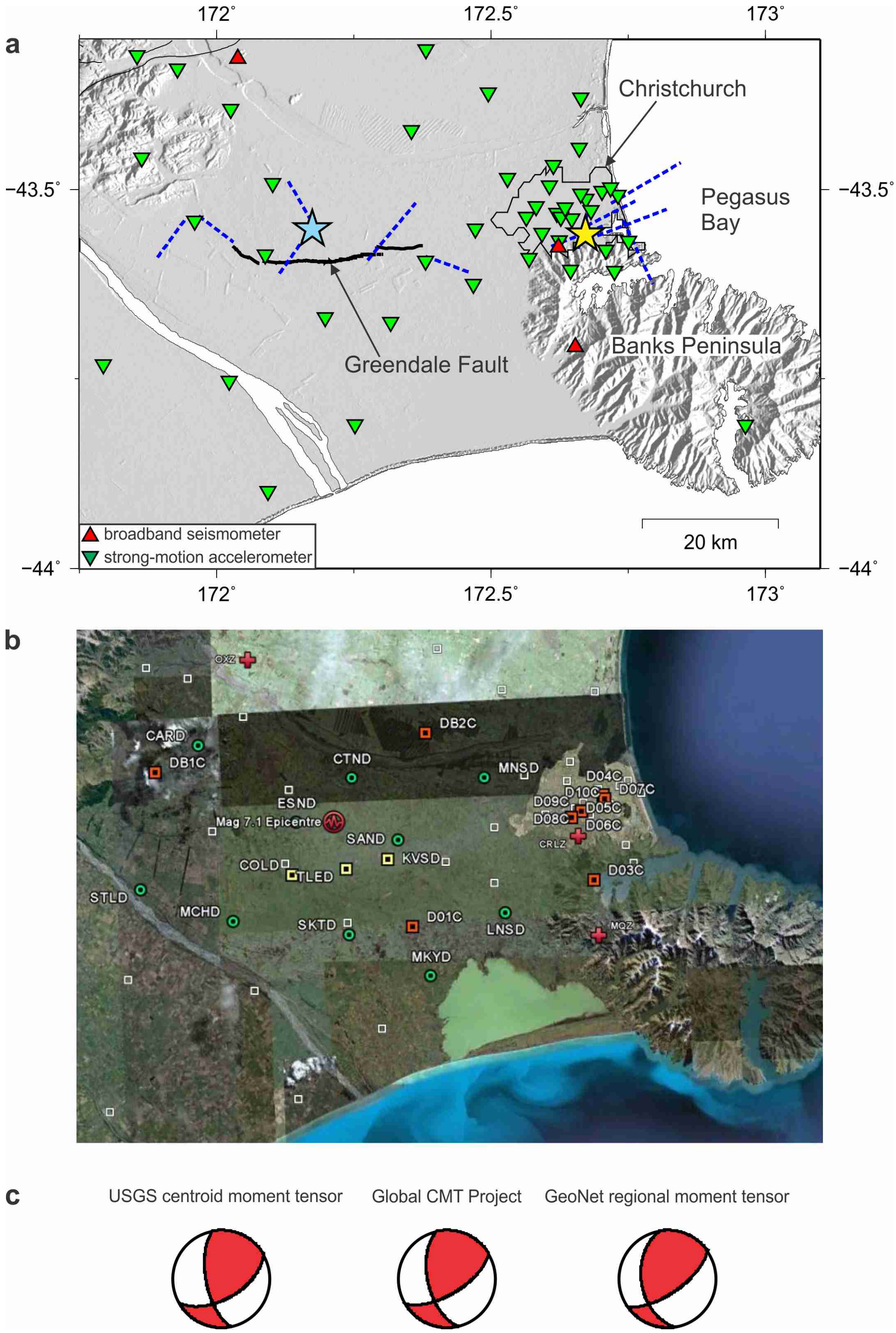

Figure 8.2: *(a) Seismograph network in the Canterbury region at the time of the M_W 7.1 Darfield earthquake (blue star). The yellow star is the location of the M_W 6.2 Christchurch earthquake. Inferred subsurface faults (dashed lines) are those of Beavan et al. (2012), Elliot et al. (2012) and Atzori et al. (2012). Broadband seismometers are indicated by red triangles and regional Canterbury CanNet strong-motion accelerometers by inverted green triangles. (b) Temporary short-period seismometer (green circles), accelerometer (yellow and orange squares) network installed immediately following the Darfield earthquake, along with CanNet strong-motion accelerometers (white squares). (c) Focal mechanisms for the Christchurch earthquake from the USGS centroid moment tensor solution, the Global CMT Project solution and the GeoNet regional moment tensor solution.*

***Table 8.1:** Source parameters for the February 2011 Christchurch earthquake.*

Agency/Type	strike/dip/rake	strike/dip/rake	Mo (Nm)	M_w	Depth (km)
USGS centroid moment tensor	59/59/147	168/62/36	1.86E+18	6.1	12
Global CMT Project	59/64/143	167/57/32	1.92E+18	6.1	12
GeoNet regional moment tensor	55/66/129	172/44/35	2.46E+18	6.2	4

Darfield earthquake (Kaiser *et al.* 2012).

One of the most notable features of the Christchurch earthquake were the high peak ground accelerations (PGA's), observed up to 2.2 g vertically and 1.7 g horizontally at Heathcote Valley ∽2 km from the epicentre. In the city centre vertical PGA's of 0.8 g and horizontal PGA's of 0.7 g (Figure 8.3) were recorded (Kaiser *et al.* 2012). The deep Christchurch sedimentary basin likely led to a waveguide effect for the seismic waves, which resulted in increased ground motion durations and long-period amplitudes (Bradley and Cubrinovski 2011; Bradley 2013). These PGA's are among the highest recorded worldwide; a similar analogue globally is the 2008 M_W 7.2 Iwate-Miyagi, Japan earthquake with PGA $>$ 3.9 g (Suzuki *et al.* 2010).

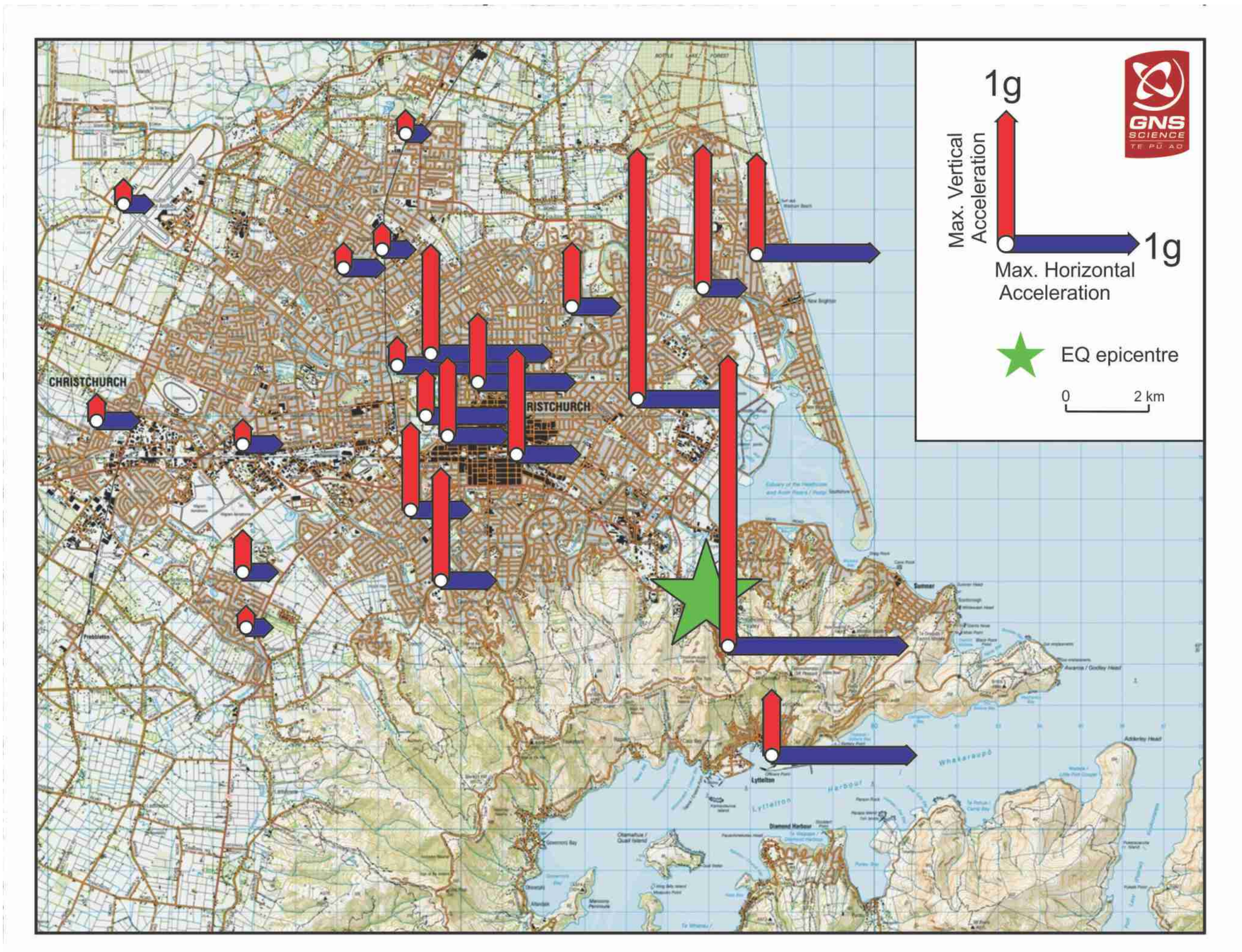

***Figure 8.3:** Map of the Christchurch urban area showing maximum PGA (vertical and horizontal components).*

A kinematic source model for the Christchurch earthquake with a rupture velocity of 2.8 km/s and a maximum slip of 4.2 m (Figure 8.4) was calculated using data from 11 strong-motion stations within 20 km of the epicentre (Holden 2011). The slip model, in which the maximum slip is located at ∽4 km depth and occurred north and up-dip of the hypocentre, shows the S-wave energy being directed up-dip towards Christchurch. A high rupture velocity is also noted in Fry *et al.* (2011); based on data filtered up to 5 Hz, they require a rupture velocity of 3.2 km/s to reproduce the high accelerations near the source. The waveform data used for the kinematic source model shows a dominant peak in the velocity records a few seconds after the main rupture. For stations in central Christchurch this signal is larger than the signal modelled from the initial slip and suggests more than one subevent may have been involved in the rupture. A similar result was found in the kinematic model of Serra *et al.* (2013). Fry and Gerstenberger (2011) calculated radiated energy (ES) estimates from broadband P-waves that gave an energy magnitude of Me 6.8 for the Christchurch earthquake. Apparent stress, defined as the product of rigidity and ES per unit moment, was calculated by Fry and Gerstenberger (2011) to be ∽4.1 MPa, higher than global averages (e.g. Choy *et al.* 2001; Atkinson and Boore 2006).

As with the Darfield earthquake, geodetic studies of the Christchurch earthquake involving GPS and InSAR data have been carried out by Beavan *et al.* (2012), Elliot *et al.* (2012) and Atzori *et al.* (2012). All of the geodetic models require multiple fault segments to be active during the rupture. Beavan *et al.* (2011) presented single-fault and two-fault models of the rupture, but acknowledged that a region of apparent ground uplift in eastern Christchurch was not fit by their models. Beavan *et al.* (2012) incorporated LiDAR data for the region into their geodetic model, to better constrain the uplift in eastern Christchurch, and proposed a three-fault model (Figure 8.5) with the eastern section having oblique reverse/right-lateral faulting, the western section having mainly right-lateral faulting, and the NNE-trending cross-fault having nearly pure reverse faulting. The moment release is similar for all three segments with a total moment release of M_0 4.07×10^{18} Nm, equivalent to an event with M_W 6.4. The multiple fault segments required by the geodetic models are consistent with the kinematic source model, and the large strike-slip segment required by Beavan *et al.* (2012) agrees with the kinematic results. The two-fault geodetic models proposed by Elliot *et al.* (2012) and Atzori *et al.* (2012) have most of the moment release along a reverse faulting segment, but also require a large strike-slip segment.

The crustal structure in the Canterbury region is dominated by the Hikurangi Plateau – a large igneous province subducted ∽100 million years ago. The Hikurangi Plateau is extremely strong and remains attached to the crust, capped by schist and greywackes containing east-west Cretaceous faults (Reyners *et al.* 2014). Reyners *et al.* (2014) found unusually low P- to S-wave ratios of 1.60, in contrast to velocity ratios of 1.71 before the Darfield earthquake. They interpreted the reduced velocity ratios as a signature that the greywackes had been weakened by the rupture front producing widespread cracking around the fault zone, and suggested that recovery of rock strength between the Darfield and Christchurch earthquakes could explain the long delay between the two events.

As mentioned above, the Christchurch earthquake was far more devastating to the city of Christchurch than the Darfield earthquake, despite being much smaller. The most important factor was the proximity of the Christchurch earthquake to the city compared with Darfield. The Christchurch earthquake occurred beneath the outer suburbs of Christchurch ∽6 km SE of the city centre, whereas the Darfield earthquake occurred ∽40 km west of Christchurch and the eastern end of the rupture zone was ∽20 km

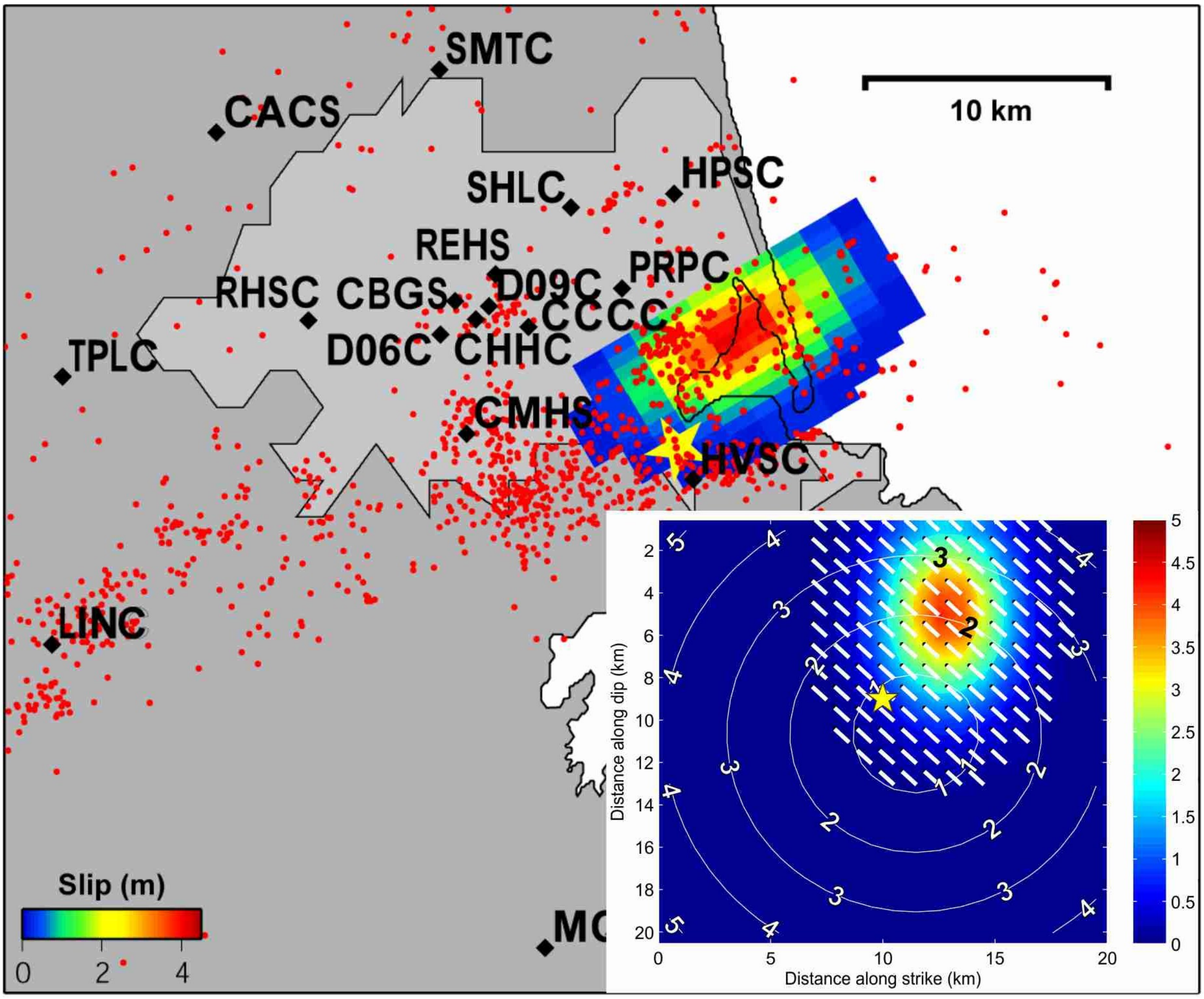

Figure 8.4: *Map view of the slip distribution on a plane with strike 59º and dip 67º SSE. Aftershock locations (red dots) and the Christchurch epicentre (yellow star) are from Bannister et al. (2011), and black diamonds are strong-motion instruments used to calculate the slip distribution. The inset shows the vertical projection of the slip distribution with the slip direction indicated by the white vectors, showing the energy being directed updip towards Christchurch. Rupture front propagation timing in seconds is indicated by the white contours (from Holden, 2011).*

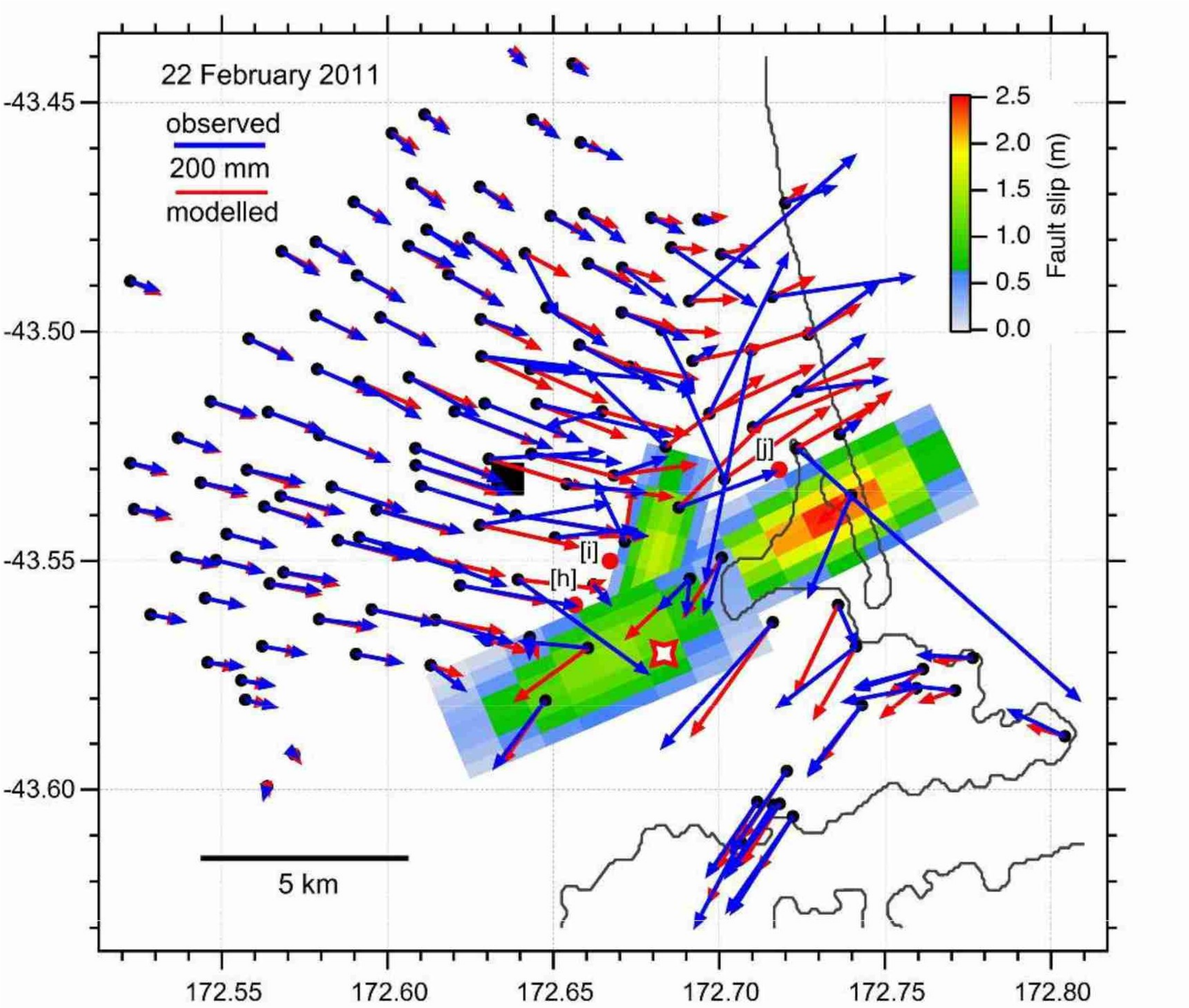

Figure 8.5: *Observed (blue) and modelled (red) displacements at GPS sites and the slip model derived from GPS and DInSAR data for the Christchurch earthquake. Red dots with adjacent letters in square brackets (e.g. [a]) are located where the centres of the fault segments would outcrop if extended to the surface (from Beavan et al. 2012).*

west of Christchurch. Another important factor was the great amount of radiated energy produced and the effects of strong source directivity where much of the energy was directed towards the city (Fry *et al.* 2011; Holden 2011).

A third important factor involved the response of the shallow subsurface to extreme ground motions. Fry *et al.* (2011) found that strong-motion recordings at several near-source sites in the city contained much higher frequency content on the vertical component compared with the corresponding horizontal component. They interpreted this phenomenon as being due to the presence of a shallow water table that dramatically attenuated the propagation of high-frequency shear waves. The vertical components exhibited a high degree of asymmetry (Figure 8.6) with maximum accelerations in the upward direction ($> 1\ g$) exceeding accelerations in the downward direction ($< 1\ g$).

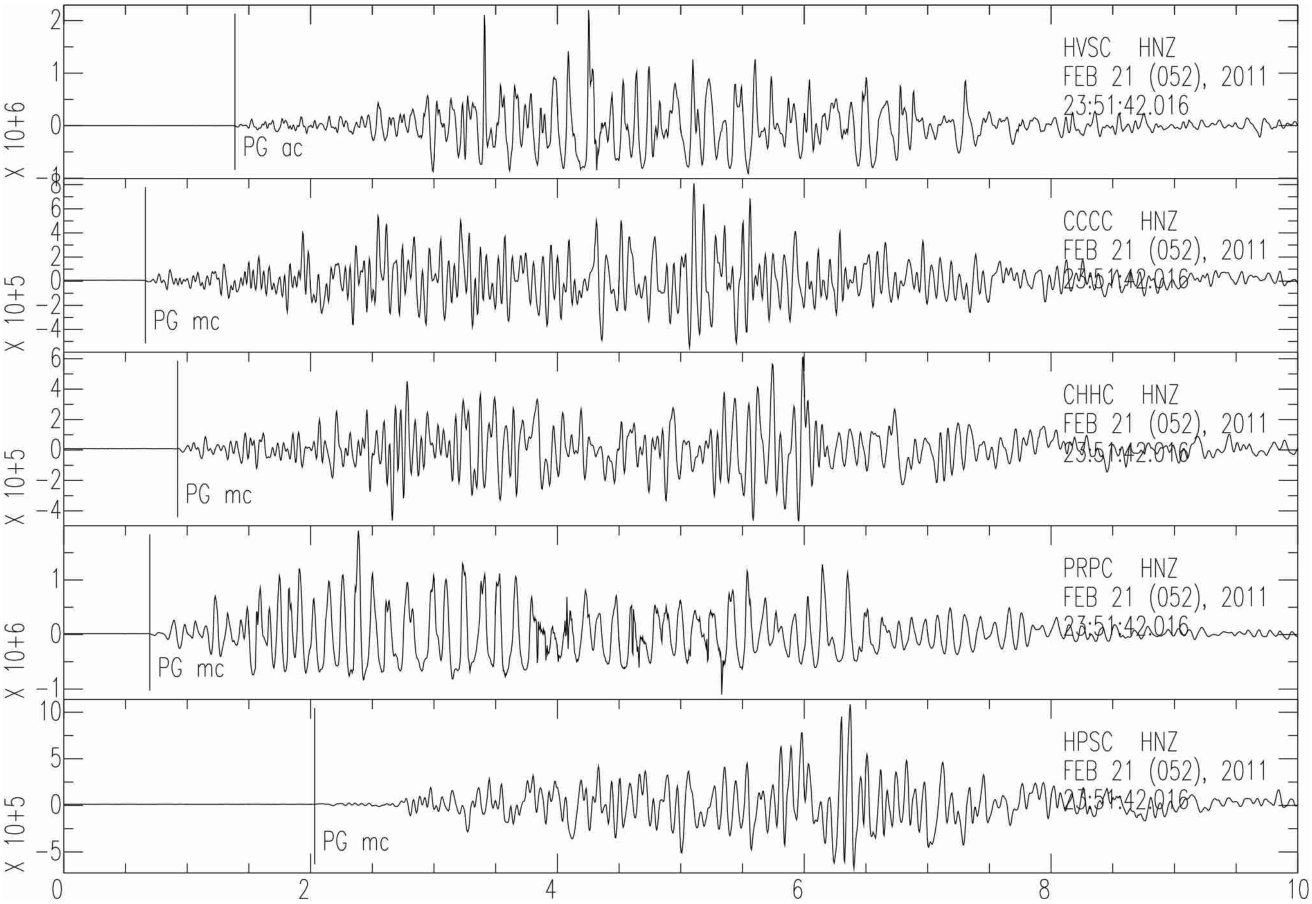

Figure 8.6: *Vertical acceleration waveforms from strong-motion sites in the Christchurch region, showing larger positive accelerations than negative ones. Many of the negative acceleration troughs are also broader than the narrow positive spikes (from Fry et al. 2011).*

Asymmetric vertical recordings were also noted during the 2008 M_W 6.9 Iwate-Miyagi Nairiku, Japan earthquake (Aio *et al.* 2008; Yamada *et al.* 2009) and attributed to a "trampoline" effect. Aoi *et al.* (2008) describe the asymmetry as due to the decoupling of near-surface materials during high-amplitude downward acceleration, resulting in an approximate free-fall of the material. Yamada *et al.* (2009) suggests that the large positive accelerations are further enhanced by "slapdown", as free-falling upper soil layers impact with deeper layers that are returning upwards following the earthquake wave cycle. Fry *et al.* (2011) interpreted the asymmetry in the Christchurch vertical accelerations as being due to the "trampoline" and "slapdown" effects, which further intensified the ground shaking and subsequent damage.

8.1.3 Effects on the built environment

Liquefaction

One of the significant effects of the Christchurch earthquake was widespread liquefaction throughout the urban areas of the city (Figure 8.7), causing extensive damage to residential properties, water and wastewater networks, high-rise buildings and bridges. Liquefaction was evident from massive sand boils and from large amounts of sand/silt ejecta and water throughout the city. Nearly 15 000 homes were severely damaged, with more than half beyond repair (Cubrinovski *et al.* 2012; Reid *et al.* 2012; Cox *et al.* 2012). The greatest damage occurred along the Avon River, which flows through the city centre, with permanent lateral spreading at the riverbanks of up to 2 – 3 m that progressed as far as 200 – 250 m inland, causing significant damage to structures within the spreading zone (Cubrinovski *et al.* 2012).

Landslides

The large accelerations, combined with the proximity of the earthquake to the Port Hills, triggered numerous landslides in the southern suburbs of Christchurch (e.g. Massey *et al.* 2014). At least five deaths there were attributed to falling rocks. Several hundred homes were evacuated because they were close to the foot or top of dangerous cliffs. Four main types of earthquake-triggered mass movements were identified: rockfalls, shallow landslides, deep-seated landslides and tension cracks (Figure 8.8). Rockfalls made up the majority of the mass movements and caused substantial damage to properties. Some rockfalls travelled large distances to smash through houses and ranged from single boulders to large masses of rock. Many slopes showed deep tension cracks and rents that indicated rock sections with potential for further collapse.

Building damage

The damage to buildings in Christchurch varied considerably depending on the site location, extent of liquefaction at the site and the building characteristics. The building stock in Christchurch consists of unreinforced masonry buildings, timber buildings, reinforced concrete buildings and tilt-up (pre-fabricated) industrial buildings. Damage to masonry buildings including churches (e.g. Figure 8.9; Figure 8.10) was widespread across the city. Residential and commercial unreinforced masonry buildings also performed poorly and suffered significant structural damage (Figure 8.10). Timber homes generally performed better; however, many homes suffered significant damage due to lateral spreading from liquefaction (e.g. Fleischman *et al.* 2014; Sritharan *et al.* 2014). Modern reinforced buildings generally performed well, mostly sustaining only moderate damage. But in the Christchurch city centre, many of the fatalities resulted from the almost complete collapse of the Canterbury Television (CTV) building and the Pyne Gould building. Another example of severe damage was the historic Time Ball Station in Lyttelton, SE of Christchurch.

Figure 8.7: *(a) Liquefaction area behind the Catholic Basilica, Christchurch, photographer Margaret Low, copyright GNS Science, VML ID 6141. (b) Car trapped by liquefaction, photographer Andrew King, copyright GNS Science, VML ID 101933.*

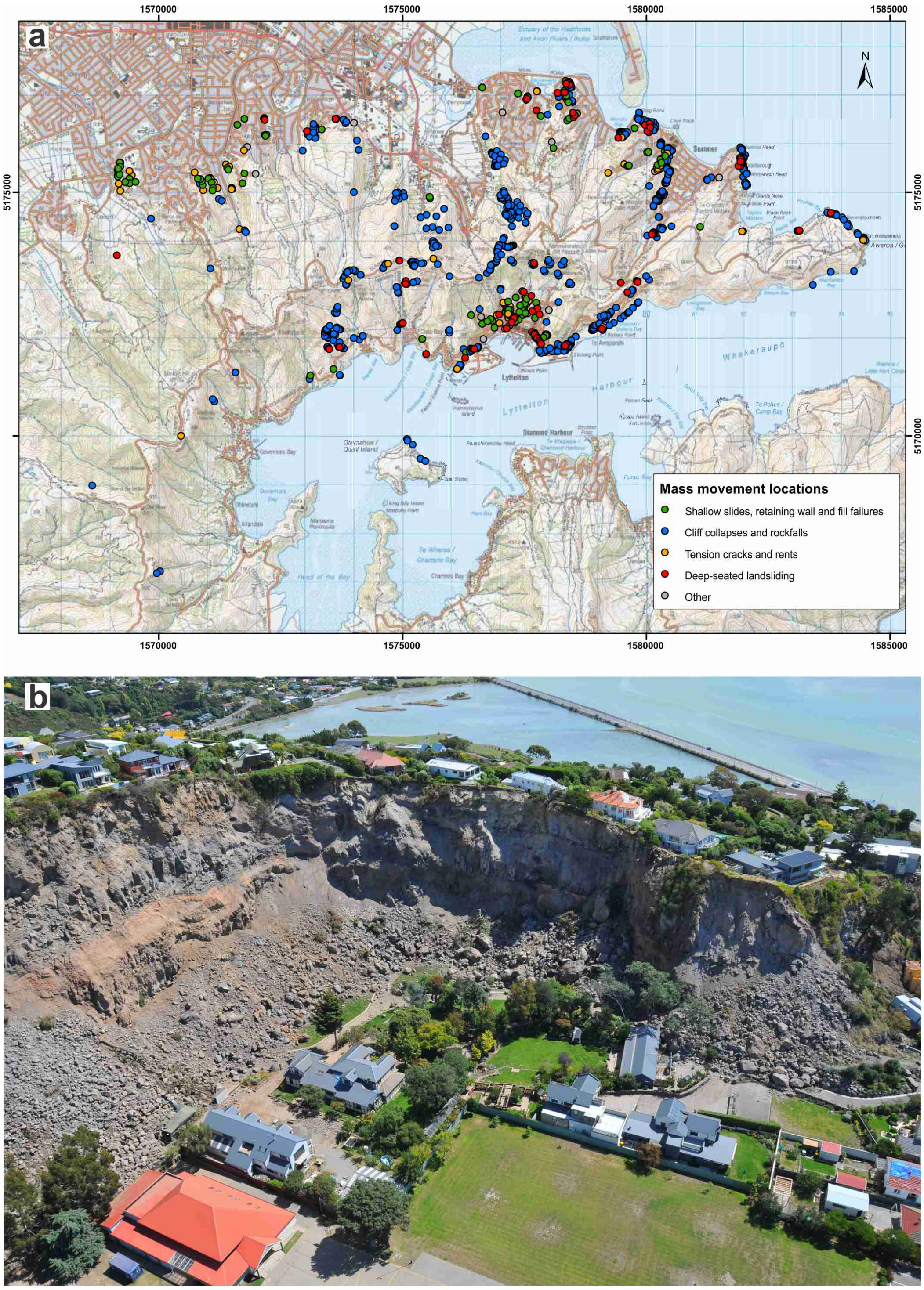

__Figure 8.8:__ (a) Map showing the distribution of mass movements caused by the Christchurch earthquake (from Massey et al. 2014). (b) Example of earthquake induced mass movement showing the proximity of homes at the top and base of the cliff, photographer Graham Hancox, copyright GNS Science/EQC, VML ID 130503.

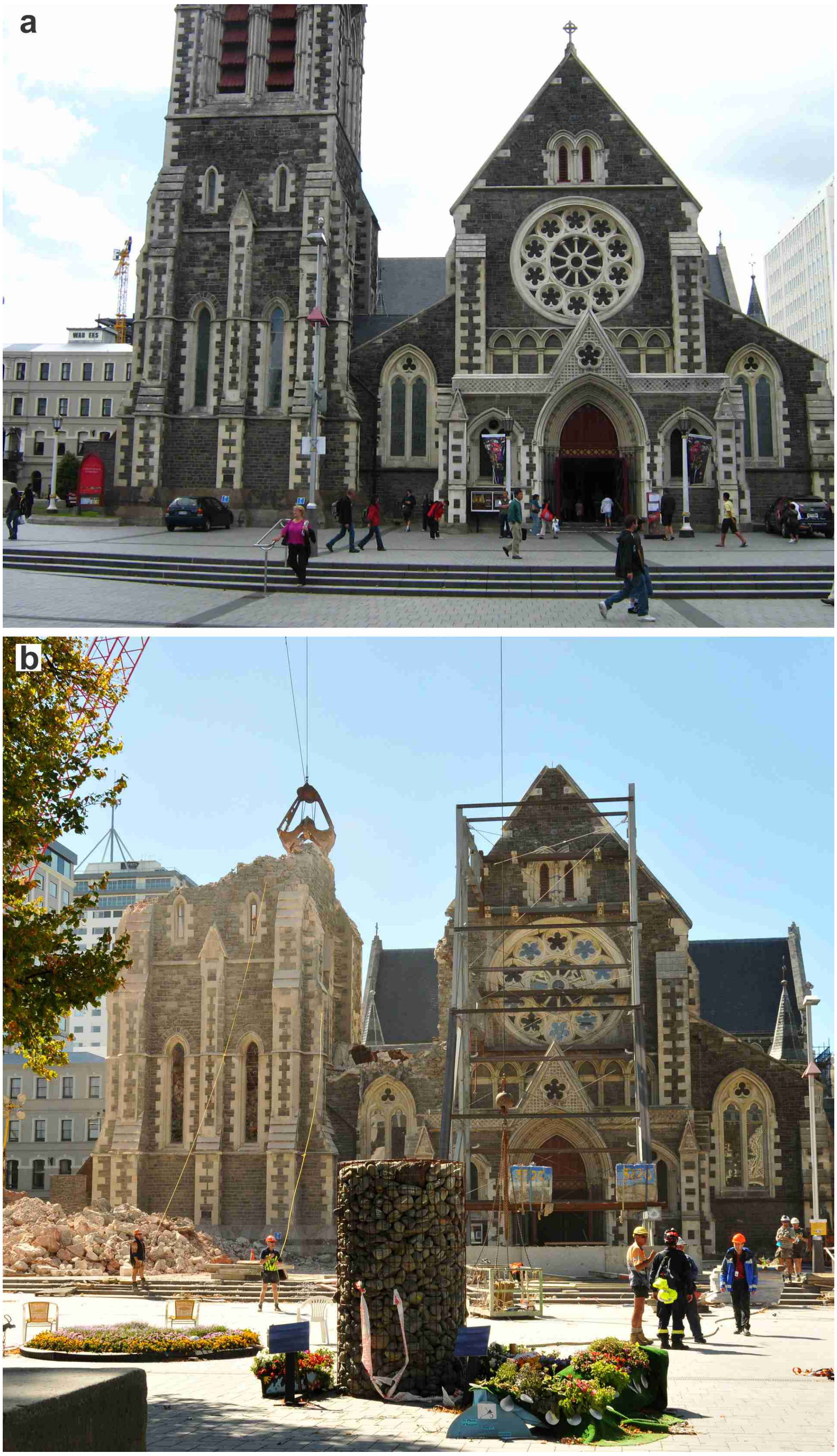

Figure 8.9: *(a) The historic Christchurch Cathedral in the city centre before the Christchurch earthquake. (b) Christchurch Cathedral after the Christchurch earthquake, photographer Margaret Low, copyright GNS Science, VML ID 6175.*

Figure 8.10: *(a) Damage to the Cathedral of the Blessed Sacrament, photographer Margaret Low, copyright GNS Science, VML ID 6128. (b) Damaged building, photographer Margaret Low, copyright GNS Science, VML ID 101912. (c) Building damage in the Christchurch central business district, photographer Margaret Low, copyright GNS Science, VML ID 101881.*

8.1.4 Aftershock Sequence

The M_W 6.2 Christchurch earthquake initiated a rejuvenated aftershock sequence, mainly centred near the city of Christchurch and the Pegasus Bay offshore region (Figure 8.11 a). More than 4400 of the aftershocks, with $M_L \geq 1.0$ and with 13 $M_W \geq 5.0$, were relocated using a double-difference tomography method (Bannister *et al.* 2011). The most significant of these included the M_W 6.0 aftershock of 13 June 2011 UTC, located ∽4 km east of the Christchurch earthquake epicentre, and a later sequence of large M_W 5.4 – 5.9 aftershocks on 23 December 2011 UTC, which occurred in Pegasus Bay, NE of the Christchurch earthquake epicentre. The aftershocks from 21 February – 13 June 2011 occurred mainly in the southern parts of Christchurch with some extension west of the city. A feature of the aftershocks is that they do not clearly define the fault plane of the Christchurch earthquake as defined by either the moment tensor solution or the geodetic model (Bannister *et al.* 2011), suggesting that there may have been very little post-seismic slip on the fault.

The M_W 6.0 earthquake of 13 June 2011 UTC was a strike-slip event that occurred ∽4 km east of the Christchurch earthquake epicentre (Figure 8.11; Sibson *et al.* 2011). The geodetic model from Beavan *et al.* (2012) suggests two possibilities for this event. The first possibility is a single-fault model with the rupture on a NNW-SSE striking plane. The second possibility is a two-fault model with rupture on a NNW-SSE striking plane and on a ENE-WSW striking plane, with approximately equal moment release on each plane. Beavan *et al.* (2012) were unable to distinguish between the two options, but preferred the two-fault model that was mainly consistent with the kinematic source model of Holden and Beavan (2012). The first event on the ENE-WSW plane ruptured a region 6 km × 5 km with a maximum slip of 3 m, and the second event on the NNW-SSE plane ruptured a region 11 km × 7 km with a maximum slip of 2.6 m (Holden and Beavan 2012).

The 13 June 2011 earthquake reinvigorated the sequence with many aftershocks extending SE into Banks Peninsula where little aftershock activity had occurred previously. It caused further damage and liquefaction in Christchurch but its effects were significantly less than for the Christchurch earthquake. Whereas the Christchurch earthquake had mainly reverse faulting, focal mechanisms derived from regional moment tensor solutions for aftershocks to the Christchurch earthquake and this later earthquake indicated mainly strike-slip faulting, though there were some with reverse or oblique-reverse faulting (Figure 8.11 b).

Three earthquakes on 23 December 2011 UTC (M_W 5.4 – 5.9) centred near Pegasus Bay, east of Christchurch, triggered a NE-SW series of aftershocks that extended offshore. These earthquakes were widely felt in Christchurch but damage was minimal due to their offshore location (Ristau *et al.* 2013). The M_W 5.9 event indicated reverse faulting and the kinematic solution favoured a SE-dipping fault plane with a slip region of 18 km × 15 km with a maximum slip of 0.8 m. Due to the offshore location it was not possible to determine a well-constrained geodetic model. Fifty-three focal mechanisms were determined for events in Pegasus Bay with a majority (45 of 53) indicating reverse or oblique-reverse faulting. This is in contrast with the rest of the Canterbury aftershock sequence where ∽74% of the focal mechanism determinations indicated strike-slip faulting (Ristau *et al.* 2013).

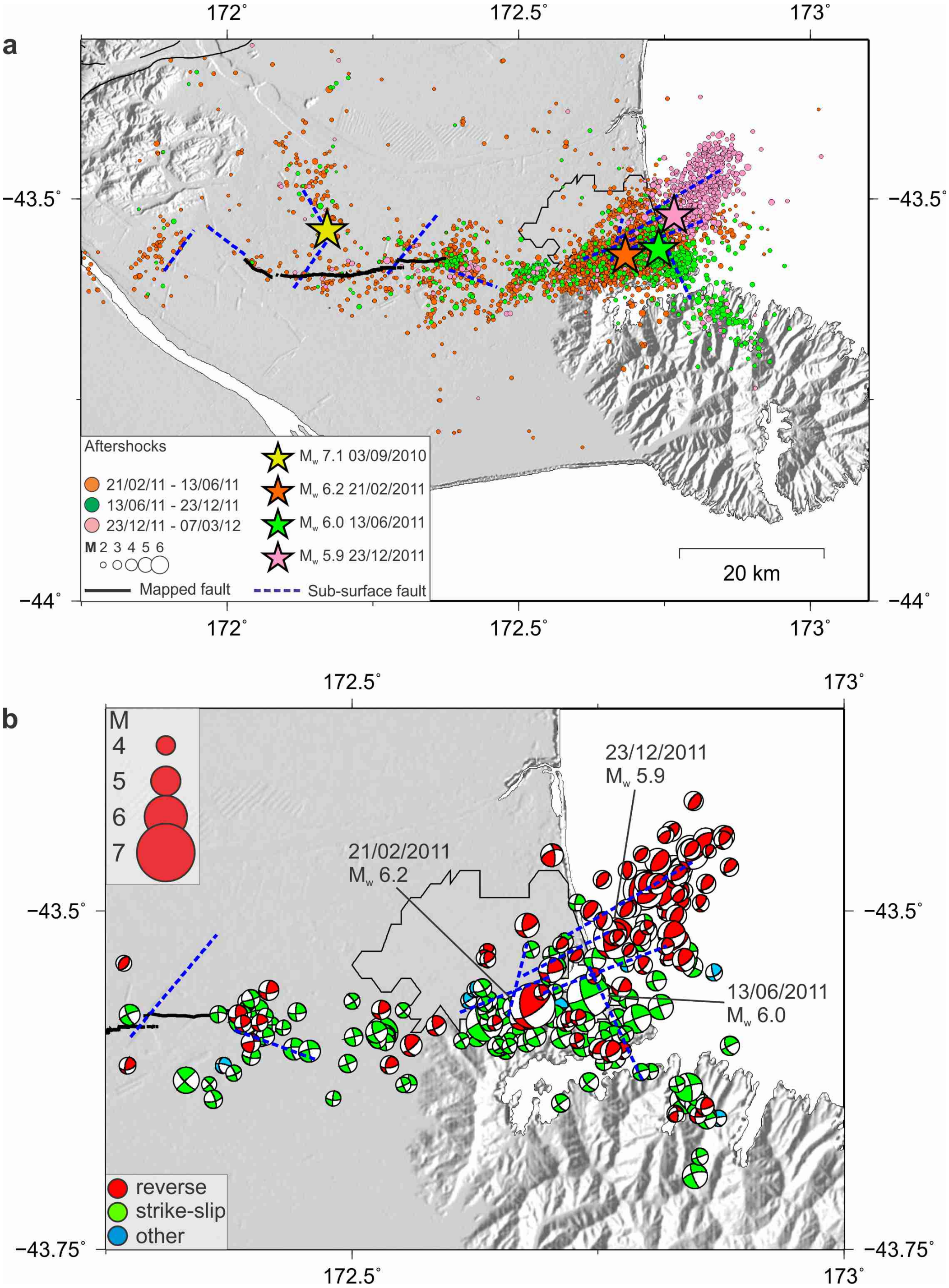

Figure 8.11: *(a) Relocated aftershocks for the period 21 February 2011 – 31 January 2012. The solid black line represents the Greendale Fault and the dashed blue lines the inferred subsurface faults. Stars show the epicentres of the Darfield earthquake, the Christchurch earthquake, and later large aftershocks closer to Pegasus Bay. Aftershocks symbols are colour coded to correspond to each of the main earthquakes and before the next earthquake. Aftershocks preceding the Christchurch earthquake are not shown. (b) Focal mechanisms derived from 204 regional moment tensor solutions for the period 21 February 2011 – 20 November 2013.*

8.1.5 Stress Studies and Aftershock Forecasts

Steacy *et al.* (2014) studied stress triggering during the Canterbury earthquake sequence by comparing maps of Coulomb stress changes with the location of later events. They investigated whether later large aftershocks were consistent with stress triggering, and whether a simple stress map produced shortly after the Darfield earthquake would have accurately indicated the regions where subsequent activity occurred. Steacy *et al.* (2014) found that all aftershocks with $M > 5.5$ occurred in areas of increased failure stress computed using a slip model for Darfield that was available within 10 days of its occurrence. The Christchurch earthquake was in a region of small positive stress induced by the Darfield earthquake (Figure 8.12; C. Williams pers. comm.); however, the Christchurch earthquake was preceded by a M 5 earthquake on 7 September 2010, centred ∽2.3 km away that may have increased the stress locally by 4.2 MPa (Steacy *et al.* 2014). The June 2011 earthquake also occurred in a region of positive stress induced by the Darfield earthquake and was preceded by four $M \geq 5$ events (22 February, 5 March, 16 April, and 13 June 2011) within a few kilometres of its epicentre (Steacy *et al.* 2014). Ristau *et al.* (2013) examined the Coulomb stress changes near Pegasus Bay using the modelled Darfield, Christchurch and June 2011 events as source faults. They found that the epicentral region for the December 2011 Pegasus Bay earthquakes had positive stress regions at very shallow depths (∽6 km), but mainly regions of negative stress at greater depths. The hypocentres for the Pegasus Bay earthquakes were largely at depths greater than ∽5 km with an average depth of ∽10 km.

The aftershock probability forecasts continued to evolve throughout the Canterbury earthquake sequence as each large earthquake reinvigorated the aftershock sequence (e.g. Gerstenberger *et al.* 2014). Table 8.2 shows how the expected number aftershocks in the M 4.0 – 4.9 and $M \geq 5.0$ ranges changed later in the Canterbury aftershock sequence. Immediately after the Christchurch earthquake the expected number of aftershocks with $M \geq 4.0$ had decreased to low levels and it then increased dramatically afterwards. The same pattern occurred immediately before and after the June 2011 earthquake. The aftershock forecasts underestimated the number of aftershocks in the M 4.0 – 4.9 range immediately following each main earthquake, as had been the case also after the Darfield earthquake. Subsequently the observed numbers of aftershocks were mainly in agreement with the forecasts.

Table 8.3 shows one-week, one-month, and one-year aftershock probabilities for M 5.0 – 5.9, M 6.0 – 6.9 and M 7.0+ at three dates after the Christchurch earthquake. These probabilities are valid for the entire Canterbury Plains region, including Christchurch, but were calculated while the catalogue was still being revised and completed (A. Christophersen, pers. comm.). Following the Christchurch earthquake the one-week and one-month probabilities were ∽2 – 3 times above earlier 27 January 2011 forecasts, but the one-year probabilities remained about the same. From 1 November 2013 the one-year probability for a M 5.0 – 5.9 was still high (68%), but low for $M \geq 6.0$, with similar results for 1 April 2014. Thus the aftershock probabilities are diminishing but not negligible. The lesson here has been that the Canterbury sequence has been long-lasting with multiple reinvigoration.

8.1.6 Discussion

In this paper I have summarised some of the major findings of the M_W 6.2 Christchurch earthquake, the subsequent aftershock sequence and its relationship to the M_W 7.1 Darfield earthquake. The Canter-

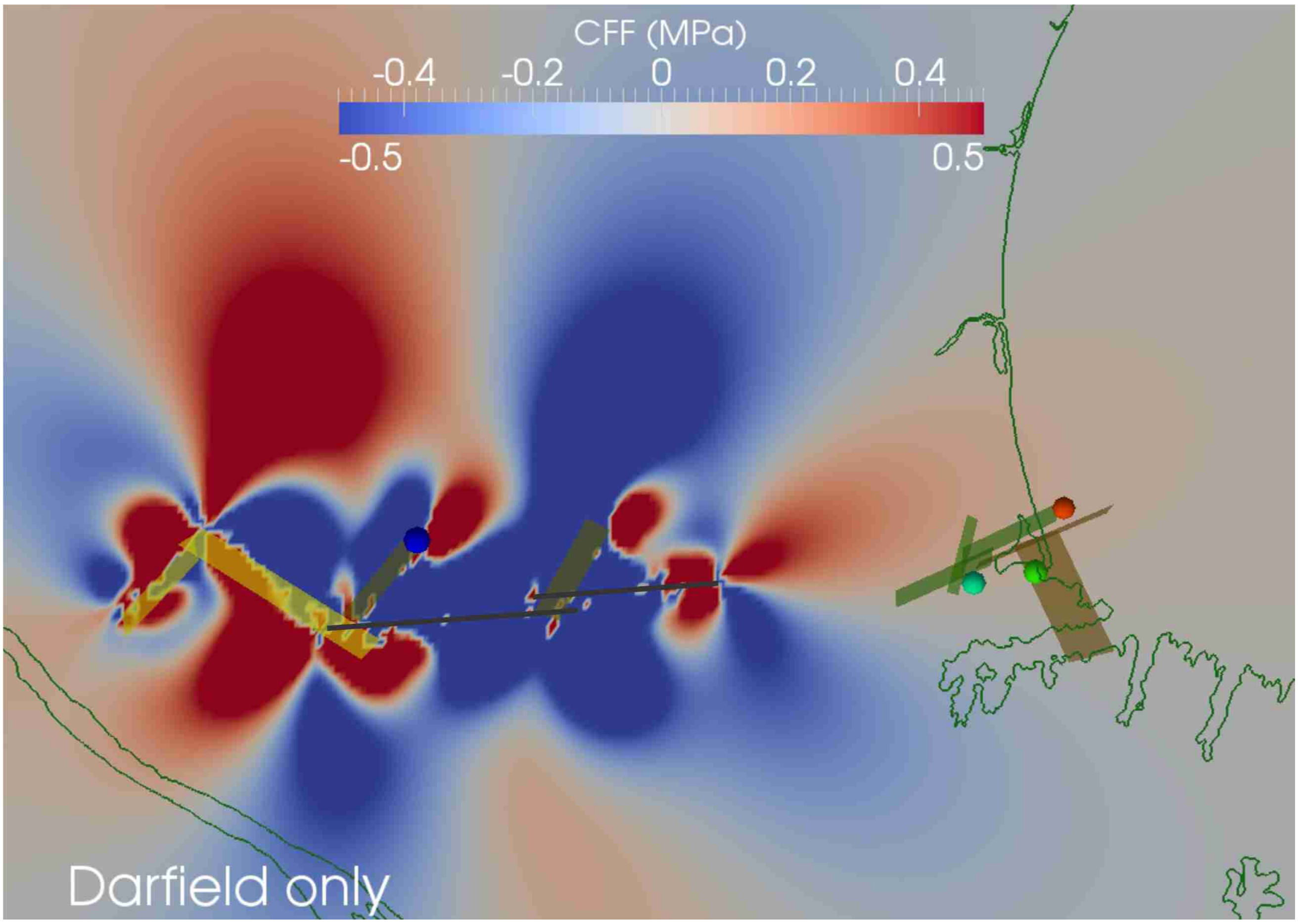

Figure 8.12: *Coulomb stress modelling for the Greendale Fault rupture (black line) after the Darfield earthquake and its effect on the Christchurch region resolved at a depth of 5 km. Green dots are the epicentres of the Christchurch earthquake and June 2011 earthquakes, and the red dot indicates the epicentral region of the Pegasus Bay earthquakes. Fault segments (green/brown/yellow rectangular regions) are those of Beavan et al. (2012). The eastern end where the Christchurch earthquake occurred is a small region where the failure stress increased due to the Darfield earthquake.*

bury earthquakes can be regarded as an intraplate sequence, remote from the main Alpine-Marlborough fault system that defines the Pacific/Australian plate boundary (e.g. Sibson *et al.* 2013; Fry *et al.* 2014). Considerable research is still required to fully characterise the complexity of the entire Canterbury earthquake sequence. However, preliminary modelling involving seismology, geodesy, finite-element source-modelling and geology has provided much data constraining interpretations for the earthquake sequence. Over a period of many months the Canterbury earthquake sequence evolved from a relatively standard aftershock sequence of the M_W 7.1 Darfield earthquake into a complex, long lasting series of earthquakes (Figure 8.13). By early 2014, the aftershock activity in the Canterbury region had decreased significantly compared with 2012; however, the probability for significant aftershocks, e.g. $M \geq 5$, remains high (Table 8.3). There are still many questions about why the Darfield earthquake and subsequent Canterbury aftershock sequence occurred where it did, and what effect it will have on the potential for future earthquakes in the region.

One feature of the aftershock sequence that has generated considerable debate is the region that has become known as “the gap” (e.g. Bannister and Gledhill 2012). The Greendale Fault rupture of the Darfield earthquake terminated ∽15 – 20 km west of Christchurch, and the Christchurch earthquake

Table 8.2: *Expected and observed numbers of aftershocks later in the Canterbury sequence.*

Date (NZST)	Expected number of aftershocks M 4.0 - 4.9	Observed	Expected number of aftershocks M >= 5.0	Observed
22 - 28 February - M_W 6.2	12 - 29	67	0 - 5	3
1 - 7 March	1 - 10	4	0 - 2	1
8 - 14 March	0 - 6	7	0 - 2	0
15 - 21 March	2 - 11	1	0 - 2	0
22 - 28 March	0 - 7	2	0 - 2	0
29 March - 4 April	0 - 5	2	0 - 1	0
5 - 11 April	0 - 4	1	0 - 1	0
12 - 18 April	0 - 4	1	0 - 1	1
19 April - 18 May	2 - 11	7	0 - 2	2
19 May - 13 June	1 - 10	5	0 - 2	3
13 June - 12 July - M_W 6.0	11 - 28	46	0 - 5	3
13 July - 12 August	1 - 10	2	0 - 2	1
13 August - 12 September	1 - 8	9	0 - 2	0
13 September - 12 October	0 - 7	7	0 - 2	1

Table 8.3: *Aftershock probabilities for given magnitude ranges.*

Date	M 5.0 - 5.9			M 6.0 - 6.9			M 7.0+		
2 Mar 2011	34%	68%	98%	4%	10%	32%	0.40%	1%	3.5%
1 Nov 2013	n/a	11%	68%	n/a	1%	9%	n/a	0.07%	0.7%
1 Apr 2014	n/a	10%	70%	n/a	1%	9%	n/a	<1%	1%

was centred SE of the city centre. Between the eastern end of the Greendale Fault rupture zone and Christchurch city there is a region of decreased aftershock activity where no large ($M > 6.0$) aftershocks have occurred. The moment release in this region is less than that to the west or to the east despite continued aftershock activity (Beavan *et al.* 2012; Elliot *et al.* 2012). If this region were to rupture in a single event it could produce a M 6.0 – 6.5 earthquake. Bannister and Gledhill (2012) noted that focal mechanisms for the largest aftershocks suggest a degree of NNW-SSE left-lateral faulting, which would indicate short fault segments that may not be capable of generating larger earthquakes. However, right-lateral strike-slip faulting is likely towards the western edge of southern Christchurch. The likelihood of a large aftershock in the gap is nevertheless unresolved.

Another concern is the effect of the Canterbury earthquake sequence on faults outside the aftershock zone. Steacy *et al.* (2014) examined stress changes from all the main Canterbury events and found a stress increase of up to 0.24 MPa on the Porter's Pass Fault – an active fault ∽80 km NW of Christchurch capable of generating a M_W 7.5 earthquake. In the Canterbury Plains most of the aftershock activity has been located close to the Greendale Fault and the inferred fault segments. In the Christchurch region, the aftershock activity is more diffuse with most of it not closely associated with the various inferred fault segments. This may suggest increased fracturing of the crust beneath Christchurch, but the nature of the faulting remains unclear. The Canterbury region consists of strong, brittle crust, with no shallow brittle-ductile transition. The geology of the region is complicated by the presence of Banks Peninsula,

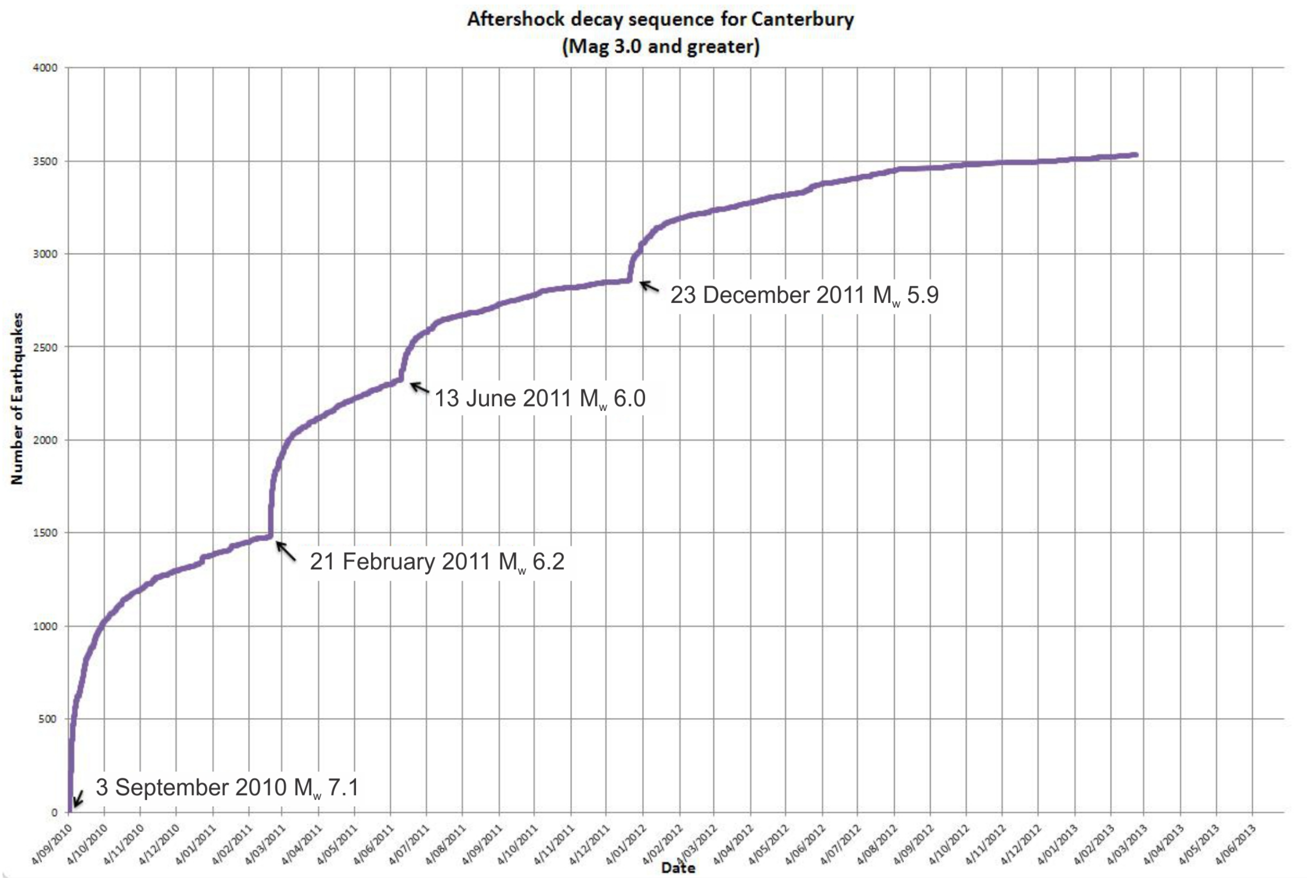

Figure 8.13: *Aftershock decay ($M \geq 3$) for the Canterbury earthquake sequence showing an increase in aftershock activity following each of the main earthquakes in the sequence.*

an intraplate, basaltic shield volcano that was active 12 – 6 Myr ago. What part this structure played in concentrating changes in Coulomb failure stress from the Darfield earthquake near Christchurch is a question that still needs addressing.

8.1.7 Conclusions

The M_W 6.2 February Christchurch earthquake was the deadliest and most damaging earthquake in New Zealand since the 3 February 1931 Hawkes Bay earthquake (M_W 7.4 – 7.6). As a result of the network of strong-motion instruments in operation in the Canterbury Plains and Christchurch regions before the Darfield and Christchurch mainshock occurrences, the Canterbury earthquake sequence is one of the best recorded earthquake sequences anywhere in the world. The near-field strong-motion dataset will be invaluable to future seismic hazard and engineering studies, in New Zealand and elsewhere in the world. The Canterbury earthquake sequence will influence thinking on seismic hazard and risk in New Zealand and worldwide for decades to come. We have learned a great deal about the Canterbury earthquake sequence since the initial 3 September 2010 M_W 7.1 Darfield earthquake; however, a great deal of research is still needed to fully understand the complexity of the Canterbury earthquake sequence.

8.1.8 Acknowledgements

This paper would not have been possible without many valuable discussions and much input from Stephen Bannister, John Beavan, Anne-Marie Christophersen, Susan Ellis, Bill Fry, Matt Gerstenberger, Caroline Holden, Anna Kaiser, Martin Reyners, Rick Sibson, Sandy Steacy and Charles Williams. Several of the figures were created using Generic Mapping Tools (GMT) (Wessel and Smith 1991). Figure 8.9 is from the author's collection: other photographic images are reproduced with kind permission of GNS Science/EQC.

8.1.9 References

Abercrombie, R.E., T.H. Webb, R. Robinson, P.G. McGinty, J. Mori, and R.J. Beavan (2000). The enigma of the Arthur's Pass, New Zealand earthquake 1. Reconciling a variety of data for an unusual earthquake sequence. *Journal of Geophysical Research* 105, 16119-16137.

Anderson, H., and T. Webb (1994). New Zealand seismicity: patterns revealed by the upgraded national seismograph network. *New Zealand Journal of Geology and Geophysics* 37, 477-493.

Atkinson, G.M., and D.M. Boore (2006). Earthquake ground-motion prediction equations for eastern North America. *Bulletin of the Seismological Society of America* 96, 2181-2205.

Aoi, S., T. Kunugi, and H. Fujiwara (2008). Trampoline effect in extreme ground motion. *Science* 322, 727-730, doi:10.1126/science.1163113

Atzori, S., C. Tolomei, A. Antonioli, J.P. Merryman Boncori, S. Bannister, E. Trasatti, P. Pasquali, and S. Salvi (2012). The 2010-2011 Canterbury, New Zealand, seismic sequence: multiple source analysis from InSAR data and modeling. *Journal of Geophysical Research* 117, B08305, doi:10.1029/2012JB009178

Avery, H.R., J.B. Berrill, P.F. Coursey, B.L. Deam, M.B. Dewe, C.C. Francois, J.R. Pettinga, and M.D. Yetton (2004). The Canterbury University strong-motion recording project. Proceedings of 13th World Conference on Earthquake Engineering, Vancouver, British Columbia, 1-6 August 2004. *Canadian Association for Earthquake Engineering* paper no. 1335.

Bannister, S., B. Fry, M. Reyners, J. Ristau, and H. Zhang (2011). Fine-scale relocation of aftershocks of the 22 February M_W 6.2 Christchurch earthquake using double-difference tomography. *Seismological Research Letters* 82, 839-845, doi:10.1785/gssrl.82.6.839

Bannister, S., and K. Gledhill (2012). Evolution of the 2010-2012 Canterbury earthquake sequence. *New Zealand Journal of Geology and Geophysics* 55, 295-304, doi:10.1080/00288306.2012.680475

Beavan, J., E. Fielding, M. Motagh, S. Samsonov, and N. Donnelly (2011). Fault location and slip distribution of the 22 February 2011 M_W 6.2 Christchurch, New Zealand earthquake from geodetic data. *Seismological Research Letters* 82, 789-799, doi:10.1785/gssrl.82.6.789

Beavan, J., M. Motagh, E. Fielding, N. Donnelly, and D. Collett (2012). Fault slip models of the 2010-2011 Canterbury, New Zealand, earthquakes from geodetic data, and observations of postseismic ground deformation. *New Zealand Journal of Geology and Geophysics* 55, 207-221, doi:10.1080/00288306.2012.697472

Berryman, K.R., U.A. Cochran, K.J. Clark, G.P. Biasi, R.M. Langridge, and P. Villamor (2012). Major earthquakes occur regularly on an isolated plate boundary. *Science* 336, 1690-1693, doi:10.1126/science.1218959

Bradley, B.A. (2013). Ground motions observed in the Darfield and Christchurch earthquakes and the importance of local site response effects. *New Zealand Journal of Geology and Geophysics* 55, 279-286, doi:10.1080/00288306.2012.674049

Bradley, B.A., and M. Cubrinovski (2011). Near-source strong ground motions observed in the 22 February 2011 Christchurch earthquake. *Seismological Research Letters* 82, 853-865, doi:10.1785/gssrl.82.6.853

Choy, G.L., J.L. Boatwright, and S. Kirby (2001). The radiated seismic energy and apparent stress of interplate and intraplate earthquakes at subduction zone environments: implications for seismic hazard estimate. *USGS Open-File Report* 01-005, 10 p.

Cochran, E.S., J.F. Lawrence, C. Christensen, and R.S. Jakka (2009). The Quake-Catcher Network: citizen science expanding seismic horizons. *Seismological Research Letters* 80, 26-30.

Cochran, E.S., J.F. Lawrence, A. Kaiser, B. Fry, A. Chung, and C. Christensen (2011). Comparison between low-cost and traditional MEMS accelerometers: a case study from the M 7.1 Darfield, New Zealand, aftershock deployment. *Annals of Geophysics* 54, 728-737, doi:10.4401/ag-5268

Cooper, A.F., and R.J. Norris (1990). Estimates for timing of the last coseismic displacement on the Alpine fault, northern Fiordland, New Zealand. *New Zealand Journal of Geology and Geophysics* 33, 309-307.

Cowan, H.A. (1991). The North Canterbury earthquake of September 1, 1888. *Bulletin of the New Zealand Society for Earthquake Engineering* 43, 222-227.

Cox, S.C., H.K. Rutter, A. Sims, M. Manga, J.J. Weir, T. Ezzy, P.A. White, T.W. Horton, and D. Scott (2012). Hydrological effects of the M_W 7.1 Darfield (Canterbury) earthquake, 4 September 2010, New Zealand. *New Zealand Journal of Geology and Geophysics* 55, 231-247, doi:10.1080/00288306.2012.680474

Cubrinovski, M., K. Robinson, M. Taylor, M. Hughes, and R. Orense (2012). Lateral spreading and its impacts in urban areas in the 2010-2011 Christchurch earthquakes. *New Zealand Journal of Geology and Geophysics* 55, 255-269, doi:10.1080/00288306.2012.699895

Dorn, C., A.G. Green, R. Jongens, S. Carpentier, A.E. Kaiser, F. Campbell, H. Horstmeyer, J. Campbell, M. Finnemore, and J. Pettinga (2010). High-resolution seismic images of potentially seismogenic structures beneath the northwest Canterbury Plains, New Zealand. *Journal of Geophysical Research* 115, B11303, doi:10.1029/2010JB007459

Doser, D.I., T.H. Webb, and D.E. Maunder (1999). Source parameters of large historical (1918-1962) earthquakes, South Island, New Zealand. *Geophysical Journal International* 139, 769-794.

Elliot, J.R., E.K. Nissen, P.C. England, J.A. Jackson, S. Lamb, Z. Li, M. Oehlers, and B. Parsons (2012). Slip in the 2010-2011 Canterbury earthquakes, New Zealand. *Journal of Geophysical Research* 117, B03401, doi:10.1029/2011jb008868

Fleischman, R.B., J.I. Restrepo, S. Pampanin, J.R. Maffei, K. Seeber, and F.A. Zahn (2014). Damage evaluations of precast concrete structures in the 2010-2011 New Zealand earthquake sequence. *Earthquake Spectra* 30, 277-306, doi:10.1193/031213EQS068M

Fry, B., and M.C. Gerstenberger (2011). Large apparent stresses from the Canterbury earthquakes of 2010 and 2011. *Seismological Research Letters* 82, 833-838, doi:10.1785/gssrl.82.6.833

Fry, B., R. Benites, and A. Kaiser (2011). The character of accelerations in the M_W 6.2 Christchurch earthquake. *Seismological Research Letters* 82, 846-852, doi:10.1785/gssrl.82.6.846

Fry, B., F.J. Davey, D. Eberhart-Phillips, and S. Lebedev (2014). Depth variable crustal anisotropy, patterns of crustal weakness, and destructive earthquakes in Canterbury, New Zealand. *Earth and Planetary Science Letters* 392, 50-57, doi:10.1016/j.epsl.2014.02.013

Gerstenberger, M., G. McVerry, D. Rhoades, and M. Stirling (2014). Seismic hazard modeling for the recovery of Christchurch, New Zealand. *Earthquake Spectra* 30, 17-29, doi:10.1193/021913EQS037M

Gledhill, K., R., Robinson, R. Abercrombie, T. Webb, J. Beavan, J. Cousins, and D. Eberhart-Phillips (2000). The M_W 6.2 Cass, New Zealand earthquake of 24 November 1995: reverse faulting in a strike-slip regime. *New Zealand Journal of Geology and Geophysics* 43, 255-269.

Holden, C. (2011). Kinematic source model of the 22 February 2011 M_W 6.2 Christchurch earthquake using strong-motion data. *Seismological Research Letters* 82, 783-788, doi:10.1785/gssrl.82.6.783

Holden, C., and J. Beavan (2012). Kinematic source studies of the ongoing (2010-2011) sequence of recent large earthquakes in Canterbury. Paper 061 (8 p) in Implementing lessons learnt: 2012 Conference, 13-15 April, Christchurch, New Zealand, Christchurch: *New Zealand Society for Earthquake Engineering.*

Kaiser, A., C. Holden, J. Beavan, D. Beetham, R. Benites, A. Celentano, D. Collet, J. Cousins, M. Cubrinovski, G. Dellow, P. Denys, E. Fielding, B. Fry, M. Gerstenberger, R. Langridge, C. Massey, M. Motagh, N. Pondard, G. McVerry, J. Ristau, M. Stirling, J. Thomas, S.R. Uma, and J. Zhao (2012). The M_W 6.2 Christchurch earthquake of February 2011: preliminary report. *New Zealand Journal of Geology and Geophysics* 55, 67-90, doi:10.1080/00288306.2011.641182

Lawrence, J.F., E.S. Cochran, A. Chung, A. Kaiser, C.M. Christensen, R. Allen, J.W. Baker, B. Fry, T. Heaton, D. Kilb, M.D. Kohler and M. Taufer (2014). Rapid earthquake characterization using MEMS accelerometers and volunteer hosts following the M 7.2 Darfield, New Zealand, earthquake. *Bulletin of the Seismological Society of America* 104, 184-192, doi:10.1785/0120120196

Massey, C.I., M.J. McSaveney, T. Taig, L. Richards, N.J. Litchfield, D.A. Rhoades, G.H. McVerry, B. Lukovic, D.W. Heron, W. Ries, and R.J. Van Dissen (2014). Determining rockfall risk in Christchurch using rockfalls triggered by the 2010-2011 Canterbury earthquake sequence. *Earthquake Spectra* 30, 155-181, doi:10.1193/021413EQS026M

Petersen, T., K. Gledhill, M. Chadwick, N.H. Gale, and J. Ristau (2011). The New Zealand national seismograph network. *Seismological Research Letters* 82, 9-20, doi:10.1785/gssrl.82.1.9

Reid, C.M., N.K. Thompson, J.R.M. Irvine, and T.E. Laird (2012). Sand volcanoes in the Avon-Heathcote estuary produced by the 2010-2011 Christchurch earthquakes: implications for geological preservation and expression. *New Zealand Journal of Geology and Geophysics* 55, 249-254, doi:10.1080/00288306.2012.674051

Reyners, M., D. Eberhart-Phillips, and S. Martin (2014). Prolonged Canterbury earthquake sequence linked to widespread weakening of strong crust. *Nature Geoscience* 7, 34-37, doi:10.1038/ngeo2013

Rhoades, D.A., and R.J. Van Dissen (2003). Estimates of the time varying hazard of rupture of the Alpine fault, New Zealand, allowing for uncertainties. *New Zealand Journal of Geology and Geophysics* 46, 479-488.

Ristau, J. (2011). Focal mechanism analysis of Christchurch boxing day aftershocks. *GNS Science Consultancy Report* 2011/43, 7 p.

Ristau, J., C. Holden, A. Kaiser, C. Williams, S. Bannister, and B. Fry (2013). The Pegasus Bay aftershock sequence of the M_W 7.1 Darfield (Canterbury), New Zealand earthquake. *Geophysical Journal International* 195, 444-459, doi:10.1093/gji/ggt222

Serra, E.M.T., B. Delouis, A. Emolo, and A. Zollo (2013). Combining strong-motion, InSAR and GPS data to refine the fault geometry and source kinematics of the 2011, M_W 6.2 Christchurch earthquake (New Zealand). *Geophysical Journal International* 194, 1760-1777, doi:10.1093/gji/ggt186

Sibson, R., F. Ghisetti, and J. Ristau (2011). Stress control of an evolving strike-slip fault system during the 2010-2011 Canterbury, New Zealand, earthquake sequence. *Seismological Research Letters* 82, 824-832, doi:10.1785/gssrl.82.6.824

Sritharan, S., K. Beyer, R.S. Henry, Y.H. Chai, M. Kowalsky, and D. Bull (2014). Understanding poor seismic performance of concrete walls and design implications. *Earthquake Spectra* 30, 307-334, doi:10.1193/021713EQS036M

Steacy, S., A. Jiménez, and C. Holden (2014). Stress triggering and the Canterbury earthquake sequence. *Geophysical Journal International* 196, 473-480, doi:10.1093/gji/ggt380

Stirling, M., M. Gerstenberger, N. Litchfield, G. McVerry, W. Smith, J. Pettinga, and P. Barnes (2008). Seismic hazard of the Canterbury region, New Zealand: new earthquake source model and methodology. *Bulletin of the New Zealand Society for Earthquake Engineering* 41, 51-67.

Sutherland, R.D. *et al.* (2007). Do great earthquakes occur on the Alpine fault in central South Island, New Zealand?, in A Continental Plate Boundary: Tectonics at South Island, New Zealand, p. 235-251, eds. Okaya, D., Stern, T., and Davey, F., Geophysical Monograph 175, *American Geophysical Union*, Washington, DC.

Suzuki, W., S. Aoi, and H. Sekiguchi (2010). Rupture process of the 2008 Iwate-Miyagi Nairiku, Japan, earthquake derived from near-source strong-motion records. *Bulletin of the Seismological Society of America* 100, 256-266.

Wessel, P., and W.H.F. Smith (1991). Free software helps map and display data. *EOS Transactions* AGU 71, 441.

Yamada, M., J. Mori, and T. Heaton (2009). The slapdown phase in high-acceleration records of large earthquakes. *Seismological Research Letters* 80, 559-564, doi:10.1785/gssrl.80.4.559

Yetton, M.D., A. Wells, and N. Traylen (1998). The probability and consequences of the next Alpine fault earthquake, *EQC Research Report* 95/193, New Zealand Earthquake Commission, Wellington, New Zealand.

8.2 An overview of the M_W 9, 11 March 2011, Tohoku earthquake

Ryota HINO
Tohoku University
Japan

8.2.1 Introduction

On March 11 2011, a great earthquake struck the eastern part of Japan. The origin time and hypocenter determined by the Japan Meteorological Agency (JMA) were 05:46:18.1 (UT) and 38.103N, 142.860E, 24 km. This hypocenter is located about 150 km offshore from northeastern Japan (Tohoku district) and beneath the landward side of the Japan Trench. Although the epicenter was not very close to land, very strong shaking with maximum ground accelerations reaching 1–2 g (Furumura *et al.*, 2011) caused serious damage in eastern Japan, including Tokyo about 400 km from the epicenter. A large tsunami devastated the coastal area. The tsunami inundated more than 5 km inland into the Sendai plain, and huge inundation heights and run-ups occurred along the rugged coast in the northern part (Mori *et al.*, 2011). The earthquake was named "the 2011 off the Pacific coast of Tohoku earthquake" by JMA, but here it will be denoted as "the Tohoku earthquake."

The Centroid Moment Tensor (CMT) solution presented by JMA showed that this earthquake was a low-angle-thrust type, with strike, dip and slip angles of 193, 10 and 79 degrees respectively. This solution is consistent with thrust faulting along the boundary between the subducting Pacific plate and the overriding North American (or Amur) plate. The scalar moment was $4.2x10^{22}$ Nm (moment magnitude M_W 9.0). The Global CMT (Nettles *et al.*, 2011) and USGS W-phase moment tensor (Duptel *et al.*, 2011) solutions are almost the same as the JMA solution but with larger moment estimates, $5.3x10^{22}$ Nm (GCMT) and $4.5x10^{22}$ Nm (USGS). This earthquake is thus the largest instrumentally recorded earthquake in Japan, and the fourth largest in the world.

At the Japan Trench subduction zone, cold and old Pacific plate (110 Ma; Nakanishi and Winterer, 1998) is subducted with a convergence rate of 7 - 8.5 cm/year (e.g. Altamimi *et al.*, 2007). In terms of comparative subductology (Ruff and Kanamori, 1980) this subduction zone is different from the Chilean type, where large interplate earthquakes repeatedly occur. The seismic coupling coefficient here was estimated at less than 0.3, based on the recurrence history of interplate earthquakes along the Japan Trench (e.g. Kanamori, 1977; Seno, 1979; Peterson and Seno, 1984; Pacheco *et al.*, 1993).

The slip deficit rate along the subduction interface has been estimated from the deformation data provided by the nation-wide dense GPS network (e.g. Nishimura *et al.*, 2004; Suwa *et al.*, 2006; Hashimoto *et al.*, 2009; Loveless and Meade, 2010). The results indicate that the strength of interplate coupling is largely heterogeneous, having several peaks whose locations are well correlated with the rupture areas, estimated from analysis of historic seismograms, for the M 7–8 class Japanese earthquakes since about 1900 (Yamanaka and Kikuchi, 2004). Yamanaka and Kikuchi (2004) found a persistence of asperity locations throughout the earthquake cycle from these asperity maps and argued that large interplate earthquakes were repeating ruptures related to the asperities. Coincidence of the locked portions identified from geodetic observations with asperities for previous large earthquakes reinforced this idea. This suggested that aseismic slip takes place around the asperities and analysis of geodetic data showed that large-scale post-seismic slip after these large earthquakes occurred in 1978 (Ueda *et al.*, 2001), 1989 (Kawasaki *et al.*, 2001), 1992 (Kawasaki *et al.*, 1995) and 1994 (Heki *et al.*, 1997). All these afterslips released significant amounts of seismic moment around the asperities of the corresponding mainshocks.

Numerous small repeating earthquakes along the subduction interface have been observed on the outskirts of the asperities (Uchida *et al.*, 2003). These observations provided the basis for the assumption that large interplate earthquakes along the Japan Trench obey the characteristic earthquake model: the history of major earthquakes can be attributed to repeating failures of persistent asperities at quite regular intervals. The Earthquake Research Committee (ERC) in Japan have determined probabilities for large subduction earthquakes, based on historical records for more than 400 years, to make long-term forecasts of large earthquakes in the vicinity of Japan (http://www.jishin.go.jp/main/index-e.htm).

In the middle part of the main subduction zone, the Miyagi-oki region, where the Tohoku earthquake occurred, the ERC evaluated that a series of M 7 class earthquakes should recur at intervals of about 40 years. In this assessment, the earthquake in 1978 (M_W 7.4) was regarded as the typical type of earthquake in the region. However, Umino *et al.* (2006) discussed the diversity of the rupture patterns of earthquakes in the Miyagi-oki region, and considered that the 1978 earthquake was due to a compound rupture of smaller asperities that caused a series of M 7 class earthquakes in the 1930s. In 2005, an interplate earthquake of M_W 7.1 occurred in the region, and this was interpreted as a partial re-rupture of the asperity causing the anticipated M 7.5 class earthquake (Okada *et al.*, 2005) but leaving a substantial portion unbroken. Under these circumstances, the ERC evaluated that the forthcoming earthquake was imminent.

On the other hand, the ERC also indicated that an earthquake of $M > 8$ could occur as a consequence of synchronized failure of the Miyagi-oki asperity and an unknown asperity probably located on the trenchward side of the Miyagi-oki region, based on historical documents indicating a large earthquake associated with a significant tsunami in 1793. There were also several palaeoseismological studies indicating a sporadic occurrence of extraordinary earthquakes much larger than in the instrumental record. Tsunami deposits associated with the A.D. 869 Jogan and other similar earthquakes were identified on the Sendai plain and the broad areas to the south (Minoura *et al.*, 2001; Shishikura *et al.*, 2007; and Shishikura *et al.*, 2010). By modeling the inundation and subsidence, Sawai *et al.* (2012) estimated the Jogan earthquake as being of moment magnitude 8.4 or larger, with a fault rupture area 200 km long.

As explained so far, it had been believed that the state of interplate coupling was well understood along the Japan Trench subduction system. Therefore, the occurrence of the M 9 earthquake was surprising for most seismologists not only in Japan but also around the world. The most fundamental question raised by the Tohoku earthquake was how an M 9 earthquake could happen in a subduction zone characterized by the frequent recurrence of $M < 8$ earthquakes and broad aseismic slip. To address this question, it is important to characterize the rupture process of the Tohoku earthquake not only during the dynamic rupture of the mainshock but also in the periods before and after. This review examines results of extensive studies of the source of the Tohoku earthquake, of the plate boundary processes before the occurrence of the earthquake and also of the consequences of this great earthquake.

8.2.2 Rupture process of the Tohoku earthquake

Numerous source models of the Tohoku earthquake have been estimated based on seismic, geodetic, and tsunami observations made immediately after the rupture occurred. All the models, including those derived from joint inversion of different kinds of data sets (e.g. seismic + geodetic, geodetic + tsunami, seismic + geodetic + tsunami), estimated the total moment release in the range from $3to5x10^{22}$ Nm, remarkably consistent with one another, regardless of the data sources and methods, and also with the CMT solutions based on point source approximations. Nevertheless, the spatial distribution images presented for the coseismic slip show considerable diversity.

Numerous offshore observations made in and around the rupture region of the Tohoku earthquake have provided invaluable information constraining the rupture models for the earthquake. Tsunami waveform records without severe distortion due to non-linear effects near the coast showed several important features of the tsunami source (Hayashi *et al.*, 2011), as did the ocean-bottom pressure data obtained by the cabled systems (Maeda *et al.*, 2011) and the offline Bottom Pressure Recorders (BPR, Saito *et al.*, 2011). There were seven seafloor benchmarks of the GPS/acoustic seafloor geodetic survey within the rupture area, and observed large coseismic displacements, from 10 to 31 m horizontally (Sato *et al.*, 2011; Kido *et al.*, 2011), were solid evidence of large slip along the plate boundary fault. Y. Ito *et al.* (2011) reported very large horizontal displacements, greater than 50 m, at sites located close to the trench axis. The BPR deployed in the rupture area showed pressure changes associated with permanent vertical displacements (Y. Ito *et al.*, 2011; Iinuma *et al.*, 2012; Hino *et al.*, 2013a) of the order of several metres. Fujiwara *et al.* (2011) indicated the change in topographic profile near the Japan Trench by comparing multibeam bathymetric data obtained before and after the mainshock. That analysis revealed that the displacements extended out as far as the Japan Trench, suggesting that the fault rupture reached the trench axis.

Among the various source models, tsunami inversions tended to resolve very large slip near the trench (Maeda *et al.*, 2011; Fujii *et al.*, 2011, Saito *et al.*, 2011; Gusman *et al.*, 2012; Hooper *et al.*, 2013; Satake *et al.*, 2013). The analyses of onshore geodetic data yielded models with a broad slip distribution spanning an area of 400 km x 200 km (Ozawa *et al.*, 2011; Nishimura *et al.*, 2011; Iinuma *et al.*, 2011; Pollitz *et al.*, 2011), but the slip model derived by including offshore deformation data mostly required a compact area of extremely large slip along the trench axis (T. Ito *et al.*, 2011; Loveless and Meade, 2011; Pollitz *et al.*, 2011, Romano *et al.*, 2012; Iinuma *et al.*, 2012) except for the model presented by Hashimoto *et al.* (2012). Although some models derived from seismic waveform data showed a peak slip located close to the hypocenter, about 100 km away from the trench axis (Ammon *et al.*, 2011; Y. Yoshida *et al.*, 2011; Koketsu *et al.*, 2011; Yokota *et al.*, 2011), others with the largest slip nearer the trench have been presented (Ide *et al.*, 2011; Lay *et al.*, 2011a; Shao *et al.*, 2011; K. Yoshida *et al.*, 2011; Hayes, 2011; Lee *et al.*, 2011; Suzuki *et al.*, 2011; Yagi and Fukahata, 2011; Yue and Lay, 2011, 2013; Kubo and Kakehi, 2013).

Sources of coherent short-period seismic-wave radiation from the Tohoku earthquake were imaged by back-projection (BP) of the seismic waveform records obtained by seismic arrays located at local and at teleseismic distances (Honda *et al.*, 2011; Simons *et al.*, 2011; Wang and Mori, 2011a, b; Ishii 2011; Zhang *et al.*, 2011; Meng *et al.*, 2011; Koper *et al.*, 2011a, b; Yao *et al.*, 2012; Kiser and Ishii, 2012). All these studies reported that the origin locations of the high-frequency radiation derived from the BP analyses were significantly different from the areas of very large slip. Sources of high-frequency seismic waves tended to be located along the deeper portions of coseismic slip but did not simply correlate with the locations of peak slip. Koper *et al.* (2011b) and Kiser and Ishii (2012) demonstrated that the locations of the imaged sources were strongly dependent on the frequencies used for the BP analysis and that the sources were located systematically on the more down-dip side for the shorter periods. Roten *et al.* (2012) applied BP methods to image the source radiating long-period Rayleigh waves, and found that the imaged Rayleigh wave sources were located significantly trenchward of the source locations of the short-period P-waves, supporting the interpretation of a frequency-dependent seismic-wave radiation.

Strong-motion records obtained by the local network were composed of three main identifiable wave packets as well as several less evident sub-events. Kurahashi and Irikura (2011, 2013), Asano and Iwata (2012) and Kumagai *et al.* (2013) tried to locate each strong-motion generation area (SMGA) for these strong-motion sub-events. All the SMGAs were located on the down-dip side of the patches of large coseismic slip determined from the inversions using the broad-band seismic data, geodetic data and tsunami data, but no SMGAs were located trenchward of the Tohoku earthquake hypocenter.

Bilek *et al.* (2012) and Ye *et al.* (2013) analyzed the dependence of source character on focal depth for other earthquakes along the Japan Trench and concluded that depth-varying source processes along the plate boundary fault in the area accounts for the frequency-depth relation observed for the seismic waves radiated from the Tohoku earthquake. Lay *et al.* (2012) identified similar variations in the frequency content of seismic waves in the records of the 2004 Sumatra-Andaman (M_W 9.1) and 2010 Chile (M_W 8.8) earthquakes and related the frequency dependence to the depth-varying frictional properties along the plate boundary fault. The heterogeneous radiation of different frequency content may therefore distort the slip distributions imaged by the seismic observations and account for the diversity of the source models.

As discussed earlier, the spatial variation of vertical deformation is expected to place strong constraints on the slip distribution. Although the tsunami wavefield basically reflects the vertical seafloor deformation, it could be distorted by several effects other than the pure vertical displacement associated with the fault motion: for example, additional tsunami generation caused by horizontal motion of a steep seafloor (Tanioka and Satake, 1996a; Hooper *et al.*, 2013), inelastic deformation of the sedimentary layer along the inner side of the trench (Tanioka and Seno, 2001) or a possible submarine landslide (Kawamura *et al.*, 2012; Grilli *et al.*, 2013). In this review, the slip model obtained by Iinuma *et al.* (2012) is used as the reference model to characterize the spatial pattern of coseismic slip associated with the Tohoku earthquake, because that study used the BPR seafloor-displacement data as well as all other available seafloor geodetic observations.

The largest coseismic slip was estimated to be larger than 50 m and the area of large slip was constrained to be 150 km x 50 km: main-patch M in (Figure 8.14). There is another area with significant coseismic slip of more than 10 m extending out to the down-dip side of the hypocenter: sub-patch A. The location of sub-patch A corresponds to the location of the rupture area of normally expected Miyagi-oki earthquakes but the amount of slip during the Tohoku earthquake was much larger than the coseismic slip usually associated with the M 7.5 class earthquakes repeatedly occurring in the region. There is also another patch of significant coseismic slip to the south of the hypocenter: sub-patch B.

Slip distributions with the largest slip near the trench and two minor patches in the Miyagi-oki and

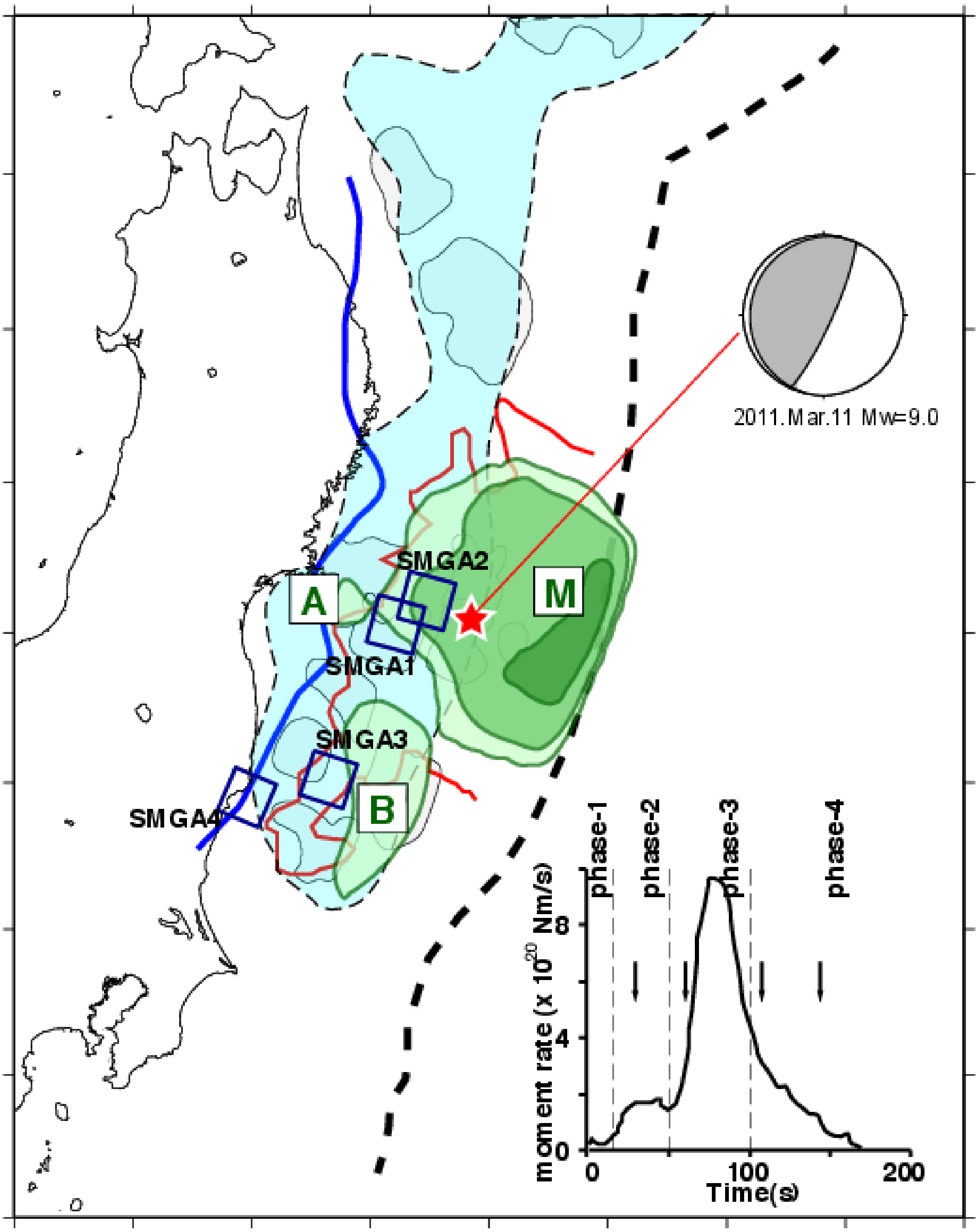

Figure 8.14: Source model (Iinuma et al., 2012) and source-time function of the Tohoku earthquake (Suzuki et al., 2011). Areas are shaded light green for coseismic slip > 10m, green for slip > 20 m and dark green for slip > 50 m (Iinuma et al., 2012). Squares represent SMGAs (Asano and Iwata, 2012). Rupture timing of each SMGA is shown beside the source-time function. The red line shows the outer limit of shallow interplate aftershock activity (Kato and Igarashi, 2012). The light blue area shows the zone strongly coupled before the mainshock (Hashimoto et al., 2009). Other shaded patches indicate rupture areas of previous M <8 class interplate earthquakes (Yamanaka and Kikuchi, 2004). The blue line represents the down-dip limit of interplate seismicity (Igarashi et al., 2001), and the dashed black line represents the axis of the Japan Trench.

Fukushima-oki regions were also imaged in several of the studies, not just in geodetic data inversions (e.g. T. Ito *et al.*, 2011; Pollitz *et al.*, 2011, Romano *et al.*, 2012) but also in seismic and tsunami data investigations (Yagi and Fukahata, 2011; Yue and Lay, 2011, 2013; Fujii *et al.*, 2011).

Several models derived from the seismic data (Ide *et al.*, 2011; Lay *et al.*, 2011a, Shao *et al.* 2011; K. Yoshida *et al.*, 2011; Hayes, 2011; Suzuki *et al.*, 2011; Kubo and Kakehi, 2013) have a large slip area along the trench that extends much further to the south than in the reference model. However, these models did not have any moderate slip in the deeper portion corresponding to sub-patch B. Since the seafloor geodetic observations cannot be explained by the presence of significant fault slip near the trench in the south (Iinuma *et al.*, 2012), the resolution in the dip direction for these slip models may have been poorer in the southern part of the rupture area of the Tohoku earthquake.

Spatiotemporal variation of coseismic slip along the plate boundary fault during the Tohoku earthquake was studied mostly using the analyses of broad-band seismograms recorded by local strong-motion networks, the global digital-seismographic network or from GPS data recorded at a high rate of sampling. Similarity among the moment-rate functions obtained in these studies is considerably high, indicating that temporal variation of the moment releasing rate is robustly constrained. Satake *et al.* (2013) attempted to reveal the space-time development of fault slip from tsunami observations, but that model differed mostly from the other seismic waveform inversions not only in the slip pattern but also in the moment rate function.

According to seismic data analyses, the length of significant moment release was about 160s. Duputel *et al.* (2013) considered that this earthquake was characterized by a temporally compact moment-rate function compared to other M-9 class earthquakes such as the 2004 Sumatra-Andaman, 1964 Alaska (M_W 9.2) and 1960 Chile (M_W 9.5) earthquakes. Okal (2013) also remarked, after analysis of ultra-long-period seismograms, that the Tohoku earthquake cannot be categorized along with slow-rupturing earthquakes.

From the source-time functions, the following four phases can be identified in common during the rupture process for the Tohoku earthquake (Figure 8.14):

Phase-1: an initial, very weak, energy radiation (0-10 s in lapse-time);
Phase-2: a moderate moment release with duration 40 seconds (10-50 s);
Phase-3: the largest moment release with duration 50 s, but up to 70 s (50 – 100 s);
Phase-4: a relatively long-lasting ($>$ 60 s) moment release of moderate intensity (100s and later).

Ide *et al.* (2011) noted that the first three seconds of the Tohoku earthquake showed an emergent, relatively weak onset. Hoshiba and Iwakiri (2011) mentioned not only the weakness of the initial seismic signals but also the strangeness of the frequency content. In particular, high frequencies early in the seismogram were more abundant than expected for an M 9 class earthquake and indistinguishable from that of the M-6 class foreshocks. Chu *et al.* (2011) examined the location, size, mechanism and the frequency content of the first four seconds of the earthquake and found that the Tohoku earthquake began as a small (M_W 4.9) thrust event. Uchide (2013) performed a multi-scale slip inversion analysis to show a complex rupture process during phase 1, in which the rupture direction changed, making the apparent rupture velocity very slow. Also, the M 7.3 foreshock occurring two days before in the vicinity of the mainshock hypocenter could have been a factor influencing the complex rupture propagation path for the Tohoku mainshock,

After the small but complex initial rupture process around the hypocenter, the ruptured region started to grow rapidly through the next three phases (2 to 4). Although the observed seismic amplitudes were too small for analyses of local strong-motion records, the high-rate GPS data and the BP method gave good indications of the spatio-temporal development during these latter three phases.

The onsets of phase-2, phase-3 and phase-4 synchronized with the three major sub-events corresponding to the failure of SMGAs identified in the analysis off the local strong-motion data. The first two major slips occurred near the hypocenter, and a third occurred in the southern part of the rupture region (Kurahashi and Irikura, 2011, 2013; Asano and Iwata, 2012; Kumagai *et al.*, 2013). These three energetic subevents were also identified in the BP analysis (Zhang *et al.*, 2011).

One of the virtues of the BP method is that it tracks the source of high-frequency (HF) seismic signals during the rupture process. The BP studies using teleseismic data (Ishii, 2011; Wang and Mori, 2011a, b; Zhang *et al.*, 2011; Meng *et al.*, 2011; Yao *et al.*, 2012) consistently indicated that the center of the HF source moved quite slowly for approximately the first 90 s. Then the HF source center moved rapidly to the south and southwest. The timing of the sudden speed change roughly coincides with the onset of the phase-3 identified from the source-time function analyses.

Since the frequency content of the radiated seismic waves is dependent on the depth of the source, it may be difficult for the BP method to resolve the fault motion in the dip direction accompanying a change in depth. It is thus plausible that the very slow speed of rupture propagation estimated by the BP studies is indicative that the rupture propagation in the first 100 s occurred mostly in the fault-dip direction in the vicinity of the hypocenter. The rupture propagation process was also studied using the seismograms obtained at a dense seismic array located within a few hundred kilometres of the rupture area (Honda *et al.*, 2011; Nakahara *et al.*, 2011). These studies should give the trajectory of the HF sources at a higher resolution. Honda *et al.* (2011) showed bi-lateral rupture from the hypocenter in the up-dip and down-dip directions for about the first 40 s, whereas Nakahara *et al.* (2011) suggested predominantly down-dip rupture propagation in the same window.

The first moment release large enough to be detected by the high-rate GPS data started about 35 km west of the mainshock hypocenter at about 20 s lapse-time (Fukahata *et al.*, 2012). Because the location of this slip subevent is co-located with sub-patch A and its timing coincides well with phase-2 identified from the source-time function, it can be interpreted that phase-2 was the rupture of sub-patch A triggered by the rupture front propagating from the hypocenter. The first ruptured SMGA was also in the vicinity of sub-patch A (Asano and Iwata, 2012; Kurahashi and Irikura, 2013). The location of sub-patch A matches the source area that was expected for the next Miyagi-oki earthquake. However, the moment release from sub-patch A during the phase-2 was equivalent to M_W 8.5, which is much larger than the expected size of a Miyagi-oki earthquake (M 7.5).

It follows that phase-3 was the rupturing of the main-patch with an extremely large coseismic slip located along the trench releasing the largest moment, almost half the total. Yue and Lay (2011) reached the same conclusion. The BP analysis using seismic records in several different frequency bands (Ishii, 2011; Kiser and Ishii, 2012) showed that the radiation peak contemporaneous with the moment-rate peak was more prominent in the lower frequency bands, indicating predominant radiation from the large shallow fault.

Kurahashi and Irikura (2013) located the SMGA broken at the onset of phase-3 at the down-dip edge of the main rupture area, whereas Asano and Iwata (2012) and Kumagai *et al.* (2013) placed the source of high-frequency radiation nearer the hypocenter in the main patch. The latter location could reasonably be explained if the radiation of short-period seismic signals reflected the actual onset of the main-patch rupture as suggested by Frankel (2013).

Based on results of the BP studies, the rupture process during phase-4 can be characterized by a rapid propagation towards the south, and with a moderate moment release from sub-patch B, located in the southern part of the ruptured region and elongated along the strike direction. In phase-4, high-frequency components were more dominant in the radiated intensities obtained by BP analysis (Ishii, 2011; Kiser and Ishii, 2012) than in phase-3, consistent with sub-patch B not lying along the trench. Multi-frequency BP analysis showed a revival of the low-frequency components during the final stage of the rupture history (lapse-time $>$ 180 s), suggesting failure of the shallow fault (Kiser and Ishii, 2012). According to Kiser and Ishii (2012), this shallow rupture during the final stage could have acted as a tsunami source, although its contribution must have been quite minor because the amount of moment released after 180 s was considerably smaller in the source-time function.

8.2.3 Seismicity and slow slip along the plate boundary before the Tohoku earthquake

It is well known that the Tohoku earthquake was preceded by evident foreshock activity near the hypocenter of the mainshock. The region of this activity, shown in (Figure 8.15), was located almost near the up-dip extent of background interplate seismicity occurring before the Tohoku earthquake (Suzuki *et al.*, 2012; Ito *et al.*, 2013). An increase in seismicity of the region had started in February 2011, and a spatial expansion of this seismicity has been noted (Kato *et al.*, 2012; Suzuki *et al.*, 2012). The activity became significantly intense after the occurrence of the largest (M_W 7.3) foreshock on March 9, two days before the mainshock rupture. As shown by Marsan and Enescu (2012), the activity for the two days before the mainshock occurrence can be regarded as normal aftershock activity for an M_W 7.3 foreshock, as if nothing peculiar had happened.

It is common that aftershock activity after M-7 class interplate earthquakes is followed by evident afterslip in the Japan Trench region (e.g. Kawasaki *et al.*, 2001). Expansion of the aftershock regions have also been recognized (e.g. Tajima and Kennett, 2012), and these occurrences have been considered to be caused by aseismic slip and chain-reaction rupturing of small asperities along the plate boundary fault (Matsuzawa *et al.*, 2004). During the aftershock activity associated with the M_W 7.3 foreshock, clear expansion of this aftershock region (Ando and Imanishi, 2011; Kato *et al.*, 2012; Suzuki *et al.*, 2012) and evident crustal deformation was observable (Miyazaki *et al.*, 2011; Munekane, 2012; Ohta *et al.*, 2012), suggesting afterslip occurrence.

Kato *et al.* (2012) inferred, from a spatio-temporal evolution of tiny repeating earthquakes among the secondary aftershock activity for the largest foreshock, that aseismic afterslip propagated towards the hypocenter region of the mainshock. Ohta *et al.* (2012) showed that the afterslip occurred on the up-dip side of the M_W 7.3 foreshock hypocenter, whereas its coseismic rupture propagated in the down-dip

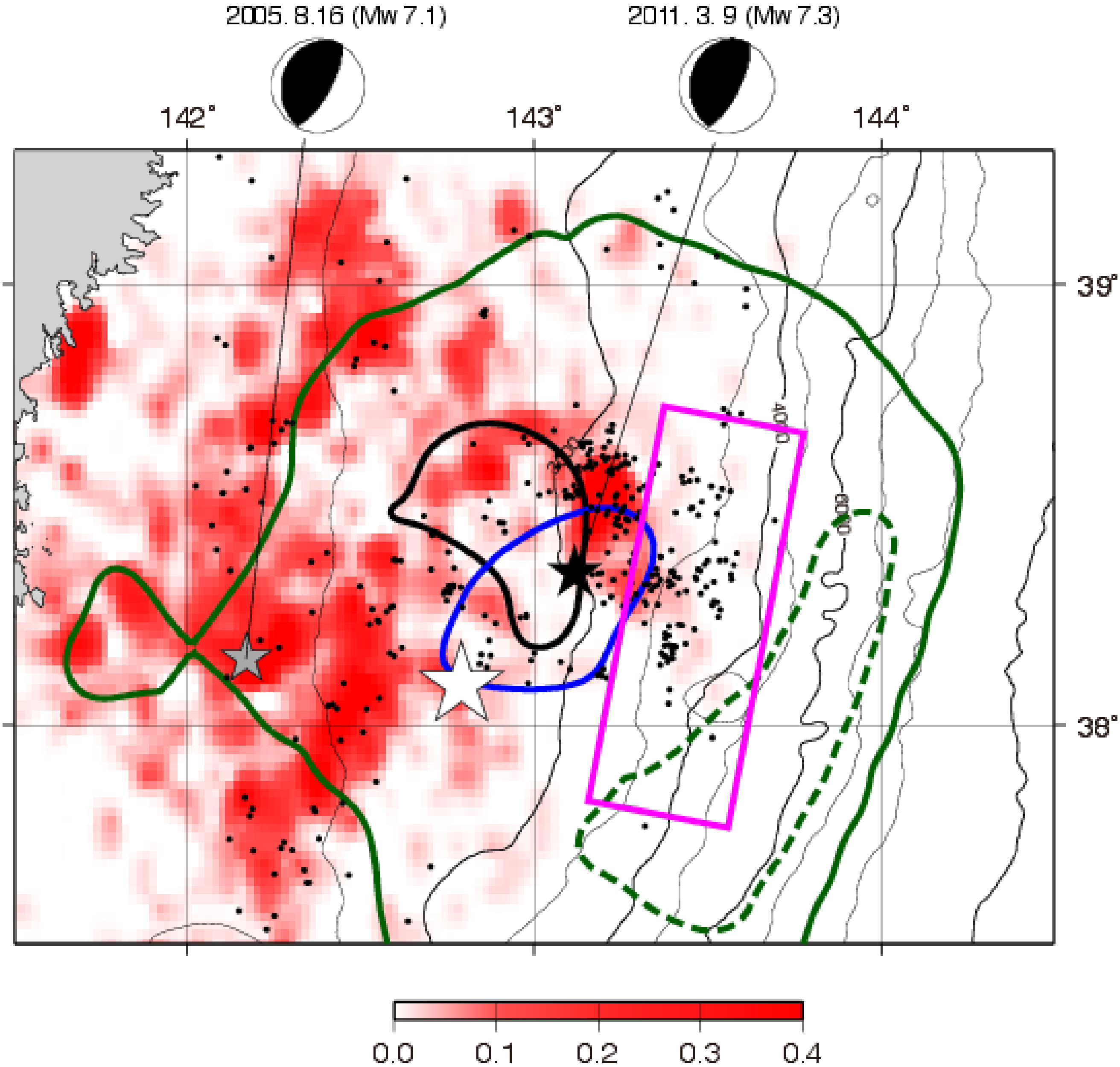

Figure 8.15: *Seismicity and aseismic slip in the vicinity of the Tohoku earthquake before the occurrence of the mainshock. The reddish color scale shows a normalized density of epicenters in the background seismicity. Dots indicate epicenters of foreshocks, from the time of the largest foreshock (March 9) until the mainshock occurrence. The black contour represents the rupture region of the largest foreshock (slip > 0.5 m). The blue contour represents the afterslip region for the largest foreshock (March 9 to 11, slip > 0.3 m). The dark green solid and dashed lines represent contours of coseismic slip, at 10 m and 50 m respectively, for the Tohoku earthquake rupture. The pink rectangular outline indicates the source region of slow-slip, starting in February, 2011). Stars indicate epicenters of significant seismic events, including the previous most recent thrust earthquake in the Miyagi-oki region in 2005 (M_W 7.1).*

direction (Ohta *et al.*, 2012; Gusman *et al.*, 2013). This afterslip released seismic moment equivalent to an M_W 6.8 event. The location of the afterslip region corresponds well with the aftershock distribution for the largest foreshock, and the mainshock hypocenter was located at the southwestern edge of this region. As usually observed for aftershock/afterslip phenomena in the Japan Trench subduction zone, there must have been some chain reaction for the continued activity, but what is most remarkable here is that one of the triggered small ruptures (M 5) grew into the great Tohoku earthquake through the rupture process as outlined in the previous section.

Ito *et al.* (2013) reported that another different type of aseismic slip event had occurred before this pre-imminent activity had started. That slip had occurred since the middle of February along the up-dip side of the afterslip zone associated with the March 9 foreshock. The region of this shallow slip was also associated with an increase in interplate seismicity, as pointed out by Kato *et al.* (2012), with the speculation that this shallow slow-slip had continued until the mainshock rupture occurred and then facilitated the large slip along the shallowest part of the plate boundary.

As explained so far, there were several indications of substantial aseismic slip in the vicinity of the Tohoku earthquake hypocenter, but there were no clear indications of any accelerated deformation occurring before the mainshock. Hirose (2011) and Hino *et al.* (2013b) inspected the continuous records from onshore tilt-meters and from offshore BPRs but could not identify any discernible changes in the deformation rate. Based on the detection level for these observations, Hino *et al.* (2013b) concluded that any accelerated aseismic slip related to nucleation for the mainshock rupture had to be smaller than for an M_W 6.2 event, if it occurred. Lack of any detectable precursory slip might be related to the nature of the initiation process of the Tohoku earthquake, but if the earthquake grew as the result of a cascading of very small earthquakes, its precursor must have been too small to be detected from the geodetic measurements of the earth surface.

In 1981, an M 7.1 earthquake occurred (Yamanaka and Kikuchi, 2004) almost in the same region, and although this must have been associated with similar afterslip and aftershock activity as in 2011 it did not trigger a great earthquake at that time. Sato *et al.* (2013) considered that the state of stress for the region was quite different in 1981 from that later in 2011, and that a series of $M<7$ earthquakes had in the meantime loaded the region, priming it for rupture. Mitsui *et al.* (2012) suggested similarly.

Several studies have indicated that the Tohoku earthquake was preceded by precursory anomalies with a time scale of about 10 years, distinct from the shorter-term phenomena discussed so far. For the Miyagi-oki region, where large coseismic slip due to the mainshock and foreshock activity occurred, the b-value in the Gutenberg-Richter relationship was remarkably reduced before the Tohoku earthquake (Nanjo *et al.*, 2012), since about 2005. Tanaka (2012) reported on a tidal triggering of earthquakes, for several to ten years before the Tohoku earthquake, in almost the identical region to that where the b-value reduction was observed. Huang and Ding (2012) reported a reduced level of seismicity. Reduced seismicity has also been discussed by Katsumata (2011) but with the conclusion that the anomaly started much earlier, more than 20 years before the Tohoku earthquake.

Geodetic observations have led to proposals of an unzipping process for the plate boundary that had been tightly coupled in the earlier period. Suito *et al.* (2011) and Ozawa *et al.* (2012) showed that the durations and sizes of afterslip associated with the $M7$ class interplate earthquakes had tended to increase since 2005. The total moment of the aseismic slip for the nine years before the Tohoku earthquake was equivalent to that of an M_W 7.7 earthquake, surpassing the total moment of the coseismic slip for the five largest earthquakes in the same period. Uchida and Matsuzawa (2013) noted that small but distinct increases in the slip rate in the period of about three years before the Tohoku earthquake near the area of large coseismic slip suggested there was pre-seismic unfastening of the locked area in the last stage of the earthquake cycle. Based on the synchronicity of these observed anomalies, it is likely that unfastening of the plate boundary fault accelerated aseismic slip and increased the shear stress along the fault.

8.2.4 Aftershock activity and postseismic deformation

Hirose *et al.* (2011) gave a general outline of the aftershock activity revealed by JMA monitoring. Soon after the occurrence of the Tohoku earthquake, extensive seismicity affected a broad area of Japanese territory, not only near the mainshock rupture region but also in inland areas ((Figure 8.16)). The number of aftershocks exceeded those following the 2004 Sumatra-Andaman earthquake and the 2010 Chile earthquake. In this section, the review will be concentrated on the seismicity on the Pacific Ocean side of Honshu, and the induced shallow crustal seismicity will be explained in a later section.

The area of the aftershock activity off Honshu was 500 x 100 km2. In this region, three $M>7$ earthquakes occurred within 40 minutes after the mainshock 05:46 origin-time. The first of these occurred at 06:08 to the north and the second at 06:15 to the south. These two large aftershocks were interplate events, judging from their thrust-type focal mechanisms, with magnitudes M_W 7.4 and M_W 7.7 respectively; the latter aftershock is the largest so far. At 06:25, an M_W 7.5 earthquake occurred beneath the outer rise of the Japan Trench, with a normal-type focal mechanism, indicating that this aftershock was an intraplate event within the shallow Pacific plate. The source models of these major aftershocks have also been estimated from onshore GPS data (Munekane, 2012). All these aftershocks were followed by their own sequences of (secondary) aftershocks.

Few interplate aftershocks with thrust focal mechanisms occurred within the large coseismic slip region, but several occurred instead in the surrounding regions (Asano *et al.*, 2011). Detailed focal-depth distributions obtained from event relocations using ocean bottom seismographic data (Suzuki *et al.*, 2012) demonstrated that the active interplate seismicity before the Tohoku mainshock had later completely ceased in the vicinity of the mainshock hypocenter. Tajima and Kennett (2011) pointed out that the aftershock area did not show significant expansion after the Tohoku earthquake and the two immediate large aftershocks, whereas all previous major interplate earthquakes, including the largest foreshock on March 9, had had a significant enlargement of aftershock area associated with them. To the north of the mainshock rupture, interplate moment release in previous large earthquakes (e.g. M_W 7.7 in 1994) and the subsequent slow slip may have prevented the propagation of slip along the plate boundary fault (Kosuga and Watanabe, 2011). Kubo *et al.* (2013) examined the coseismic slip model for the largest aftershock and found that its rupture expansion was inhibited by the existence of the Philippine Sea plate, which is subducted from the south between the inland plate and the Pacific plate.

Low seismicity along the rupture region of the mainshock has been reported for the aftershock activity following several large earthquakes (e.g. Scholz, 2002; Hino *et al.*, 2000; Hino *et al.*, 2006). Kato and Igarashi (2012) pointed out that there was a clear border for the low in-plane seismicity and suggested that this border could be considered to be the outer rim of the high-slip zone during the Tohoku earth-

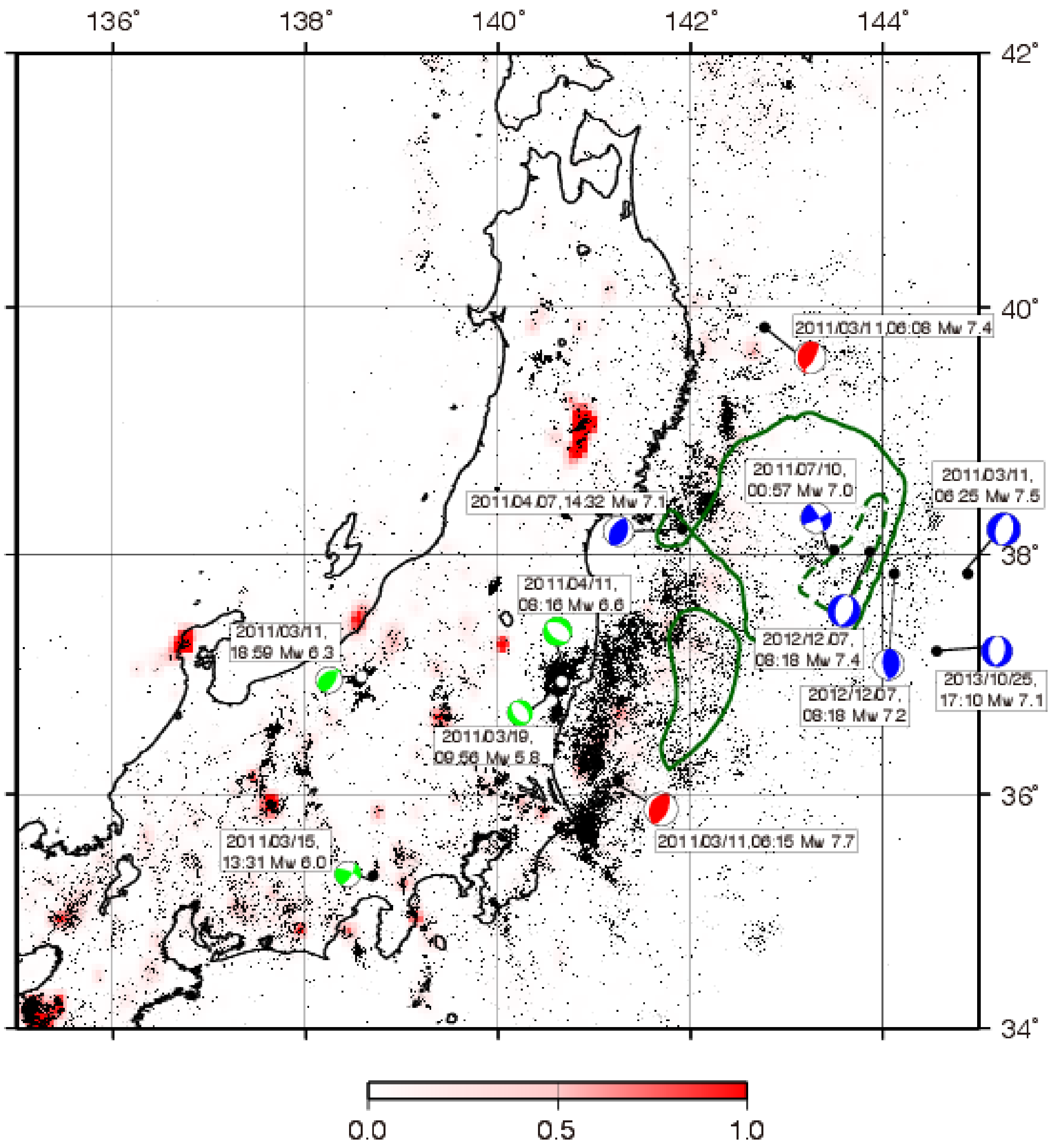

Figure 8.16: Aftershock epicenters and remote induced seismicity from March 11 to December 31, 2011. Epicenters are from the JMA catalog. Focal mechanism solutions for notable recent earthquakes are those determined by F-net, except for the intraslab doublet on December 7, 2011. For the doublet, CMT solutions provided by JMA (2013) are shown. Red, blue and green solutions represent interplate, intraplate in the Pacific plate, and shallow crustal earthquakes, respectively. The reddish color scale shows a normalized density of background seismicity.

quake. Outside this border, active aftershock seismicity was probably caused by the stress concentration due to a large contrast in fault slip.

After the intra-Pacific-plate earthquake beneath the outer rise of the Japan Trench at 06:25 on March 11 (M_W 7.5), all the subsequent aftershocks with $M > 7$ occurred within the Pacific plate. There are several previous examples where shallow normal-faulting earthquakes in the outer-rise trench regions have been triggered by large megathrust earthquakes (Lay *et al.*, 2011b). In the Japan Trench subduction zone, the large M_W 8.3 normal faulting earthquake in 1933 is considered to have been triggered by the shallow thrust-faulting earthquake in 1896. Hypocenters in the 2011 normal-faulting aftershock region were not distributed along a simple plane corresponding to the rupture plane of the M_W 7.5 aftershock, but were instead located along several parallel planes (Obana *et al.*, 2012), suggesting that several shallow normal faults in the outer rise region were all activated at about the same time by the Tohoku earthquake.

In the outer region of the Japan Trench, intraplate seismicity formed a double-planed structure: an upper plane in the lower crust and uppermost mantle of the oceanic lithosphere, and a lower plane located about 30 km beneath it. The focal mechanisms of the upper plane earthquakes were mostly of the normal-faulting type with trench-normal T-axes, whereas those in the lower plane were of the reverse-faulting type with trench-normal P-axes, (Gamage *et al.*, 2009; Hino *et al.*, 2009). These observations indicated that the upper and lower planes were under tensional and compressional stress respectively, caused by downward bending of the oceanic slab. Obana *et al.* (2012) reported that normal-faulting earthquakes were recognized down to 40 km in depth, well below the upper-plane seismicity, and suggested that the bending stress increased in response to the Tohoku earthquake.

A large, shallow, normal-faulting earthquake of M_W 7.1 occurred on October 25, 2013, about 100 km south-southwest of the M_W 7.5 aftershock, showing that the enhancement of the bending stress has lasted for quite some time along a broad region of the outer trench slope. Nearer the trench axis region, a pair of large earthquakes successively occurred within 14 s on December 7, 2012. This doublet began with an M_W 7.2 thrust-faulting event 50–70 km deep in the Pacific plate and was followed by a shallower M_W 7.1–7.2 normal-faulting event 10–30 km deep (Lay *et al.*, 2013). The occurrence of this doublet can also be explained as due to enhancement of the bending stress near the trench caused by the Tohoku mainshock (Harada *et al.*, 2013; Obana *et al.*, 2014).

Normal-faulting seismicity was also observed generally occurring within the subducted Pacific slab, mostly beneath the large coseismic slip region of the Tohoku mainshock (Asano *et al.*, 2011). These normal-faulting aftershocks near the trench and in the outer-rise region occurred mainly in the up-dip portion of the slab, where a tensional stress change can be attributed to the thrust-faulting of the mainshock. On July 10, 2011, an intraslab earthquake (M_W 7.1) occurred near the hypocenter of the Tohoku mainshock. This aftershock had a strike-slip mechanism with the T-axis oriented in the dip direction of the slab. The secondary aftershocks of this aftershock formed two orthogonal planes, conforming to the nodal planes for the focal mechanism of that large July 10 aftershock. That aftershock was interpreted as due to the reactivation of pre-existing weak faults, possibly related to irregularities in the formation process of the oceanic lithosphere (Obana *et al.*, 2013). Stress-tensor inversions from focal mechanisms of these shallow intraslab earthquakes revealed that the minimum principal stress axis was oriented in the plate-convergent direction in the postseismic period (Hasegawa *et al.*, 2012). This change in stress regime in the slab is consistent with mainshock-slip models having an extremely large coseismic slip near the trench.

In contrast, an increase in the compressional stress in the slab is expected near the down-dip end of the high-slip region of the Tohoku earthquake. Indeed, an earthquake (M_W 7.1) occurred in the Pacific slab on 7 April. This aftershock occurred within the upper plane of the double-planed deep seismic zone beneath the northeastern Japan (Hasegawa *et al.*, 1978) and its down-dip compressional focal mechanism is consistent with those of the upper-plane events in the background seismicity. However, the M_W 7.1 earthquake rupture extended below the deeper limit of the usual distribution for the upper-plane seismicity and it was suggested that the down-dip compressional stress was largely intensified (Ohta *et al.*, 2011).

In the hanging wall, several small normal-faulting earthquakes occurred after the Tohoku earthquake. The T-axis directions of these aftershocks were diverse (Asano *et al.*, 2011). Shallow normal-faulting events were also identified in the aftershock activity following the 1994 Sanriku earthquake (Hino *et al.*, 2000), located to the north of the rupture region of the Tohoku earthquake. These shallow aftershocks occurred as a result of stress changes caused by the mainshock. A larger size of coseismic slip, in terms of area and slip amount, resulted in more intensive activity in the broader region in 2011 than it had in 1994.

Hasegawa *et al.* (2011) and Chiba *et al.* (2012) evaluated the stress field in the hanging wall using stress tensor inversions from focal mechanism solutions. Because there had been seismicity in the hanging wall before the Tohoku earthquake, the difference in the stress field before and after this great interplate earthquake could be estimated. From the comparison, it turned out that the maximum compressive-stress axis, having a usual direction aligned with the plate convergence, rotated by 30 to 35 degrees during the rupture of the Tohoku earthquake. This large coseismic rotation of the stress axis was interpreted as being caused by the complete stress release associated with the Tohoku earthquake. Hardebeck (2012) reported that the stress axes rotated rapidly back again to the usual orientation in the months following the Tohoku earthquake. It was considered that this rapid postseismic rotation was possible because the near-complete stress drop left very little background stress at the beginning of the postseismic reloading. Yagi and Fukahata (2011) also pointed out, based on their analysis of the mainshock rupture process, that the Tohoku earthquake released almost all the accumulated shear stress along the fault.

The Tohoku earthquake was followed by a large postseismic deformation across a broad region of eastern Japan. In early studies characterizing the afterslip, it was usually assumed that the observed postseismic deformation had been caused by slip along the plate boundary fault. Ozawa *et al.* (2011) showed significant expansion of the afterslip area extending out of the down-dip side of the coseismic rupture and also a fast moment release equivalent to M_W 8.3 within the two weeks after the mainshock occurrence. Ozawa *et al.* (2012) pointed out that afterslip along the deep plate interface continued for half a year but that the total slip tended to be smaller on the down-dip side of the Miyagi-oki region where the peak of coseismic slip was imaged.

A detailed account of postseismic slip in the earliest stage has been given by Munekane (2012). Within the 10-minute period between the mainshock and M_W 7.3 interplate aftershock to the north, afterslip propagated into the adjacent region to the north and downdip of the mainshock rupture region, releasing seismic moment equivalent to an event of M_W 7.1. In the four-hour period after the largest aftershock (M_W 7.6) to the south of the mainshock, the slip propagated into the regions up-dip and down-dip of the initial slip area, with a moment release equivalent to M_W 7.8. Johnson *et al.* (2012) and Fukuda *et al.* (2013) assessed the frictional properties of the plate boundary fault, based on the spatio-temporal evolution of the post-Tohoku earthquake slip, focusing on the complementary nature of the coseismic and postseismic slips and the moment-rate release dependency.

Although the afterslip estimates in these studies were based on the onshore GPS data, offshore observations of postseismic motion are required to describe the afterslip distribution precisely. The postseismic deformation patterns reported by Japan Coast Guard (2012) and Japan Coast Guard and Tohoku University (2013) were significantly different from the one estimated from the onshore observations. The most striking features in the offshore GPS observations were landward motions recorded in the Miyagi-oki region with the largest coseismic slip during the mainshock and subsidence across a broad region. It is unlikely that these features can be explained by afterslip alone and an alternative mechanism must also have been involved in the post-Tohoku earthquake deformation.

The most plausible mechanism controlling postseismic deformation other than afterslip on the fault is viscoelastic relaxation of the earthquake-induced stress (e.g. Wang *et al.* (2012). Diao *et al.* (2014) estimated that the effect of the viscoelastic relaxation within this initial stage only played a secondary role. However, the offshore postseismic displacements, completely opposite to those in the onshore region, indicated the importance of viscoelastic relaxation in interpreting the crustal deformation after the large stress perturbation induced by the Tohoku earthquake. Iinuma *et al.* (2014) computed the postseismic deformation observed at onshore and offshore sites as a combination of effects of afterslip and viscoelastic deformation.

Because of poor knowledge of the rheological structure in the subduction system, it is still difficult to obtain a reliable afterslip distribution along the plate interface. Nevertheless, the following three features were robustly obtained: 1) significant slip occurred on the deep extension of the mainshock rupture zone, 2) the amount of afterslip was minimal in the large coseismic slip area located in the Miyagi-oki region, and 3) occurrence of afterslip near the trench in the southern area, near the up-dip side of sub-patch B.

Heki and Mitsui (2013) pointed out that finite viscosity of the asthenosphere could have caused acceleration of the subducting motion of the Pacific plate due to a postseismic adjustment of the force balance acting on the slab, and argued that acceleration of the slab motion and rapid restoration of interplate coupling may have accounted for the landward postseismic motion in the Miyagi-oki region.

On the other hand, the activity of small repeating earthquakes along the plate boundary seems to have been driven solely by fault slip in a region free from the complexity of postseismic deformation. Uchida and Matsuzawa (2013) indicated an evident increase of the repeating earthquake activity in the regions surrounding the mainshock rupture zone, not only on the deeper side but also in the shallower part where the occurrence of significant afterslip was revealed by Iinuma *et al.* (2014). The slip rate estimated from the repeating earthquakes showed a more abrupt increase after the mainshock in the region closer to the source, suggesting outward propagation of afterslip from the rupture area.

8.2.5 Shallow crustal seismicity induced by the Tohoku earthquake

Shallow crustal seismicity was increased immediately after the Tohoku mainshock over a broad region of eastern Japan including several remote regions (Hirose *et al.*, 2011). The induced seismicity in remote regions included several $M>6$ earthquakes that caused severe damage around their focal regions. Okada *et al.* (2011), Toda *et al.* (2011a) and Ishibe *et al.* (2011) reported that static stress transfer after the Tohoku earthquake was responsible for these phenomena. Okada *et al.* (2011) pointed out that the estimated positive Coulomb stress change was mainly due to the reduction of normal stress on the fault planes. Toda and Stein (2013) warned that the probability of a large earthquake occurrence near the Tokyo metropolitan area had increased two-and-a-half times above that estimated before the Tohoku earthquake struck, due to the static stress change applied to the region following the Tohoku earthquake.

Kato *et al.* (2011) examined the coseismic static stress change in the coastal region of southern Tohoku where an M_W 5.8 normal-faulting earthquake occurred on March 19 and concluded that the earthquake occurred in response to an abrupt flip of the stress field from the pre-seismic trench-normal horizontal compression (e.g. Terakawa and Matsu'ura, 2010) to east-west extension after the Tohoku mainshock. Yoshida *et al.* (2012) showed that the directions of principal stress axes inferred from post-Tohoku focal mechanisms at several places in eastern Japan were consistent with those resulting from stress perturbations due to the Tohoku earthquake. Because the magnitudes of the applied stress changes were estimated at less than 1 MPa, a low differential stress before the Tohoku earthquake is a necessary condition at these locations.

On the other hand, Toda *et al.* (2011b) demonstrated that seismicity can occur in the nominal stress shadow of a mainshock as long as small geometrically diverse active faults exist. Imanishi *et al.* (2012) found that the pre-Tohoku earthquake stress field in the southern Tohoku region, for which the coseismic flip of the stress field was supposed by Kato *et al.* (2011), was a normal-faulting stress regime in contrast to the predominant reverse-faulting regime in northeastern Japan. In that southern region, small-scale heterogeneity had already existed and fractures in the normal-faulting region were reactivated by the enhancement of trench-normal extension after the Tohoku earthquake, causing intense shallow crustal seismicity. These arguments emphasize the importance of small-scale heterogeneity of the pre-mainshock stress state when interpreting an apparent coseismic change in the dominant focal mechanisms. Coseismic change in pore-fluid pressure can be another factor increasing the seismicity of the shallow crust in inland regions. Terakawa *et al.* (2013) argue that several induced earthquakes from unfavorably oriented faults after the Tohoku earthquake turn to optimally oriented faults with the ambient fluid pressure.

Among the induced inland seismicity, the largest earthquake of M_W 6.6 occurred in the southern part of the coastal region on 11 April 2011 (the Fukushima-ken-Hamadori earthquake or Iwaki earthquake) and ruptured two previously mapped faults. It was supposed that previous activity on these faults was related to earlier great interplate earthquakes like the Tohoku earthquake, assuming that the large ruptures along these faults had been induced exclusively by similar interplate earthquakes. A paleoseismic trench (Toda and Tsutsumi, 2013) across one of these faults exposed evidence for the penultimate earthquake that occurred about 15,000 years ago but there was no evidence that the fault ruptured during or immediately after the A.D. 869 Jogan earthquake.

There have been several reports of the induced seismicity being caused by dynamic stress change (e.g. Yukutake *et al.*, 2011; Kato *et al.*, 2013). Miyazawa (2011) showed that early post-seismic events triggered by the Tohoku earthquake propagated systematically across Japan. The propagation speed of the front of seismicity was consistent with that of the large amplitude surface waves. It was also found that small amplitude P-waves from the Tohoku earthquake could trigger non-volcanic tremor along the

Nankai Trough subduction zone (Miyazawa, 2012).

8.2.6 Discussion

Coseismic phenomena associated with the Tohoku earthquake have provided important clues to resolve the question of how a M-9 class earthquake could occur in the Japan Trench subduction margin, normally characterized by the frequent recurrence of M<8 earthquakes and broad aseismic slip. In the most trenchward zone where the coseismic slip was the largest, the background seismicity was especially low. In contrast, the deeper portion of the plate boundary, where M 7.5 earthquakes have repeatedly occurred, slipped by about a third of that in the trench region. Taking the 1978 earthquake as a representative example, past earthquakes resulted in a dislocation of about 2 m due to coseismic activity and afterslip, and the total amount of this slip accounts for about two thirds of the slip deficit that accumulated within the recurrence interval (40 years) at a convergence rate of 0.08 m/year. The proportion of the coseismic slip between the deep seismogenic zone and the trenchward zone (1:3) is reasonably explained if the trenchward aseismic zone had been fully coupled and if the Tohoku earthquake released the strain accumulated since the previous M 9 earthquake, which may have occurred more than 600 years ago.

From this inference, it is emphasized that restoration of the history of large events associated with slip near the trench is indispensable to understanding the entire process of deformation, strain accumulation and release, caused by the subduction of the Pacific plate at the Japan Trench. Even though tsunami deposits along the coast are important records of past gigantic tsunami, the area of inundation of coastal regions such as the Sendai plain is not sensitive to the amount of slip near the trench (Sawai *et al.*, 2012). Besides onshore geologic investigations, systematic offshore studies for records of past large slip along the shallow subduction thrust zone are also required. Kodaira *et al.* (2012) reported that large-scale deformation structures near the trench axis have been developed by not only the large slip associated with the Tohoku earthquake but also in similar events repeatedly occurring in the past. These deformation structures could be indications of slip breaking through to the trench. A detail survey of submarine geologic structures should help to find where large earthquakes occurred previously. Strasser *et al.* (2013) studied sediment cores retrieved from the trench region and found evidence of large-scale slumping triggered by slip towards the trench. Analyses of sediment cores, which may provide direct or indirect indications of sudden large slips, may shed light on the recurrence history of the large-scale shallow faulting events.

Afterslip distribution provides key information on frictional properties along the plate boundary fault. Numerous efforts have been made to explain the rupture process of the Tohoku earthquake (e.g. Kato and Yoshida, 2011; Mitsui *et al.*, 2012), and the earthquake cycle along the Japan Trench, particularly the coexistence of regular M 8 and sporadic M 9 earthquakes (e.g. Hori and Miyazaki, 2011; Shibazaki *et al.*, 2011; Ide and Aochi, 2013). In all these models, frictional properties were important but not well constrained by the observations. As explained in the previous section, monitoring the activity of small repeating earthquakes puts strong constraints on the afterslip distributions. Along the Japan Trench, seafloor geodetic observations have been reinforced (Kido *et al.*, 2012) to understand better the postseismic deformation near the large coseismic slip area for the Tohoku earthquake.

On the other hand, it is also important to determine from the geodetic observations the extent of deformation due to viscoelastic relaxation. To this end, realistic modeling of the rheological structure is critically important and this might also be resolved by the geodetic observations of the post-Tohoku earthquake deformation. Takahashi (2011) and Ohzono *et al.* (2012) reported strain changes as large as $45x10^{-6}$ in the onshore Tohoku region and pointed out that there were significant irregularities in the strain field induced by the Tohoku earthquake. These irregularities reflect spatial heterogeneity of the rheological structure and correlate with the spatial patterns of strain concentration observed before the mainshock. By including the spatio-temporal variation of postseismic deformation in the modeling, the rheological structure beneath the Japan Trench subduction zone could be resolved.

Stress changes associated with the Tohoku earthquake have provided invaluable opportunities to understand the stress field in the crust. Because the Tohoku earthquake was considered to release completely the shear stress accumulated along the plate boundary fault (Hasegawa *et al.*, 2011; Yagi and Fukahata, 2011), the level of differential stress on the plate interface can be estimated from the stress drop for this earthquake, 10 MPa. As the stress field after the earthquake can be expressed as the sum of the pre-seismic field and the coseismic static-stress change, Hasegawa *et al.* (2012) estimated the magnitude of the differential stress to be 10 MPa in the hanging wall of the large coseismic slip region.

The estimated magnitude of deviatoric stress implies that the strength of the plate boundary fault was weak, as it was also for faults in the hanging wall. Similarly, the significant difference in the stress field in the inland crust before and after the Tohoku earthquake (Kato *et al.*, 2011; Yoshida *et al.*, 2012) may also indicate that the shallow crustal faults were extremely weak, because the magnitude of the static stress change must have been very small ($<$ 1 MPa) in the areas of significant changes in focal mechanisms. However, careful re-assessments regarding these proposals may be required since the observed stress changes may be merely apparent, caused by small-scale spatial variations of the stress field in the vicinity of the induced seismicity (Imanishi *et al.*, 2012).

As most of the tsunami inversion results indicated, the large coseismic slip near the central Japan Trench generally accounted for the size of the tsunami associated with the Tohoku earthquake. However, these models were unable to reproduce the magnitude of the observed tsunami run-up along the coastal region north of 39°N, whereas misfits of the model-predicted values were very small for the other observations, the run-up or inundation in the south and the offshore tsunami waveforms (MacInnes *et al.*, 2013). It was suspected that there must have been an additional source of tsunamigenic energy responsible for the large run-up in the northern coastal region. As reviewed by Satake and Fujii (2014), the observed coastal tsunami height distribution seemed to require a delayed tsunami source in the north of the earthquake source region. For example, the tsunami source model of Satake *et al.* (2013) with a delay (of more than three minutes after the mainshock initiation) in the rupture of the shallowest part of the fault near the northern Japan Trench, where no significant slips had been imaged by the previous studies, overcame the anomalies. However, the moment-rate time-series and source-time function of that time-dependent tsunami source model were not consistent with the other results derived from the seismic observations.

Since the delayed tsunami source was located near the source region of the 1896 tsunami earthquake (Tanioka and Satake, 1996b), the real nature of this enhanced tsunami source needs to be known. The size of delayed source was equivalent to a fault slip of more than 10 m, much larger than the slip deficit accumulated during about 100 years, even assuming 100% coupling.

8.2.7 Summary

The Tohoku earthquake has become an unprecedentedly well-described M-9 earthquake through a diversity of observations, including seismic and tsunami waveforms recorded in the far-field using global networks and large-scale arrays in North America and Europe, and non-clipped data in the near-field provided by overwhelmingly dense networks deployed in Japan. Emerging observation technology, such as high-rate GPS data collection as well as offshore tsunami, earthquake and geodetic observations, has helped to constrain the unique character of the Tohoku earthquake, with an extremely large slip along the shallowest portion of the subduction plate boundary. The frequency content of the radiated seismic energy was found to be strongly dependent on the depth, with higher frequencies predominantly from the deeper region in contrast to lower frequencies from the shallow fault region that was characterized by large slip.

Although the rupture spanned a large region beneath the landward slope of the Japan Trench, there was a more compact patch near the hypocenter where most of the moment release was concentrated. The earthquake completely released the shear stress accumulated along the plate boundary fault for more than a hundred years and caused a remarkable increase in seismicity across a broader region of Japan. Several lines of evidence have indicated that the Tohoku earthquake was preceded by an unloosening of the interplate coupling over an interval of about ten years, but no evident acceleration was observed to be related to the nucleation of a great earthquake except for foreshock activity associated with aseismic slip near the hypocenter.

Extensive afterslip along the down-dip extension of coseismic fault slip accounted for the postseismic deformation observed onshore, but the deformation included a substantial contribution from viscoelastic relaxation after the large coseismic slip, especially in the offshore area. The large impact of the Tohoku earthquake on the stress-strain field of the subduction zone has provided an invaluable opportunity to understand various aspects of the rheological characteristics of the lithosphere: absolute magnitude of crustal stress, fault strength, structure of viscosity, and so on. Efforts to monitor seismicity and crustal deformation will continue to be increasingly important.

8.2.8 Acknowledgements

The author wishes to thank Akira Hasegawa, Toru Matsuzawa, and Shinji Toda for discussions regarding the generation processes of the Tohoku-oki earthquake and its consequences. I would like to express respect for all the institutions around the world running seismological, geodetic and tsunami observation networks, providing invaluable data. In particular, outstanding contributions of the local networks operated by Japan Metrological Agency (JMA), National Research Institute for Earth Science and Disaster Prevention (NEID), Geospatial Information Authority of Japan (GSI) and Japan Coast Guard (JCG) must be acknowledged. Offshore observations in the source area of the Tohoku-oki earthquake have been conducted for more than ten years under support of Ministry of Education, Culture, Sports, Science and Technology (MEXT), Japan. All the figures were made using GMT.

8.2.9 References

Ammon, C.J., T. Lay, H. Kanamori, M. Cleveland, 2011. A rupture model of the 2011 off the Pacific coast of Tohoku Earthquake, *Earth Planets Space*, 63, 7, 693-696, doi:10.5047/eps.2011.05.015

Altamimi, Z., X. Collilieux, J. Legrand, B. Garayt, and C. Boucher, 2007. ITRF2005: A new release of the International Terrestrial Reference Frame based on time series of station positions and Earth Orientation Parameters, *J. Geophys. Res.*, 112, B09401, doi:10.1029/2007JB004949

Ando, R. and K. Imanishi, 2011. Possibility of M_W 9.0 mainshock triggered by diffusional propagation of after-slip from M_W 7.3 foreshock, *Earth Planets Space*, 63, 7, 767-771, doi:10.5047/eps.2011.05.016

Asano, Y., T. Saito, Y. Ito, Y., K. Shiomi, H. Hirose, T. Matsumoto, S. Aoi, S. Hori, and S. Sekiguchi, 2011. Spatial distribution and focal mechanisms of aftershocks of the 2011 off the Pacific coast of Tohoku Earthquake, *Earth Planets Space*, 63, 7, 669-673, doi:10.5047/eps.2011.06.016

Asano, K. and T. Iwata, 2012. Source model for strong ground motion generation in 0.1-10 Hz during the 2011 Tohoku earthquake, *Earth Planets Space*, 64, 12, 1111-1123, doi:10.5047/eps.2012.05.003

Bilek, S.L., H. R. DeShon, and E. R. Engdahl, 2012. Spatial variations in earthquake source characteristics within the 2011 $M_W = 9.0$ Tohoku, Japan rupture zone, *Geophys. Res. Lett.*, 39, 9, L09304, doi:10.1029/2012GL051399

Chiba, K., Y. Iio, and Y. Fukahata, 2012. Detailed stress fields in the focal region of the 2011 off the Pacific coast of Tohoku Earthquake—Implication for the distribution of moment release—, *Earth Planets Space*, 64, 12, 1157-1165, doi:10.5047/eps.2012.07.008

Chu, R., S. Wei, D. V. Helmberger, Z. Zhan, L. Zhu, and H. Kanamori, 2011. Initiation of the great M_W 9.0 Tohoku-Oki earthquake, *Earth planet. Sci. Lett.*, 308, 3-4, 277-283, doi:10.1016/j.epsl.2011.06.031

Diao, F., X. Xiong, R. Wang, Y. Zheng, T. R. Walter, H. Weng, and J. Li, 2014. Overlapping post-seismic deformation processes: afterslip and viscoelastic relaxation following the 2011 M_W 9.0 Tohoku (Japan) earthquake, *Geophys. J. Int.*, 196, 1, 218-229, doi:10.1093/gji/ggt376

Duputel, Z., L. Rivera, H. Kanamori, G. P. Hayes, B. Hirshom, and S. Weinstein, 2011. Real-time W phase inversion during the 2011 off the Pacific coast of Tohoku earthquake, *Earth Planets Space*, 63, 7, 535-539, doi:10.5047/eps.2011.05.032

Duputel, Z., V. C. Tsai, L. Rivera, H. Kanamori, 2013. Using centroid time-delays to characterize source durations and identify earthquakes with unique characteristics, *Earth planet. Sci. Lett.*, 374, 92-100, doi:10.1016/j.epsl.2013.05.024

Frankel, A., 2013. Rupture History of the 2011 M 9 Tohoku Japan Earthquake Determined from Strong-Motion and High-Rate GPS Recordings: Subevents Radiating Energy in Different Frequency Bands, *Bull. seism. Soc. Am.*, 103, 2B, 1290-1306, doi:10.1785/0120120148

Fujii, Y., K. Satake, S. Sakai, M. Shinohara, and T. Kanazawa, 2011. Tsunami source of the 2011 off the Pacific coast of Tohoku Earthquake, *Earth Planets Space*, 63, 7, 815-820, doi:10.5047/eps.2011.06.010

Fujiwara, T., S. Kodaira, T. No, Y. Kaiho, N. Takahashi, and Y. Kaneda, 2011. The 2011 Tohoku-Oki

Earthquake: Displacement Reaching the Trench Axis, *Science*, 334, 6060, 1240, doi:10.1126/science.1211554

Fukahata, Y., Y. Yagi, and S. Miyazaki, 2012. Constraints on early stage rupture process of the 2011 Tohoku-oki earthquake from 1 Hz GPS data, *Earth Planets Space*, 64, 12, 1093-1099, doi:10.5047/eps.2012.09.007

Fukuda, J., A. Kato, N. Kato, and Y. Aoki, 2013. Are the frictional properties of creeping faults persistent? Evidence from rapid afterslip following the 2011 Tohoku-oki earthquake, *Geophys. Res. Lett.*, 40, 14, 3613-3617, doi:10.1002/grl.50713

Furumura, T., S. Takemura, S. Noguchi, T. Takemoto, T. Maeda, K. Iwai, and S. Padhy, 2011. Strong ground motions from the 2011 off-the Pacific-Coast-of-Tohoku, Japan ($M_W = 9.0$) earthquake obtained from a dense nationwide seismic network, *Landslides*, 8, 3, 333-338, doi:10.1007/s10346-011-0279-3

Gamage, S. S. N., N. Umino, A. Hasegawa, and S. H. Kirby, 2009. Offshore double-planed shallow seismic zone in the NE Japan forearc region revealed by sP depth recorded by regional networks, *Geophys. J. Int.*, 78, 195–214, doi:10.1111/j.1365-246X.2009.04048.x

Grilli, S. T, J. C. Harris, T. S. Tajalli Bakhsh, T. L. Masterlark, C. Kyriakopoulos, J. T. Kirby, and F. Shi, 2013. Numerical simulation of the 2011 Tohoku tsunami based on a new transient FEM co-seismic souce: comparison to far- and near-field observations, *PAGEOPH*, 170, 1333-1359.

Gusman, A. R., Y. Tanioka, S. Sakai, and H. Tsushima, 2012. Source model of the great 2011 Tohoku earthquake estimated from tsunami waveforms and crustal deformation data, *Earth planet. Sci. Lett.*, 341-344, 8, 234 - 242, doi:10.1016/j.epsl.2012.06.006

Gusman, A. R., M. Fukuoka, Y. Tanioka, and S. Sakai, 2013. Effect of the largest foreshock (M_W 7.3) on triggering the 2011 Tohoku earthquake (M_W 9.0), *Geophys. Res. Lett.*, 40, 3, 497-500, doi:10.1002/grl.50153

Harada, T., S. Murotani, and K. Satake, 2013. A deep outer-rise reverse-fault earthquake immediately triggered a shallow normal-fault earthquake: The 7 December 2012 off-Sanriku earthquake (M_W 7.3), *Geophys. Res. Lett.*, 40, 4214-4219, doi:10.1002/grl.50808

Hardebeck, J. L., 2012. Coseismic and postseismic stress rotations due to great subduction zone earthquakes, *Geophys. Res. Lett.*, 39, 21, L21313, doi:10.1029/2012GL053438

Hasegawa, A., N. Umino, and A. Takagi, 1978, Double-planed structure of the deep seismic zones in the northeastern Japan arc, *Tectonophysics*, 47, 43–58.

Hasegawa, A., K. Yoshida, Okada, T., 2011. Nearly complete stress drop in the 2011 M_W 9.0 off the Pacific coast of Tohoku Earthquake, *Earth Planets Space*, 63, 7, 703-707, doi:10.5047/eps.2011.06.007

Hasegawa, A., K. Yoshida, Y. Asano, T. Okada, T. Iinuma, and Y. Ito, 2012. Change in stress field after the 2011 great Tohoku-Oki earthquake, *Earth planet. Sci. Lett.*, 355-356, 11, 231 - 243, doi:10.1016/j.epsl.2012.08.042

Hashimoto, C., A. Noda, T. Sagiya and M. Matsu'ura, 2009. Interplate seismogenic zones along the Kuril–Japan trench inferred from GPS data inversion, *Nature Geoscience*, 2, 141 – 144, doi:10.1038/ngeo421

Hashimoto, C., A. Noda, and M. Matsu'ura, 2012. The M_W 9.0 northeast Japan earthquake: total rupture of a basement asperity, *Geophys. J. Int.*, 189, 1, 1-5, doi:10.1111/j.1365-246X.2011.05368.x

Hayashi, Y., H. Tsushima, K. Hirata, K. Kimura, and K. Maeda, 2011. Tsunami source area of the 2011 off the Pacific coast of Tohoku Earthquake determined from tsunami arrival times at offshore observation stations, *Earth Planets Space*, 63, 809-813.

Hayes, G. P., 2011. Rapid source characterization of the 2011 M_W 9.0 off the pacific coast of Tohoku earthquake, *Earth Planets Space*, 63, 7, 529-534, doi:10.5047/eps.2011.05.012

Heki, K., S. Miyazaki and H. Tsuji, 1997, Silent fault slip following an interplate thrust earthquake at the Japan Trench, *Nature*, 386, 595-597.

Heki, K. and Y. Mitsui, 2013. Accelerated pacific plate subduction following interplate thrust earthquakes at the Japan trench, *Earth planet. Sci. Lett.*, 363, 2, 44 - 49, doi:10.1016/j.epsl.2012.12.031

Hino, R, S. Ito, H. Shiobara, H. Shimamura, T. Sato, T. Kanazawa, J. Kasahara, and A. Hasegawa, 2000. Aftershock distribution of the 1994 Sanriku-oki earthquake (M_W 7.7) revealed by ocean bottom seismographic observation, *J. Geophys. Res.*, 105, 21697–21710.

Hino, R., Y. Yamamoto, A. Kuwano, M. Nishino, T. Kanazawa, T. Yamada, K. Nakahigashi, K. Mochizuki, M. Shinohara, K. Minato, G. Aoki, N. Okawara, M. Tanaka, M. Abe, E. Araki, S. Kodaira, G. Fujie, and Y. Kaneda, 2006. Hypocenter distribution of the main- and aftershocks of the 2005 Off Miyagi Prefecture earthquake located by ocean bottom seismographic data, *Earth Planets Space*, 58, 1543-1548.

Hino, R., R. Azuma, Y. Ito., Y. Yamamoto, K. Suzuki, H. Tsushima, S. Suzuki, M. Miyashita, T. Tomori, M. Arizono, and G. Tange, 2009. Insight into complex rupturing of the immature bending normal fault in the outer slope of the Japan Trench from aftershocks of the 2005 Sanriku earthquake ($M_W = 7.0$) located by ocean bottom seismometry, *Geochem Geophys Geosyst*, 10(7): Q07O18, doi:10.1029/2009GC002415

Hino, R., D. Inazu, Y. Ito, Y. Ohta, and T. Iinuma, 2013a. Ocean bottom pressure records of the 2011 Tohoku-Oki earthquake, *Proc. 11th SEGJ International Symposium*, 462-465,
doi:10.1190/segj112013-117

Hino, R., D. Inazu, Y. Ohta, Y. Ito, S. Suzuki, T. Iinuma, Y. Osada, M. Kido, H. Fujimoto, Y. Kaneda, 2013b. Was the 2011 Tohoku-Oki earthquake preceded by aseismic preslip? Examination of seafloor vertical deformation data near the epicenter, Mar *Geophys Res.*, doi:10.1007/s11001-013-9208-2

Hirose, H., 2011. Tilt records prior to the 2011 off the Pacific coast of Tohoku Earthquake,*Earth Planets Space*,63, 7, 655-658, doi:10.5047/eps.2011.05.009

Hirose, F., K. Miyaoka, N. Hayashimoto, T. Yamazaki, and M. Nakamura, 2011. Outline of the 2011 off the Pacific coast of Tohoku earthquake (M_W 9.0) -seismicity: Foreshocks, mainshock, aftershocks, and induced activity, *Earth Planets Space*, 63, 7, 513-518, doi:10.5047/eps.2011.05.019

Honda, R., Y. Yukutake, H. Ito, M. Harada, T. Aketagawa, A. Yoshida, S. Sakai, S. Nakagawa, N. Hirata, K. Obara, and H. Kimura, 2011. A complex rupture image of the 2011 off the Pacific coast of Tohoku

Earthquake revealed by the MeSO-net, *Earth Planets Space*, 63, 7, 583-588, doi:10.5047/eps.2011.05.034

Hooper, A., J. Pietrzak, W. Simons, H. Cui, R. Riva, M. Naeije, A. Terwisscha van Scheltinga, E. Schrama, G. Stelling, and A. Socquet, 2013. Importance of horizontal seafloor motion on tsunami height for the 2011 M_W=9.0 Tohoku-Oki earthquake, *Earth planet. Sci. Lett.*, 361, 469-479, doi:10.1016/j.epsl.2012.11.013

Hori, T. and S. Miyazaki, 2011. A possible mechanism of M 9 earthquake generation cycles in the area of repeating M 7 8 earthquakes surrounded by aseismic sliding, *Earth Planets Space*, 63, 773-777.

Hoshiba, M. and K. Iwakiri, 2011. Initial 30 seconds of the 2011 off the Pacific coast of Tohoku Earthquake (M_W9.0) - amplitude and θc for magnitude estimation for earthquake early Warning, *Earth Planets Space*, 63, 7, 553-557, doi:10.5047/eps.2011.06.015

Huang, Q. and X. Ding, 2012. Spatiotemporal Variations of Seismic Quiescence prior to the 2011 M 9.0 Tohoku Earthquake Revealed by an Improved Region-Time-Length Algorithm, *Bull. seism. Soc. Am.*, 102, 4, 1878-1883, doi:10.1785/0120110343

Ide, S., A. Baltay, and G. C. Beroza, 2011. Shallow dynamic overshoot and energetic deep rupture in the 2011 M_W 9.0 Tohoku-Oki earthquake, *Science*, 332, 6036, 1426-1429, doi:10.1126/science.1207020

Ide, S. and H. Aochi, 2013. Historical seismicity and dynamic rupture process of the 2011 Tohoku-Oki earthquake, *Tectonophysics*, 600, 1-13, doi:10.1016/j.tecto.2012.10.018

Igarashi, T., T. Matsuzawa, N. Umino, and A. Hasegawa, 2001. A. Spatial distribution of focal mechanisms for interplate and intraplate earthquakes associated with the subducting Pacific plate beneath the northeastern Japan arc: A triple-planed deep seismic zone, *J. Geophys. Res.*, 106, 2177-2191.

Iinuma, T., M. Ohzono, Y. Ohta, and S. Miura , 2011. Coseismic slip distribution of the 2011 off the Pacific coast of Tohoku Earthquake (M 9.0) estimated based on GPS data—Was the asperity in Miyagi-oki ruptured?, *Earth Planets Space*, 63, 643-648.

Iinuma, T., R. Hino, M. Kido, D. Inazu, Y. D. Osada, Y. Ito, M. Ohzono, H. Tsushima, S. Suzuki, H. Fujimoto, and S. Miura, 2012. Coseismic slip distribution of the 2011 off the Pacific Coast of Tohoku Earthquake (M9.0) refined by means of seafloor geodetic data, *J. geophys. Res.*, 117, B7, B07409, doi:10.1029/2012JB009186

Iinuma, T., R. Hino, M. Kido, Y. Osada, D. Inazu, Y. Ito, S. Suzuki, Y. Ohta, and H. Fujimoto, 2014. Investigation on the postseismic deformation associated with the 2011 Tohoku earthquake based on terrestrial and sea geodetic observations - to evaluate the further seismic hazard potential on the plate interface beneath the northeastern Japanese Islands, *proceedings IAG international symposium* (in press).

Imanishi, K., R. Ando, and Y. Kuwahara, 2012. Unusual shallow normal-faulting earthquake sequence in compressional northeast Japan activated after the 2011 off the Pacific coast of Tohoku earthquake, *Geophys. Res. Lett.*, 39, 9, L09306, doi:10.1029/2012GL051491

Ishii, M., 2011. High-frequency rupture properties of the M_W 9.0 off the Pacific coast of Tohoku Earthquake, *Earth Planets Space*, 63, 7, 609-614, doi:10.5047/eps.2011.07.009

Ishibe, T., K. Shimazaki, K. Satake, and H. Tsuruoka, 2011. Change in seismicity beneath the Tokyo metropolitan area due to the 2011 off the Pacific coast of Tohoku Earthquake, *Earth Planets Space*, 63, 7, 731-735, doi:10.5047/eps.2011.06.001

Ito, T., K. Ozawa, T. Watanabe, and T. Sagiya, 2011. Slip distribution of the 2011 off the Pacific coast of Tohoku Earthquake inferred from geodetic data, *Earth Planets Space*, 63, 7, 627-630, doi:10.5047/eps.2011.06.023

Ito, Y., T. Tsuji, Y. Osada, M. Kido, D. Inazu, Y. Hayashi, H. Tsushima, R. Hino, and H. Fujimoto, 2011. Frontal wedge deformation near the source region of the 2011 Tohoku-Oki earthquake, *Geophys. Res. Lett.*, 38, 15, L00G05, doi:10.1029/2011GL048355

Ito, Y., R. Hino, M. Kido, H. Fujimoto, Y. Osada, D. Inazu, Y. Ohta, T. Iinuma, M. Ohzono, S. Miura, M. Mishina, K. Suzuki, T. Tsuji, and J. Ashi, 2013. Episodic slow slip events in the Japan subduction zone before the 2011 Tohoku-Oki earthquake, *Tectonophysics*, 600, 14-26, doi:10.1016/j.tecto.2012.08.022

Japan Coast Guard, 2012. Seafloor movements by seafloor geodetic observations before and after the 2011 off the Pacific coast of Tohoku earthquake. Report of the coordinating Committee for Earthquake Prediction, Japan 87, Chapter 3–7. Japan Coast Guard and Tohoku University, 2013. Seafloor movements observed by seafloor geodetic observations after the 2011 off the Pacific coast of Tohoku Earthquake, *Report of Coordinating Committee of Earthquake Prediction*, Vol. 90, 3-4, http://cais.gsi.go.jp/YOCHIREN/report/kaihou90/03_04.pdf

Japan Metrological Agency, 2013. *Seismic activity in and around the Tohoku district (November 2012 – April 2013)*, Vol. 90, 3-41, http://cais.gsi.go.jp/YOCHIREN/report/kaihou90/03_01.pdf

Johnson, K. M., J. Fukuda, and P. Segall, 2012. Challenging the rate-state asperity model: Afterslip following the 2011 M9 Tohoku-oki, Japan, earthquake, *Geophys. Res. Lett.*, 39, 20, L20302, doi:10.1029/2012GL052901

Kanamori, H., 1977, Seismic and aseismic slip along subdcution zones and their tectonic implications, In: Talwani, M. Pitman, W.C. (Eds.), Island Arcs, Deep Sea Trenches and Back-Arc Basins, *AGU*, Washington, DC, pp.163-174, http://dx.doi.org.10.1029/ME01p0163

Kato, N. and S. Yoshida, 2011. A shallow strong patch model for the 2011 great Tohoku-oki earthquake: A numerical simulation, *Geophys. Res. Lett.*, 38, doi:10.1029/2011GL048565

Kato, A., S. Sakai, and K. Obara, 2011. A normal-faulting seismic sequence triggered by the 2011 off the Pacific coast of Tohoku Earthquake: Wholesale stress regime changes in the upper plate, *Earth Planets Space*, 63, 7, 745-748, doi:10.5047/eps.2011.06.014

Kato, A. and T. Igarashi, 2012. Regional extent of the large coseismic slip zone of the 2011 M_W 9.0 Tohoku-Oki earthquake delineated by on-fault aftershocks, *Geophys. Res. Lett.*, 39, 15, L15301, doi:10.1029/2012GL052220

Kato, A., K. Obara, T. Igarashi, H. Tsuruoka, S. Nakagawa, S. and N. Hirata, 2012. Propagation of Slow Slip Leading Up to the 2011 M_W 9.0 Tohoku-Oki Earthquake, *Science*, 335, 2, 705-708, doi:10.1126/science,1215141

Kato, A., J. Fukuda, and K. Obara, 2013. Response of seismicity to static and dynamic stress changes induced by the 2011 M9.0 Tohoku-Oki earthquake, *Geophys. Res. Lett.*, 40, 14, 3572-3578, doi:10.1002/grl.50699

Katsumata, K., 2011. A long-term seismic quiescence started 23 years before the 2011 off the Pacific coast of Tohoku Earthquake ($M = 9.0$), *Earth Planets Space*, 63, 7, 709-712, doi:10.5047/eps.2011.06.033

Kawamura, K., T. Sasaki, T. Kanamatsu, A. Sakaguchi, and Y. Ogawa, 2012. Large submarine landslides in the Japan Trench: A new scenario for additional tsunami generation, *Geophys. Res. Lett.*, 39, 5, L05308, doi:10.1029/2011GL050661

Kawasaki, I., Y. Asai, Y. Tamura, T. Sagiya, N. Mikami, Y. Okada, M. Sakata and M. Kasahara, 1995. The 1992 Sanriku-Oki, Japan, Ultra-slow earthquake, *J. Phys. Earth*, 43, 105-116.

Kawasaki, I., Y. Asai and Y. Tamura, 2001. Space-time distribution of interplate moment release including slow earthquakes and the seismo-geodetic coupling in the Sanriku-oki region along the Japan trench, *Tectonophysics*, 330, 267-283.

Kido, M., Y. Osada, H. Fujimoto, R. Hino, and T. Ito, 2011. Trench-normal variation in observed seafloor displacements associated with the 2011 Tohoku-Oki earthquake, *Geophys. Res. Lett.*, 38, 24, L24303, doi:10.1029/2011GL050057

Kido, M., H. Fujimoto, Y. Osada, Y. Ohta, J. Yamamoto, K. Tadokoro, T. Okuda, T. Watanabe, S. Nagai, and K. Yasuda, 2012. Development of GPS/A Seafloor Geodetic Network Along Japan Trench and Onset of Its Operation, Abstract T13F-2697 presented at 2012 Fall Meeting, AGU, San Francisco, Calif., 3-7 Dec.

Kiser, E. and M. Ishii, 2012. The March 11, 2011 Tohoku-oki earthquake and cascading failure of the plate interface, *Geophys. Res. Lett.*, 39, L00G25, doi:10.1029/2012GL051170

Kodaira, S., T. No, Y. Nakamura, T. Fujiwara, Y. Kaiho, S. Miura, N. Takahashi, Y. Kaneda, and A. Taira, 2012. Coseismic fault rupture at the trench axis during the 2011 Tohoku-oki earthquake, *Nature Geoscience*, 5(9), 646-650, doi:10.1038/ngeo1547

Koper, K. D., A. R. Hutko, T. Lay, C. J. Ammon,. and H. Kanamori, 2011a. Frequency-dependent rupture process of the 2011 M_W 9.0 Tohoku Earthquake: Comparison of short-period P wave backprojection images and broadband seismic rupture models, *Earth Planets Space*, 63, 7, 599-602, doi:10.5047/eps.2011.05.026

Koper, K. D., A. R. Hutko, and T. Lay, 2011b. Along-dip variation of teleseismic short-period radiation from the 11 March 2011 Tohoku earthquake (M_W 9.0), *Geophys. Res. Lett.*, 38, 21, L21309, doi:10.1029/2011GL049689

Koketsu, K., Y. Yokota, N. Nishimura, Y. Yagi, S. Miyazaki, K. Satake, Y. Fujii, H. Miyake, S. Sakai, Y. Yamanaka, and T. Okada, 2011. A unified source model for the 2011 Tohoku earthquake, *Earth planet. Sci. Lett.*, 310, 3-4, 480-487, doi:10.1016/j.epsl.2011.09.009

Kosuga, M. and K. Watanabe, 2011. Seismic activity around the northern neighbor of the 2011 off the Pacific coast of Tohoku Earthquake with emphasis on a potentially large aftershock in the area, *Earth Planets Space*, 63, 719-723.

Kubo, H. and Y. Kakehi, 2013. Source Process of the 2011 Tohoku Earthquake Estimated from the Joint Inversion of Teleseismic Body Waves and Geodetic Data Including Seafloor Observation Data: Source Model with Enhanced Reliability by Using Objectively Determined Inversion Settings, *Bull. seism. Soc. Am.*, 103, 2B, 1195-1220, doi:10.1785/0120120113

Kubo, H., K. Asano, and T. Iwata, 2013. Source-rupture process of the 2011 Ibaraki-oki, Japan, earthquake (M_W 7.9) estimated from the joint inversion of strong-motion and GPS Data: Relationship with seamount and Philippine Sea Plate, *Geophys. Res. Lett.*, 40, 12, 3003-3007, doi:10.1002/grl.50558

Kumagai, H., N. Pulido, E. Fukuyama, and S. Aoi, 2013. High-frequency source radiation during the 2011 Tohoku-Oki earthquake, Japan, inferred from KiK-net strong-motion seismograms, *J. geophys. Res.*, 118, 1, 222-239, doi:10.1029/2012JB009670

Kurahashi, S. and K. Irikura, 2011. Source model for generating strong ground motions during the 2011 off the Pacific coast of Tohoku Earthquake, *Earth Planets Space*, 63, 7, 571-576, doi:10.5047/eps.2011.06.044

Kurahashi, S. and K. Irikura, 2013. Short-Period Source Model of the 2011 M_W 9.0 Off the Pacific Coast of Tohoku Earthquake, *Bull. seism. Soc. Am.*, 103, 2B, 1373-1393, doi:10.1785/0120120157

Lay, T., C. J. Ammon, H. Kanamori, L. Xue, and M. J. Kim, 2011a. Possible large near-trench slip during the 2011 M_W 9.0 off the Pacific coast of Tohoku earthquake, *Earth Planets Space*, 63, 7, 687-692, doi:10.5047/eps.2011.05.033

Lay, T., C. J. Ammon, H. Kanamori, M. J. Kim, and L. Xue, 2011b. Outer trench-slope faulting and the 2011 M_W 9.0 off the Pacific coast of Tohoku Earthquake, *Earth Planets Space*, 63, 7, 713-718, doi:10.5047/eps.2011.05.006

Lay, T., H. Kanamori, C. J. Ammon, K. D. Koper, A. R. Hutko, L. Ye, H. Yue, and T. M. Rushing, 2012. Depth-varying rupture properties of subduction zone megathrust faults, *J. geophys. Res.*, 117, B4, B04311, doi:10.1029/2011JB009133

Lay, T., Z. Duputel, L.Ye, and H. Kanamori, 2013. The December 7, 2012 Japan Trench intraplate doublet (M_W 7.2, 7.1) and interactions between near-trench intraplate thrust and normal faulting, *Phys. Earth planet. Interiors*, 220, 73-78, doi:10.1016/j.pepi.2013.04.009

Lee, S.-J., B.-S. Huang, M. Ando, H.-C. Chiu, and J.-H. Wang, 2011. Evidence of large scale repeating slip during the 2011 Tohoku-Oki earthquake, *Geophys. Res. Lett.*, 38, 19, L19306, doi:10.1029/2011GL049580

Loveless, J. P. and B. J. Meade, 2010. Geodetic imaging of plate motions, slip rates, and partitioning of deformation in Japan, *J. Geophys. Res.*, 115, B02410, doi:10.1029/2008JB006248

Loveless, J. P. and B. J. Meade, 2011. Spatial correlation of interseismic coupling and coseismic rupture extent of the 2011 $M_W = 9.0$ Tohoku-oki earthquake, *Geophys. Res. Lett.*, 38, 17, L17306, doi:10.1029/2011GL048561

MacInnes B. T., A. R. Gusman, R. J. LeVeque, and Yuichiro Tanioka, 2013. Comparison of Earthquake Source Models for the 2011 Tohoku Event Using Tsunami Simulations and Near-Field Observations, *Bulletin of the Seismological Society of America*, 103:1256-1274; doi:10.1785/0120120121

Maeda, T., T. Furumura, S. Sakai, and M. Shinohara, 2011. Significant tsunami observed at ocean-bottom pressure gauges during the 2011 off the Pacific coast of Tohoku Earthquake, *Earth Planets Space*, 63, 7, 803-808, doi:10.5047/eps.2011.06.005

Marsan, D. and B. Enescu, 2012. Modeling the foreshock sequence prior to the 2011, M_W 9.0 Tohoku, Japan, earthquake, *J. geophys. Res.*, 117, B6, B06316, doi:10.1029/2011JB009039

Matsuzawa T., N. Uchida, T. Igarashi, T. Okada, and A. Hasegawa, 2004. Repeating earthquakes and quasi-static slip on the plate boundary east off northern Honshu, Japan, *Earth Planets Space*, 56, 803-811.

Meng, L., A. Inbal, and J.-P. Ampuero, 2011. A window into the complexity of the dynamic rupture of the 2011 M_W 9 Tohoku-Oki earthquake, *Geophys. Res. Lett.*, 38, L00G07, doi:10.1029/2011GL048118

Minoura, K., Imamura, F., Sugawara, D., Kono, Y., Iwashita, T., 2001. The 869 Jogan tsunami deposit and recurrence interval of large-scale tsunami on the Pacific coast of northeast Japan, *Journal of Natural Disaster Science*, 23, 83–88.

Mitsui, Y., N. Kato, Y. Fukahata, and K. Hirahara, 2012. Megaquake cycle at the Tohoku subduction zone with thermal fluid pressurization near the surface, *Earth and Planetary Science Letters*, 325–326, 21–26.

Miyazaki, S., J. J. McGuire, and P. Segall, 2011. Seismic and aseismic fault slip before and during the 2011 off the Pacific coast of Tohoku Earthquake, *Earth Planets Space*, 63, 7, 637-642, doi:10.5047/eps.2011.07.001

Miyazawa, M., 2011. Propagation of an earthquake triggering front from the 2011 Tohoku-Oki earthquake, *Geophys. Res. Lett.*, 38, 23, L23307, doi:10.1029/2011GL049795

Miyazawa, M., 2012. Detection of seismic events triggered by P-waves from the 2011 Tohoku-Oki earthquake, *Earth Planets Space*, 64, 12, 1223-1229, doi:10.5047/eps.2012.07.003

Mori, N., Takahashi, T., Yasuda, T. and Yanagisawa, H., 2011. Survey of 2011 Tohoku earthquake tsunami inundation and run-up, *Geophys. Res. Lett.*, 38, L00G14, doi:10.1029/2011GL049210

Munekane, H., 2012. Coseismic and early postseismic slips associated with the 2011 off the Pacific coast of Tohoku Earthquake sequence: EOF analysis of GPS kinematic time series, *Earth Planets Space*, 64, 12, 1077-1091, doi:10.5047/eps.2012.07.009

Nakahara, H., Sato, H., Nishimura, T. and Fujiwara, H., 2011. Direct observation of rupture propagation during the 2011 off the Pacific coast of Tohoku Earthquake (M_W 9.0) using a small seismic array, *Earth Planets Space*, 63, 7, 589-594, doi:10.5047/eps.2011.06.002

Nakanishi, M. and E., L. Winterer, 1998. Tectonic history of the Pacific-Farallon-Phoenix triple junction from late Jurassic to early Cretaceous: An abandoned Mesozoic spreading system in the central Pacific Basin, *J. Geophys. Res.*, 103, 12453-12468.

Nanjo, K. Z., N. Hirata, K. Obara, and K. Kasahara, 2012. Decade-scale decrease in b value prior to the M9-class 2011 Tohoku and 2004 Sumatra quakes, *Geophys. Res. Lett.*, 39, 20, L20304, doi:10.1029/2012GL052997

Nettles, M., G. Ekström, and H. C. Koss, 2011. Centroid-moment-tensor analysis of the 2011 off the Pacific coast of Tohoku Earthquake and its larger foreshocks and aftershocks, *Earth Planets Space*, 63, 7, 519-523, doi:10.5047/eps.2011.06.009

Nishimura, T., T. Hirasawa, S. Miyazaki, T. Sagiya, T. Tada, S. Miura, and K. Tanaka, 2004. Temporal change of interplate coupling in northeastern Japan during 1995 – 2002 estimated from continuous GPS observations, *Geophys J. Int.*, 157, 901-916

Nishimura, T., Munekane, H. and Yarai, H., 2011. The 2011 off the Pacific coast of Tohoku Earthquake and its aftershocks observed by GEONET, *Earth Planets Space*, 63, 7, 631-636, doi:10.5047/eps.2011.06.025

Obana, K., G. Fujie, T. Takahashi, Y. Yamamoto, Y. Nakamura, S. Kodaira, N. Takahashi, Y. Kaneda, and M. Shinohara, 2012. Normal-faulting earthquakes beneath the outer slope of the Japan Trench after the 2011 Tohoku earthquake: Implications for the stress regime in the incoming Pacific plate, *Geophysical Research Letters*, 39, 7, doi:10.1029/2011gl050399

Obana K., S. Kodaira, M. Shinohara, R. Hino, K. Uehira, H. Shiobara, K. Nakahigashi, T. Yamada, H. Sugioka, A. Ito, Y. Nakamura, S. Miura, T. No, and N. Takahashi, 2013. Aftershocks near the updip end of the 2011 Tohoku-Oki earthquakes, *Earth Planet Sci Lett*, 382(0):111–116, doi:10.1016/j.epsl.2013.09.007

Obana, K., S. Kodaira, Y. Nakamura, T. Sato, G. Fujie, T. Takahashi, and Yojiro Yamamoto, 2014. Aftershocks of the December 7, 2012 intraplate doublet near the Japan Trench axis, *Planets and Space 2014*, 66:24, http://www.earth-planets-space.com/content/66/1/24

Ohta, Y., S. Miura, M. Ohzono, S. Kita, T. Iinuma, T. Demachi, K. Tachibana, T. Nakayama, S. Hirahara, S. Suzuki, T. Sato, N. Uchida, A. Hasegawa, and N. Umino, 2011. Large intraslab earthquake (2011 April 7, M 7.1) after the 2011 off the Pacific coast of Tohoku Earthquake (M 9.0): Coseismic fault model based on the dense GPS network data, *Earth Planets Space*, 63, 1207–1211

Ohta, Y., R. Hino, D. Inazu, M. Ohzono, Y. Ito, M. Mishina, T. Iinuma, J. Nakajima, Y. Osada, K. Suzuki, H. Fujimoto, K. Tachibana, T. Demachi, S. Miura, 2012. Geodetic constraints on afterslip characteristics following the March 9, 2011, Sanriku-oki earthquake, Japan, *Geophys. Res. Lett.*, 39, L16304, doi:10:1029/2012GL052430

Ohzono, M., Y. Yabe, T. Iinuma, Y. Ohta, S. Miura, K. Tachibana, T. Sato, and T. Demachi, 2012. Strain anomalies induced by the 2011 Tohoku Earthquake (M_W 9.0) as observed by a dense GPS network in northeastern Japan, *Earth Planets Space*, 64, 12, 1231-1238, doi:10.5047/eps.2012.05.015

Okada, T., T. Yaginuma, N. Umino, T. Kono, T. Matsuzawa, S. Kita and A. Hasegawa, 2005, The 2005 M7.2 MIYAGI-OKI earthquake, NE Japan: Possible rerupturing of one of asperities that caused the previous M7.4 earthquake, doi:10.1029/2005GL024613

Okada, T., K. Yoshida, S. Ueki, J. Nakajima, N. Uchida, T. Matsuzawa, N. Umino, N., and A. Hasegawa, 2011. Shallow inland earthquakes in NE Japan possibly triggered by the 2011 off the Pacific coast of Tohoku Earthquake, *Earth Planets Space*, 63, 7, 749-754, doi:10.5047/eps.2011.06.027

Okal, E. A., 2013. From 3-Hz P Waves to 0S2: No Evidence of A Slow Component to the Source of the

2011 Tohoku Earthquake, *Pure appl. Geophys.*, 170, 6-8, 963-973, doi:10.1007/s00024-012-0500-x

Ozawa, S., T. Nishimura, H, Suito, T. Kobayashi, M. Tobita, and T. Imakiire, 2011. Coseismic and postseismic slip of the 2011 magnitude-9 Tohoku-Oki earthquake, *Nature*, doi:10.1038/nature10227

Ozawa, S., T. Nishimura, H. Munekane, H. Suito, T. Kobayashi, M. Tobita, and T. Imakiire, 2012. Preceding, coseismic, and postseismic slips of the 2011 Tohoku earthquake, Japan, *J. geophys. Res.*, 117, B7, B07404, doi:10.1029/2011JB009120

Pacheco, J. F., L. R. Sykes, C. H. Scholz, 1993. Nature of seismic coupling along simple plate boundaries of the subduction type, *J. Geophys. Res.*, 98, 14133–14159, http://dx.doi.org/10.1029/93JB00349

Peterson, E. T., T. Seno, 1984. Factors affecting seismic moment release rates in subduction zones, *J. Geophys. Res.*, 89,10233–10248, http://dx.doi.org/10.1029/JB089iB12p10233

Pollitz, F. F., R. Bürgmann, and P. Banerjee, 2011. Geodetic slip model of the 2011 M9.0 Tohoku earthquake, *Geophys. Res. Lett.*, 38, L00G08, doi:10.1029/2011GL048632

Romano, F., A. Piatanesi, S. Lorito, N. D'Agostino, K. Hirata, S. Atzori, Y. Yamazaki, and M. Cocco, 2012. Clues from joint inversion of tsunami and geodetic data of the 2011 Tohoku-oki earthquake, *Sci. Rep.*, 2, 385, 1-8, doi:10.1038/srep00385

Roten, D., H. Miyake, and K. Koketsu, 2012. A Rayleigh wave back-projection method applied to the 2011 Tohoku earthquake, *Geophys. Res. Lett.*, 39, 2, L02302, doi:10.1029/2011GL050183

Ruff, L., and H. Kanamori, 1980. Seismicity and the subduction process, *Phys. Earth Planet. Inter.*, 23, 240-252.

Saito, T., Y. Ito, D. Inazu, and R. Hino, 2011. Tsunami source of the 2011 Tohoku-Oki earthquake, Japan: Inversion analysis based on dispersive tsunami simulations, *Geophys. Res. Lett.*, 38, L00G19, doi:10.1029/2011GL049089

Satake, K., Y. Fujii, T. Harada, and Y. Namegaya, 2013. Time and Space Distribution of Coseismic Slip of the 2011 Tohoku Earthquake as Inferred from Tsunami Waveform Data, *Bull. seism. Soc. Am.*, 103, 2B, 1473-1492, doi:10.1785/0120120122

Satake, K. and Y. Fujii, 2014. Source Models of the 2011 Tohoku Earthquake and Long-Term Forecast of Large Earthquakes, *J. Disaster Res.*, 9 (in press).

Sato, M., T. Ishikawa, N. Ujihara, S. Yoshida, M. Fujita, M. Mochizuki, and A. Asada, 2011. Displacement Above the Hypocenter of the 2011 Tohoku-Oki Earthquake, *Science*, 332, 6036, 1395, doi:10.1126/science.1207401

Sato, T., S. Hiratsuka, and J. Mori, 2013. Precursory Seismic Activity Surrounding the High-Slip Patches of the 2011 M_W 9.0 Tohoku-Oki Earthquake, *Bull. seism. Soc. Am.*, 106, 6, 3104-3114, doi:10.1785/0120130042

Sawai, Y., Y. Namegaya, Y. Okamura, K. Satake, and M. Shishikura, 2012. Challenges of anticipating the 2011 Tohoku earthquake and tsunami using coastal geology, *Geophys. Res. Lett.*, 39, 21, L21309, doi:10.1029/2012GL053692

Scholz, C. H., 2002. *The Mechanics of Earthquakes and Faulting*, 471 pp, Cambridge Univ. Press, Cambridge.

Seno, T., 1979. Intraplate seismicity in Tohoku and Hokkaido and large interplate earthquakes: a possibility of a large interplate earthquake off the southern Sanriku coast, northern Japan., *J. Phys. Earth*, 27, 21–51, http://dx.doi.org/10.4294/jpe1952.27.21

Shao, G., X. Li, C. Ji, and T. Maeda, 2011. Focal mechanism and slip history of the 2011 M_W 9.1 off the Pacific coast of Tohoku earthquake, constrained with teleseismic body and surface waves, *Earth Planets Space*, 63, 7, 559-564, doi:10.5047/eps.2011.06.028

Shibazaki, B., T. Matsuzawa, A. Tsutsumi, K. Ujiie, A. Hasegawa, and Y. Ito, 2011. 3D modeling of the cycle of a great Tohoku-oki earthquake, considering frictional behavior at low to high slip velocities, *Geophys. Res. Lett.*, 38, L21305, doi:10.1029/2011GL049308

Shishikura, M., Y. Sawai, Y. Okamura, J. Komatsubara, T.-T. Aung, T. Ishiyama, O. Fujiwara, and S. Fujino, S., 2007. Age and distribution of tsunami deposit in the Ishinomaki plain, northeastern Japan. *Annual Report on Active Fault and Paleoearthquake Researches*, 7, 31–46.

Shishikura, M., Y. Sawai, Y. Yukutani, and Y, Okamura, 2010. Simulation of the gigantic tsunami during Heian period — the 869 tsunami in Jogan era (in Japanese). *Active Fault and Earthquake Research Center News*, 16 August, 1–16.

Simons, M., S. E. Minson, A. Sladen, F. Ortega, J. Jiang, S.E. Owen, L. Meng, J.-P. Ampuero, S. Wei, R. Chu, D. V. Helmberger, H. Kanamori, E. Hetland, A.W. Moore, and F. H. Webb, 2011. The 2011 magnitude 9.0 Tohoku-Oki earthquake: Mosaicking the megathrust from seconds to centuries, *Science*, 332, 6036, 1421-1425, doi:10.1126/science.1206731

Strasser, M., M. Koelling, C. dos Santos Ferreira, H. G. Fink, T. Fujiwara, S. Henkel, K. Ikehara, T. Kanamatsu, K. Kawamura, S. Kodaira, M. Roemer and G. Wefer, R/V Sonne Cruise SO219A scientists, and JAMSTEC Cruise MR12-E01 scientists, 2013. A slump in the trench; tracking the impact of the 2011 Tohoku-Oki earthquake, *Geology*, 41, 935-938, doi:10.1130G34477.1

Suito, H., T. Nishimura, M. Tobita, T. Imakiire, and S. Ozawa, 2011. Interplate fault slip along the Japan Trench before the occurrence of the 2011 off the Pacific coast of Tohoku Earthquake as inferred from GPS data, *Earth Planets Space*, 63, 7, 615-619, doi:10.5047/eps.2011.06.053

Suwa, Y., S. Miura, A. Hasegawa, T. Sato and K. Tachibana, 2006, Interplate coupling beneath NE Japan inferred from three-dimensional displacement field, doi:10.1029/2004JB003203

Suzuki, W., S. Aoi, H. Sekiguchi, and T. Kunugi, 2011. Rupture process of the 2011 Tohoku-Oki mega-thrust earthquake (M9.0) inverted from strong-motion data, *Geophys. Res. Lett.*, 38, L00G16, doi:10.1029/2011GL049136

Suzuki, K., R. Hino, Y. Ito, Y. Yamamoto, S. Suzuki, H. Fujimoto, M. Shinohara, M. Abe, Y. Kawaharada, Y. Hasegawa, and Y. Kaneda, 2012. Seismicity near the hypocenter of the 2011 off the Pacific coast of Tohoku earthquake deduced by using ocean bottom seismographic data, *Earth Planets Space*, 64, 12, 1125-1135, doi:10.5047/eps.2012.04.010

Takahashi, H., 2011. Static strain and stress changes in eastern Japan due to the 2011 off the Pacific coast of Tohoku Earthquake, as derived from GPS data, *Earth Planets Space*, 63, 7, 741-744, doi:10.5047/eps.2011.06.049

Tajima, F. and B. L. N. Kennett, 2012. Interlocking of heterogeneous plate coupling and aftershock area expansion pattern for the 2011 Tohoku-Oki M_W9 earthquake, *Geophys. Res. Lett.*, 39, 5, L05307, doi:10.1029/2011GL050703

Tanaka, S., 2012. Tidal triggering of earthquakes prior to the 2011 Tohoku-Oki earthquake (M_W 9.1), *Geophys. Res. Lett.*, 39, L00G26, doi:10.1029/2012GL051179

Tanioka, Y., and K. Satake, 1996a. Tsunami generation by horizontal displacement of ocean bottom, Geophys. Res. Lett. 23, 8, 861–864.

Tanioka, Y. and K. Satake, 1996b, Fault parameters of the 1896 Sanriku Tsunami Earthquake estimated from Tsunami Numerical Modeling, *Geophys. Res. Lett.*, 23, 1549–1552.

Tanioka, Y., and T. Seno, 2001. Sediment effect on tsunami generation of the 1896 Sanriku tsunami earthquake, *Geophys. Res. Lett.*, 28, 17, 3389–3392.

Terakawa T. and M. Matsu'ura, 2010. The 3-D tectonic stress fields in and around Japan inverted from centroid moment tensor data of seismic events, *Tectonics*, doi:10.1029/2009TC002626

Terakawa, T., C. Hashimoto, and M. Matsu'ura, 2013. Changes in seismic activity following the 2011 Tohoku-oki earthquake: Effects of pore fluid pressure, *Earth planet. Sci. Lett.*, 365, 3, 17 - 24, doi:10.1016/j.epsl.2013.01.017

Toda, S., J. Lin, and R. S. Stein, 2011a. Using the 2011 M_W 9.0 off the Pacific coast of Tohoku Earthquake to test the Coulomb stress triggering hypothesis and to calculate faults brought closer to failure, *Earth Planets Space*, 63, 7, 725-730, doi:10.5047/eps.2011.05.010

Toda, S., R. S. Stein, and J. Lin, 2011b. Widespread seismicity excitation throughout central Japan following the 2011 M=9.0 Tohoku earthquake and its interpretation by Coulomb stress transfer, *Geophys. Res. Lett.*, 38, L00G03, doi:10.1029/2011GL047834

Toda, S. and R. S. Stein, 2013. The 2011 $M = 9.0$ Tohoku oki earthquake more than doubled the probability of large shocks beneath Tokyo, *Geophys. Res. Lett.*, 40, 11, 2562-2566, doi:10.1002/grl.50524

Toda, S. and H. Tsutsumi, 2013. Simultaneous reactivation of two, subparallel, inland normal faults during the M_W 6.6 11 April 2011 Iwaki earthquake triggered by the M_W 9.0 Tohoku-oki, Japan, earthquake, *Bull. Seism. Soc. Am.*, 103, 2B, 1584-1602, doi:10.1785/0120120281

Uchida, N, T. Matsuzawa, A. Hasegawa, and T. Igarashi, 2003. Interplate quasi-static slip off Sanriku, NE Japan, estimated from repeating earthquakes, *Geophys. Res. Lett.*, 30, doi:10.1029/2003GL017452

Uchida, N. and T. Matsuzawa, 2013. Pre- and postseismic slow slip surrounding the 2011 Tohoku-oki earthquake rupture, *Earth planet. Sci. Lett.*, 374, 81-91, doi:10.1016/j.epsl.2013.05.021

Uchide, T., 2013. High-speed rupture in the first 20 s of the 2011 Tohoku earthquake, Japan, *Geophys. Res. Lett.*, 40, 12, 2993-2997, doi:10.1002/grl.50634

Ueda, H., M. Ohtake, H. Sato, 2001. Afterslip of the plate interface following the 1978 Miyagi-Oki, Japan, earthquake, as revealed from geodetic measurement data, *Tectonophysics*, 338. 45-57.

Umino, N., T. Kono, T. Okada, J. Nakajima, T. Matsuzawa, N. Uchida, A. Hasegawa, Y. Tamura, and G. Aoki, 2006, Revisiting the three M 7 Miyagi-oki earthquakes in the 1930s: possible seismogenic slip on asperities that were re-ruptured during the 1978 M=7.4 Miyagi-oki earthquake, *Earth Planets Space*, 58, 587-1592.

Wang, D. and J. Mori, 2011a. Rupture process of the 2011 off the Pacific coast of Tohoku Earthquake (M_W 9.0) as imaged with back-projection of teleseismic P-waves, *Earth Planets Space*, 63, 7, 603-607, doi:10.5047/eps.2011.05.029

Wang, D. and J. Mori, 2011b. Frequency-dependent energy radiation and fault coupling for the 2010 M_W8.8 Maule, Chile, and 2011 M_W9.0 Tohoku, Japan, earthquakes, *Geophys. Res. Lett.*, 38, 22, L22308, doi:10.1029/2011GL049652

Wang, K., Y. Hu, J. He, 2012, Deformation cycles of subduction earthquakes in a viscoelastic Earth, *Nature*, 484, 327–332.

Yagi, Y. and Y. Fukahata, 2011. Rupture process of the 2011 Tohoku-oki earthquake and absolute elastic strain release, *Geophys. Res. Lett.*, 38, 19, L19307, doi:10.1029/2011GL048701

Yamanaka, Y. and M. Kikuchi, 2004, Asperity map along the subduction zone in northeastern Japan inferred from regional seismic data, *J. Geophys. Res.*, 109, B07307, doi:10.1029/2003JB002683

Yao, H., P. M. Shearer, and P. Gerstoft, 2012. Subevent location and rupture imaging using iterative backprojection for the 2011 Tohoku M_W 9.0 earthquake, *Geophys. J. Int.*, 190, 2, 1152-1168, doi:10.1111/j.1365-246X.2012.05541.x

Ye, L., T. Lay, and H. Kanamori, 2013. Ground Shaking and Seismic Source Spectra for Large Earthquakes around the Megathrust Fault Offshore of Northeastern Honshu, Japan, *Bull. seism. Soc. Am.*, 103, 2B, 1221-1241, doi:10.1785/0120120115

Yokota, Y., K. Koketsu, Y. Fujii, K. Satake, S. Sakai, M. Shinohara, and T. Kanazawa, 2011. Joint inversion of strong motion, teleseismic, geodetic, and tsunami datasets for the rupture process of the 2011 Tohoku earthquake, *Geophys. Res. Lett.*, 38, L00G21, doi:10.1029/2011GL050098

Yoshida, K., K. Miyakoshi, and K. Irikura, 2011. Source process of the 2011 off the Pacific coast of Tohoku Earthquake inferred from waveform inversion with long-period strong-motion records, *Earth Planets Space*, 63, 577-582.

Yoshida, Y., H. Ueno, D. Muto, and S. Aoki, 2011. Source process of the 2011 off the Pacific coast of Tohoku Earthquake with the combination of teleseismic and strong motion data, *Earth Planets Space*, 63, 7, 565-569, doi:10.5047/eps.2011.05.011

Yoshida, K., A. Hasegawa, T. Okada, T., Iinuma, Y. Ito, and Y. Asano, 2012. Stress before and after the 2011 great Tohoku-oki earthquake and induced earthquakes in inland areas of eastern Japan, *Geophys. Res. Lett.*, 39, 3, L03302, doi:10.1029/2011GL049729

Yue, H. and T. Lay, 2011. Inversion of high-rate (1 sps) GPS data for rupture process of the 11 March 2011 Tohoku earthquake (M_W 9.1), *Geophys. Res. Lett.*, 38, L00G09, doi:10.1029/2011GL048700

Yue, H. and T. Lay, 2013. Source Rupture Models for the M_W 9.0 2011 Tohoku Earthquake from Joint Inversions of High-Rate Geodetic and Seismic Data, *Bull. seism. Soc. Am.*, 103, 1242-1255, doi:10.1785/0120120119

Yukutake, Y., R. Honda, M. Harada, T. Aketagawa, H. Ito, and A. Yoshida, 2011. Remotely-triggered seismicity in the Hakone volcano following the 2011 off the Pacific coast of Tohoku Earthquake, *Earth Planets Space*, 63, 737-740.

Zhang, H., Z. Ge, and L. Ding, 2011. Three sub-events composing the 2011 off the Pacific coast of Tohoku Earthquake (M_W 9.0) inferred from rupture imaging by back-projecting teleseismic P waves, *Earth Planets Space*, 63, 7, 595-598, doi:10.5047/eps.2011.06.021

9

Statistics of Collected Data

9.1 Introduction

The ISC Bulletin is based on the parametric data reports received from seismological agencies around the world. With rare exceptions, these reports include the results of waveform review done by analysts at network data centres and observatories. These reports include combinations of various bulletin elements such as event hypocentre estimates, moment tensors, magnitudes, event type and felt and damaging data as well as observations of the various seismic waves recorded at seismic stations.

Data reports are received in different formats that are often agency specific. Once an authorship is recognised, the data are automatically parsed into the ISC database and the original reports filed away to be accessed when necessary. Any reports not recognised or processed automatically are manually checked, corrected and re-processed. This chapter describes the data that are received at the ISC before the production of the reviewed Bulletin.

Notably, the ISC integrates all newly received data reports into the automatic ISC Bulletin (available on-line) soon after these reports are made available to ISC, provided it is done before the submission deadline that currently stands at 12 months following an event occurrence.

With data constantly being reported to the ISC, even after the ISC has published its review, the total data shown as collected, in this chapter, is limited to two years after the time of the associated reading or event, i.e. any hypocentre data collected two years after the event are not reflected in the figures below.

9.2 Summary of Agency Reports to the ISC

A total of 131 agencies have reported data for January 2011 to June 2011. The parsing of these reports into the ISC database is summarised in Table 9.1.

Table 9.1: *Summary of the parsing of reports received by the ISC from a total of 131 agencies, containing data for this summary period.*

	Number of reports
Total collected	2646
Automatically parsed	2015
Manually parsed	631

Data collected by the ISC consists of multiple data types. These are typically one of:

- Bulletin, hypocentres with associated phase arrival observations.
- Catalogue, hypocentres only.
- Unassociated phase arrival observations.

In Table 9.2, the number of different data types reported to the ISC by each agency is listed. The number of each data type reported by each agency is also listed. Agencies reporting indirectly have their data type additionally listed for the agency that reported it. The agencies reporting indirectly may also have 'hypocentres with associated phases' but with no associated phases listed - this is because the association is being made by the agency reporting directly to the ISC. Summary maps of the agencies and the types of data reported are shown in Figure 9.1 and Figure 9.2.

Table 9.2: *Agencies reporting to the ISC for this summary period. Entries in bold are for new or renewed reporting by agencies since the previous six-month period.*

Agency	Country	Directly or indirectly reporting (D/I)	Hypocentres with associated phases	Hypocentres without associated phases	Associated phases	Unassociated phases	Amplitudes
TIR	Albania	D	127	99	236	8	0
CRAAG	Algeria	D	668	251	3426	591	0
LPA	Argentina	D	0	0	0	360	9
SJA	Argentina	D	3907	40	53817	114	7193
NSSP	Armenia	D	78	96	504	0	0
AUST	Australia	D	702	1	13421	0	0
IDC	Austria	D	27482	0	577233	0	528640
VIE	Austria	D	2639	696	19823	0	17219
AZER	Azerbaijan	D	147	132	4072	0	2
BELR	Belarus	D	0	0	0	5169	1245
UCC	Belgium	D	0	44	0	5799	1603
SCB	**Bolivia**	**D**	**225**	**0**	**1019**	**0**	**0**
SAR	**Bosnia and Herzegovina**	**I CSEM**	**0**	**339**	**0**	**0**	**0**
VAO	Brazil	D	0	0	0	259	0
SOF	Bulgaria	D	148	0	1153	3895	0
OTT	Canada	D	1278	38	33419	0	4124
PGC	Canada	I OTT	833	0	18586	0	0
GUC	Chile	D	2914	61	44607	586	11081
BJI	China	D	2954	41	210937	44177	124167
ASIES	Chinese Taipei	D	0	62	0	0	0
TAP	Chinese Taipei	D	11377	4	250617	0	0
RSNC	Colombia	D	5434	6	82948	8613	23474
CASC	Costa Rica	D	499	27	10822	0	419
HDC	Costa Rica	I NEIC	0	3	0	0	0
UCR	Costa Rica	I CASC	1	7	0	0	0
ZAG	Croatia	D	0	0	0	11553	0
SSNC	Cuba	D	1	0	23	0	14
NIC	Cyprus	D	201	163	1448	801	0
IPEC	Czech Republic	I CSEM	0	506	0	0	0
PRU	Czech Republic	D	5977	1746	53333	761	10877
WBNET	Czech Republic	D	333	0	6113	0	6019
DNK	Denmark	D	0	193	0	8994	4044
ARO	Djibouti	D	80	0	779	0	0
IGQ	Ecuador	D	28	5	973	0	0
HLW	Egypt	D	337	158	3082	0	372
SNET	El Salvador	I NEIC	1	6	0	0	0
SSS	El Salvador	I CASC	0	5	0	0	0
EST	Estonia	I HEL	435	38	0	0	0
AAE	Ethiopia	D	0	0	0	749	0
SKO	FYR Macedonia	D	712	369	3703	3165	1875
FIA0	Finland	I HEL	77	15	0	0	0

Table 9.2: *(continued)*

Agency	Country	Directly or indirectly reporting (D/I)	Hypocentres with associated phases	Hypocentres without associated phases	Associated phases	Unassociated phases	Amplitudes
HEL	Finland	D	6481	5940	104850	17	13434
CSEM	France	D	45043	65838	905842	0	170642
LDG	France	D	1411	1408	28158	0	12051
STR	France	D	924	319	10290	264	0
PPT	French Polynesia	D	1588	1	11743	463	12177
TIF	Georgia	D	0	1528	0	17489	0
AWI	Germany	D	1465	1	4491	1510	0
BGR	Germany	D	114	312	4461	0	211
BNS	Germany	I BGR	3	44	0	0	0
BRG	Germany	D	0	0	0	6808	5580
BUG	Germany	I BGR	17	1	0	0	0
CLL	Germany	D	0	0	0	13291	5194
GDNRW	Germany	I BGR	0	27	0	0	0
GFZ	Germany	I INMG	7	0	0	0	0
LEDBW	Germany	I BGR	24	4	0	0	0
ATH	Greece	D	8062	7946	226710	0	69837
THE	Greece	D	3933	3954	92132	13894	26944
UPSL	Greece	I CSEM	0	297	0	0	0
GCG	Guatemala	I NEIC	0	1	0	0	0
HKC	Hong Kong	D	0	0	0	190	0
BUD	Hungary	D	0	44	0	5427	0
REY	Iceland	D	42	35	1284	0	0
HYB	India	D	1534	0	11765	15	3606
NDI	India	D	536	379	13780	7438	4791
DJA	Indonesia	D	3134	32	70986	0	74176
TEH	Iran	D	1326	1268	27947	0	13915
THR	Iran	D	198	524	1954	0	828
ISN	Iraq	D	225	87	1299	0	5
DIAS	Ireland	D	0	0	0	177	0
GII	Israel	D	147	127	3115	0	0
GEN	Italy	I CSEM	0	584	0	0	0
ROM	Italy	D	8989	6872	118850	0	50234
TRI	Italy	D	0	0	0	5883	0
LIC	Ivory Coast	D	630	0	1890	0	1140
JSN	Jamaica	D	98	0	641	10	0
JMA	Japan	D	122391	17	869948	676	0
MAT	Japan	D	0	0	0	48701	0
NIED	Japan	D	0	4569	0	0	0
SYO	Japan	D	0	0	0	3609	0
JSO	Jordan	D	22	33	192	0	0
NNC	Kazakhstan	D	7683	112	61290	0	53594
SOME	**Kazakhstan**	**D**	**3089**	**141**	**55947**	**0**	**0**
SIK	Kosovo	I CSEM	0	96	0	0	0
KNET	Kyrgyzstan	D	558	0	4782	0	1160
KRNET	Kyrgyzstan	D	2163	0	33359	0	0
LVSN	**Latvia**	**I CSEM**	**0**	**463**	**0**	**0**	**0**
GRAL	Lebanon	D	318	296	2158	619	0
LIB	Libya	I CSEM	0	44	0	0	0
LIT	Lithuania	D	324	370	2437	624	1454
MCO	**Macao, China**	**D**	**0**	**0**	**0**	**132**	**0**
KLM	Malaysia	D	483	0	3598	0	0
ECX	Mexico	D	1193	5	20255	0	2958
MEX	Mexico	D	2157	244	17532	0	0
MOLD	Moldova	D	0	0	0	2352	881
OBM	Mongolia	D	35	0	1355	0	445
PDG	Montenegro	D	571	384	11392	0	6648
CNRM	Morocco	I CSEM	0	108	0	0	0
NAM	**Namibia**	**D**	**4**	**0**	**22**	**8**	**0**
DMN	Nepal	D	2835	0	23267	0	18488
DBN	Netherlands	D	0	0	0	2290	854
WEL	New Zealand	D	8101	6	231826	7496	75982
INET	Nicaragua	I CASC	0	6	0	0	0

Table 9.2: *(continued)*

Agency	Country	Directly or indirectly reporting (D/I)	Hypocentres with associated phases	Hypocentres without associated phases	Associated phases	Unassociated phases	Amplitudes
BER	Norway	D	2241	1941	29227	1109	7052
NAO	Norway	D	5563	1460	8909	0	4640
OMAN	Oman	D	1098	132	11192	0	0
MSSP	Pakistan	D	0	0	0	654	0
UPA	**Panama**	**I CASC**	**0**	**8**	**0**	**0**	**0**
ARE	Peru	I NEIC	0	6	0	0	0
LIM	Peru	I IRIS	1	0	0	0	0
MAN	Philippines	D	0	1056	0	19407	5955
QCP	Philippines	D	0	0	0	157	0
WAR	Poland	D	0	377	0	15882	235
IGIL	Portugal	D	666	0	3219	0	1049
INMG	Portugal	D	1394	874	43484	2132	14294
PDA	Portugal	I CSEM	430	410	0	0	0
SVSA	Portugal	D	508	0	8540	1854	3366
KMA	Republic of Korea	D	29	0	396	0	0
BUC	Romania	D	686	70	9832	54675	0
ASRS	Russia	D	14	0	164	0	0
BYKL	Russia	D	180	1	12539	0	4480
KOLA	Russia	D	92	0	337	0	0
KRSC	Russia	D	613	0	17762	0	0
MOS	Russia	D	3690	246	695094	0	280151
NERS	Russia	D	35	1	820	0	340
SKHL	Russia	D	500	501	16746	0	7535
YARS	Russia	D	1341	1193	30867	12	12531
SGS	Saudi Arabia	D	2801	2392	35862	0	0
BEO	Serbia	D	1839	1478	24981	91	0
BRA	Slovakia	D	0	0	0	24632	0
LJU	Slovenia	D	1033	1076	13368	6587	4274
HNR	Solomon Islands	D	0	0	0	1540	0
PRE	South Africa	D	1279	0	18221	15	6111
MDD	Spain	D	2692	5499	77330	0	60666
MRB	Spain	I CSEM	0	13	0	0	0
SFS	Spain	I CSEM	0	225	0	0	0
UPP	Sweden	D	552	3799	5875	0	0
ZUR	Switzerland	D	308	325	3781	0	3137
NSSC	Syria	D	1589	954	30373	76	12543
BKK	Thailand	D	2395	24	27057	0	33125
TRN	Trinidad and Tobago	D	3	706	0	18750	0
TUN	Tunisia	I CSEM	0	17	0	0	0
DDA	Turkey	D	13114	9088	138467	16050	0
ISK	Turkey	D	12	14857	0	115288	0
AEIC	U.S.A.	I VIE	58	53	0	0	0
ANF	U.S.A.	I IRIS	1264	1085	0	0	0
BRK	U.S.A.	I NEIC	0	0	0	0	0
BUT	U.S.A.	I IRIS	5	3	0	0	0
CERI	U.S.A.	I IRIS	375	148	0	0	0
GCMT	U.S.A.	D	0	4383	0	0	0
HON	U.S.A.	I NEIC	0	20	0	0	0
HVO	U.S.A.	I NEIC	0	1	0	0	0
IASPEI	U.S.A.	D	0	0	0	93	18
IRIS	U.S.A.	D	3761	4150	383751	0	0
NCEDC	U.S.A.	I IRIS	125	79	0	0	0
NEIC	U.S.A.	D	21861	6475	980198	0	381829
OGSO	**U.S.A.**	**I IRIS**	**1**	**0**	**0**	**0**	**0**
PAS	U.S.A.	I IRIS	86	117	0	0	0
PMR	U.S.A.	I NEIC	0	54	0	0	0
PNSN	U.S.A.	D	44	160	0	0	0
REN	U.S.A.	I IRIS	144	65	0	0	0
RSPR	U.S.A.	D	905	2	11174	0	0
SCEDC	U.S.A.	I IRIS	142	120	0	0	0
SEA	U.S.A.	I IRIS	18	48	0	0	0

Table 9.2: *(continued)*

Agency	Country	Directly or indirectly reporting (D/I)	Hypocentres with associated phases	Hypocentres without associated phases	Associated phases	Unassociated phases	Amplitudes
SIO	U.S.A.	D	770	0	1923	0	1922
SLC	U.S.A.	I IRIS	3	3	0	0	0
SLM	U.S.A.	I NEIC	0	0	0	0	0
TUL	U.S.A.	I IRIS	36	0	0	0	0
TVA	**U.S.A.**	**I NEIC**	**0**	**1**	**0**	**0**	**0**
UUSS	**U.S.A.**	**I IRIS**	**0**	**3**	**0**	**0**	**0**
WES	U.S.A.	I NEIC	0	2	0	0	0
SIGU	Ukraine	D	82	82	2494	0	256
DSN	United Arab Emirates	D	552	170	3020	0	0
BGS	United Kingdom	D	254	154	9319	0	3142
EMSC	**Unknown**	**I HYB**	**1**	**0**	**0**	**0**	**0**
CAR	Venezuela	I NEIC	0	4	0	0	0
FUNV	Venezuela	D	1194	0	16723	0	0
PLV	Vietnam	D	30	1	598	0	173
DHMR	Yemen	D	813	45	8269	3091	2404
LSZ	**Zambia**	**D**	**17**	**0**	**78**	**25**	**0**
BUL	Zimbabwe	D	456	0	2401	489	0

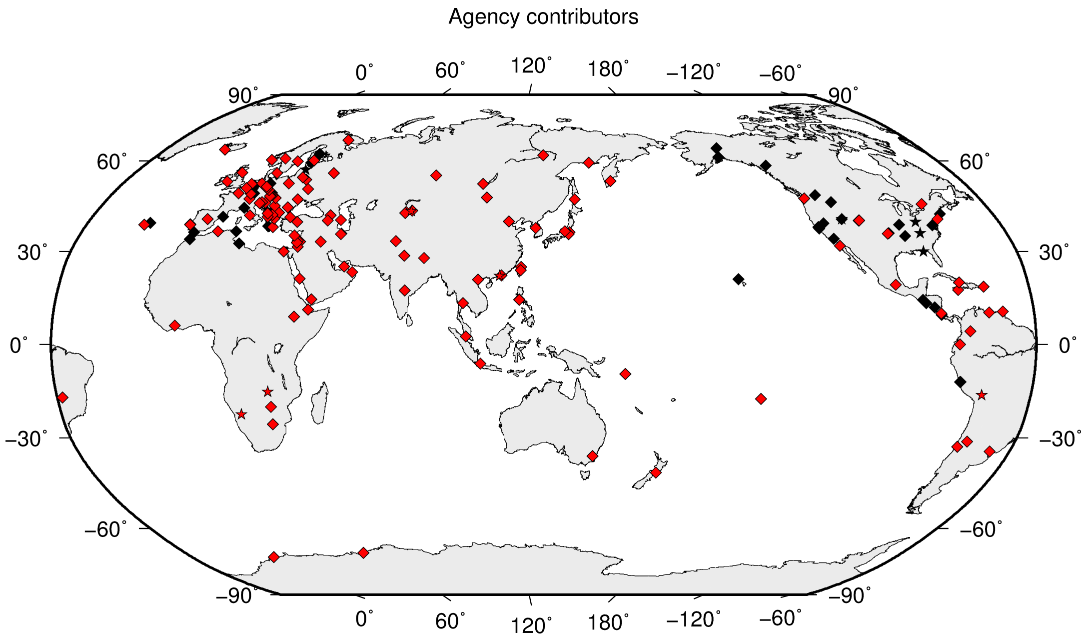

Figure 9.1: *Map of agencies that have contributed data to the ISC for this summary period. Agencies that have reported directly to the ISC are shown in red. Those that have reported indirectly (via another agency) are shown in black. Any new or renewed agencies, since the last six-month period, are shown by a star. Each agency is listed in Table 9.2.*

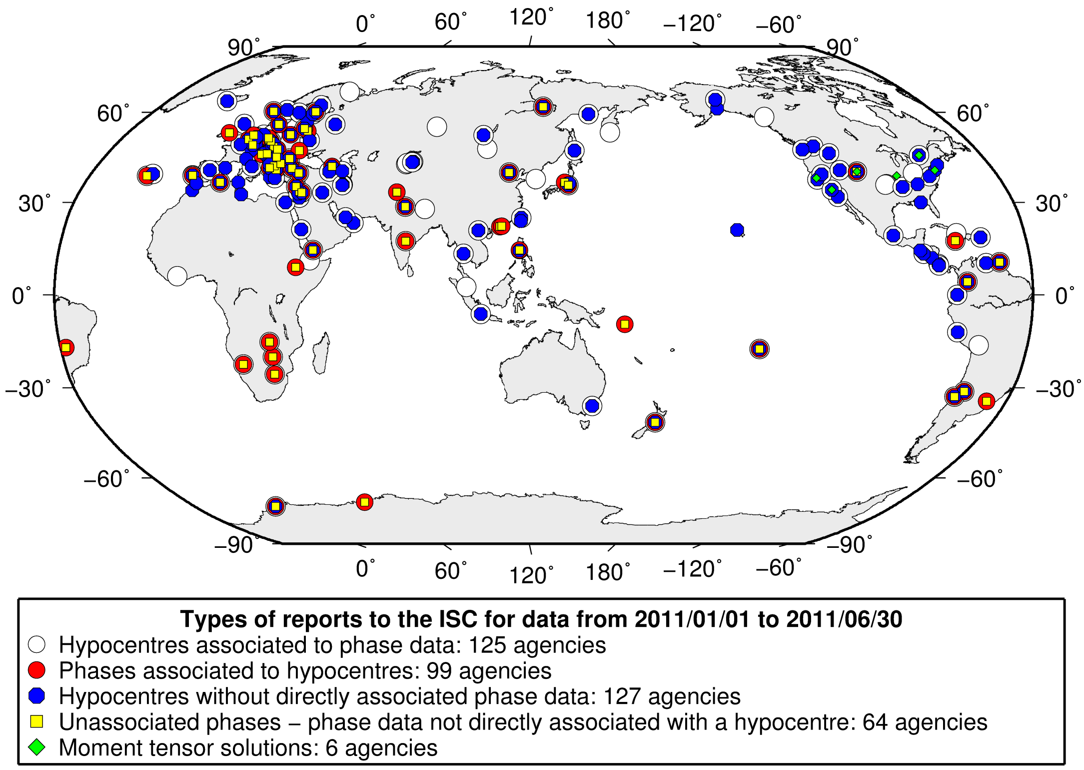

Figure 9.2: *Map of the different data types reported by agencies to the ISC. A full list of the data types reported by each agency is shown in Table 9.2.*

9.3 Arrival Observations

The collection of phase arrival observations at the ISC has increased dramatically with time. The increase in reported phase arrival observations is shown in Figure 9.3.

The reports with phase data are summarised in Table 9.3. This table is split into three sections, providing information on the reports themselves, the phase data, and the stations reporting the phase data. A map of the stations contributing these phase data is shown in Figure 9.4.

The ISC encourages the reporting of phase arrival times together with amplitude and period measurements whenever feasible. Figure 9.5 shows the percentage of events reported by each station was accompanied with amplitude and period measurements.

Figure 9.6 indicates the number of amplitude and period measurement for each station.

Together with the increase in the number of phases (Figure 9.3), there has been an increase in the number of stations reported to the ISC. The increase in the number of stations is shown in Figure 9.7. This increase can also be seen on the maps for stations reported each decade in Figure 9.8.

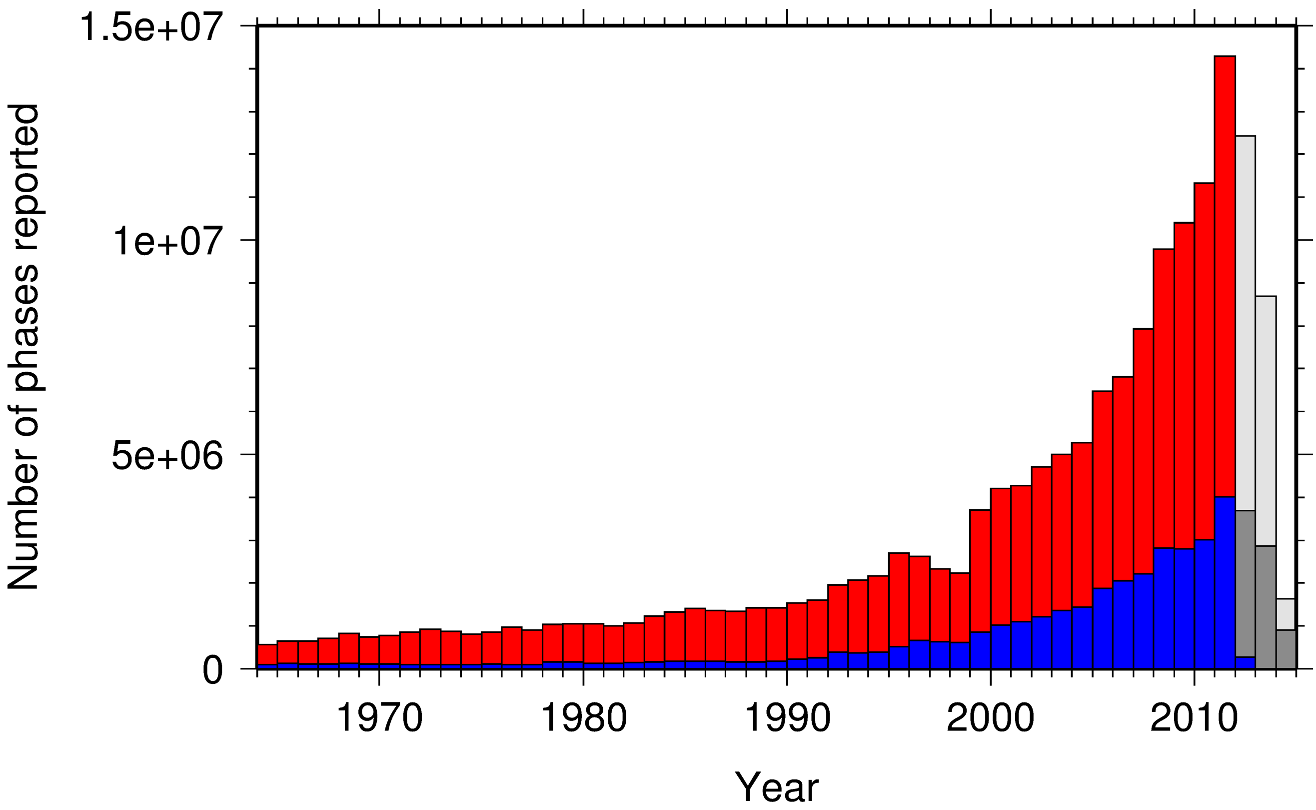

Figure 9.3: *Histogram showing the number of phases (red) and number of amplitudes (blue) collected by the ISC for events each year since 1964. The data in grey covers the current period where data are still being collected before the ISC review takes place and is accurate at the time of publication.*

Table 9.3: *Summary of reports containing phase arrival observations.*

Reports with phase arrivals	2068
Reports with phase arrivals including amplitudes	630
Reports with only phase arrivals (no hypocentres reported)	236
Total phase arrivals received	7560940
Total phase arrival-times received	7084501
Number of duplicate phase arrival-times	1426780 (20.1%)
Number of amplitudes received	2266088
Stations reporting phase arrivals	6513
Stations reporting phase arrivals with amplitude data	2743
Max number of stations per report	2154

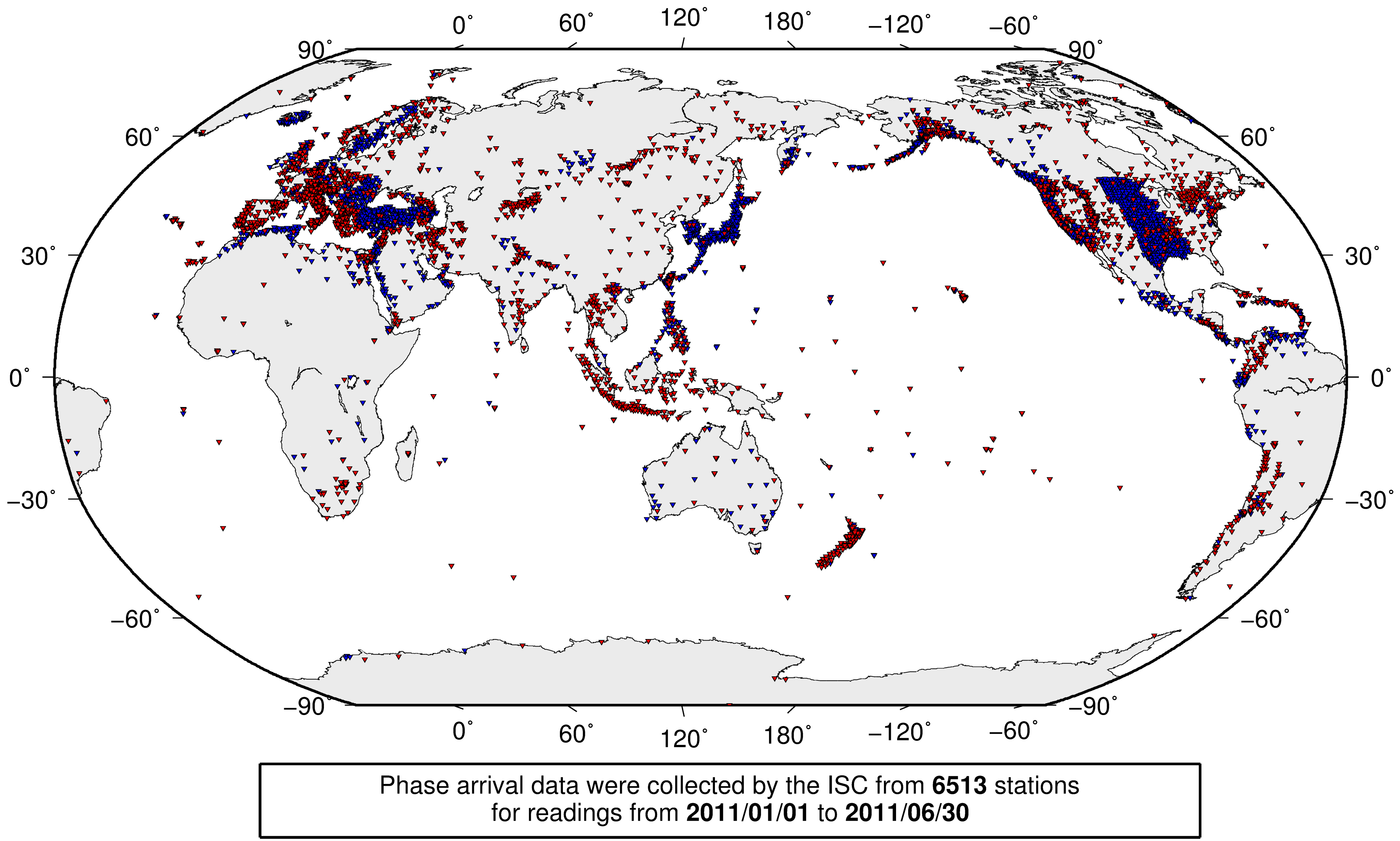

Figure 9.4: *Stations contributing phase data to the ISC for readings from January 2011 to the end of June 2011. Stations in blue provided phase arrival times only; stations in red provided both phase arrival times and amplitude data.*

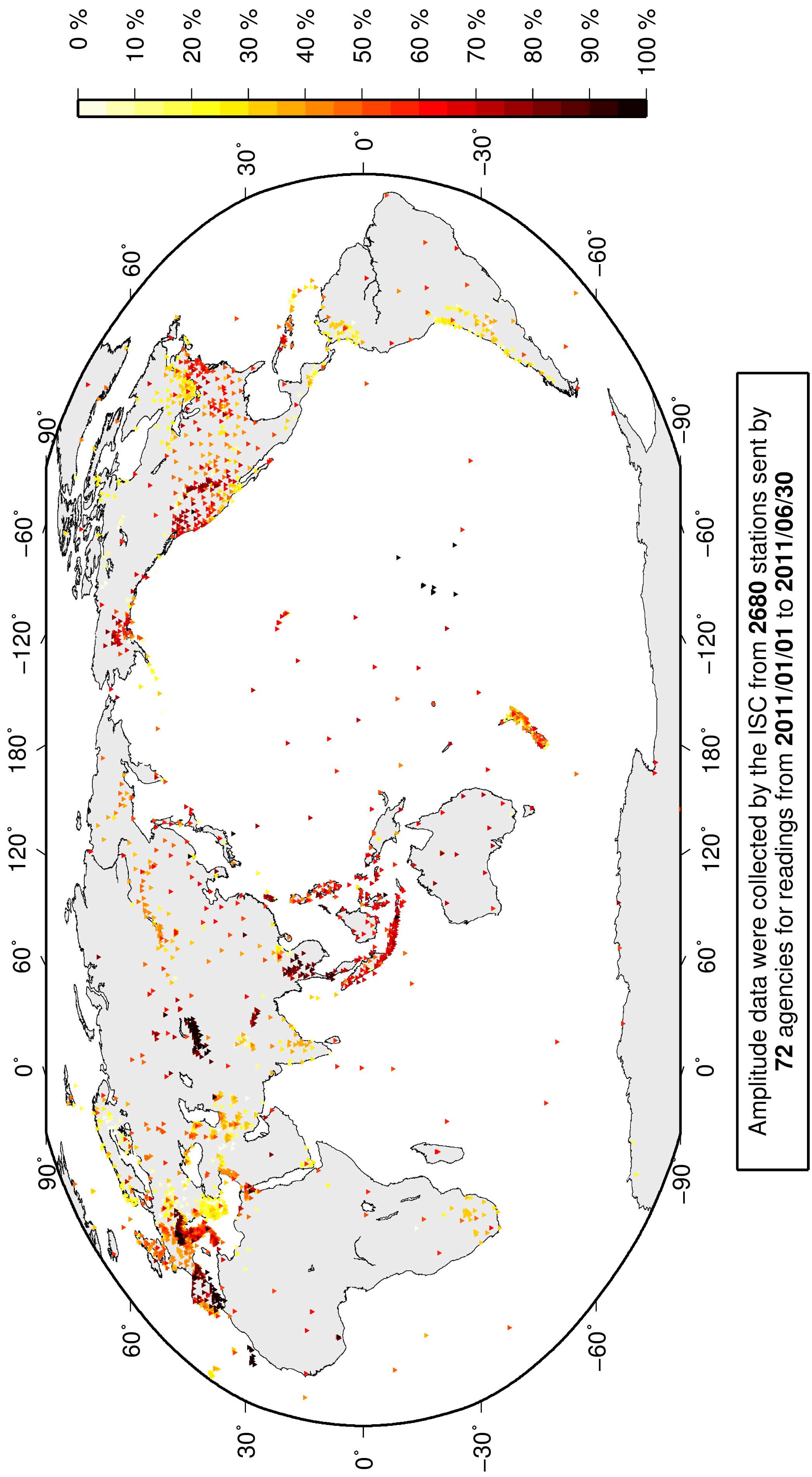

Figure 9.5: *Percentage of events for which phase arrival times from each station are accompanied with amplitude and period measurements.*

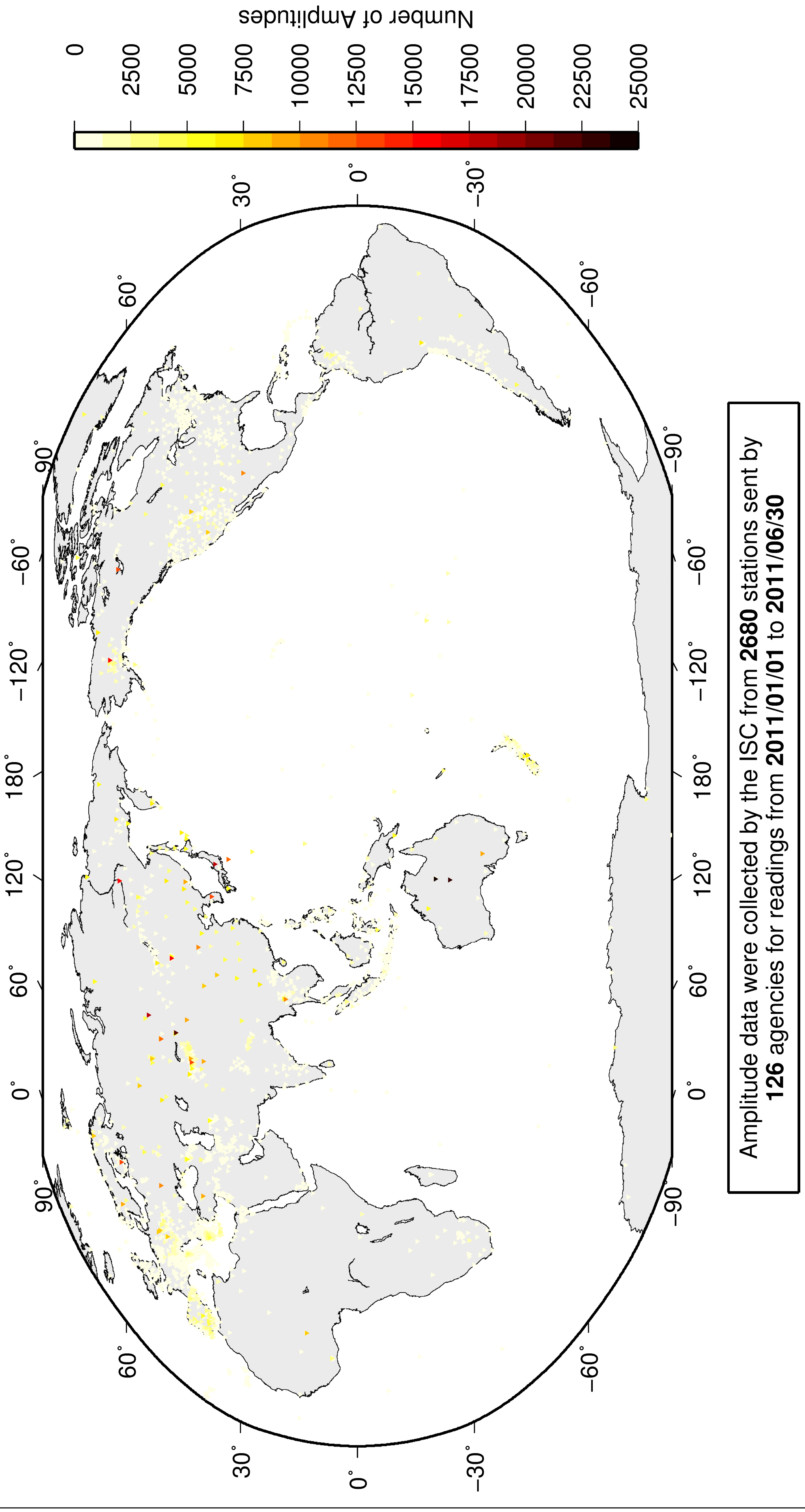

Figure 9.6: *Number of amplitude and period measurements for each station.*

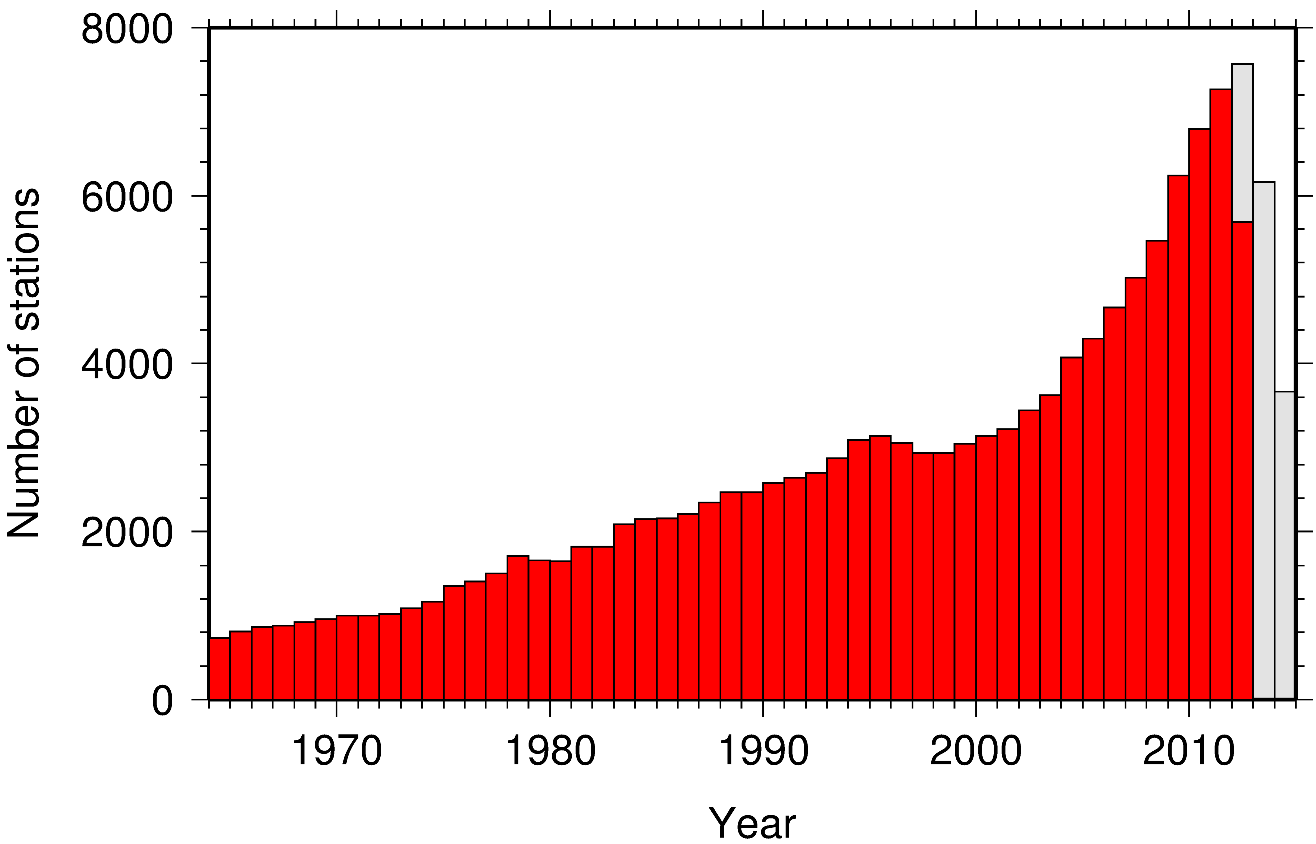

Figure 9.7: *Histogram showing the number of stations reporting to the ISC each year since 1964. The data in grey covers the current period where station information is still being collected before the ISC review of events takes place and is accurate at the time of publication.*

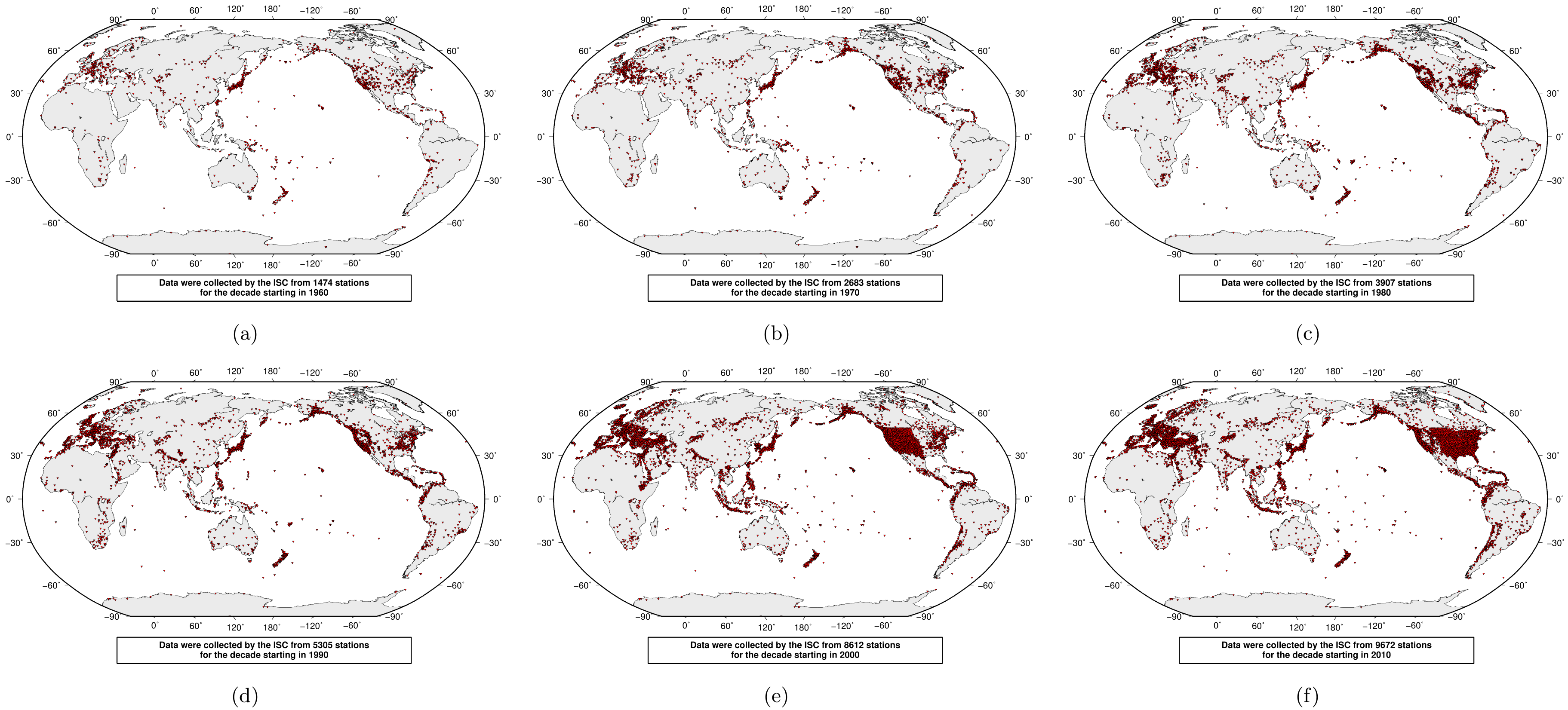

Figure 9.8: *Maps showing the stations reported to the ISC for each decade since 1960. Note that the last map covers a shorter time period.*

9.4 Hypocentres Collected

The ISC Bulletin groups multiple estimates of hypocentres into individual events, with an appropriate prime hypocentre solution selected. The collection of these hypocentre estimates are described in this section.

The reports containing hypocentres are summarised in Table 9.4. The number of hypocentres collected by the ISC has also increased significantly since 1964, as shown in Figure 9.9. A map of all hypocentres reported to the ISC for this summary period is shown in Figure 9.10. Where a network magnitude was reported with the hypocentre, this is also shown on the map, with preference given to reported values, first of M_W followed by M_S, m_b and M_L respectively (where more than one network magnitude was reported).

Table 9.4: *Summary of the reports containing hypocentres.*

Reports with hypocentres	2410
Reports of hypocentres only (no phase readings)	578
Total hypocentres received	471376
Number of duplicate hypocentres	91182 (19.3%)
Agencies determining hypocentres	158

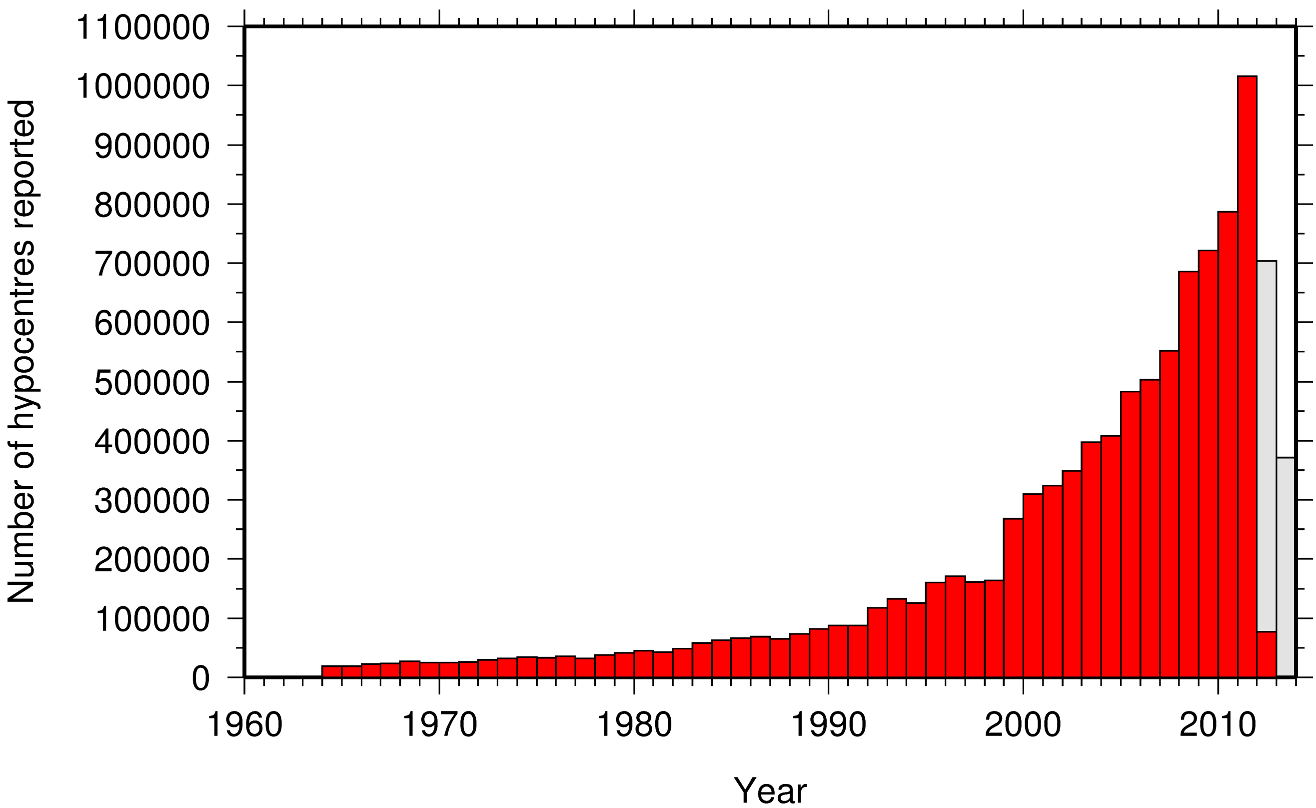

Figure 9.9: *Histogram showing the number of hypocentres collected by the ISC for events each year since 1964. For each event, multiple hypocentres may be reported.*

All the hypocentres that are reported to the ISC are automatically grouped into events, which form the basis of the ISC Bulletin. For this time period 403422 hypocentres (including ISC) were grouped into 192375 events, the largest of these having 81 hypocentres in one event. The total number of events

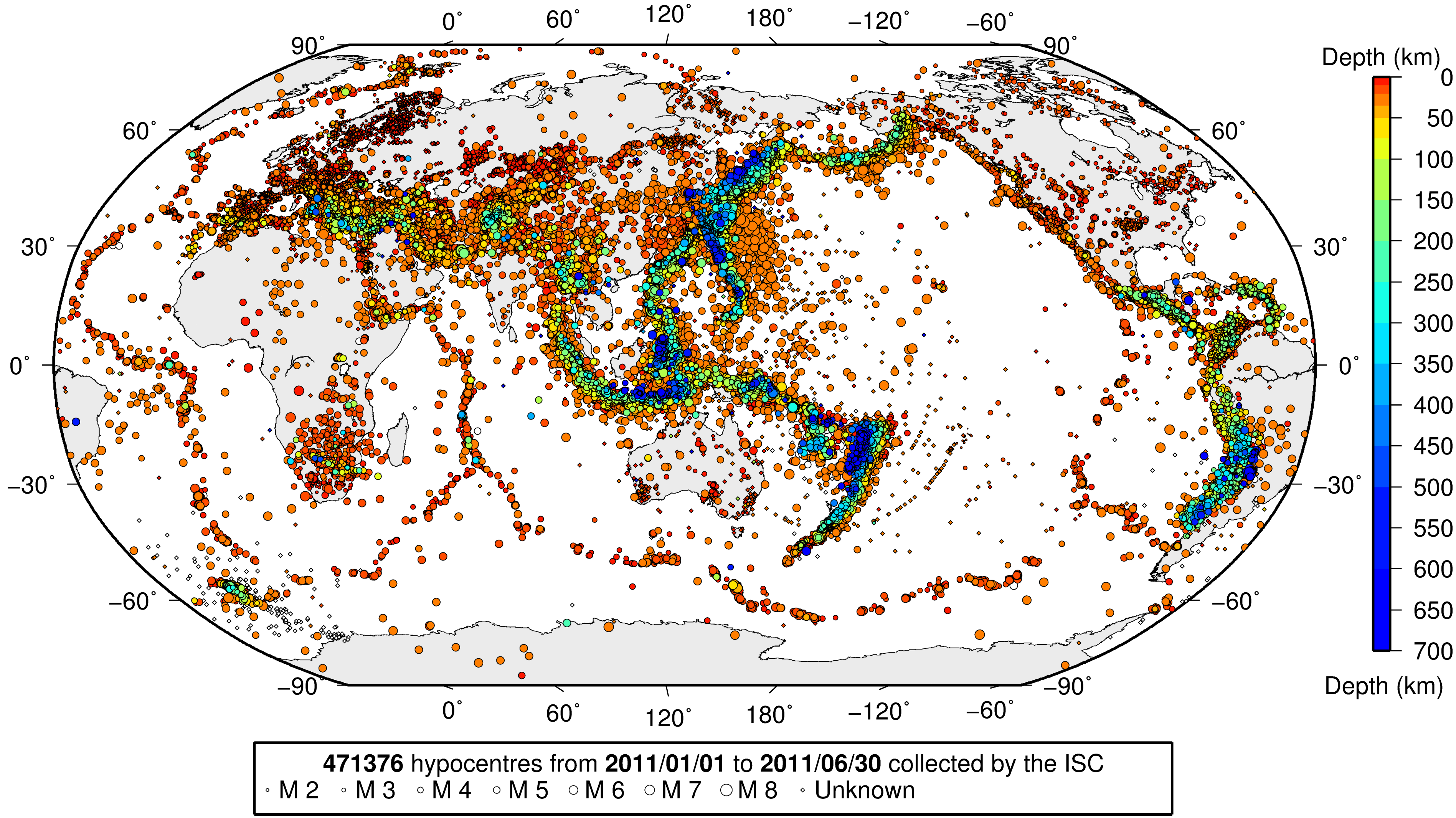

Figure 9.10: *Map of all hypocentres collected by the ISC. The scatter shows the large variation of the multiple hypocentres that are reported for each event. The magnitude corresponds with the reported network magnitude. If more than one network magnitude type was reported, preference was given to values of* M_W*,* M_S*,* m_b *and* M_L *respectively. Compare with Figure 10.2*

shown here is the result of an automatic grouping algorithm, and will differ from the total events in the published ISC Bulletin, where both the number of events and the number of hypocentre estimates will have changed due to further analysis. The process of grouping is detailed in Section 3.3.1. Figure 10.2 on page 159 shows a map of all prime hypocentres.

9.5 Collection of Network Magnitude Data

Data contributing agencies normally report earthquake hypocentre solutions along with magnitude estimates. For each seismic event, each agency may report one or more magnitudes of the same or different types. This stems from variability in observational practices at regional, national and global level in computing magnitudes based on a multitude of wave types. Differences in the amplitude measurement algorithm, seismogram component(s) used, frequency range, station distance range as well as the instrument type contribute to the diversity of magnitude types. Table 9.5 provides an overview of the complexity of reported network magnitudes reported for seismic events during the current period.

Table 9.5: *Statistics of magnitude reports to the ISC; M – average magnitude of estimates reported for each event.*

	$M < 3.0$	$3.0 \leq M < 5.0$	$M \geq 5.0$
Number of seismic events	190445	50064	818
Average number of magnitude estimates per event	1.7	5.0	24.1
Average number of magnitudes (by the same agency) per event	1.3	2.7	3.8
Average number of magnitude types per event	1.1	4.2	10.0
Number of magnitude types	19	27	27

Table 9.6 gives the basic description, main features and scientific paper references for the most commonly reported magnitude types.

Table 9.6: *Description of the most common magnitude types reported to the ISC.*

Magnitude type	Description	References	Comments
M	Unspecified		Often used in real or near-real time magnitude estimations
mB	Medium-period and Broad-band body-wave magnitude	*Gutenberg* (1945a); *Gutenberg* (1945b); *IASPEI* (2005); *IASPEI* (2013); *Bormann et al.* (2009); *Bormann and Dewey* (2012)	
mb	Short-period body-wave magnitude	*IASPEI* (2005); *IASPEI* (2013); *Bormann et al.* (2009); *Bormann and Dewey* (2012)	Classical mb based on stations between 21°-100° distance

Table 9.6: *continued*

Magnitude type	Description	References	Comments
mb1	Short-period body-wave magnitude	*IDC* (1999) and references therein	Reported only by the IDC; also includes stations at distances less than 21°
mb1mx	Maximum likelihood short-period body-wave magnitude	*Ringdal* (1976); *IDC* (1999) and references therein	Reported only by the IDC
mbtmp	short-period body-wave magnitude with depth fixed at the surface	*IDC* (1999) and references therein	Reported only by the IDC
mbLg	Lg-wave magnitude	*Nuttli* (1973); *IASPEI* (2005); *IASPEI* (2013); *Bormann and Dewey* (2012)	Also reported as MN
Mc	Coda magnitude		
MD (Md)	Duration magnitude	*Bisztricsany* (1958); *Lee et al.* (1972)	
ME (Me)	Energy magnitude	*Choy and Boatwright* (1995)	Reported only by NEIC
MJMA	JMA magnitude	*Tsuboi* (1954)	Reported only by JMA
ML (Ml)	Local (Richter) magnitude	*Richter* (1935); *Hutton and Boore* (1987); *IASPEI* (2005); *IASPEI* (2013)	
MLSn	Local magnitude calculated for Sn phases	*Balfour et al.* (2008)	Reported by PGC only for earthquakes west of the Cascadia subduction zone
MLv	Local (Richter) magnitude computed from the vertical component		Reported only by DJA and BKK
MN (Mn)	Lg-wave magnitude	*Nuttli* (1973); *IASPEI* (2005)	Also reported as mbLg
MS (Ms)	Surface-wave magnitude	*Gutenberg* (1945c); *Vaněk et al.* (1962); *IASPEI* (2005)	Classical surface-wave magnitude computed from station between 20°-160° distance
Ms1	Surface-wave magnitude	*IDC* (1999) and references therein	Reported only by the IDC; also includes stations at distances less than 20°
ms1mx	Maximum likelihood surface-wave magnitude	*Ringdal* (1976); *IDC* (1999) and references therein	Reported only by the IDC

Table 9.6: *continued*

Magnitude type	Description	References	Comments
Ms7	Surface-wave magnitude	*Bormann et al.* (2007)	Reported only by BJI and computed from records of a Chinese-made long-period seismograph in the distance range 3°-177°
MW (Mw)	Moment magnitude	*Kanamori* (1977); *Dziewonski et al.* (1981)	Computed according to the *IASPEI* (2005) and *IASPEI* (2013) standard formula
Mw(mB)	Proxy Mw based on mB	*Bormann and Saul* (2008)	Reported only by DJA and BKK
Mwp	Moment magnitude from P-waves	*Tsuboi et al.* (1995)	Reported only by DJA and BKK and used in rapid response
mbh	Unknown		
mbv	Unknown		
MG	Unspecified type		Contact contributor
Mm	Unknown		
msh	Unknown		
MSV	Unknown		

Table 9.7 lists all magnitude types reported, the corresponding number of events in the ISC Bulletin and the agency codes along with the number of earthquakes.

Table 9.7: *Summary of magnitude types in the ISC Bulletin for this summary period. The number of events with values for each magnitude type is listed. The agencies reporting these magnitude types are listed, together with the total number of values reported.*

Magnitude type	Events	Agencies reporting magnitude type (number of values)
M	3111	BEO (1821), BKK (714), SKO (597), FDF (111), PRU (17)
mB	2895	BJI (2631), DJA (506), BKK (94)
MB	3	RSNC (3)
mb	33264	IDC (26486), NEIC (9135), NNC (3967), MOS (3466), BJI (2550), KRNET (2112), MAN (1004), DJA (788), VIE (667), CSEM (506), SKHL (336), MDD (201), KLM (108), BKK (107), DSN (95), NIC (77), SIGU (71), GII (33), IGQ (28), STR (9), CRAAG (3), PDA (3), DMN (2), DHMR (2), NDI (2), OTT (1), IASPEI (1), HYB (1)
mb1	27184	IDC (27184)
mb1mx	27184	IDC (27184)
mbh	4	SKHL (4)
mbLg	2467	MDD (2467)
mbtmp	27184	IDC (27184)

Table 9.7: Continued.

Magnitude type	Events	Agencies reporting magnitude type (number of values)
MD	32147	CSEM (15176), DDA (9854), ROM (8257), ISK (6219), MEX (2462), ATH (1356), RSPR (1255), LDG (1095), ECX (1042), BER (841), BUC (685), TRN (587), CASC (415), SJA (383), PDA (371), NSSC (341), GRAL (315), HLW (262), PDG (181), GII (143), PNSN (139), CERI (119), NCEDC (117), SOF (109), CNRM (108), INMG (58), JSN (55), TUL (33), SEA (32), HVO (32), SNET (31), TUN (17), LSZ (11), IGQ (10), JSO (5), HDC (5), BUT (5), UCR (5), SSS (3), WES (3), NAM (2), INET (2), BUL (1), LDO (1), OBM (1), UPA (1), SDD (1), SLC (1), HYB (1)
ME	134	NEIC (134)
MG	377	AEIC (277), WEL (73), GUC (20), ARE (7)
MJMA	119974	JMA (119974)
ML	95815	CSEM (27165), IDC (17974), TAP (11392), ROM (8754), WEL (8100), ATH (6790), HEL (6017), RSNC (5425), THE (3917), UPP (3275), GUC (3028), SJA (2748), DDA (1583), ISK (1464), LDG (1372), TEH (1315), PRE (1283), AEIC (1228), ECX (1210), LJU (1197), BER (1144), NSSC (1111), MAN (1015), VIE (935), INMG (922), PGC (794), DHMR (777), NAO (722), KRSC (611), SKO (599), GEN (584), CRAAG (523), IPEC (506), IGIL (435), PDA (405), PDG (382), BJI (333), ZUR (306), HLW (272), STR (268), WB-NET (249), PAS (247), CASC (246), THR (232), SFS (223), ISN (212), NIC (202), SCB (139), NEIC (134), DSN (124), BGR (114), REN (108), TIR (105), NDI (103), PPT (94), KNET (93), FIA0 (91), ARO (77), OTT (75), KLM (61), BGS (57), BNS (47), NCEDC (46), UCC (44), SLC (37), OBM (35), PLV (30), HVO (23), BUG (18), NSSP (16), MRB (13), BUT (11), DMN (10), ARE (9), AUST (7), HYB (5), LDO (4), SEA (3), UPA (3), INET (3), UCR (3), REY (2), SSS (2), HON (2), SZGRF (1), LEDBW (1), SOF (1), ZAG (1), BEO (1), RSPR (1), BUC (1), ALG (1)
MLSn	35	PGC (35)
MLv	2568	DJA (1902), BKK (701)
MN	548	OTT (427), TEH (61), NEIC (58), CERI (7), WES (5), TUL (4), OGSO (3), MDD (3)
mpv	4193	NNC (4193)
MS	12828	IDC (11620), BJI (2296), MAN (1022), MOS (823), NEIC (291), NSSP (78), CSEM (69), KLM (59), SOME (47), DSN (42), SKHL (27), VIE (13), ASRS (13), GUC (1), LDG (1)
Ms1	11620	IDC (11620)
ms1mx	11620	IDC (11620)
Ms7	2295	BJI (2295)
msh	52	SKHL (52)

Table 9.7: *Continued.*

Magnitude type	Events	Agencies reporting magnitude type (number of values)
MW	9665	NIED (4569), SJA (2532), GCMT (1200), FUNV (1191), NEIC (633), PGC (293), WAR (89), CSEM (37), BRK (26), GUC (19), OTT (18), WEL (17), SLM (9), UPA (5), CASC (3), PLV (3), IEC (3), MDD (3), CRAAG (2), CAR (2), PAS (2), BER (2), SSS (1), NCEDC (1), RSNC (1), ROM (1), ECX (1), PDA (1)
Mw(mB)	98	BKK (98)
Mwp	42	DJA (36), BKK (8)

The most commonly reported magnitude types are short-period body-wave, surface-wave, local (or Richter), moment, duration and JMA magnitude type. For a given earthquake, the number and type of reported magnitudes greatly vary depending on its size and location. The large earthquake of October 25, 2010 gives an example of the multitude of reported magnitude types for large earthquakes (Listing 9.1). Different magnitude estimates come from global monitoring agencies such as the IDC, NEIC and GCMT, a local agency (GUC) and other agencies, such as MOS and BJI, providing estimates based on the analysis of their networks. The same agency may report different magnitude types as well as several estimates of the same magnitude type, such as NEIC estimates of Mw obtained from W-phase, centroid and body-wave inversions.

Listing 9.1: *Example of reported magnitudes for a large event*

```
Event   15264887 Southern Sumatera
   Date        Time         Err   RMS Latitude Longitude  Smaj  Smin  Az Depth   Err Ndef Nsta Gap  mdist  Mdist Qual   Author      OrigID
2010/10/25 14:42:22.18   0.27 1.813  -3.5248  100.1042 4.045 3.327  54  20.0  1.37 2102 2149  23   0.76 176.43 m i de ISC       01346132
 (#PRIME)

Magnitude  Err Nsta Author      OrigID
mb      6.1       61 BJI       15548963
mB      6.9       68 BJI       15548963
Ms      7.7       85 BJI       15548963
Ms7     7.5       86 BJI       15548963
mb      5.3 0.1   48 IDC       16686694
mb1     5.3 0.1   51 IDC       16686694
mb1mx   5.3 0.0   52 IDC       16686694
mbtmp   5.3 0.1   51 IDC       16686694
ML      5.1 0.2    2 IDC       16686694
MS      7.1 0.0   31 IDC       16686694
Ms1     7.1 0.0   31 IDC       16686694
ms1mx   6.9 0.1   44 IDC       16686694
mb      6.1      243 ISCJB     01677901
MS      7.3      228 ISCJB     01677901
M       7.1      117 DJA       01268475
mb      6.1 0.2  115 DJA       01268475
mB      7.1 0.1  117 DJA       01268475
MLv     7.0 0.2   26 DJA       01268475
        7.1 0.4  117 DJA       01268475
Mwp     6.9 0.2  102 DJA       01268475
mb      6.4       49 MOS       16742129
MS      7.2       70 MOS       16742129
mb      6.5      110 NEIC      01288303
ME      7.3          NEIC      01288303
MS      7.3      143 NEIC      01288303
MW      7.7          NEIC      01288303
MW      7.8      130 GCMT      00125427
mb      5.9          KLM       00255772
ML      6.7          KLM       00255772
MS      7.6          KLM       00255772
mb      6.4       20 BGR       16815854
Ms      7.2        2 BGR       16815854
mb      6.3 0.3  250 ISC       01346132
MS      7.3 0.1  237 ISC       01346132
```

An example of a relatively small earthquake that occurred in northern Italy for which we received magnitude reports of mostly local and duration type from six agencies in Italy, France and Austria is given in Listing 9.2.

Listing 9.2: *Example of reported magnitudes for a small event*

```
Event 15089710 Northern Italy
   Date       Time        Err   RMS Latitude Longitude  Smaj  Smin  Az Depth   Err Ndef Nsta Gap  mdist  Mdist Qual   Author      OrigID
2010/08/08 15:20:46.22   0.94 0.778  45.4846    8.3212 2.900 2.539 110   28.6  9.22  172  110  82   0.41   5.35 m i ke ISC       01249414
 (#PRIME)

Magnitude  Err Nsta Author      OrigID
ML      2.4       10 ZUR        15925566
Md      2.6 0.2   19 ROM        16861451
Ml      2.2 0.2    9 ROM        16861451
ML      2.5          GEN        00554757
ML      2.6 0.3   28 CSEM       00554756
Md      2.3 0.0    3 LDG        14797570
Ml      2.6 0.3   32 LDG        14797570
```

Figure 9.11 shows a distribution of the number of agencies reporting magnitude estimates to the ISC according to the magnitude value. The peak of the distribution corresponds to small earthquakes where many local agencies report local and/or duration magnitudes. The number of contributing agencies rapidly decreases for earthquakes of approximately magnitude 5.5 and above, where magnitudes are mostly given by global monitoring agencies.

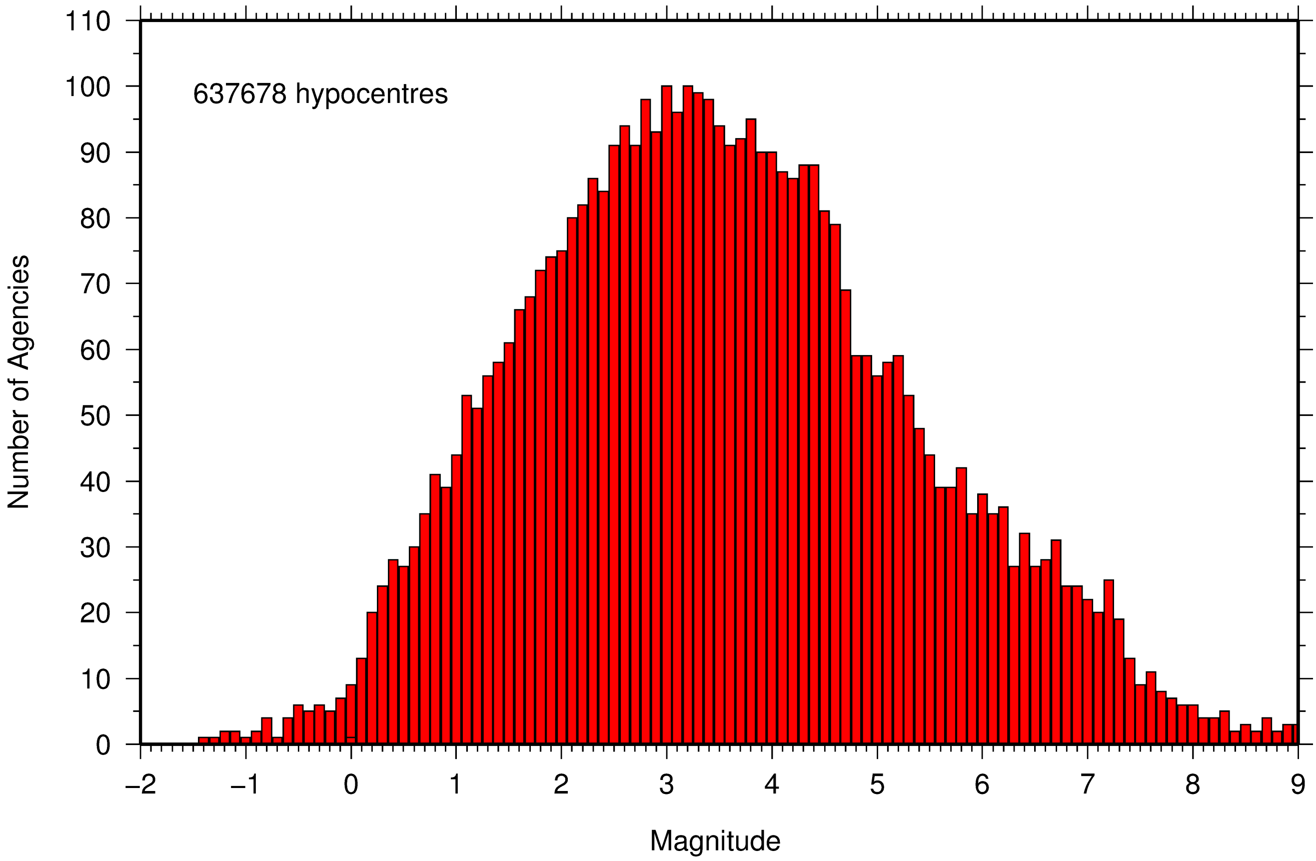

Figure 9.11: *Histogram showing the number of agencies that reported network magnitude values. All magnitude types are included.*

9.6 Moment Tensor Solutions

The ISC Bulletin publishes moment tensor solutions, which are reported to the ISC by other agencies. The collection of moment tensor solutions is summarised in Table 9.8. A histogram showing all moment tensor solutions collected throughout the ISC history is shown in Figure 9.12. Several moment tensor solutions from different authors and different moment tensor solutions calculated by different methods from the same agency may be present for the same event.

Table 9.8: *Summary of reports containing moment tensor solutions.*

Reports with Moment Tensors	15
Total moment tensors received	5812
Agencies reporting moment tensors	6

The number of moment tensors for this summary period, reported by each agency, is shown in Table 9.9. The moment tensor solutions are plotted in Figure 9.13.

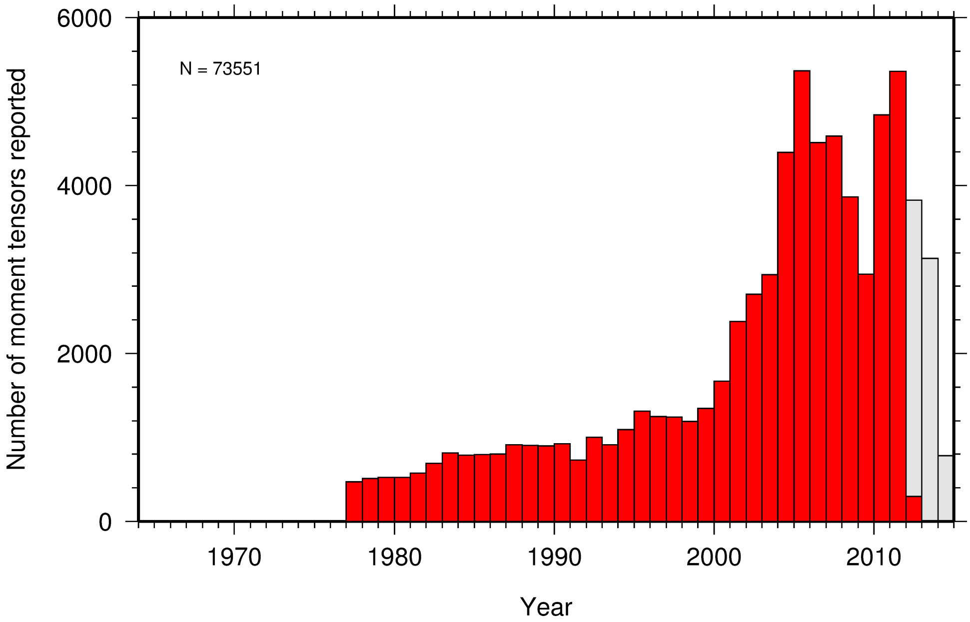

Figure 9.12: *Histogram showing the number of moment tensors reported to the ISC since 1964. The regions in grey represent data that are still being actively collected.*

Table 9.9: *Summary of moment tensor solutions in the ISC Bulletin reported by each agency.*

Agency	Number of moment tensor solutions
GCMT	1198
NEIC	579
BRK	25
OTT	13
SLM	8
PAS	1

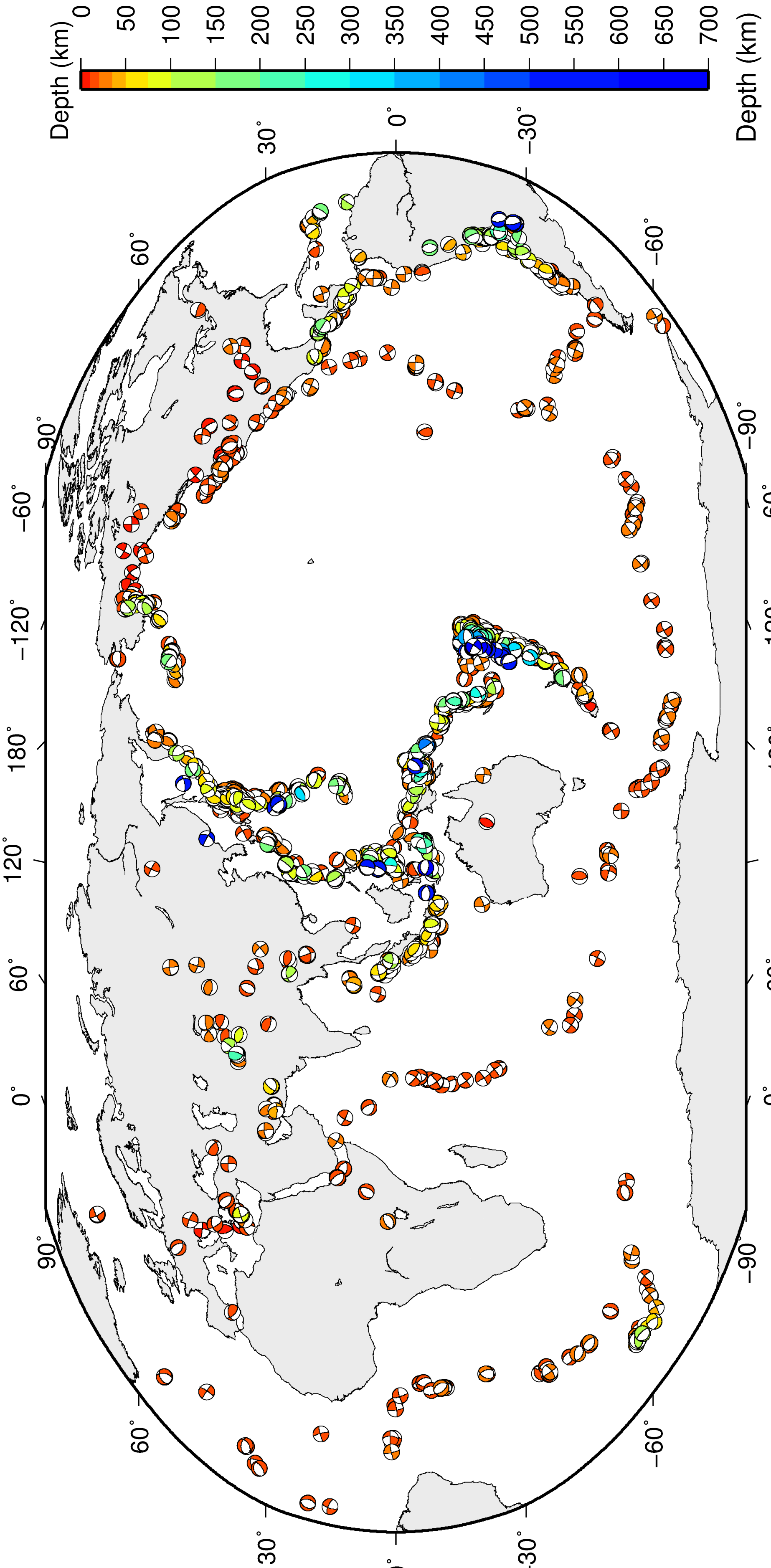

ISC Bulletin: **1824** focal mechanism solutions for **1339** events from **2011/01/01** to **2011/06/30**

Figure 9.13: *Map of all moment tensor solutions in the ISC Bulletin for this summary period.*

9.7 Timing of Data Collection

Here we present the timing of reports to the ISC. Please note, this does not include provisional alerts, which are replaced at a later stage. Instead, it reflects the final data sent to the ISC. The absolute timing of all hypocentre reports, regardless of magnitude, is shown in Figure 9.14. In Figure 9.15 the reports are grouped into one of six categories - from within three days of an event origin time, to over one year. The histogram shows the distribution with magnitude (for hypocentres where a network magnitude was reported) for each category, whilst the map shows the geographic distribution of the reported hypocentres.

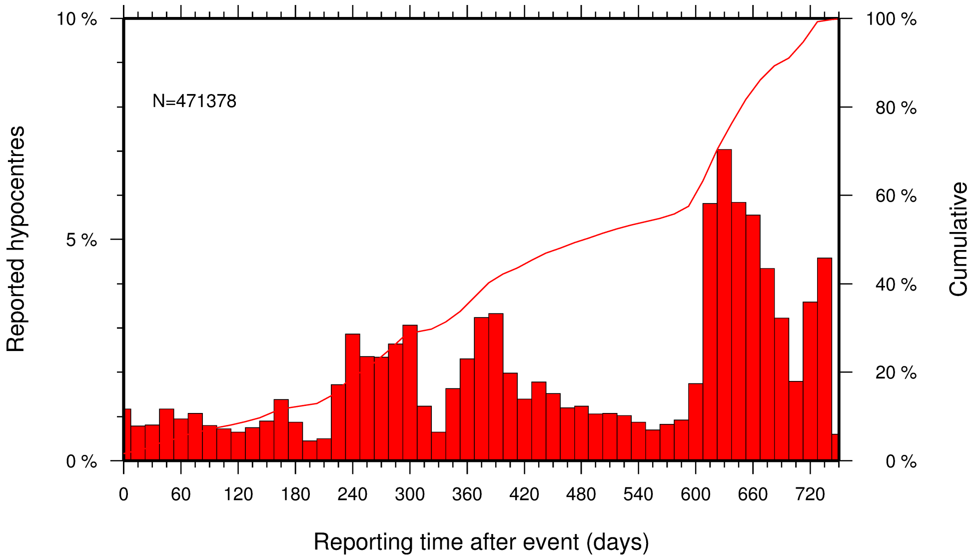

__Figure 9.14:__ Histogram showing the timing of final reports of the hypocentres (total of N) to the ISC. The cumulative frequency is shown by the solid line.

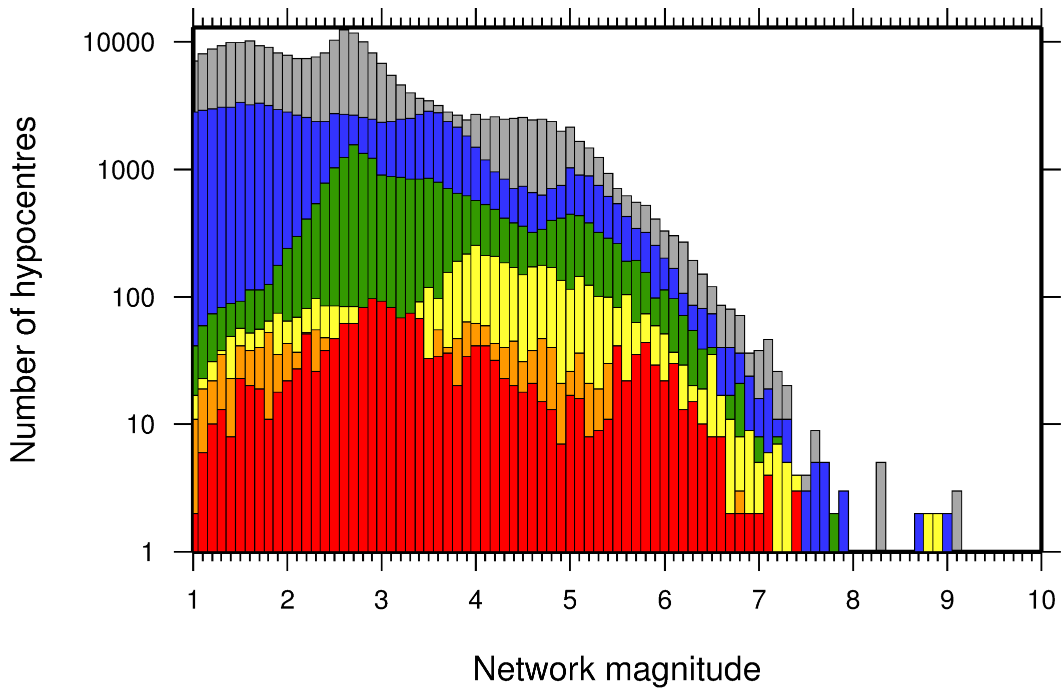

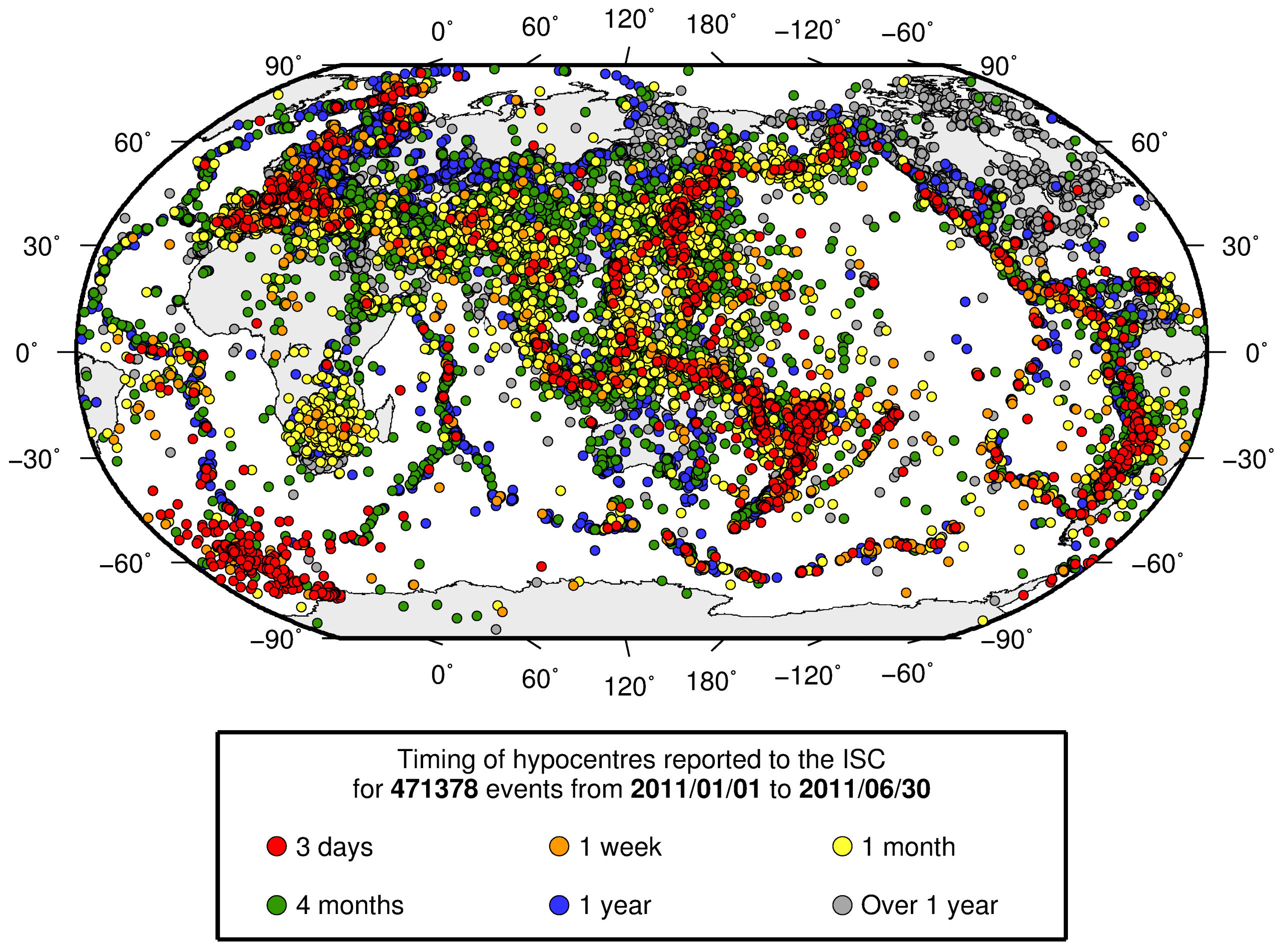

Figure 9.15: *Timing of hypocentres reported to the ISC. The colours show the time after the origin time that the corresponding hypocentre was reported. The histogram shows the distribution with magnitude. If more than one network magnitude was reported, preference was given to a value of M_W followed by M_S, m_b and M_L respectively; all reported hypocentres are included on the map. Note: early reported hypocentres are plotted over later reported hypocentres, on both the map and histogram.*

10

Overview of the ISC Bulletin

This chapter provides an overview of the seismic event data in the ISC Bulletin. We indicate the differences between all ISC events and those ISC events that are reviewed or located. We describe the wealth of phase arrivals and phase amplitudes and periods observed at seismic stations worldwide, reported in the ISC Bulletin and often used in the ISC location and magnitude determination. Finally, we make some comparisons of the ISC magnitudes with those reported by other agencies, and discuss magnitude completeness of the ISC Bulletin.

10.1 Events

The ISC Bulletin had 256276 reported events in the summary period between January and June 2011. Some 80% (205058) of the events were identified as earthquakes, the rest (51218) were of anthropogenic origin (including mining and other chemical explosions, rockbursts and induced events) or of unknown origin. As discussed in Section 3.3.3, typically about 20% of the events are selected for ISC review, and about half of the events selected for review are located by the ISC. In this summary period 18% of the events were reviewed and 11% of the events were located by the ISC. For events that are not located by the ISC, the prime hypocentre is identified according to the rules described in Section 3.3.1.

Of the 7560942 reported phase observations, 53% are associated to ISC-reviewed events, and 50% are associated to events selected for ISC location. Note that all large events are reviewed and located by the ISC. Since large events are globally recorded and thus reported by stations worldwide, they will provide the bulk of observations. This explains why only about one-fifth of the events in any given month is reviewed although the number of phases associated to reviewed events has increased nearly exponentially in the past decades.

Figure 10.1 shows the daily number of events throughout the summary period. The large increase in event numbers in March is associated with the aftershock sequence following the M_W 9.1 event off the Pacific coast of Tohoku, Japan. Figure 10.2 shows the locations of the events in the ISC Bulletin; the locations of ISC-reviewed and ISC-located events are shown in Figures 10.3 and 10.4, respectively.

Figure 10.5 shows the hypocentral depth distributions of events in the ISC Bulletin for the summary period. The vast majority of events occur in the Earth's crust. Note that the peaks at 0, 10, 35 km, and at every 50 km intervals deeper than 100 km are artifacts of analyst practices of fixing the depth to a nominal value when the depth cannot be reliably resolved.

Figure 10.6 shows the depth distribution of free-depth solutions in the ISC Bulletin. The depth of a hypocentre reported to the ISC is assumed to be determined as a free parameter, unless it is explicitly labelled as a fixed-depth solution. On the other hand, as described in Section 3.4.3, the ISC locator

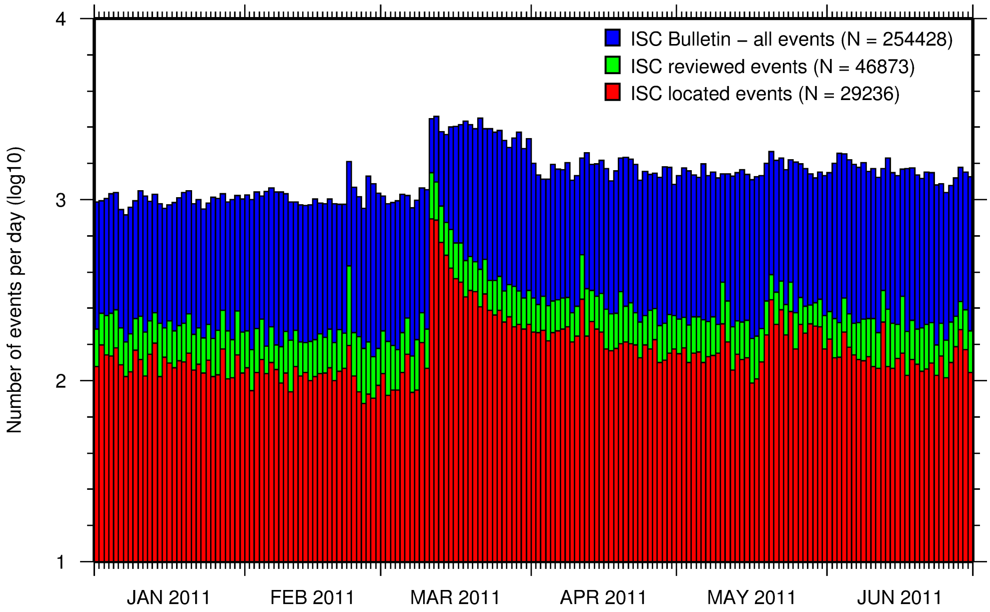

Figure 10.1: *Histogram showing the number of events in the ISC Bulletin for the current summary period. The vertical scale is logarithmic.*

attempts to get a free-depth solution if, and only if, there is resolution for the depth in the data, i.e. if there is a local network and/or sufficient depth-sensitive phases are reported.

Figure 10.7 shows the depth distribution of fixed-depth solutions in the ISC Bulletin. Except for a fraction of events whose depth is fixed to a shallow depth, this set comprises mostly ISC-located events. If there is no resolution for depth in the data, the ISC locator fixes the depth to a value obtained from the ISC default depth grid file, or if no default depth exists for that location, to a nominal default depth assigned to each Flinn-Engdahl region (see details in Section 3.4.3). During the ISC review editors are inclined to accept the depth obtained from the default depth grid, but they typically change the depth of those solutions that have a nominal (10 or 35 km) depth. When doing so, they usually fix the depth to a round number, preferably divisible by 50.

For events selected for ISC location, the number of stations typically increases as arrival data reported by several agencies are grouped together and associated to the prime hypocentre. Consequently, the network geometry, characterised by the secondary azimuthal gap (the largest azimuthal gap a single station closes), is typically improved. Figure 10.8 illustrates that the secondary azimuthal gap is indeed generally smaller for ISC-located events than that for all events in the ISC Bulletin. Figure 10.9 shows the distribution of the number of associated stations. For large events the number of associated stations is usually larger for ISC-located events than for any of the reported event bulletins. On the other hand, events with just a few reporting stations are rarely selected for ISC location. The same is true for the number of defining stations (stations with at least one defining phase that were used in the location). Figure 10.10 indicates that because the reported observations from multiple agencies are associated to the prime, large ISC-located events typically have a larger number of defining stations than any of the reported event bulletins.

The formal uncertainty estimates are also typically smaller for ISC-located events. Figure 10.11 shows the distribution of the area of the 90% confidence error ellipse for ISC-located events during the summary period. The distribution suffers from a long tail indicating a few poorly constrained event locations.

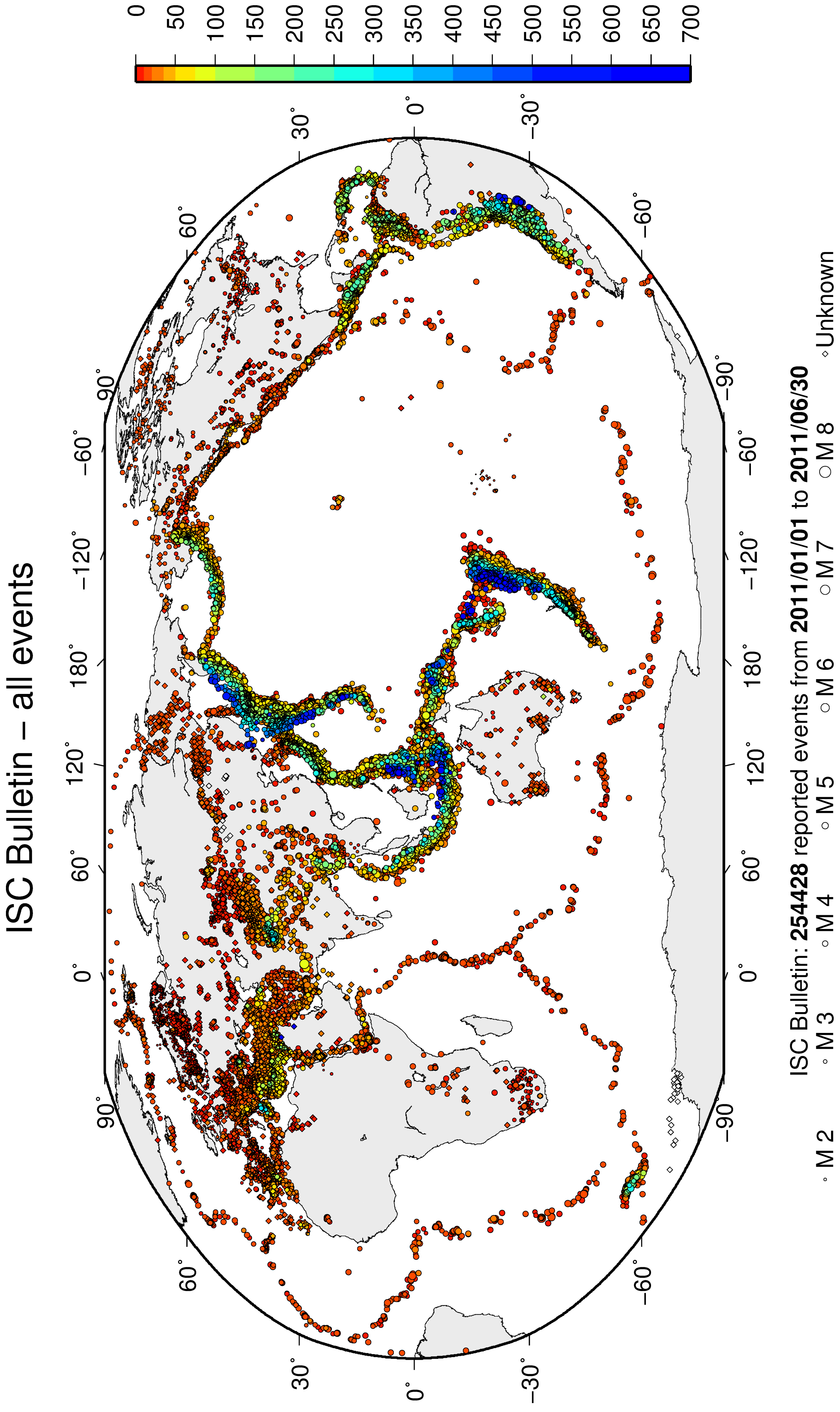

Figure 10.2: *Map of all events in the ISC Bulletin. Prime hypocentre locations are shown. Compare with Figure 9.10.*

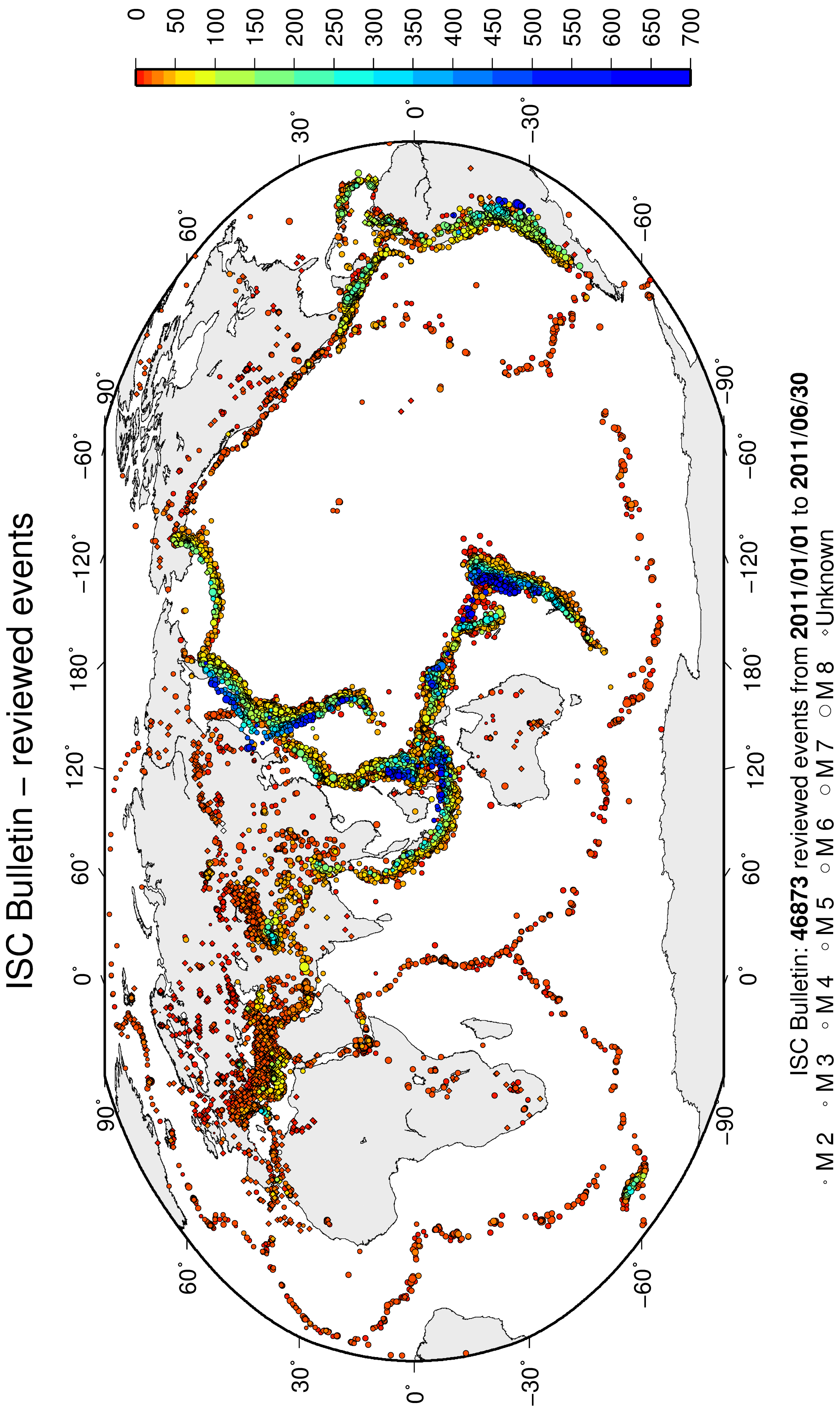

Figure 10.3: *Map of all events reviewed by the ISC for this time period. Prime hypocentre locations are shown.*

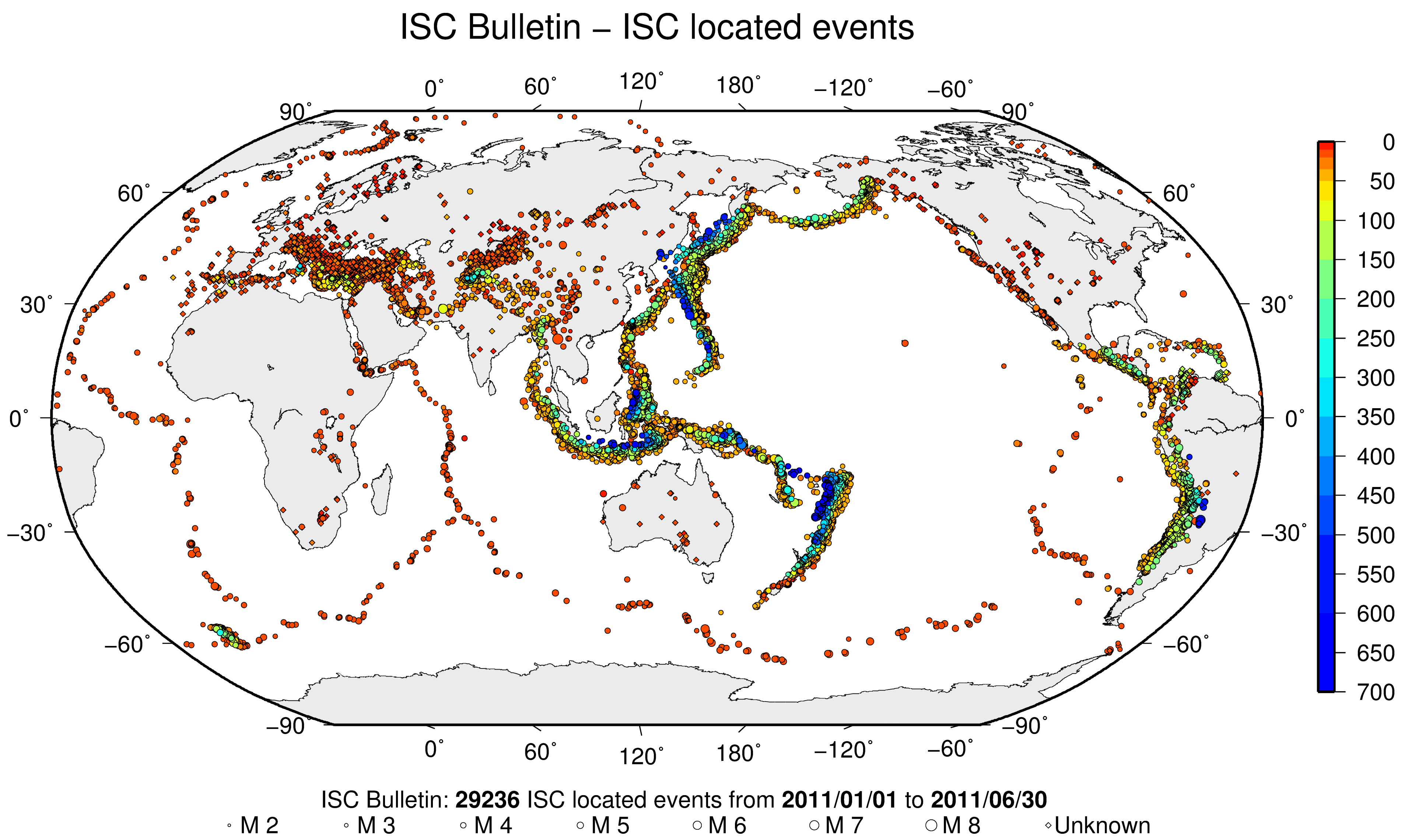

Figure 10.4: *Map of all events located by the ISC for this time period. ISC determined hypocentre locations are shown.*

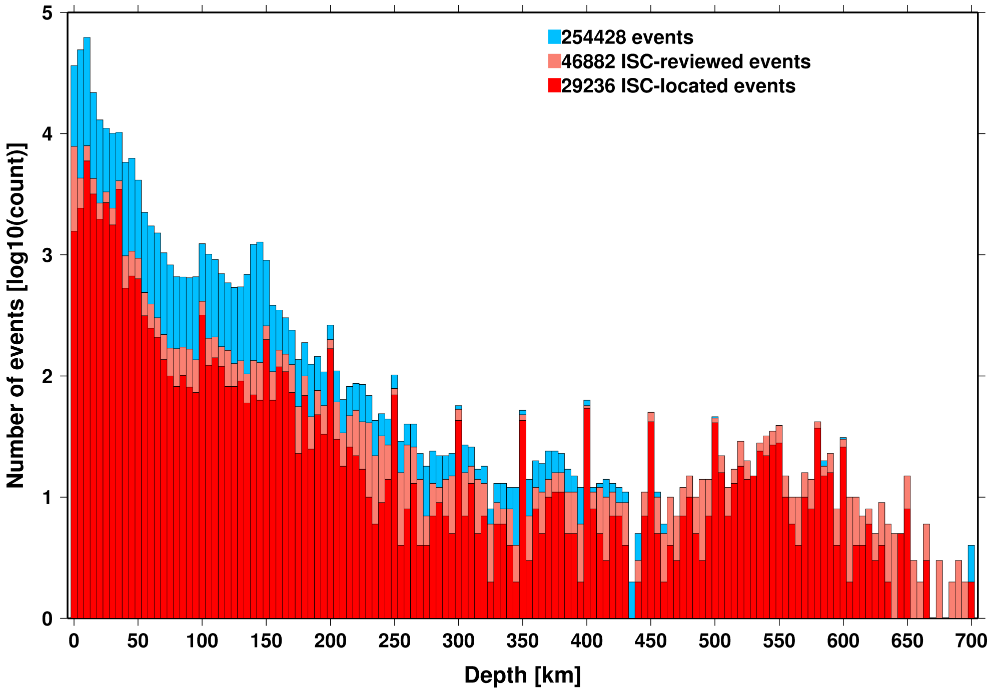

Figure 10.5: *Distribution of event depths in the ISC Bulletin (blue) and for the ISC-reviewed (pink) and the ISC-located (red) events during the summary period. All ISC-located events are reviewed, but not all reviewed events are located by the ISC. The vertical scale is logarithmic.*

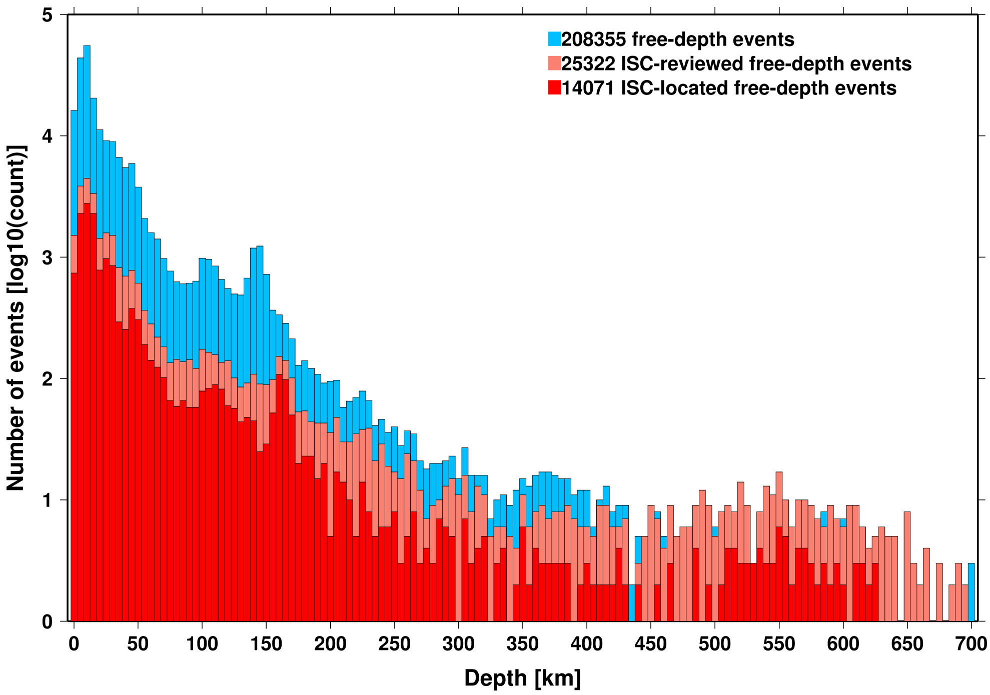

Figure 10.6: *Hypocentral depth distribution of events where the prime hypocentres are reported/located with a free-depth solution in the ISC Bulletin. The vertical scale is logarithmic.*

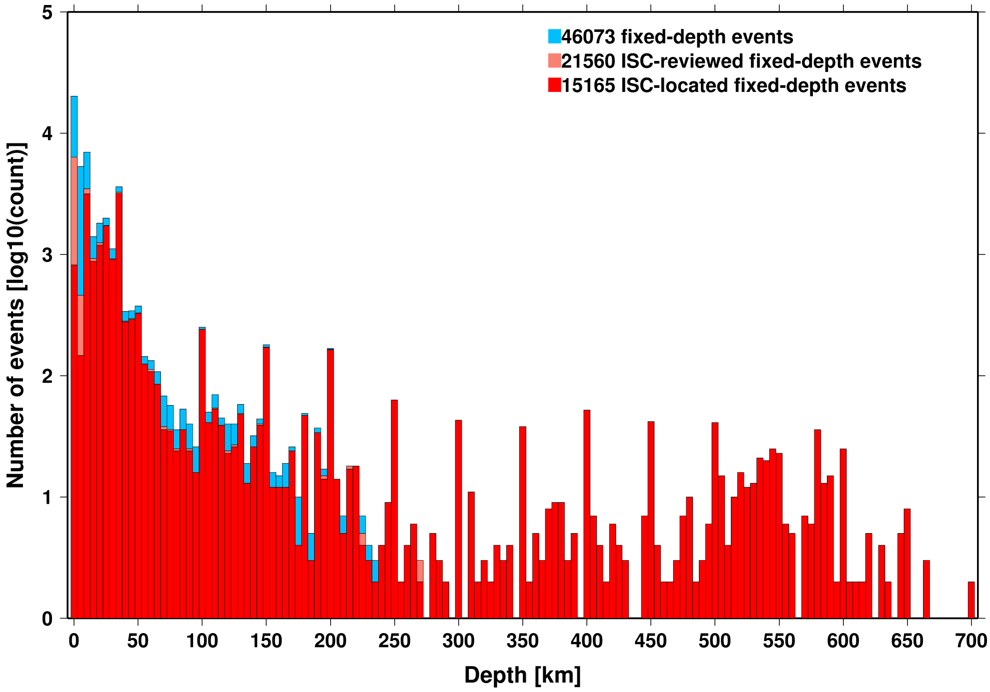

Figure 10.7: *Hypocentral depth distribution of events where the prime hypocentres are reported/located with a fixed-depth solution in the ISC Bulletin. The vertical scale is logarithmic.*

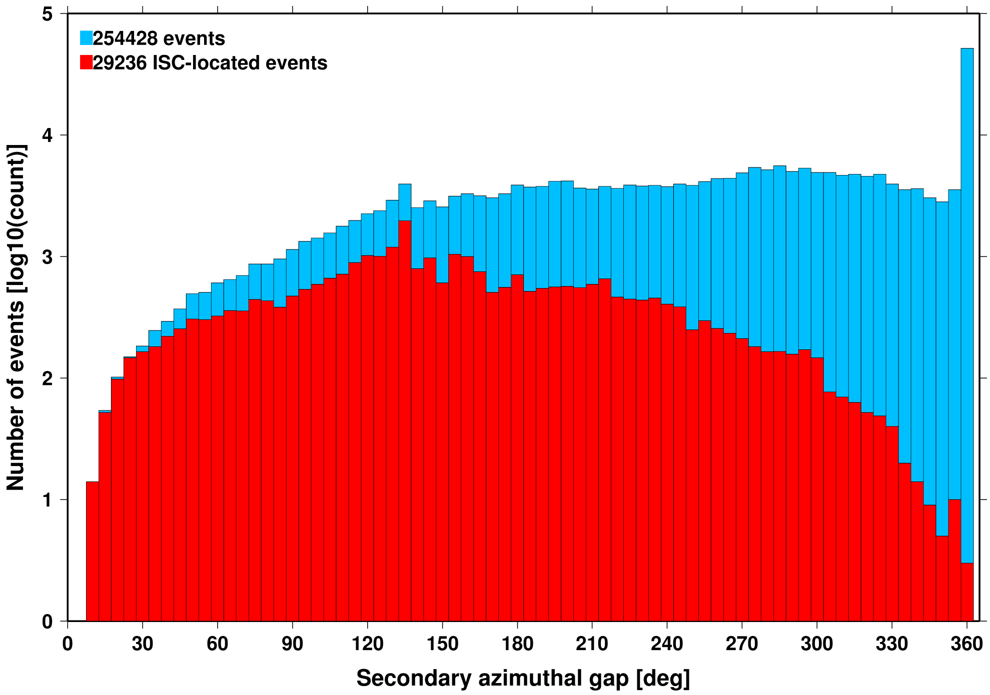

Figure 10.8: *Distribution of secondary azimuthal gap for events in the ISC Bulletin (blue) and those selected for ISC location (red). The vertical scale is logarithmic.*

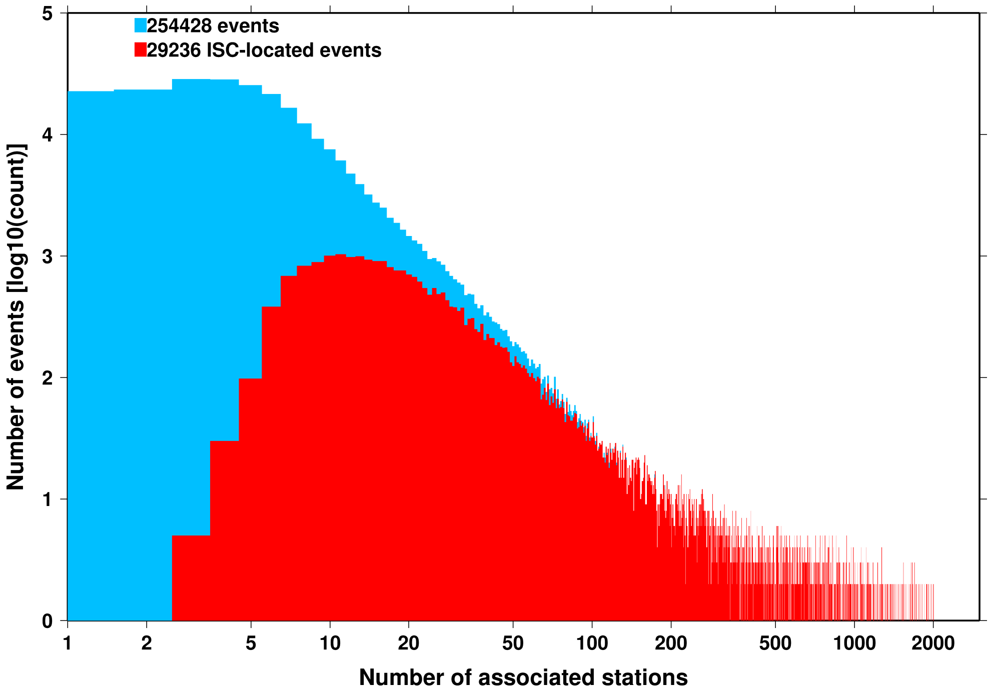

Figure 10.9: *Distribution of the number of associated stations for events in the ISC Bulletin (blue) and those selected for ISC location (red). The vertical scale is logarithmic.*

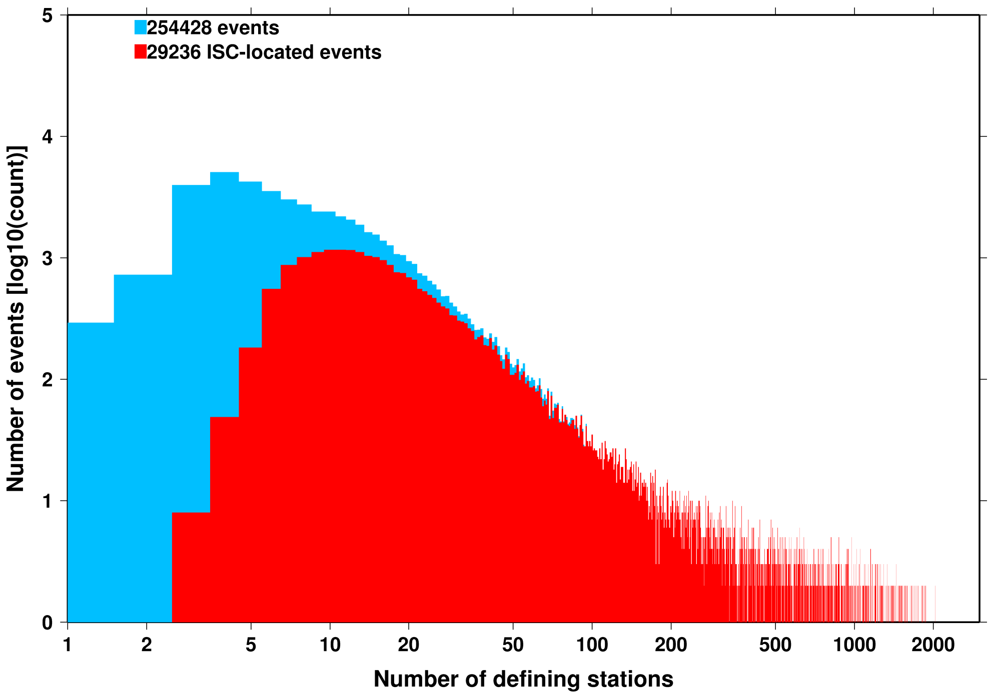

Figure 10.10: *Distribution of the number of defining stations for events in the ISC Bulletin (blue) and those selected for ISC location (red). The vertical scale is logarithmic.*

Nevertheless, half of the events are characterised by an error ellipse with an area less than 208 km^2, 90% of the events have an error ellipse area less than 1101 km^2, and 95% of the events have an error ellipse area less than 1775 km^2.

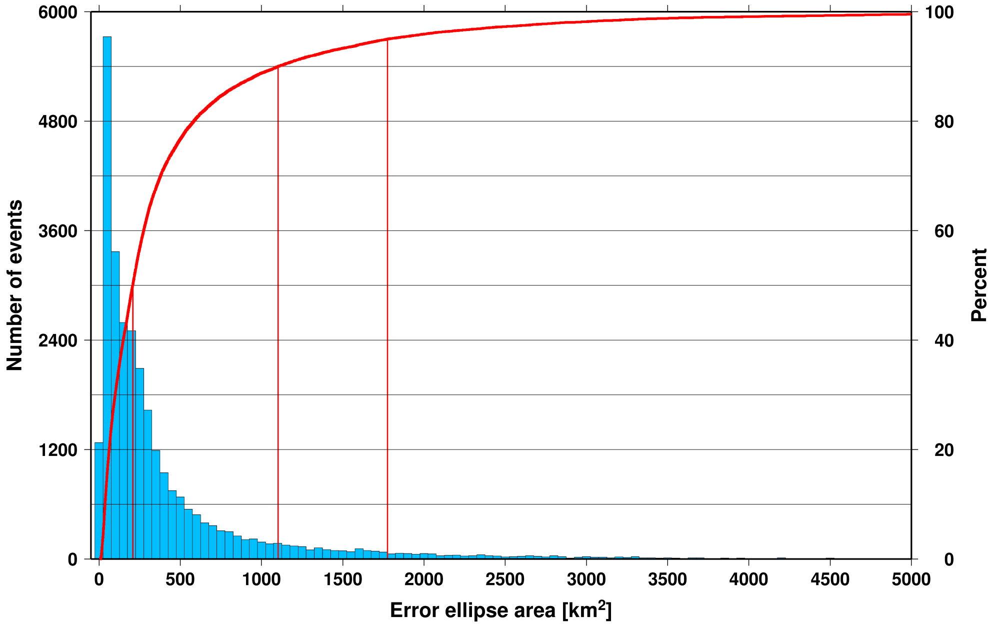

Figure 10.11: *Distribution of the area of the 90% confidence error ellipse of the ISC-located events. Vertical red lines indicate the 50th, 90th and 95th percentile values.*

Figure 10.12 shows one of the major characteristic features of the ISC location algorithm (Bondár and Storchak, 2011). Because the ISC locator accounts for correlated travel-time prediction errors due to unmodelled velocity heterogeneities along similar ray paths, the area of the 90% confidence error ellipse does not decrease indefinitely with increasing number of stations, but levels off once the information carried by the network geometry is exhausted, thus providing more realistic uncertainty estimates.

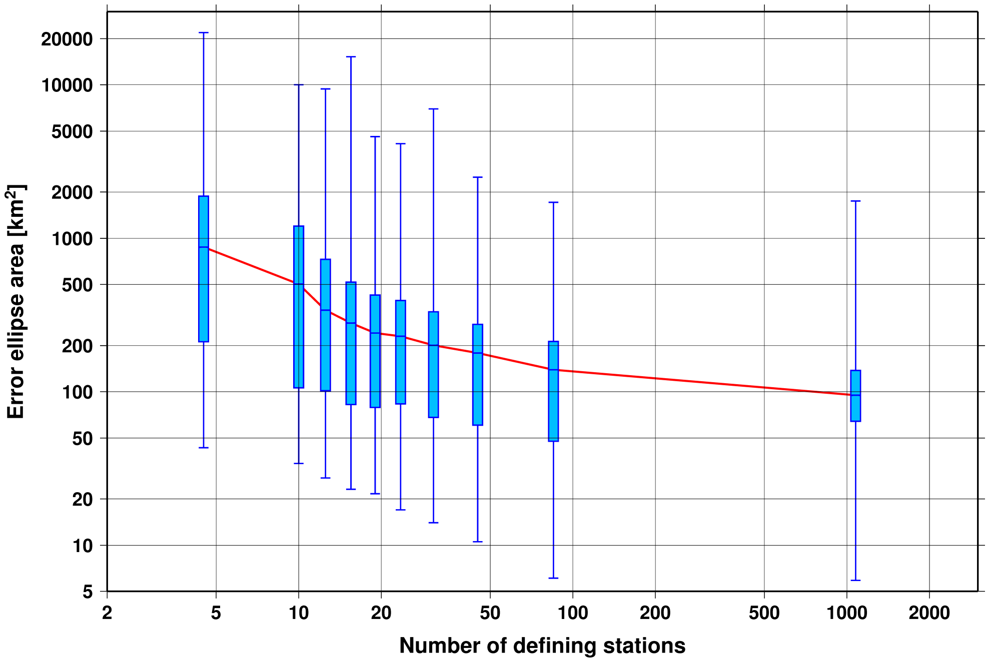

Figure 10.12: *Box-and-whisker plot of the area of the 90% confidence error ellipse of the ISC-located events as a function of the number of defining stations. Each box represents one-tenth-worth of the total number of data. The red line indicates the median 90% confidence error ellipse area.*

10.2 Seismic Phases and Travel-Time Residuals

The number of phases that are associated to events over the summary period in the ISC Bulletin is shown in Figure 10.13. Phase types and their total number in the ISC Bulletin is shown in the Appendix, Table 12.2. A summary of phase types is indicated in Figure 10.14.

In computing ISC locations, the current (for events since 2009) ISC location algorithm (*Bondár and Storchak*, 2011) uses all *ak135* phases where possible. Within the Bulletin, the phases that contribute to an ISC location are labelled as *time defining*. In this section, we summarise these time defining phases.

In Figure 10.15, the number of defining phases is shown in a histogram over the summary period. Each defining phase is listed in Table 10.1, which also provides a summary of the number of defining phases per event. A pie chart showing the proportion of defining phases is shown in Figure 10.16. Figure 10.17 shows travel times of seismic waves. The distribution of residuals for these defining phases is shown for the top five phases in Figures 10.18 through 10.22.

Table 10.1: *Numbers of 'time defining' phases (N) within the ISC Bulletin for 29236 ISC located events.*

Phase	Number of 'defining' phases	Number of events	Max per event	Median per event
P	1443957	20895	2627	10
Pn	537673	27297	1051	10
Sn	183493	23289	249	5
Pg	117658	10580	158	8
Pb	109902	13706	99	5
Sg	84467	10472	173	6
PKPdf	82580	6676	718	2
Sb	72831	13655	61	4
S	46941	4232	453	5
PKPbc	37143	5854	306	2
PcP	21391	5132	133	2
pP	20563	2747	305	3

Table 10.1: *(continued)*

Phase	Number of 'defining' phases	Number of events	Max per event	Median per event
PKPab	20479	4037	165	2
PP	14364	2415	197	2
Pdif	13612	1461	529	2
sP	11266	2326	106	2
PKiKP	9959	1244	461	2
SS	7491	2327	56	2
ScP	7328	1992	396	2
SnSn	3626	1491	13	2
PnPn	3330	1513	15	2
PKKPbc	3142	602	111	2
SKSac	2929	637	84	2
ScS	2668	1370	73	1
pPKPdf	1348	380	42	2
SKPbc	1256	312	51	2
PcS	1056	799	16	1
sS	1021	630	22	1
P'P'df	752	213	28	2
PKKPab	737	262	33	1
SKiKP	730	394	23	1
SKKSac	682	322	104	1
PKKPdf	612	272	28	1
SKSdf	610	334	12	1
PKSdf	494	325	7	1
SKPab	447	163	32	2
PnS	405	192	15	1
pPKPbc	397	231	6	1
PS	372	120	27	2
SP	250	91	20	1
Sdif	249	100	27	1
pPKPab	217	103	16	1
SKPdf	167	62	25	1
SKKPbc	120	36	20	1
pPKiKP	54	22	12	1
pPdif	45	12	13	2
SKKPab	34	12	13	1
sPdif	31	9	9	1
SPn	29	23	6	1
P'P'ab	28	21	3	1
PbPb	25	20	3	1
P'P'bc	24	10	12	1
PKSab	18	2	16	9
sPKPdf	13	13	1	1
sPKiKP	13	9	5	1
PKSbc	13	8	6	1
SKKSdf	10	10	1	1
sPKPbc	9	8	2	1
SbSb	8	7	2	1
SKKPdf	7	5	2	1
PKKSbc	7	2	6	4
pS	7	7	1	1
PKKSdf	6	1	6	6
sPn	6	3	3	2
pPn	4	3	2	1
sPKPab	4	4	1	1
pwP	2	1	2	2
sSdif	2	2	1	1
S'S'df	1	1	1	1
S'S'ac	1	1	1	1

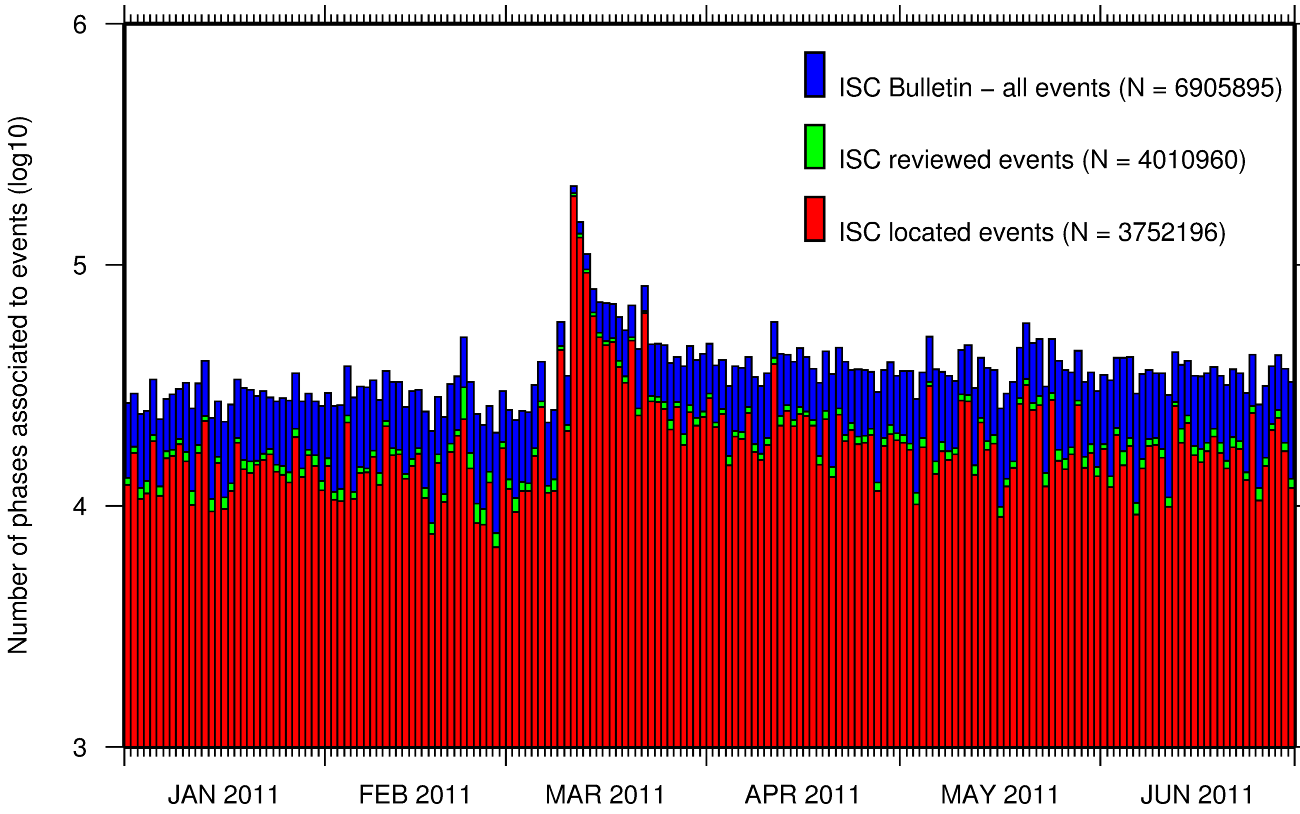

Figure 10.13: *Histogram showing the number of phases (N) that the ISC has associated to events within the ISC Bulletin for the current summary period.*

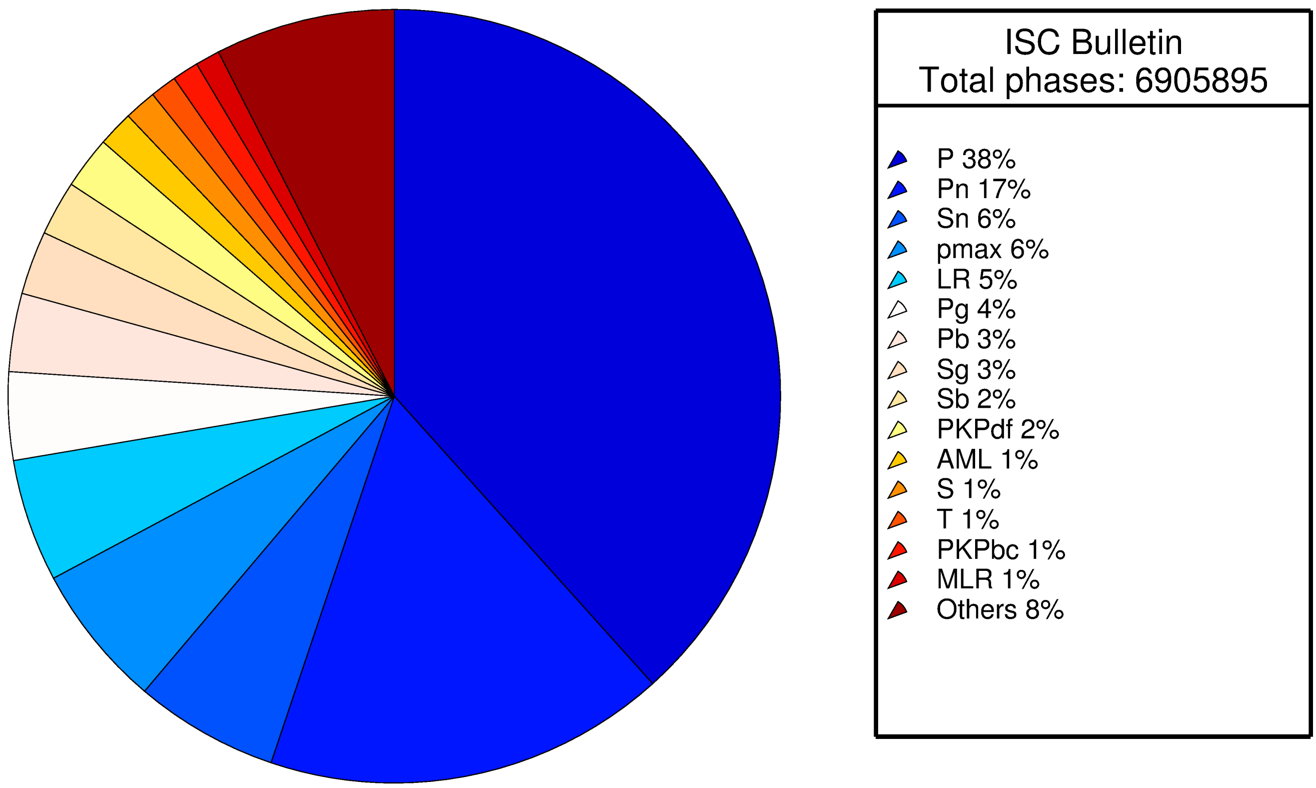

Figure 10.14: *Pie chart showing the fraction of various phase types in the ISC Bulletin for this summary period.*

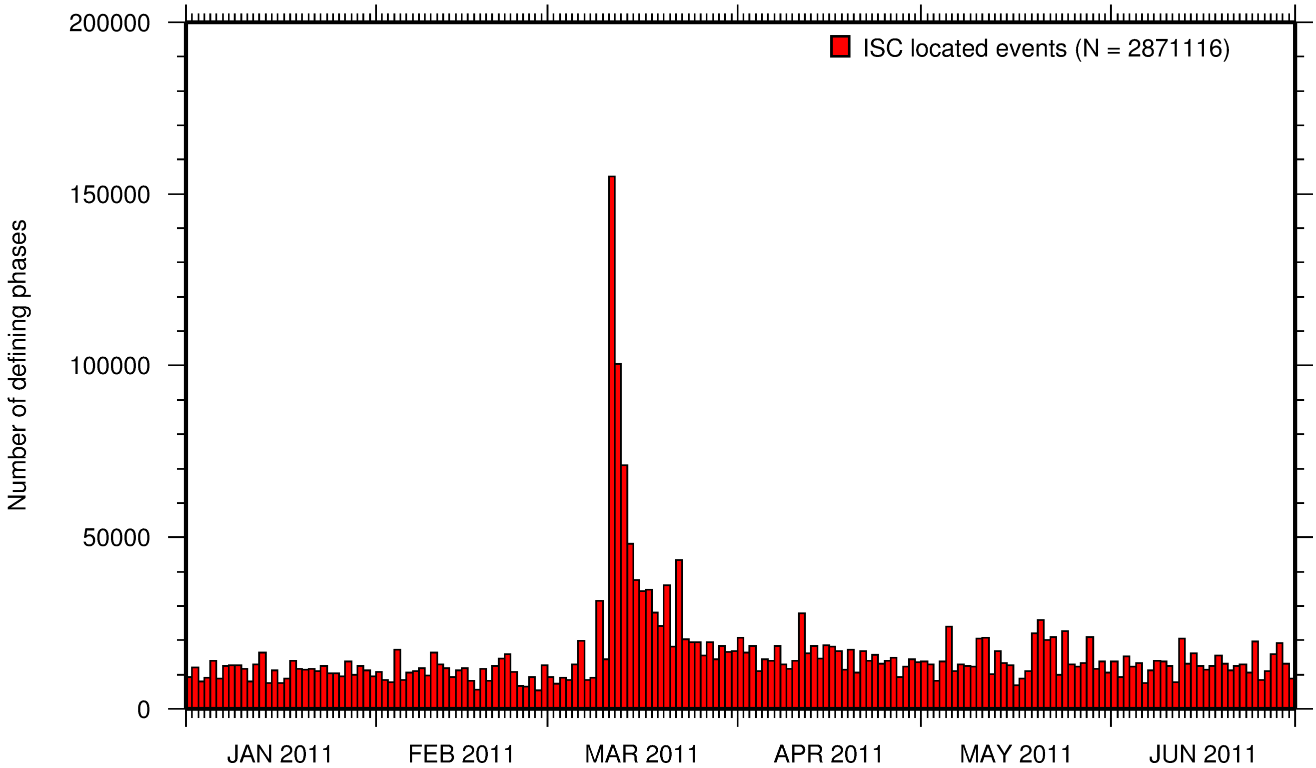

Figure 10.15: *Histogram showing the number of defining phases in the ISC Bulletin, for events located by the ISC.*

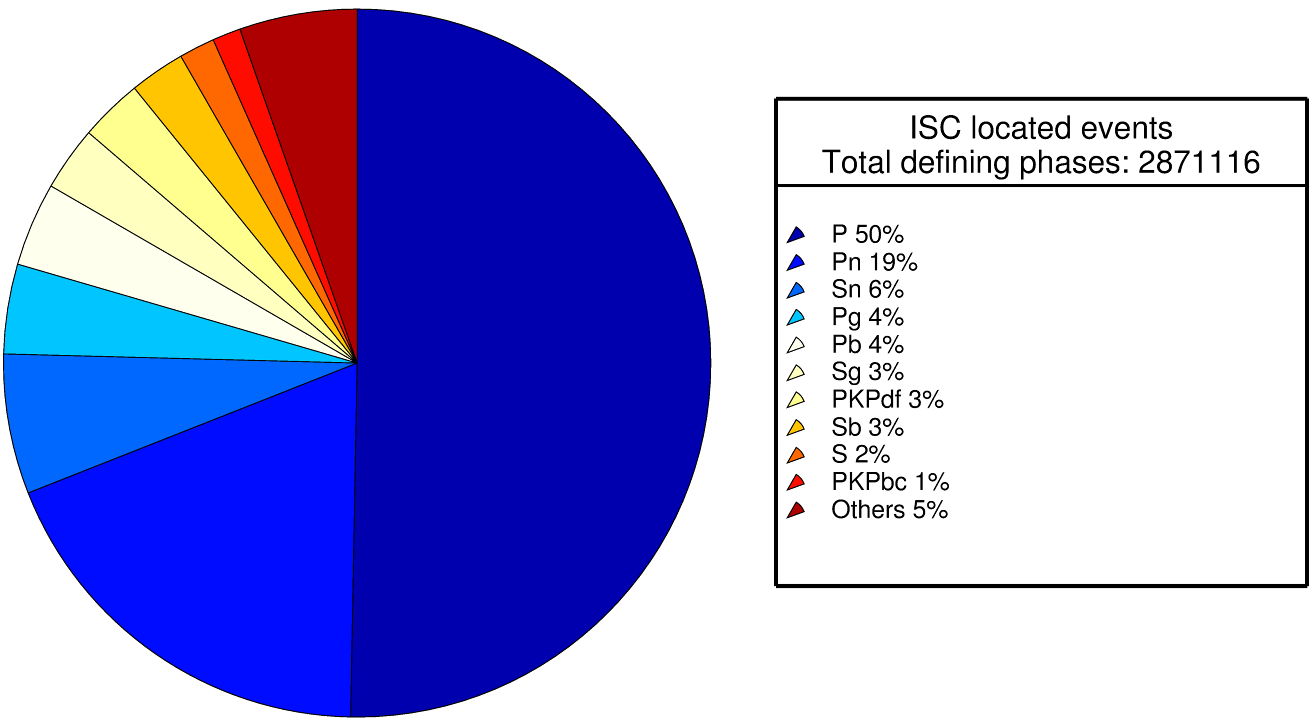

Figure 10.16: *Pie chart showing the defining phases in the ISC Bulletin, for events located by the ISC. A complete list of defining phases is shown in Table 10.1.*

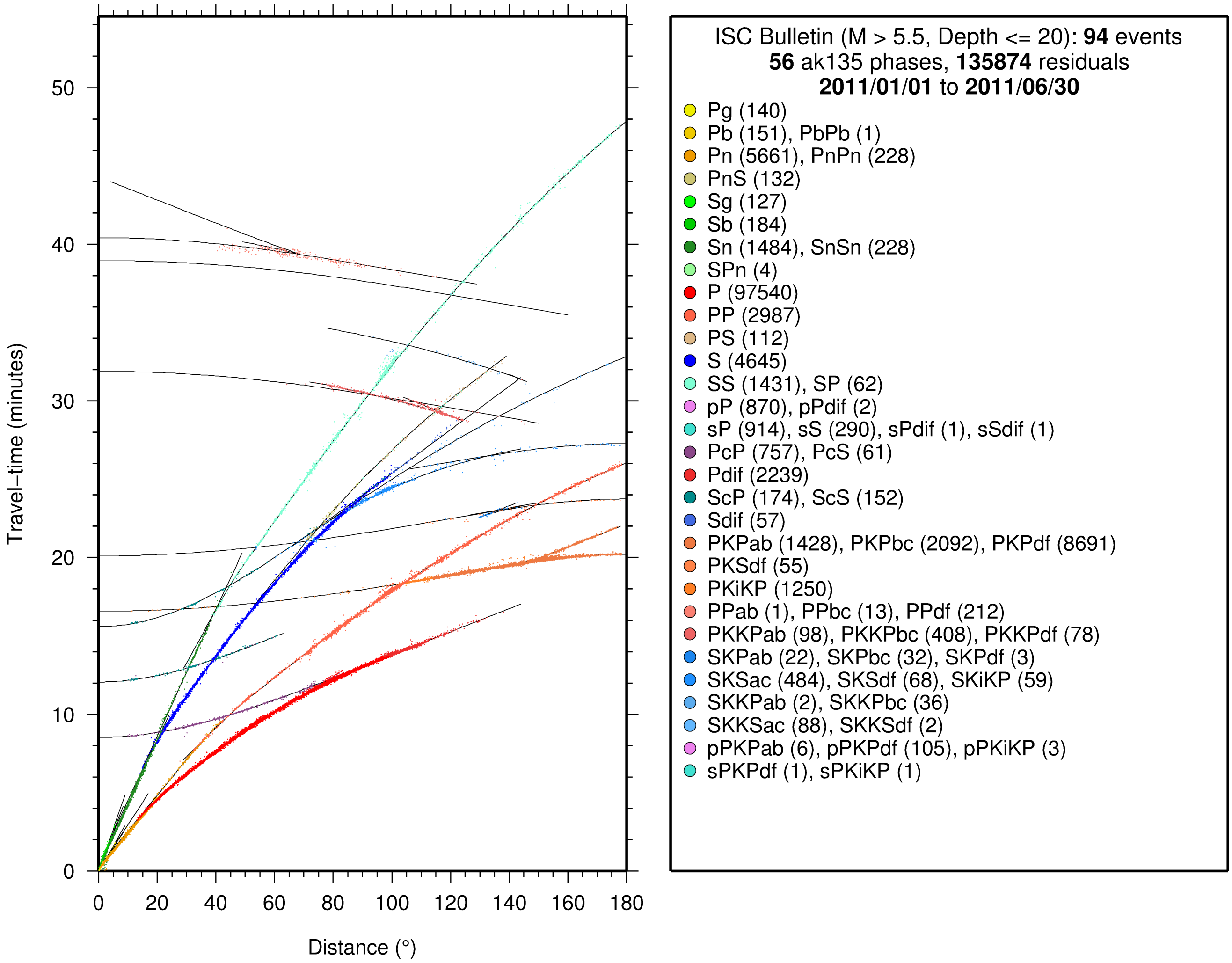

Figure 10.17: *Distribution of travel-time observations in the ISC Bulletin for events with M > 5.5 and depth less than 20 km. The travel-time observations are shown relative to a 0 km source and compared with the theoretical ak135 travel-time curves (solid lines). The legend lists the number of each phase plotted.*

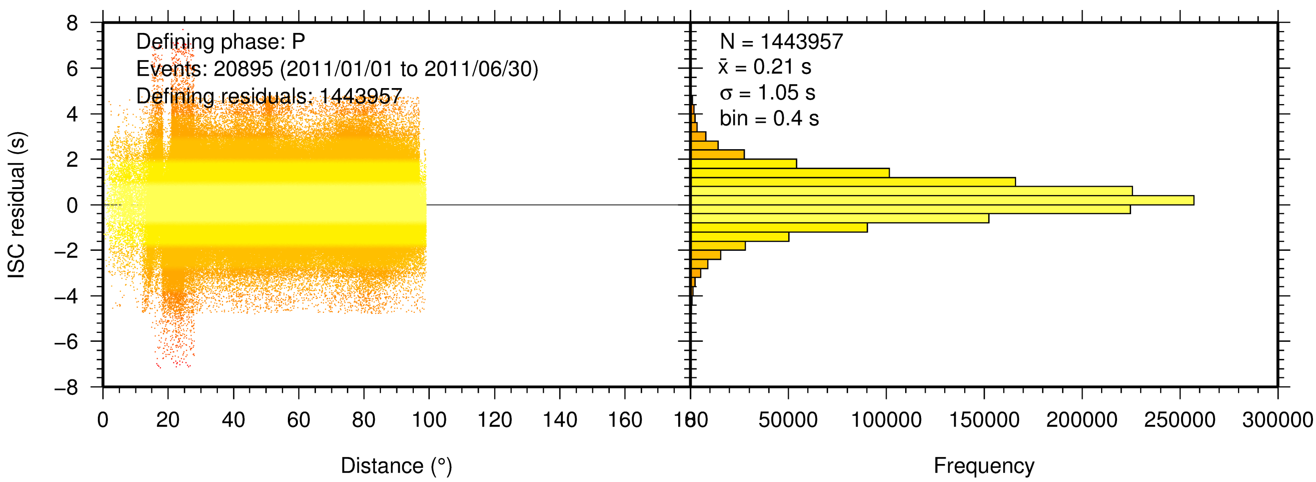

Figure 10.18: *Distribution of travel-time residuals for the defining P phases used in the computation of ISC located events in the Bulletin.*

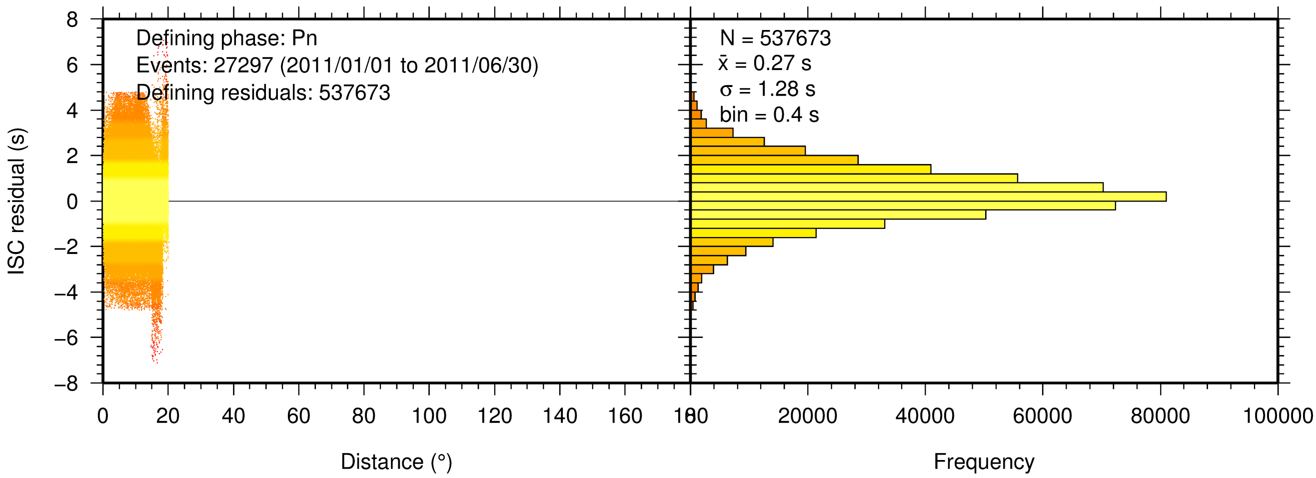

Figure 10.19: *Distribution of travel-time residuals for the defining Pn phases used in the computation of ISC located events in the Bulletin.*

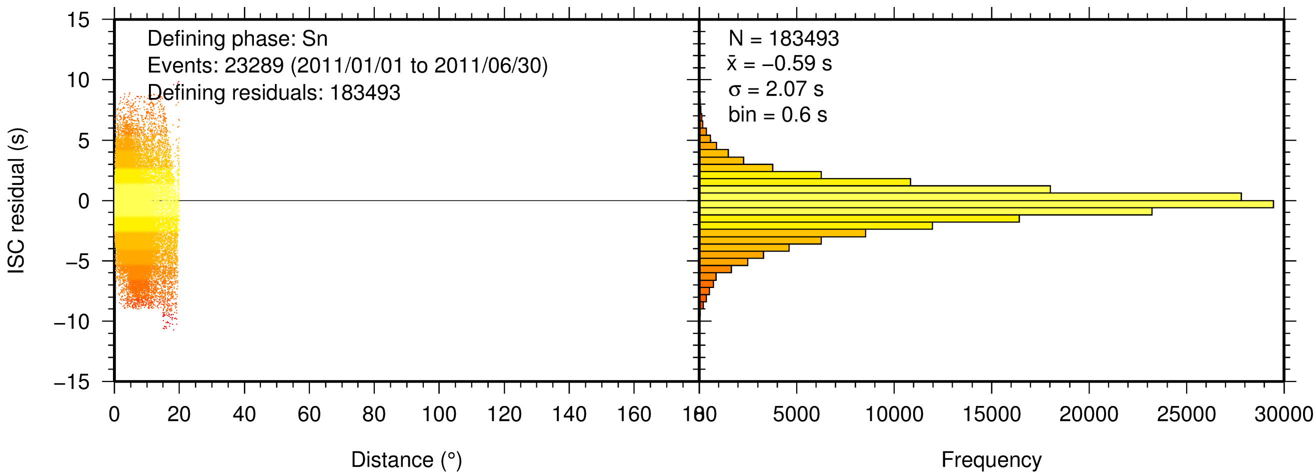

Figure 10.20: *Distribution of travel-time residuals for the defining Sn phases used in the computation of ISC located events in the Bulletin.*

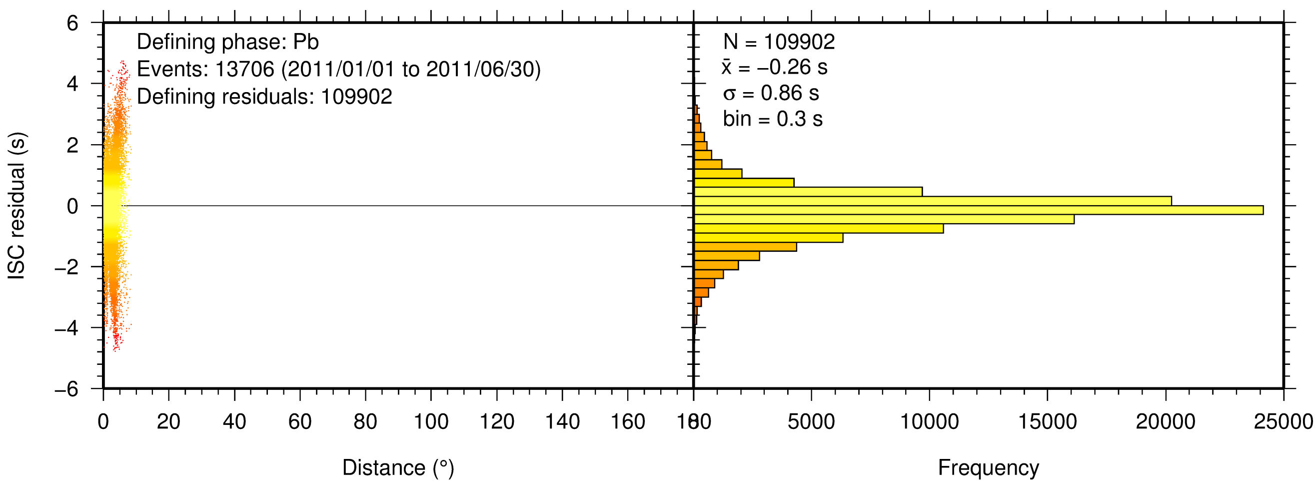

Figure 10.21: *Distribution of travel-time residuals for the defining Pb phases used in the computation of ISC located events in the Bulletin.*

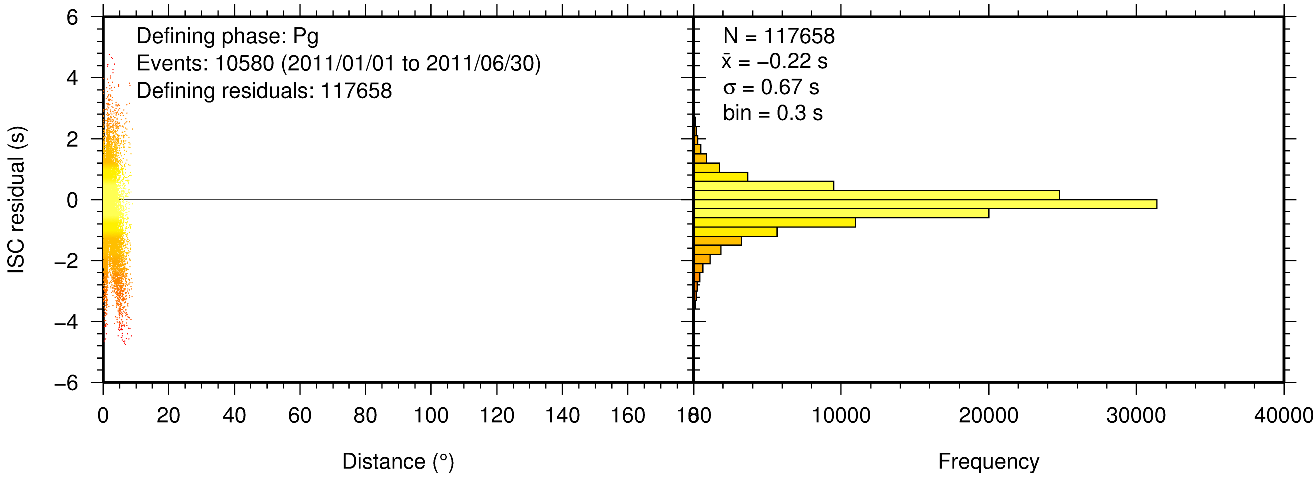

Figure 10.22: *Distribution of travel-time residuals for the defining Pg phases used in the computation of ISC located events in the Bulletin.*

10.3 Seismic Wave Amplitudes and Periods

The ISC Bulletin contains a variety of seismic wave amplitudes and periods measured by reporting agencies. For this Bulletin Summary, the total of collected amplitudes and periods is 2,266,088 (see Section 9.3). For the determination of the ISC magnitudes MS and mb, only a fraction of such data can be used. Indeed, the ISC network magnitudes are computed only for ISC located events. Here we recall the main features of the ISC procedure for MS and mb computation (see detailed description in Section 3.4). For each amplitude-period pair in a reading the ISC algorithm computes the magnitude (a reading can include several amplitude-period measurements) and the reading magnitude is assigned to the maximum A/T in the reading. If more than one reading magnitude is available for a station, the station magnitude is the median of the reading magnitudes. The network magnitude is computed then as the 20% alpha-trimmed median of the station magnitudes (at least three required). MS is computed for shallow earthquakes (depth $\leq$ 60 km) only and using amplitudes and periods on all three components (when available) if the period is within 10-60 s and the epicentral distance is between 20° and 160°. mb is computed also for deep earthquakes (depth down to 700 km) but only with amplitudes on the vertical component measured at periods $\leq$ 3 s in the distance range 21°-100°.

Table 10.2 is a summary of the amplitude and period data that contributed to the computation of station and ISC MS and mb network magnitudes for this Bulletin Summary.

Table 10.2: *Summary of the amplitude-period data used by the ISC Locator to compute MS and mb.*

	MS	mb
Number of amplitude-period data	173408	773181
Number of readings	147239	770847
Percentage of readings in the ISC located events with qualifying data for magnitude computation	10.5	50.8
Number of station magnitudes	135580	655410
Number of network magnitudes	4166	19174

A small percentage of the readings with qualifying data for MS and mb calculation have more than one amplitude-period pair. Notably, only 11% of the readings for the ISC located (shallow) events included qualifying data for MS computation, whereas for mb the percentage is much higher at 51%. This is due to the seismological practice of reporting agencies. Agencies contributing systematic reports of amplitude and period data are listed in Appendix Table 12.3. Obviously the ISC Bulletin would benefit if more agencies included surface wave amplitude-period data in their reports.

Figure 10.23 shows the distribution of the number of station magnitudes versus distance. For mb there is a significant increase in the distance range 70°-90°, whereas for MS most of the contributing stations are below 100°. The increase in number of station magnitude between 70°-90° for mb is partly due to the very dense distribution of seismic stations in North America and Europe with respect to earthquake occurring in various subduction zones around the Pacific Ocean.

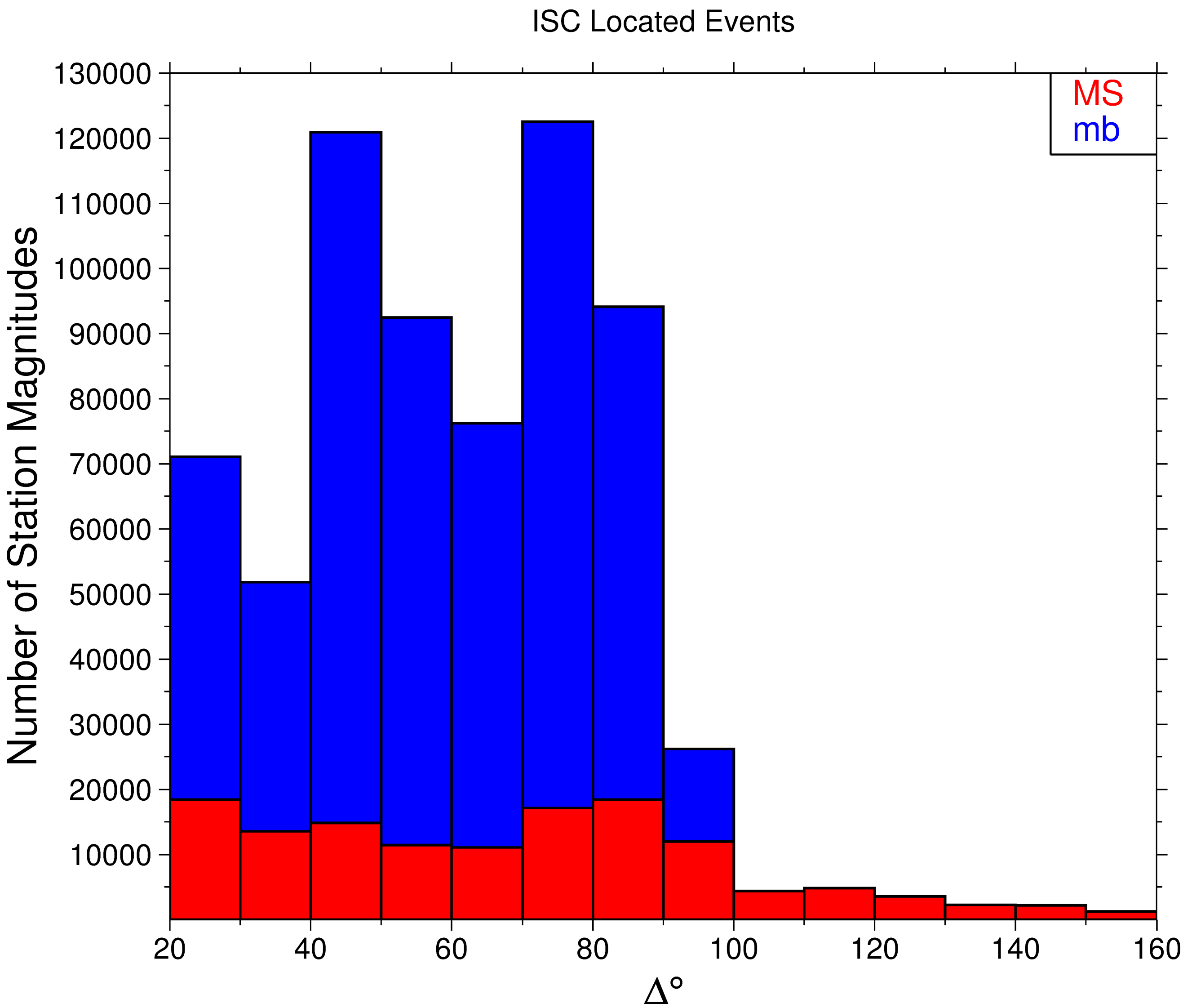

Figure 10.23: *Distribution of the number of station magnitudes computed by the ISC Locator for mb (blue) and MS (red) versus distance.*

Finally, Figure 10.24 shows the distribution of network MS and mb as well as the median number of stations for magnitude bins of 0.2. Clearly with increasing magnitude the number of events is smaller but with a general tendency of having more stations contributing to the network magnitude.

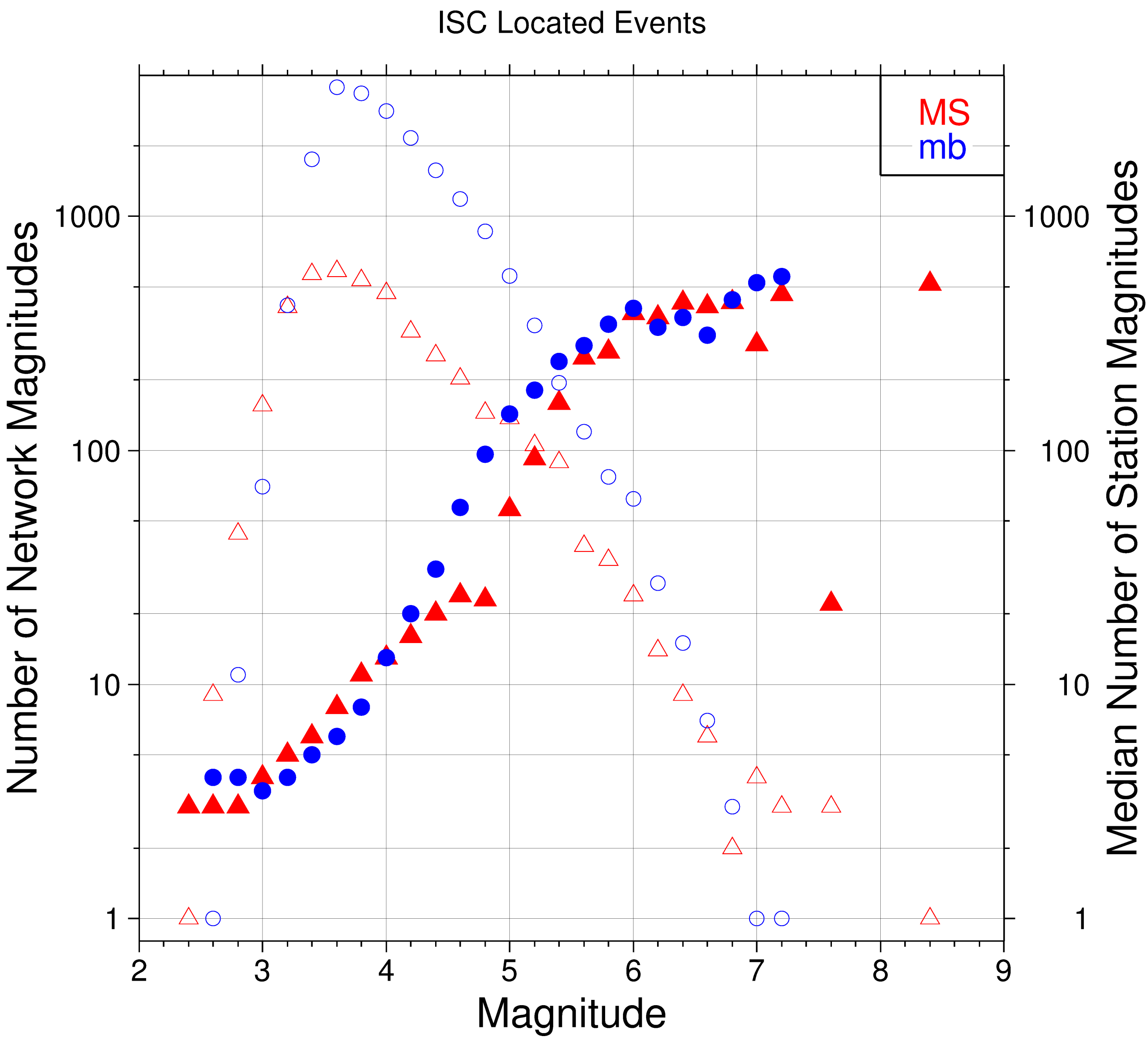

Figure 10.24: *Number of network magnitudes (open symbols) and median number of stations magnitudes (filled symbols). Blue circles refer to mb and red triangles to MS. The width of the magnitude interval δM is 0.2, and each symbol includes data with magnitude in $M \pm \delta M/2$.*

10.4 Completeness of the ISC Bulletin

The completeness of the ISC Bulletin can be expressed as a magnitude value, above which we expect the Bulletin to contain 100% of events. This magnitude of completeness, M_C can be measured as the point where the seismicity no longer follows the Gutenberg-Richter relationship. We compute an estimate of M_C using the maximum curvature technique of *Woessner and Wiemer* (2005).

The completeness of the ISC Bulletin for this summary period is shown in Figure 10.25. A history of completeness for the ISC Bulletin is shown in Figure 10.26. The step change in 1996 corresponds with the inclusion of the Prototype IDC (EIDC) Bulletin, followed by the Reviewed Event Bulletin (REB) of the IDC.

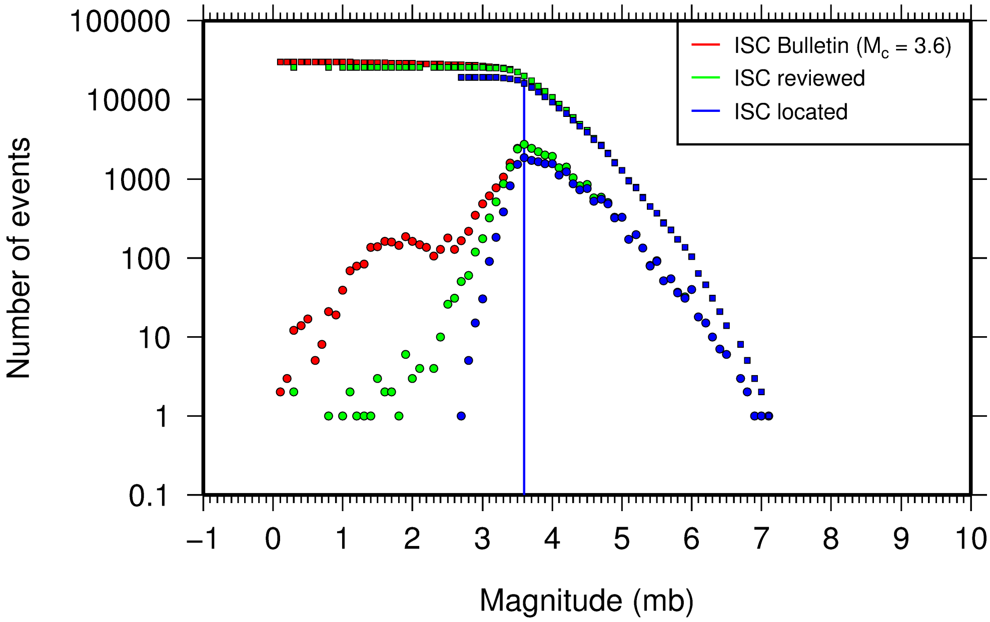

Figure 10.25: *Frequency and cumulative frequency magnitude distribution for all events in the ISC Bulletin, ISC reviewed events and events located by the ISC. The magnitude of completeness (M_C) is shown for the ISC Bulletin. Note: only events with values of mb are represented in the figure.*

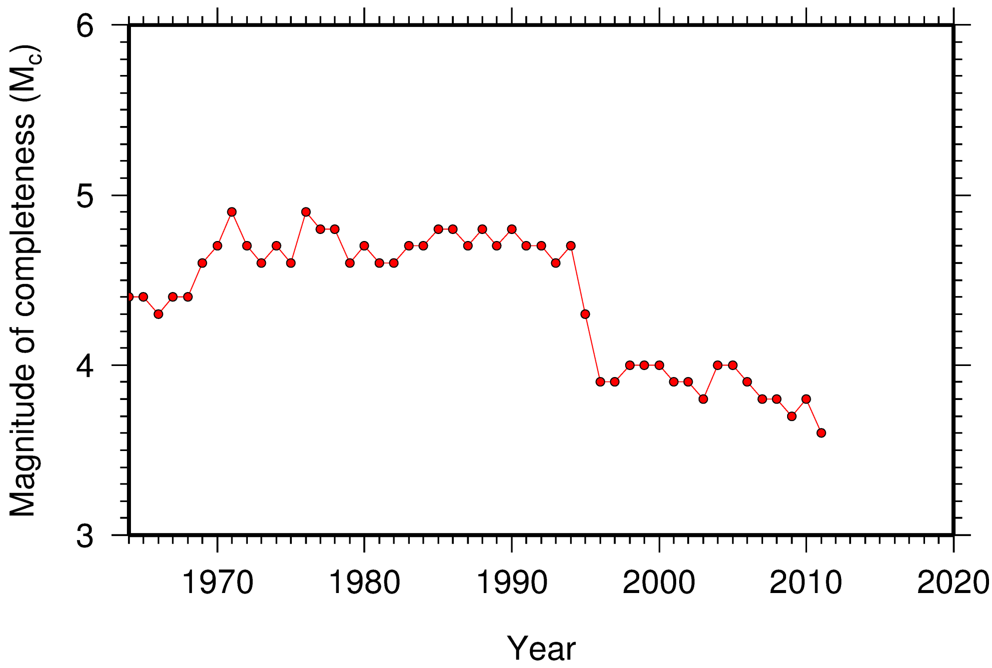

Figure 10.26: *Variation of magnitude of completeness (M_C) for each year in the ISC Bulletin. Note: M_C is calculated only using those events with values of mb.*

10.5 Magnitude Comparisons

The ISC Bulletin publishes network magnitudes reported by multiple agencies to the ISC. For events that have been located by the ISC, where enough amplitude data has been collected, the MS and mb magnitudes are calculated by the ISC (MS is computed only for depths $\leq$ 60 km). In this section, ISC magnitudes and some other reported magnitudes in the ISC Bulletin are compared.

The comparison between MS and mb computed by the ISC locator for events in this summary period is shown in Figure 10.27, where the large number of data pairs allows a colour coding of the data density. The scatter in the data reflects the fundamental differences between these magnitude scales.

Similar plots are shown in Figure 10.28 and 10.29, respectively, for comparisons of ISC mb and ISC MS with M_W from the GCMT catalogue. Since M_W is not often available below magnitude 5, these distributions are mostly for larger, global events. Not surprisingly, the scatter between mb and M_W is larger than the scatter between MS and M_W. Also, the saturation effect of mb is clearly visible for earthquakes with $M_W > 6.5$. In contrast, MS scales well with $M_W > 6$, whereas for smaller magnitudes MS appears to be systematically smaller than M_W.

In Figure 10.30 ISC values of mb are compared with all reported values of mb, values of mb reported by NEIC and values of mb reported by IDC. Similarly in Figure 10.31, ISC values of MS are compared with all reported values of MS, values of MS reported by NEIC and values of MS reported by IDC. There is a large scatter between the ISC magnitudes and the mb and MS reported by all other agencies.

The scatter decreases both for mb and MS when ISC magnitudes are compared just with NEIC and IDC magnitudes. This is not surprising as the latter two agencies provide most of the amplitudes and periods used by the ISC locator to compute MS and mb. However, ISC mb appears to be smaller than NEIC mb for $mb < 4$ and larger than IDC mb for $mb > 4$. Since NEIC does not include IDC amplitudes, it seems these features originate from observations at the high-gain, low-noise sites reported by the IDC. For the MS comparisons between ISC and NEIC a similar but smaller effect is observed for $MS < 4.5$, whereas a good scaling is generally observed for the MS comparisons between ISC and IDC.

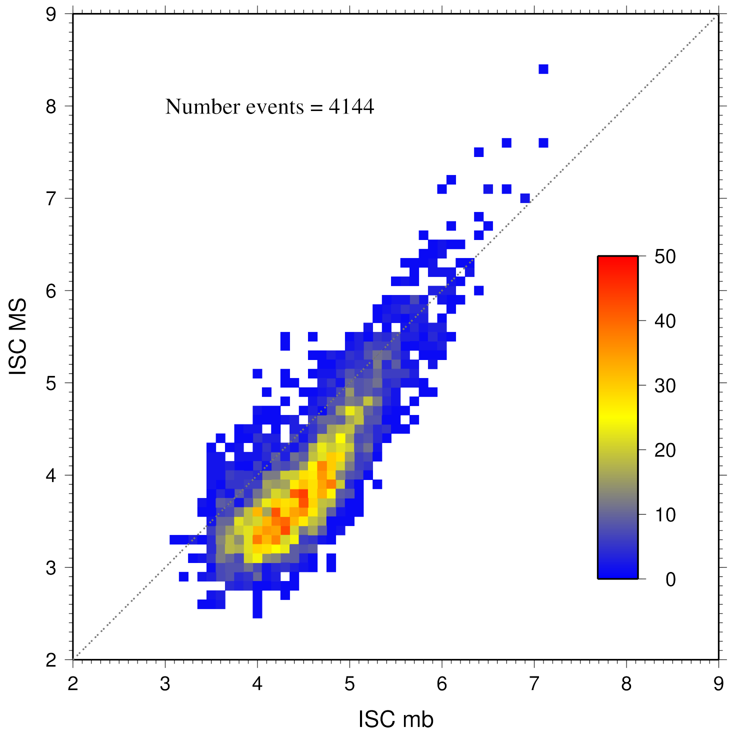

Figure 10.27: *Comparison of ISC values of MS with mb for common event pairs.*

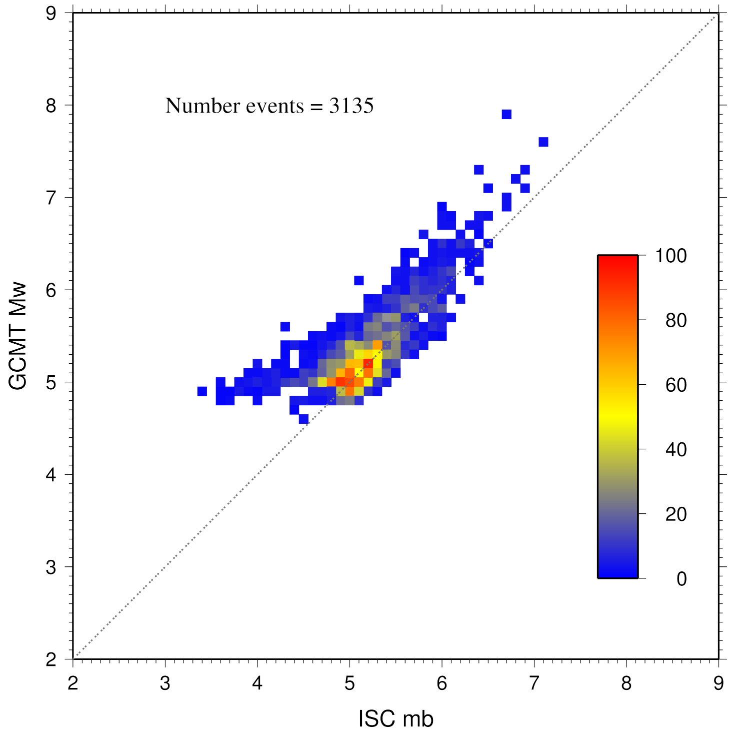

Figure 10.28: *Comparison of ISC values of mb with GCMT* M_W *for common event pairs.*

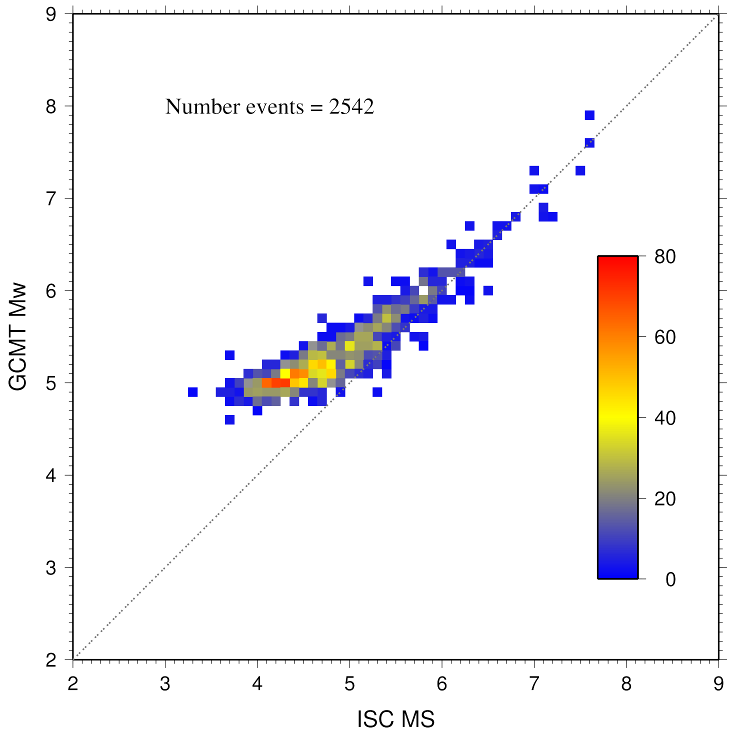

Figure 10.29: *Comparison of ISC values of* MS *with GCMT* M_W *for common event pairs.*

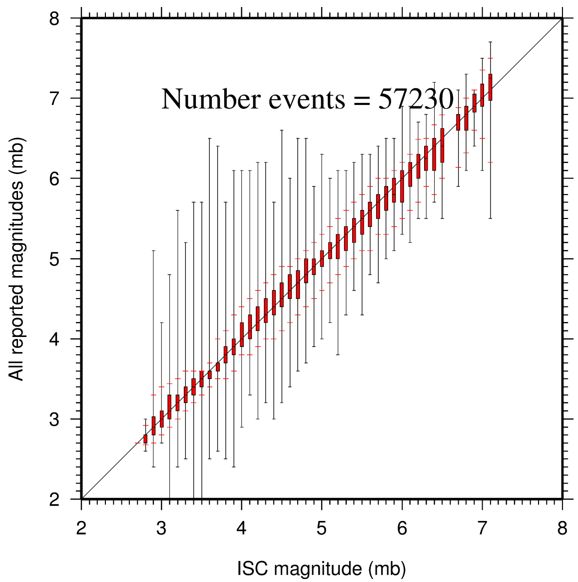

(a)

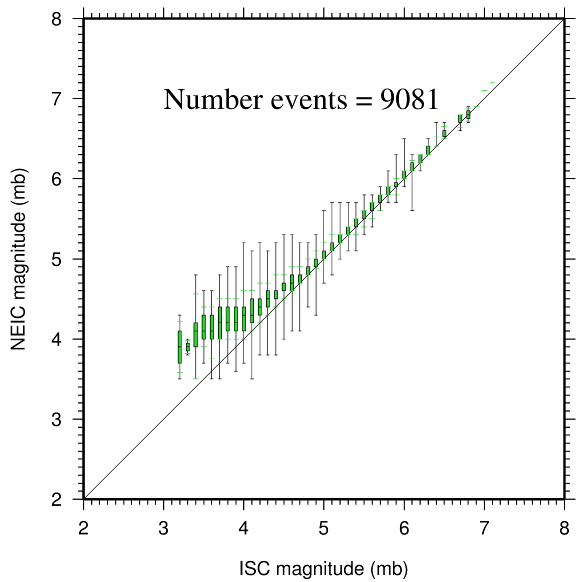

(b)

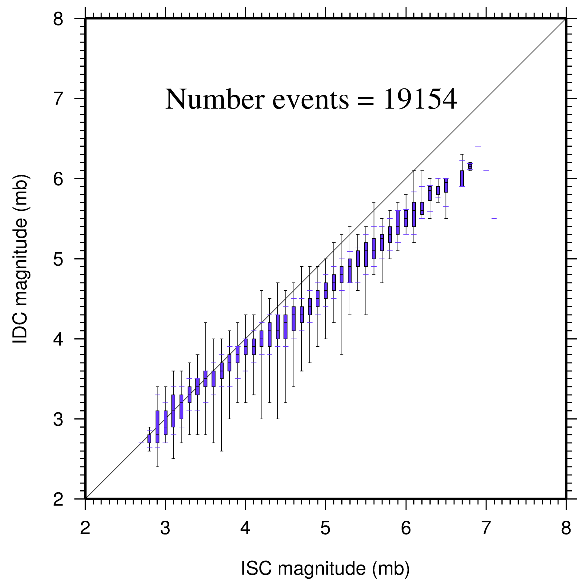

(c)

Figure 10.30: *Comparison of ISC magnitude data (mb) with additional agency magnitudes (mb). The statistical summary is shown in box-and-whisker plots where the 10th and 90th percentiles are shown in addition to the max and min values. (a): All magnitudes reported; (b): NEIC magnitudes; (c): IDC magnitudes.*

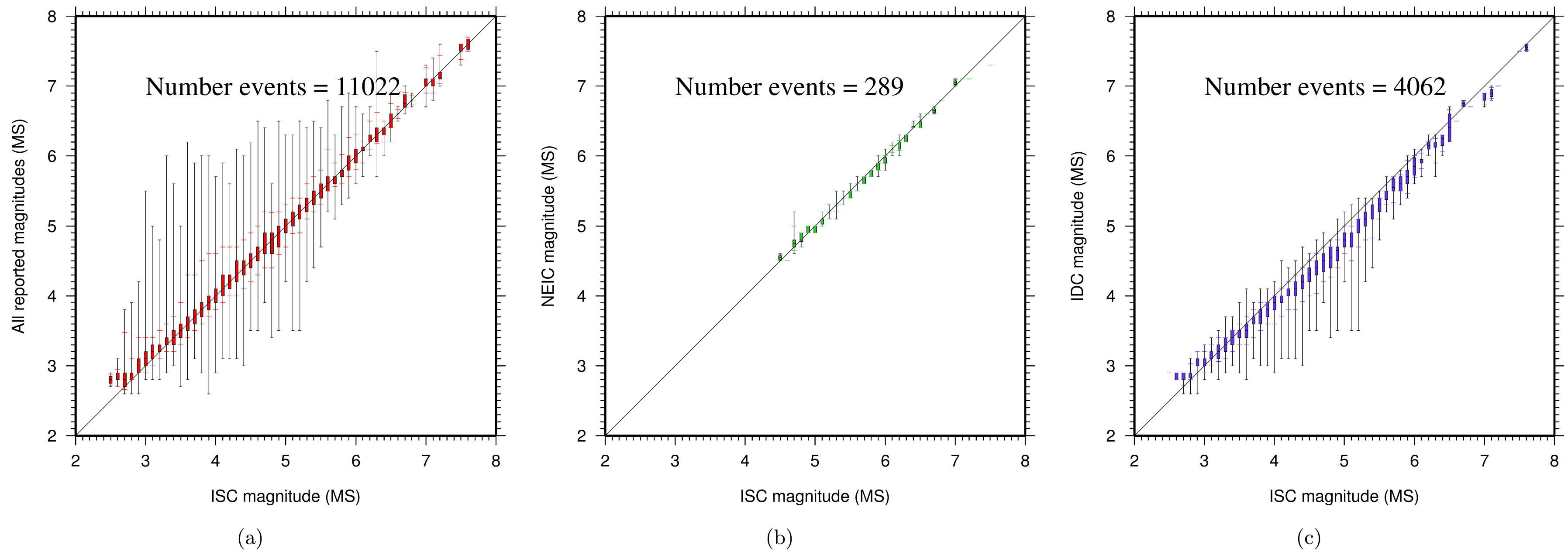

Figure 10.31: *Comparison of ISC magnitude data (MS) with additional agency magnitudes (MS). The statistical summary is shown in the box-and-whisker plots where the 10th and 90th percentiles are shown in addition to the max and min values. (a): All magnitudes reported; (b): NEIC magnitudes; (c): IDC magnitudes.*

11

The Leading Data Contributors

For the current six-month period, 131 agencies reported related bulletin data. Although we are grateful for every report, we nevertheless would like to acknowledge those agencies that made the most useful or distinct contributions to the contents of the ISC Bulletin. Here we note those agencies that:

- provided a comparatively large volume of parametric data (see Section 11.1),
- reported data that helped quite considerably to improve the quality of the ISC locations or magnitude determinations (see Section 11.2),
- helped the ISC by consistently reporting data in one of the standard recognised formats and in-line with the ISC data collection schedule (see Section 11.3).

We do not aim to discourage those numerous small networks who provide comparatively smaller yet still most essential volumes of regional data regularly, consistently and accurately. Without these reports the ISC Bulletin would not be as comprehensive and complete as it is today.

11.1 The Largest Data Contributors

We acknowledge the contribution of IDC, NEIC, MOS, BJI, USArray, NAO and a few others (Figure 11.1) that reported the majority of moderate to large events recorded at teleseismic distances. The contributions of NEIC, IDC, CSEM and several others, including JMA, MAT and NIED particularly in relation to Tohoku sequence events, are also acknowledged with respect to smaller seismic events. The contributions of JMA, NEIC, IDC, CSEM, and a number of others are also acknowledged with respect to small seismic events. Note that the NEIC bulletin accumulates a contribution of all regional networks in the USA. Similarly, the CSEM communicates contributions of many tens of European and Mediterranean networks a few of which the ISC does not always receive directly. Several agencies monitoring highly seismic regions routinely report large volumes of small to moderate magnitude events, such as those in Japan, Chinese Taipei, Turkey, Chile, Italy, Greece, New Zealand, Norway, Mexico and Columbia. Contributions of small magnitude events by agencies in regions of low seismicity, such as Finland and Saudia Arabia are also gratefully received.

We also would like to acknowledge contributions of those agencies that report a large portion of arrival time and amplitude data (Figure 11.2). For small magnitude events, these are local agencies in charge of monitoring local and regional seismicity. For moderate to large events, contributions of IDC, USArray, NEIC, MOS are especially acknowledged. Notably, three agencies (IDC, NEIC and MOS) together reported over 75% of all amplitude measurements made for teleseismically recorded events. We hope

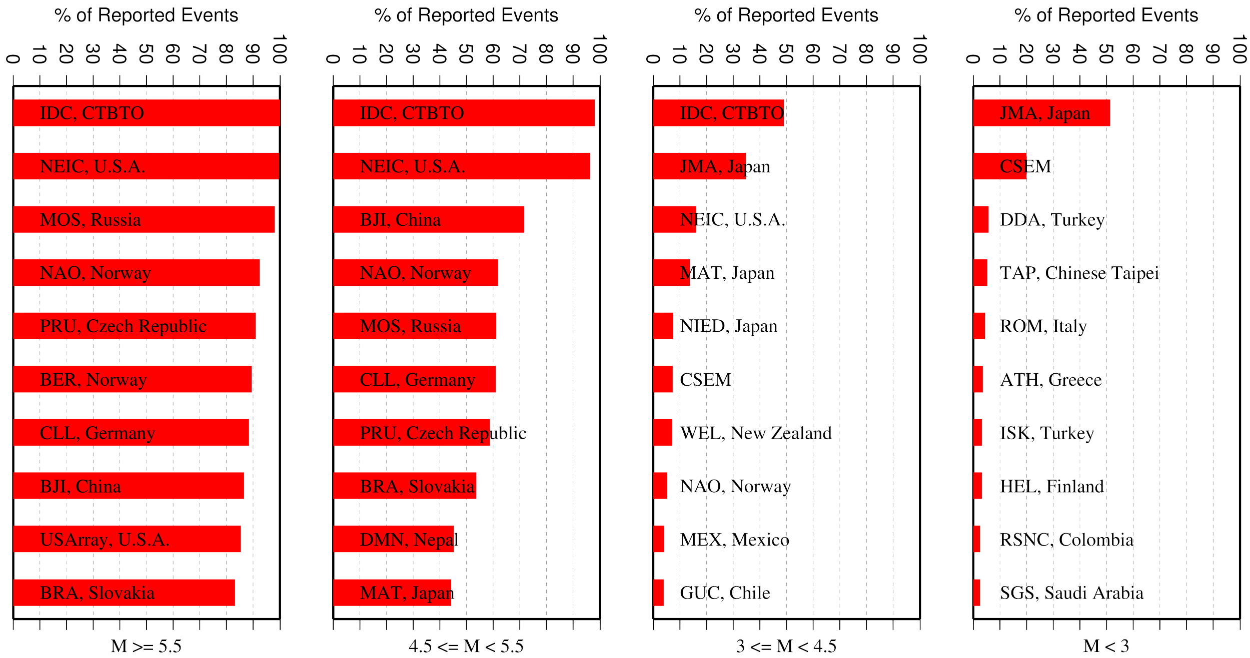

Figure 11.1: *Frequency of events in the ISC Bulletin for which an agency reported at least one item of data: a moment tensor, a hypocentre, a station arrival time or an amplitude. The top ten agencies are shown for four magnitude intervals.*

that other agencies would also be able to update their monitoring routines in the future to include the amplitude reports for teleseismic events compliant with the IASPEI standards.

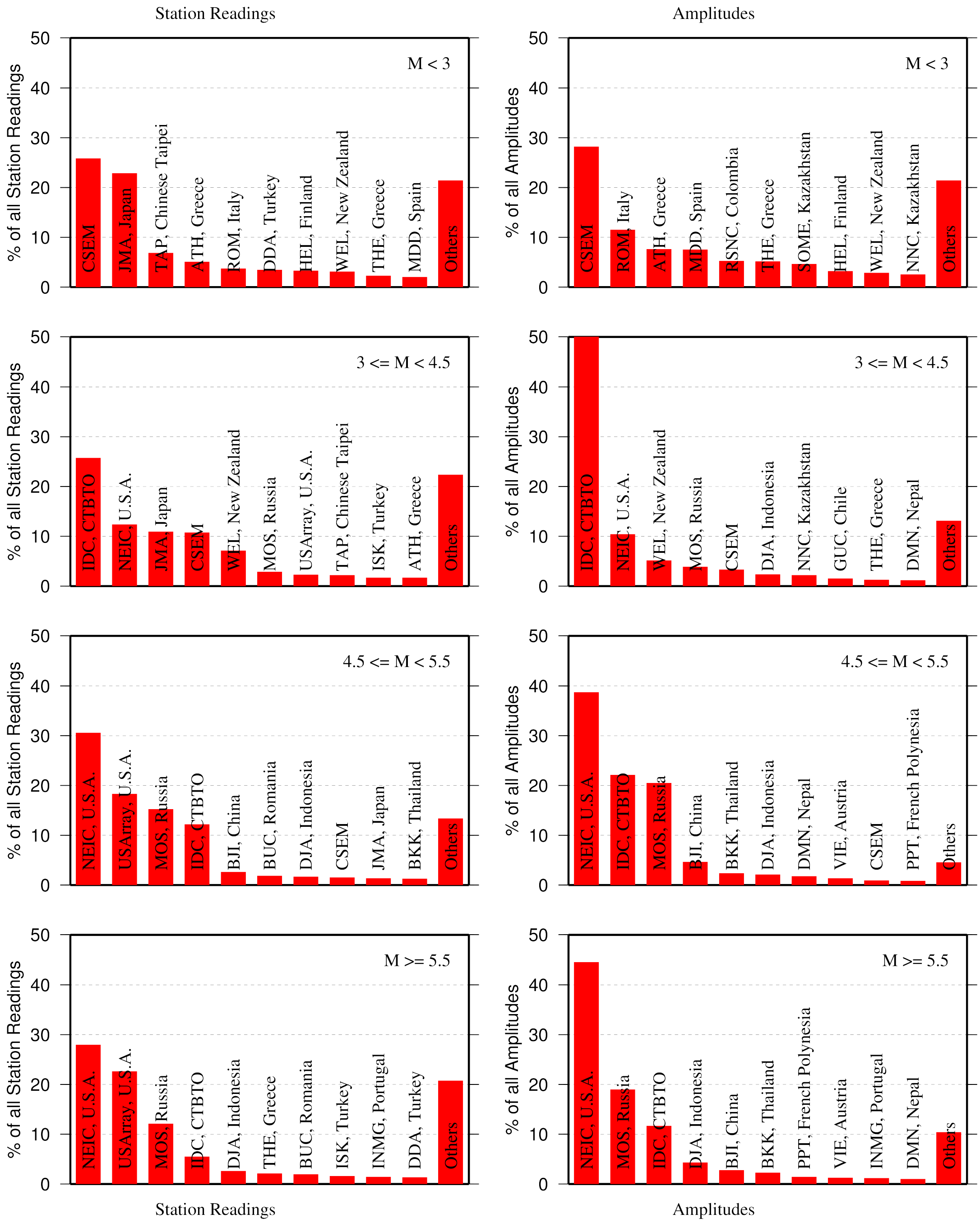

Figure 11.2: *Contributions of station arrival time readings (left) and amplitudes (right) of agencies to the ISC Bulletin. Top ten agencies are shown for four magnitude intervals.*

11.2 Contributors Reporting the Most Valuable Parameters

One of the main ISC duties is to re-calculate hypocentre estimates for those seismic events where a collective wealth of all station reports received from all agencies is likely to improve either the event location or depth compared to the hypocentre solution from each single agency. For areas with a sparse local seismic network or an unfavourable station configuration, readings made by other networks at teleseismic distances are very important. All events near mid-oceanic ridges as well as those in the majority of subduction zones around the world fall into this category. Hence we greatly appreciate the effort made by many agencies that report data for remote earthquakes (Figure 11.3). For some agencies, such as the IDC and the NEIC, it is part of their mission. For instance, the IDC reports almost every seismic event that is large enough to be recorded at teleseismic distance (20 degrees and beyond). This is largely because the International Monitoring System of primary arrays and broadband instruments is distributed at quiet sites around the world in order to be able to detect possible violations of the Comprehensive Nuclear-Test-Ban Treaty. The NEIC reported over 34% of those events as their mission requires them to report events above magnitude 4.5 outside the United States of America. For other agencies reporting distant events it is an extra effort that they undertake to notify their governments and relief agencies as well as to help the ISC and academic research in general. Hence these agencies usually report on the larger magnitude events. NAO, BJI, CLL, MOS, PRU, BRA, DMN and BUC each reported individual station arrivals for several percent of all relevant events. We encourage other agencies to report distant events to us.

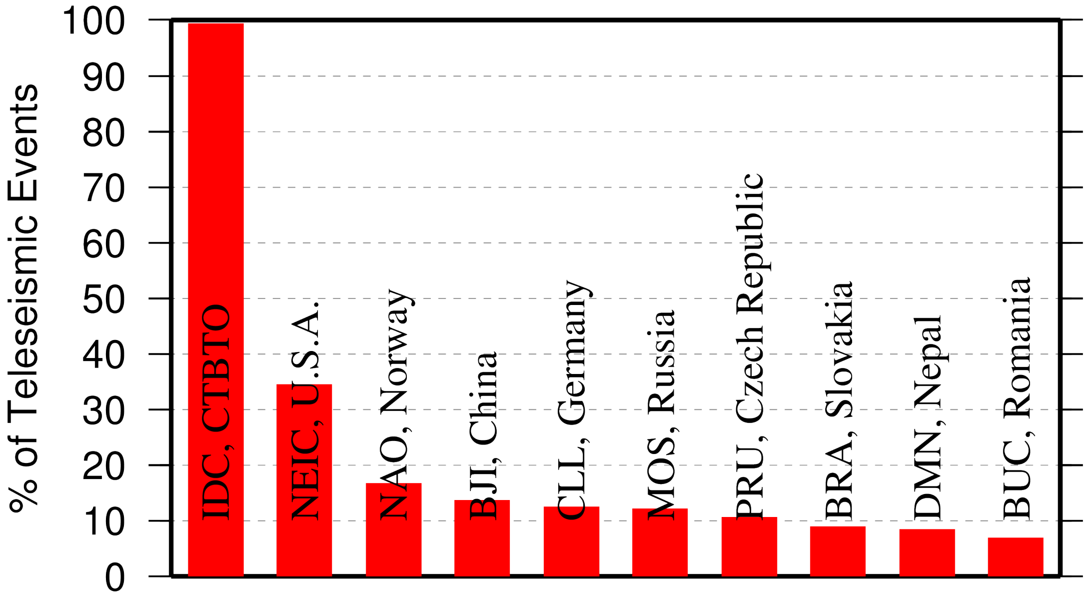

Figure 11.3: *Top ten agencies that reported teleseismic phase arrivals for a large portion of ISC events.*

In addition to the first arriving phase we encourage reporters to contribute observations of secondary seismic phases that help constrain the event location and depth: S, Sn, Sg and pP, sP, PcP (Figure 11.4). We expect though that these observations are actually made from waveforms, rather than just predicted by standard velocity models and modern software programs. It is especially important that these arrivals are manually reviewed by an operator (as we know takes place at the IDC and NEIC), as opposed to some lesser attempts to provide automatic phase readings that are later rejected by the ISC due to a generally poor quality of unreviewed picking.

Another important long-term task that the ISC performs is to compute the most definitive values of MS and mb network magnitudes that are considered reliable due to removal of outliers and consequent averaging (using alpha-trimmed median) across the largest network of stations, generally not feasible for a single agency. Despite concern over the bias at the lower end of mb introduced by the body wave amplitude data from the IDC, other agencies are also known to bias the results. This topic is further discussed in Section 10.5.

Notably, the IDC reports almost 100% of all events for which MS and mb are estimated. This is due to the standard routine that requires determination of body and surface wave magnitudes useful for

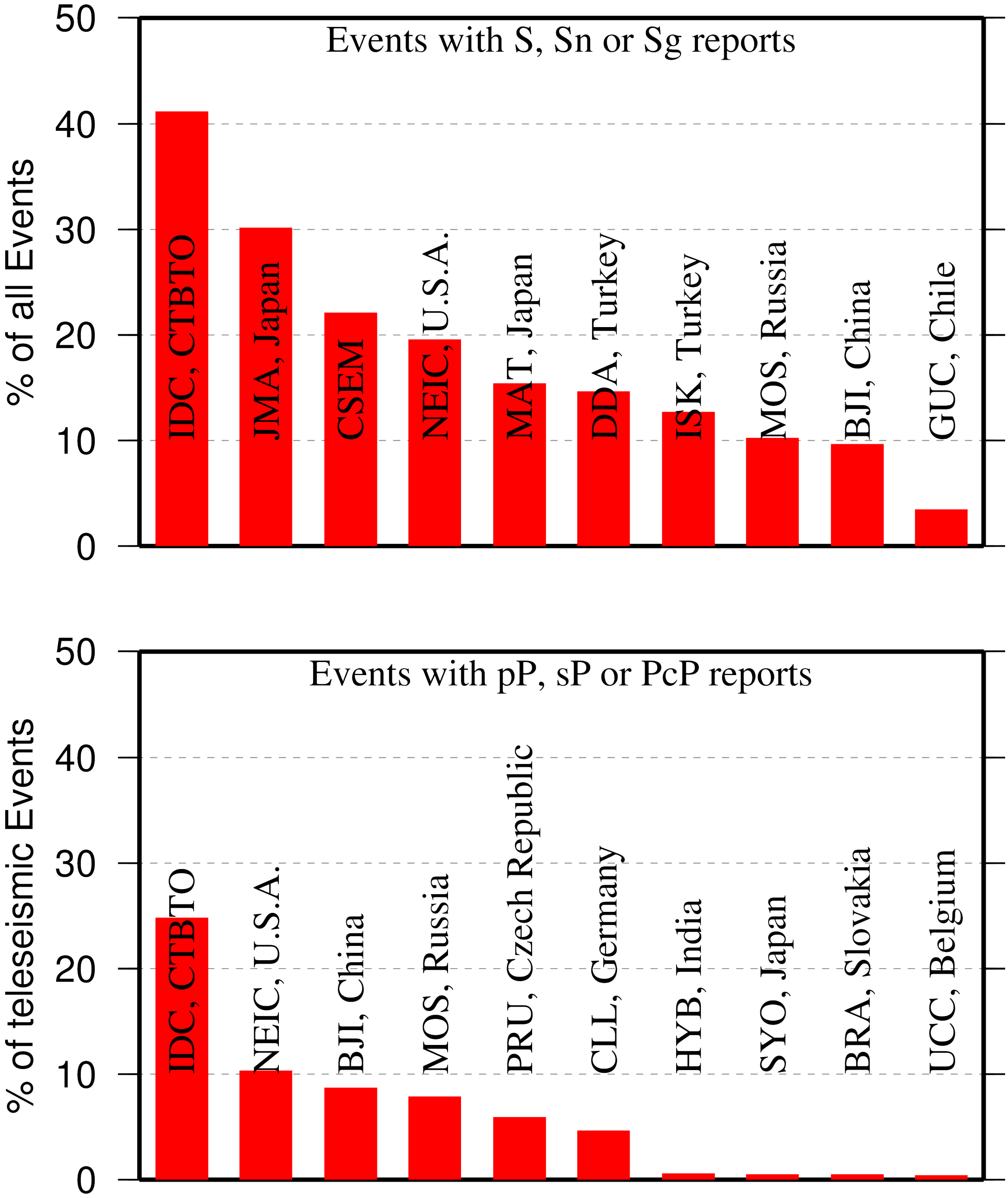

Figure 11.4: *Top ten agencies that reported secondary phases important for an accurate epicentre location (top) and focal depth determination (bottom).*

discrimination purposes. NEIC, MOS, BJI, NAO, PRU and a few other agencies (Figure 11.5) are also responsible for the majority of the amplitude and period reports that contribute towards the ISC magnitudes.

Since the ISC does not routinely process waveforms, we rely on other agencies to report moment magnitudes as well as moment tensor determinations (Figure 11.6).

Among other event parameters the ISC Bulletin also contains information on event type. We cannot independently verify the type of each event in the Bulletin and thus rely on other agencies to report the event type to us. Practices of reporting non-tectonic events vary greatly from country to country. Many agencies do not include anthropogenic events in their reports. Suppression of such events from

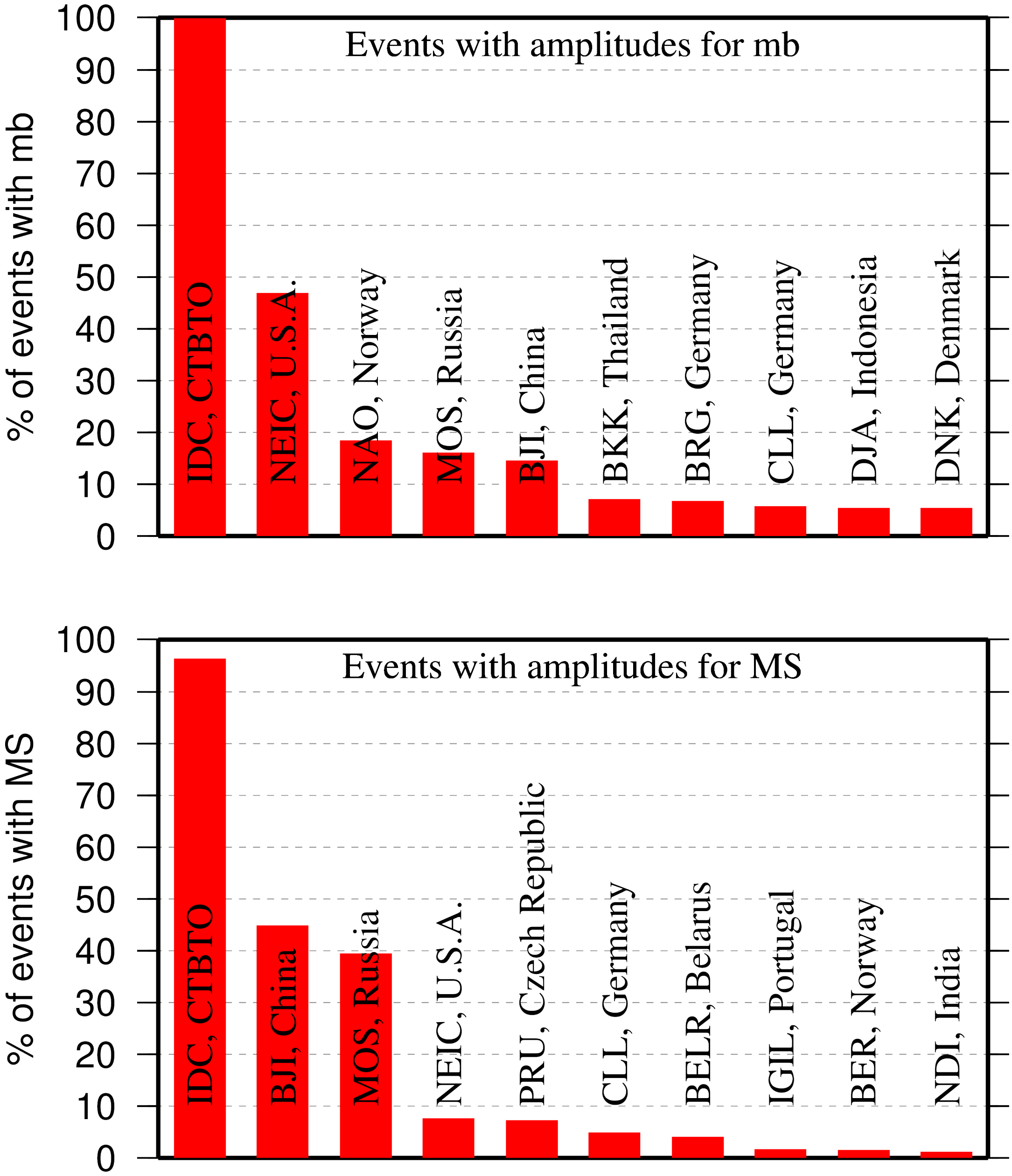

Figure 11.5: *Agencies that report defining body (top) and surface (bottom) wave amplitudes and periods for the largest fraction of those ISC Bulletin events with MS/mb determinations.*

reports to the ISC may lead to a situation where a neighbouring agency reports the anthropogenic event as an earthquake for which expected data are missing. This in turn is detrimental to ISC Bulletin users studying natural seismic hazard. Hence we encourage all agencies to join the agencies listed on Figure 11.7 and several others in reporting both natural and anthropogenic events to the ISC.

The ISC Bulletin also contains felt and damaging information when local agencies have reported it to us. Agencies listed on Figure 11.8 provide such information for the majority of all felt or damaging events in the ISC Bulletin.

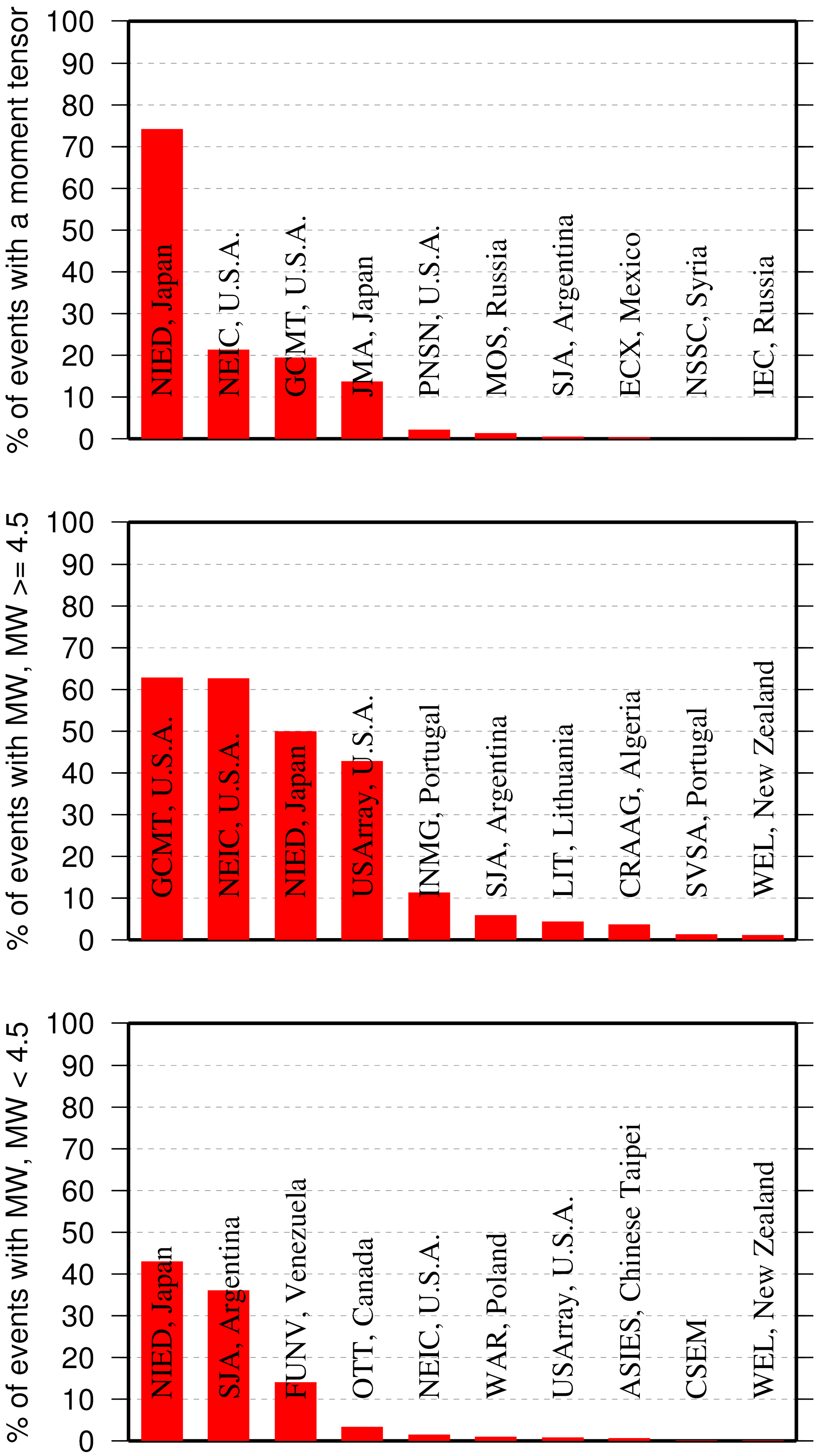

Figure 11.6: *Top ten agencies that most frequently report determinations of seismic moment tensor (top) and moment magnitude (middle/bottom for M greater/smaller than 4.5).*

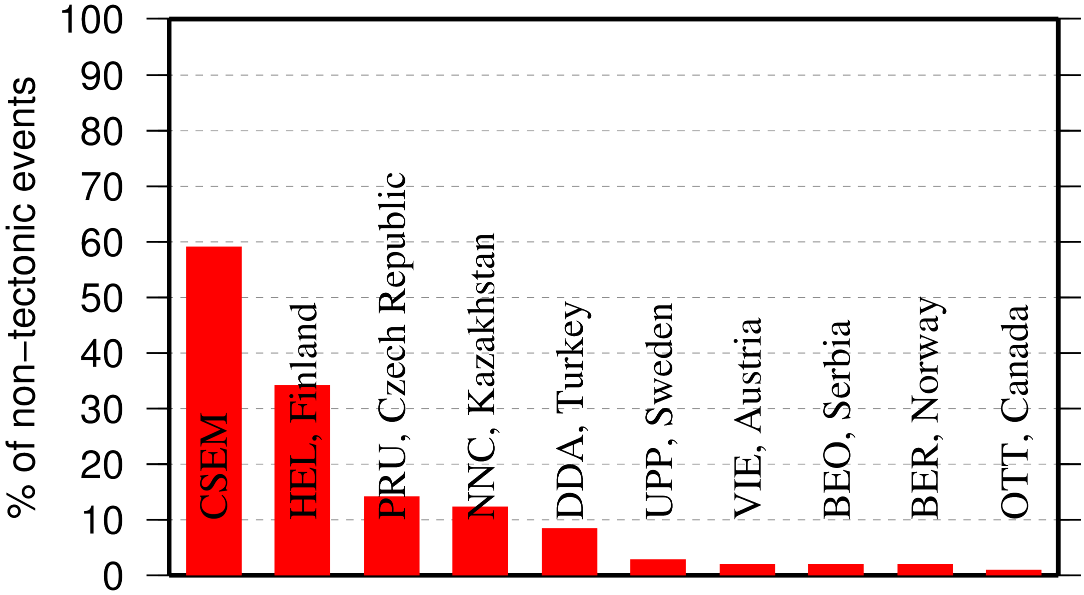

Figure 11.7: *Top ten agencies that most frequently report non-tectonic seismic events to the ISC.*

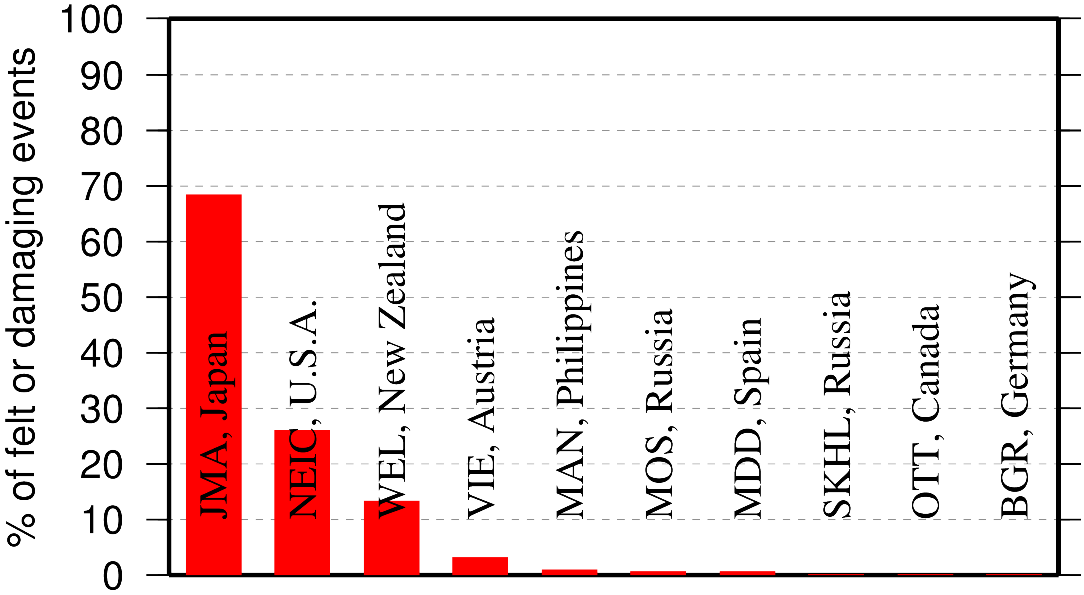

Figure 11.8: *Top ten agencies that most frequently report macroseismic information to the ISC.*

11.3 The Most Consistent and Punctual Contributors

During this six-month period, 30 agencies reported their bulletin data in one of the standard seismic formats (ISF, IMS, GSE or Nordic) and within the current 12-month deadline. Here we must reiterate that the ISC accepts reviewed bulletin data after a final analysis as soon as they are ready. These data, even if they arrive before the deadline, are immediately parsed into the ISC database, grouped with other data and become available to the ISC users on-line as part of the preliminary ISC Bulletin. There is no reason to wait until the deadline to send the data to the ISC. Table 11.1 lists all agencies that have been helpful to the ISC in this respect during the six-month period.

Table 11.1: *Agencies that contributed reviewed bulletin data to the ISC in one of the standard international formats before the submission deadline.*

Agency Code	Country	Average Delay from real time (days)
SSNC	Cuba	1
LDG	France	18
NAO	Norway	24
PPT	French Polynesia	24
PDG	Montenegro	31
LIC	Ivory Coast	34
IGIL	Portugal	35
KRSC	Russia	48
TIR	Albania	48
UCC	Belgium	49
SVSA	Portugal	53
IDC	Austria	54
DMN	Nepal	55
INMG	Portugal	77
BGR	Germany	79
SJA	Argentina	108
THE	Greece	109
ASRS	Russia	143
BER	Norway	150
BJI	China	160
AUST	Australia	171
NAM	Namibia	199
STR	France	265
BGS	United Kingdom	275
BYKL	Russia	296
GUC	Chile	313
LIT	Lithuania	321
BUL	Zimbabwe	324
ISN	Iraq	325
BUC	Romania	365

12

Appendix

Table 12.1: *Listing of all 313 agencies that have directly reported to the ISC. The 131 agencies highlighted in bold have reported data to the ISC Bulletin for the period of this Bulletin Summary.*

Agency Code	Agency Name
AAA	Alma-ata, Kazakhstan
AAE	**University of Addis Ababa, Ethiopia**
AAM	University of Michigan, USA
ADE	Primary Industries and Resources SA, Australia
ADH	Observatorio Afonso Chaves, Portugal
AEIC	Alaska Earthquake Information Center, USA
AFAR	The Afar Depression: Interpretation of the 1960-2000 Earthquakes, Israel
ALG	Algiers University, Algeria
ANF	USArray Array Network Facility, USA
ANT	Antofagasta, Chile
ARE	Instituto Geofisico del Peru, Peru
ARO	**Observatoire Géophysique d'Arta, Djibouti**
ASIES	**Institute of Earth Sciences, Academia Sinica, Chinese Taipei**
ASL	Albuquerque Seismological Laboratory, USA
ASM	University of Asmara, Eritrea
ASRS	**Altai-Sayan Seismological Centre, GS SB RAS, Russia**
ATA	The Earthquake Research Center Ataturk University, Turkey
ATH	**National Observatory of Athens, Greece**
AUST	**Geoscience Australia, Australia**
AWI	**Alfred Wegener Institute for Polar and Marine Research, Germany**
AZER	**Republic Center of Seismic Survey, Azerbaijan**
BCIS	Bureau Central International de Sismologie, France
BDF	Observatório Sismológico da Universidade de Brasília, Brazil
BELR	**Centre of Geophysical Monitoring, Belarus**
BEO	**Seismological Survey of Serbia, Serbia**
BER	**University of Bergen, Norway**
BERK	Berkheimer H, Germany
BGR	**Bundesanstalt für Geowissenschaften und Rohstoffe, Germany**
BGS	**British Geological Survey, United Kingdom**
BHUJ2	Study of Aftershocks of the Bhuj Earthquake by Japanese Research Team, Japan
BIAK	Biak earthquake aftershocks (17-Feb-1996), USA
BJI	**China Earthquake Networks Center, China**
BKK	**Thai Meteorological Department, Thailand**
BNS	Erdbebenstation, Geologisches Institut der Universität, Köl, Germany
BOG	Universidad Javeriana, Colombia
BRA	**Geophysical Institute, Slovak Academy of Sciences, Slovakia**

Table 12.1: Continued.

Agency Code	Agency Name
BRG	**Seismological Observatory Berggießhübel, TU Bergakademie Freiberg, Germany**
BRK	Berkeley Seismological Laboratory, USA
BRS	Brisbane Seismograph Station, Australia
BUC	**National Institute for Earth Physics, Romania**
BUD	**Geodetic and Geophysical Research Institute, Hungary**
BUG	Institute of Geology, Mineralogy & Geophysics, Germany
BUL	**Goetz Observatory, Zimbabwe**
BUT	Montana Bureau of Mines and Geology, USA
BYKL	**Baykal Regional Seismological Centre, GS SB RAS, Russia**
CADCG	Central America Data Centre, Costa Rica
CAN	Australian National University, Australia
CANSK	Canadian and Scandinavian Networks, Sweden
CAR	Instituto Sismologico de Caracas, Venezuela
CASC	**Central American Seismic Center, Costa Rica**
CERI	Center for Earthquake Research and Information, USA
CLL	**Geophysikalisches Observatorium Collm, Germany**
CNG	Seismographic Station Changalane, Mozambique
CNRM	Centre National de Recherche, Morocco
COSMOS	Consortium of Organizations for Strong Motion Observations, USA
CRAAG	**Centre de Recherche en Astronomie, Astrophysique et Géophysique, Algeria**
CSC	University of South Carolina, USA
CSEM	**Centre Sismologique Euro-Méditerranéen (CSEM/EMSC), France**
DASA	Defense Atomic Support Agency, USA
DBN	**Koninklijk Nederlands Meteorologisch Instituut, Netherlands**
DDA	**Disaster and Emergency Management Presidency, Turkey**
DHMR	**Yemen National Seismological Center, Yemen**
DIAS	**Dublin Institute for Advanced Studies, Ireland**
DJA	**Badan Meteorologi, Klimatologi dan Geofisika, Indonesia**
DMN	**Department of Mines and Geology, Ministry of Industry of Nepal, Nepal**
DNK	**Geological Survey of Denmark and Greenland, Denmark**
DSN	**Dubai Seismic Network, United Arab Emirates**
DUSS	Damascus University, Syria, Syria
EAF	East African Network
EAGLE	Ethiopia-Afar Geoscientific Lithospheric Experiment
EBR	Observatori de l'Ebre, Spain
EBSE	Ethiopian Broadband Seismic Experiment
ECX	**Red Sismica del Noroeste de Mexico (RESOM), Mexico**
EFATE	OBS Experiment near Efate, Vanuatu, USA
EHB	Engdahl, van der Hilst and Buland, USA
EIDC	Experimental (GSETT3) International Data Center, USA
EKA	Eskdalemuir Array Station, United Kingdom
ENT	Geological Survey and Mines Department, Uganda
EPSI	Reference events computed by the ISC for EPSI project, United Kingdom

Table 12.1: Continued.

Agency Code	Agency Name
ERDA	Energy Research and Development Administration, USA
EST	Geological Survey of Estonia, Estonia
FBR	Fabra Observatory, Spain
FDF	Fort de France, Martinique
FIA0	Finessa Array, Finland
FOR	Unknown Historical Agency, Unknown - historical agency
FUNV	**Fundación Venezolana de Investigaciones Sismológicas, Venezuela**
FUR	Geophysikalisches Observatorium der Universität München, Germany
GBZT	Marmara Research Center, Turkey
GCG	INSIVUMEH, Guatemala
GCMT	**The Global CMT Project, USA**
GDNRW	Geologischer Dienst Nordrhein-Westfalen, Germany
GEN	Dipartimento per lo Studio del Territorio e delle sue Risorse (RSNI), Italy
GFZ	Helmholtz Centre Potsdam GFZ German Research Centre For Geosciences, Germany
GII	**The Geophysical Institute of Israel, Israel**
GOM	Observatoire Volcanologique de Goma, Democratic Republic of the Congo
GRAL	**National Council for Scientific Research, Lebanon**
GSDM	Geological Survey Department Malawi, Malawi
GTFE	German Task Force for Earthquakes, Germany
GUC	**Departamento de Geofísica, Universidad de Chile, Chile**
HAN	Hannover, Germany
HDC	Observatorio Vulcanológico y Sismológico de Costa Rica, Costa Rica
HEL	**Institute of Seismology, University of Helsinki, Finland**
HFS	Hagfors Observatory, Sweden
HFS1	Hagfors Observatory, Sweden
HFS2	Hagfors Observatory, Sweden
HKC	**Hong Kong Observatory, Hong Kong**
HLUG	Hessisches Landesamt für Umwelt und Geologie, Germany
HLW	**National Research Institute of Astronomy and Geophysics, Egypt**
HNR	**Ministry of Mines, Energy and Rural Electrification, Solomon Islands**
HON	Pacific Tsunami Warning Center - NOAA, USA
HRVD	Harvard University, USA
HRVD_LR	Department of Geological Sciences, Harvard University, USA
HVO	Hawaiian Volcano Observatory, USA
HYB	**National Geophysical Research Institute, India**
HYD	National Geophysical Research Institute, India
IAG	Instituto Andaluz de Geofisica, Spain
IASPEI	**IASPEI Working Group on Reference Events, USA**
ICE	Instituto Costarricense de Electricidad, Costa Rica
IDC	**International Data Centre, CTBTO, Austria**

Table 12.1: *Continued.*

Agency Code	Agency Name
IEPN	Institute of Environmental Problems of the North, Russian Academy of Sciences, Russia
IGIL	**Instituto Geofisico do Infante Dom Luiz**, **Portugal**
IGQ	**Servicio Nacional de Sismología y Vulcanología**, **Ecuador**
IGS	Institute of Geological Sciences, United Kingdom
INDEPTH3	International Deep Profiling of Tibet and the Himalayas, USA
INET	Instituto Nicaragüense de Estudios Territoriales, Nicaragua
INMG	**Instituto Português do Mar e da Atmosfera, I.P.**, **Portugal**
IPEC	Ústav fyziky Země, Czech Republic
IPRG	Institute for Petroleum Research and Geophysics, Israel
IRIS	**IRIS Data Management Center**, **USA**
IRSM	Institute of Rock Structure and Mechanics, Czech Republic
ISK	**Kandilli Observatory and Research Institute**, **Turkey**
ISN	**Iraqi Meteorological and Seismology Organisation**, **Iraq**
ISS	International Seismological Summary, United Kingdom
IST	Institute of Physics of the Earth, Technical University of Istanbul, Turkey
JEN	Geodynamisches Observatorium Moxa, Germany
JMA	**Japan Meteorological Agency**, **Japan**
JOH	Bernard Price Institute of Geophysics, South Africa
JSN	**Jamaica Seismic Network**, **Jamaica**
JSO	**Jordan Seismological Observatory**, **Jordan**
KBC	Institut de Recherches Géologiques et Minières, Cameroon
KEW	Kew Observatory, United Kingdom
KHC	Geofysikalni Ustav, Ceske Akademie Ved, Czech Republic
KISR	Kuwait Institute for Scientific Research, Kuwait
KLM	**Malaysian Meteorological Service**, **Malaysia**
KMA	**Korea Meteorological Administration**, **Republic of Korea**
KNET	**Kyrgyz Seismic Network**, **Kyrgyzstan**
KOLA	**Kola Regional Seismic Centre, GS RAS**, **Russia**
KRL	Geodätisches Institut der Universität Karlsruhe, Germany
KRNET	**Institute of Seismology, Academy of Sciences of Kyrgyz Republic**, **Kyrgyzstan**
KRSC	**Kamchatkan Experimental and Methodical Seismological Department, GS RAS**, **Russia**
KSA	Observatoire de Ksara, Lebanon
KUK	Geological Survey Department of Ghana, Ghana
LAO	Large Aperture Seismic Array, USA
LDG	**Laboratoire de Détection et de Géophysique/CEA**, **France**
LDN	University of Western Ontario, Canada
LDO	Lamont-Doherty Earth Observatory, USA
LED	Landeserdbebendienst Baden-Württemberg, Germany
LEDBW	Landeserdbebendienst Baden-Württemberg, Germany
LER	Besucherbergwerk Binweide Station, Germany
LIB	Tripoli, Libya
LIC	**Station Géophysique de Lamto**, **Ivory Coast**
LIM	Lima, Peru
LIS	Instituto de Meteorologia, Portugal

Table 12.1: Continued.

Agency Code	Agency Name
LIT	**Geological Survey of Lithuania**, **Lithuania**
LJU	**Environmental Agency of the Republic of Slovenia**, **Slovenia**
LPA	**Universidad Nacional de La Plata**, **Argentina**
LSZ	**Geological Survey Department of Zambia**, **Zambia**
LVSN	Latvian Seismic Network, Latvia
MAN	**Philippine Institute of Volcanology and Seismology**, **Philippines**
MAT	**The Matsushiro Seismological Observatory**, **Japan**
MCO	**Macao Meteorological and Geophysical Bureau**, **Macao, China**
MDD	**Instituto Geográfico Nacional**, **Spain**
MED_RCMT	MedNet Regional Centroid - Moment Tensors, Italy
MES	Messina Seismological Observatory, Italy
MEX	**Instituto de Geofísica de la UNAM**, **Mexico**
MIRAS	Mining Institute of the Ural Branch of the Russian Academy of Sciences, Russia
MOLD	**Institute of Geophysics and Geology**, **Moldova**
MOS	**Geophysical Survey of Russian Academy of Sciences**, **Russia**
MOZ	Direccao Nacional de Geologia, Mozambique
MRB	Institut Cartogràfic de Catalunya, Spain
MSI	Messina Seismological Observatory, Italy
MSSP	**Micro Seismic Studies Programme, PINSTECH**, **Pakistan**
MUN	Mundaring Observatory, Australia
NAI	University of Nairobi, Kenya
NAM	**The Geological Survey of Namibia**, **Namibia**
NAO	**Stiftelsen NORSAR**, **Norway**
NCEDC	Northern California Earthquake Data Center, USA
NDI	**India Meteorological Department**, **India**
NEIC	**National Earthquake Information Center**, **USA**
NEIS	National Earthquake Information Service, USA
NERS	**North Eastern Regional Seismological Centre, GS RAS**, **Russia**
NIC	**Cyprus Geological Survey Department**, **Cyprus**
NIED	**National Research Institute for Earth Science and Disaster Prevention**, **Japan**
NNC	**National Nuclear Center**, **Kazakhstan**
NOU	IRD Centre de Nouméa, New Caledonia
NSSC	**National Syrian Seismological Center**, **Syria**
NSSP	**National Survey of Seismic Protection**, **Armenia**
OBM	**Research Centre of Astronomy and Geophysics**, **Mongolia**
OGSO	Ohio Geological Survey, USA
OMAN	**Sultan Qaboos University**, **Oman**
ORF	Orfeus Data Center, Netherlands
OTT	**Canadian Hazards Information Service, Natural Resources Canada**, **Canada**
PAL	Palisades, USA
PAS	California Institute of Technology, USA
PDA	Universidade dos Açores, Portugal
PDG	**Seismological Institute of Montenegro**, **Montenegro**
PEK	Peking, China

Table 12.1: Continued.

Agency Code	Agency Name
PGC	Pacific Geoscience Centre, Canada
PLV	**National Center for Scientific Research, Vietnam**
PMEL	Pacific seismicity from hydrophones, USA
PMR	Alaska Tsunami Warning Center,, USA
PNSN	**Pacific Northwest Seismic Network, USA**
PPT	**Laboratoire de Géophysique/CEA, French Polynesia**
PRE	**Council for Geoscience, South Africa**
PRU	**Geophysical Institute, Academy of Sciences of the Czech Republic, Czech Republic**
PTO	Instituto Geofísico da Universidade do Porto, Portugal
PTWC	Pacific Tsunami Warning Center, USA
QCP	**Manila Observatory, Philippines**
QUE	Pakistan Meteorological Department, Pakistan
QUI	Escuela Politécnica Nacional, Ecuador
RAB	Rabaul Volcanological Observatory, Papua New Guinea
RBA	Université Mohammed V, Morocco
REN	MacKay School of Mines, USA
REY	**Icelandic Meteorological Office, Iceland**
RMIT	Royal Melbourne Institute of Technology, Australia
ROC	Odenbach Seismic Observatory, USA
ROM	**Istituto Nazionale di Geofisica e Vulcanologia, Italy**
RRLJ	Regional Research Laboratory Jorhat, India
RSMAC	Red Sísmica Mexicana de Apertura Continental, Mexico
RSNC	**Red Sismológica Nacional de Colombia, Colombia**
RSPR	**Red Sísmica de Puerto Rico, USA**
RYD	King Saud University, Saudi Arabia
SAPSE	Southern Alps Passive Seismic Experiment, New Zealand
SAR	Sarajevo Seismological Station, Bosnia and Herzegovina
SCB	**Observatorio San Calixto, Bolivia**
SCEDC	Southern California Earthquake Data Center, USA
SDD	Universidad Autonoma de Santo Domingo, Dominican Republic
SEA	Geophysics Program AK-50, USA
SEPA	Seismic Experiment in Patagonia and Antarctica, USA
SET	Setif Observatory, Algeria
SFS	Real Instituto y Observatorio de la Armada, Spain
SGS	**Saudi Geological Survey, Saudi Arabia**
SHL	Central Seismological Observatory, India
SIGU	**Subbotin Institute of Geophysics, National Academy of Sciences, Ukraine**
SIK	Seismic Institute of Kosovo, Kosovo
SIO	**Scripps Institution of Oceanography, USA**
SJA	**Instituto Nacional de Prevención Sísmica, Argentina**
SJS	Instituto Costarricense de Electricidad, Costa Rica
SKHL	**Sakhalin Experimental and Methodological Seismological Expedition, GS RAS, Russia**
SKL	Sakhalin Complex Scientific Research Institute, Russia
SKO	**Seismological Observatory Skopje, FYR Macedonia**

Table 12.1: Continued.

Agency Code	Agency Name
SLC	Salt Lake City, USA
SLM	Saint Louis University, USA
SNET	Servicio Nacional de Estudios Territoriales, El Salvador
SNM	New Mexico Institute of Mining and Technology, USA
SNSN	Saudi National Seismic Network, Saudi Arabia
SOF	**Geophysical Institute, Bulgarian Academy of Sciences, Bulgaria**
SOME	**Seismological Experimental Methodological Expedition, Kazakhstan**
SPA	USGS - South Pole, Antarctica
SPGM	Service de Physique du Globe, Morocco
SRI	Stanford Research Institute, USA
SSN	Sudan Seismic Network, Sudan
SSNC	**Servicio Sismológico Nacional Cubano, Cuba**
SSS	Centro de Estudios y Investigaciones Geotecnicas del San Salvador, El Salvador
STK	Stockholm Seismological Station, Sweden
STR	**Institut de Physique du Globe, France**
STU	Stuttgart Seismological Station, Germany
SVSA	**Sistema de Vigilância Sismológica dos Açores, Portugal**
SYO	**National Institute of Polar Research, Japan**
SZGRF	Seismologisches Zentralobservatorium Gräfenberg, Germany
TAC	Estación Central de Tacubaya, Mexico
TAN	Antananarivo, Madagascar
TANZANIA	Tanzania Broadband Seismic Experiment, USA
TAP	**CWB, Chinese Taipei**
TAU	University of Tasmania, Australia
TEH	**Tehran University, Iran**
TEIC	Center for Earthquake Research and Information, USA
THE	**Department of Geophysics, Aristotle University of Thessaloniki, Greece**
THR	**International Institute of Earthquake Engineering and Seismology (IIEES), Iran**
TIF	**Seismic Monitoring Centre of Georgia, Georgia**
TIR	**The Institute of Seismology, Academy of Sciences of Albania, Albania**
TRI	**Istituto Nazionale di Oceanografia e di Geofisica Sperimentale (OGS), Italy**
TRN	**University of the West Indies, Trinidad and Tobago**
TTG	Titograd Seismological Station, Montenegro
TUL	Oklahoma Geological Survey, USA
TUN	Institut National de la Météorologie, Tunisia
TVA	Tennessee Valley Authority, USA
TZN	University of Dar Es Salaam, Tanzania
UAV	Red Sismológica de Los Andes Venezolanos, Venezuela
UCC	**Royal Observatory of Belgium, Belgium**
UCR	Universidad de Costa Rica, Costa Rica
UGN	Institute of Geonics AS CR, Czech Republic

Table 12.1: *Continued.*

Agency Code	Agency Name
ULE	University of Leeds, United Kingdom
UNAH	Universidad Nacional Autonoma de Honduras, Honduras
UPA	Universidad de Panama, Panama
UPP	**University of Uppsala**, **Sweden**
UPSL	University of Patras, Department of Geology, Greece
USAEC	United States Atomic Energy Commission, USA
USCGS	United States Coast and Geodetic Survey, USA
USGS	**United States Geological Survey**, **USA**
UUSS	The University of Utah Seismograph Stations, USA
UVC	Universidad del Valle, Colombia
VAO	**Instituto Astronomico e Geofísico**, **Brazil**
VIE	**Österreichischer Geophysikalischer Dienst**, **Austria**
VSI	University of Athens, Greece
WAR	**Institute of Geophysics, Polish Academy of Sciences**, **Poland**
WBNET	**West Bohemia Seismic Network**, **Czech Republic**
WEL	**Institute of Geological and Nuclear Sciences**, **New Zealand**
WES	Weston Observatory, USA
YARS	**Yakutiya Regional Seismological Center, GS SB RAS**, **Russia**
ZAG	**Seismological Survey of the Republic of Croatia**, **Croatia**
ZUR	**Swiss Seismological Sevice (SED)**, **Switzerland**
ZUR_RMT	Zurich Moment Tensors, Switzerland

Table 12.2: *Phases reported to the ISC. These include phases that could not be matched to an appropriate* ak135 *phases. Those agencies that reported at least 10% of a particular phase are also shown.*

Reported Phase	Total	Agencies reporting
P	3378314	NEIC (18%), JMA (13%)
S	1253465	JMA (33%), CSEM (12%)
Pg	337086	CSEM (53%), ROM (19%)
Pn	326173	CSEM (34%), NEIC (30%), IDC (14%)
pmax	272986	MOS (82%), BJI (18%)
Sg	235800	CSEM (50%), ROM (22%)
LR	203912	IDC (37%), NEIC (31%), BJI (29%)
PN	183347	WEL (53%), ISK (30%)
AML	168049	ATH (42%), WEL (38%)
Sn	103950	CSEM (26%), NEIC (19%), IDC (17%)
NULL	93384	MOS (49%), RSNC (25%)
Lg	93322	CSEM (46%), MDD (28%), NNC (14%)
PG	74052	ISK (43%), HEL (18%), WEL (14%)
SG	60469	HEL (27%), ISK (25%), PRU (18%), WEL (17%)
PKP	48152	IDC (41%), NEIC (29%)
MLR	45631	MOS (100%)
pP	44147	BJI (35%), NEIC (31%), IDC (16%)
T	43244	IDC (93%)
SN	32706	WEL (46%), HEL (19%)
PKPbc	32020	NEIC (49%), IDC (43%)
P*	31633	WEL (96%)
PcP	29738	NEIC (40%), IDC (36%), BJI (12%)
PFAKE	29185	NEIC (100%)
PKPdf	27116	NEIC (80%)
PP	25212	BJI (37%), NEIC (22%), IDC (14%)
PKIKP	23762	MOS (97%)
AMB	20248	TEH (69%), SKHL (18%)
Pb	17695	CSEM (54%), IRIS (43%)
Sb	17682	IRIS (52%), CSEM (46%)
IAML	17337	SJA (40%), GUC (29%), BER (22%)
A	16271	INMG (61%), SKHL (21%), SVSA (19%)
sP	15903	BJI (82%)
SS	14968	BJI (48%), MOS (33%)
PB	13531	ATH (56%), HEL (44%)
MSG	13197	HEL (100%)
smax	12590	MOS (88%), BJI (12%)
SB	12270	HEL (59%), ATH (41%)
PKPab	11999	NEIC (45%), IDC (35%)
S*	10868	WEL (97%)
Smax	9183	YARS (76%), BYKL (24%)
ScP	8903	NEIC (40%), IDC (32%), BJI (23%)
x	8527	PRU (51%), NDI (49%)
PKiKP	8468	IRIS (40%), NEIC (25%), IDC (19%)
IAmb	8082	NDI (31%), BER (27%), HYB (24%), LIT (18%)
sS	7449	BJI (99%)
*PP	6929	MOS (100%)
AMS	6573	PRU (77%), BGS (12%)
PMZ	5831	BJI (100%)
Pdiff	5438	IRIS (83%), IDC (11%)
PKKPbc	5257	IDC (50%), NEIC (49%)
Pmax	5053	YARS (66%), BYKL (32%)
PKP2	4560	MOS (97%)
Trac	4077	OTT (100%)
LG	3042	BRA (50%), OTT (48%)
ScS	2935	BJI (80%)
Pdif	2841	NEIC (80%)
PPP	2746	MOS (83%)
LE	2603	BJI (100%)
LN	2575	BJI (100%)
X	2565	JMA (84%), SYO (15%)
PKPpre	2563	NEIC (99%)
LZ	2523	BJI (100%)
SKS	2450	BJI (60%), INMG (24%)
SKPbc	2406	NEIC (50%), IDC (48%)
pPKP	2396	IDC (29%), PRU (23%), BJI (22%), NEIC (21%)

Table 12.2: *(continued)*

Reported Phase	Total	Agencies reporting
IVMs_BB	1945	HYB (75%), BER (24%)
Sm	1839	YARS (87%), SIGU (13%)
LRM	1796	BELR (34%), MOLD (34%), SOME (32%)
PKHKP	1791	MOS (100%)
PKhKP	1563	IDC (100%)
SSS	1554	MOS (67%), CLL (16%), BELR (11%)
LQ	1516	PPT (47%), INMG (22%), BELR (21%)
*SP	1507	MOS (100%)
PS	1229	MOS (44%), CLL (13%), BELR (13%)
PcS	1120	BJI (99%)
PKPPKP	1024	IDC (94%)
pPKPbc	975	IDC (53%), NEIC (33%)
PKKP	892	IDC (50%), NEIC (36%), PRU (11%)
sPKP	882	BJI (90%)
PKKPab	840	NEIC (51%), IDC (47%)
Pm	836	YARS (77%), SIGU (23%)
SKKS	776	BJI (82%)
PCP	752	PRU (82%), BRA (11%)
SKSac	742	HYB (42%), BER (13%), PPT (11%)
LMZ	731	WAR (100%)
SKP	728	IDC (44%), NEIC (32%), PRU (16%)
Rg	683	NNC (54%), BER (13%), NAO (13%), IDC (13%)
pPKPdf	662	NEIC (54%), VIE (35%)
P'P'	654	NEIC (100%)
*SS	605	MOS (100%)
IAMs_20	595	BER (52%), NDI (47%)
max	583	BYKL (100%)
PKP2bc	549	IDC (100%)
SP	535	MOS (39%), PRU (26%), PPT (15%)
PKS	532	BJI (92%)
PKPAB	522	PRU (100%)
SKKPbc	493	IDC (55%), NEIC (38%)
PM	470	BELR (100%)
L	450	BRA (30%), DBN (28%), MOLD (23%), CLL (18%)
(P)	448	CLL (61%), BRG (38%)
LmV	410	CLL (100%)
LmH	409	CLL (100%)
AMP	409	HLW (91%)
PKP1	368	LIC (97%)
Lm	355	CLL (100%)
PKKPdf	320	NEIC (62%), BUD (32%)
pPKPab	311	NEIC (43%), IDC (32%), CLL (11%)
AP	301	UCC (99%)
PDIFF	272	PRU (67%), BRA (26%)
PKPDF	233	PRU (100%)
Sgmax	215	NERS (100%)
pPcP	210	IDC (62%), NEIC (35%)
PPMZ	204	BJI (100%)
p	193	IRIS (98%)
P3KPbc	192	IDC (100%)
PPS	182	CLL (45%), MOS (30%), MOLD (14%)
P4KPbc	180	IDC (100%)
sPKPdf	168	VIE (95%)
Sgm	164	SIGU (100%)
SKPab	150	IDC (51%), NEIC (41%)
AMb	147	IGIL (61%), DHMR (24%), NDI (14%)
SKPdf	144	NEIC (72%), CLL (12%)
IVmB_BB	138	BER (100%)
Lmax	136	CLL (99%)
PKP2ab	136	IDC (100%)
pPKiKP	133	BUD (42%), VIE (22%), HYB (17%), CLL (12%)
Pgmax	119	NERS (100%)
PmP	114	BGR (100%)
SSSS	111	CLL (100%)
APKP	108	UCC (100%)
PDIF	101	BRA (96%)
Sdif	100	CLL (38%), HYB (26%), PPT (18%)

Table 12.2: *(continued)*

Reported Phase	Total	Agencies reporting
SKKP	98	IDC (44%), NEIC (32%), PRU (20%)
pwP	96	NEIC (100%)
Snm	94	SIGU (100%)
PKPPKPdf	92	BUD (88%), CLL (12%)
Pgm	92	SIGU (100%)
SKKPdf	88	BUD (98%)
P'P'ab	88	NEIC (99%)
rx	85	SKHL (100%)
(pP)	85	CLL (100%)
LQM	82	BELR (99%)
SDIF	82	PRU (96%)
P'P'df	81	NEIC (99%)
E	73	UCC (97%)
(sP)	68	CLL (100%)
SmS	67	BGR (100%)
SMN	67	BJI (100%)
SME	67	BJI (100%)
XP	64	UCC (98%)
SH	60	SYO (100%)
mb	60	OTT (80%), OMAN (20%)
P(2)	57	CLL (100%)
pPdiff	56	SYO (59%), VIE (14%), BUD (14%)
P1	55	ZUR (100%)
Pu	54	NEIC (100%)
Pnm	53	SIGU (100%)
sPKiKP	52	BUD (50%), VIE (27%), CLL (13%)
SKKSac	50	CLL (64%), WAR (22%)
pPP	47	CLL (53%), LPA (34%), LJU (11%)
SM	45	BELR (100%)
RG	41	HEL (100%)
PgPg	41	BYKL (95%)
SKiKP	40	IDC (80%), UCC (12%)
pPdif	39	HYB (85%), CLL (15%)
Smn	38	SIGU (100%)
SKSdf	38	HYB (45%), BUD (26%), WAR (24%)
Sdiff	37	BUD (35%), LJU (22%), IDC (22%), WAR (14%)
XS	36	PRU (100%)
SKSP	36	MOLD (33%), BELR (28%), CLL (22%), DBN (11%)
P3KP	36	IDC (100%)
(SS)	36	CLL (100%)
pPn	35	SKHL (40%), BUD (34%), OMAN (20%)
Plp	34	CLL (100%)
Pgd	34	WAR (100%)
PsP	33	MOLD (67%), BELR (33%)
SN4	32	ISN (100%)
sPKPbc	30	VIE (53%), IDC (20%), NEIC (13%), CLL (13%)
(PP)	30	CLL (100%)
sPP	30	CLL (87%)
Pmn	29	SIGU (100%)
PN4	29	ISN (100%)
sSS	28	CLL (93%)
sPdif	28	HYB (82%), CLL (18%)
IVMsBB	28	HYB (89%)
SCS	27	LPA (30%), PRU (26%), NDI (26%), BRG (15%)
PKKKP	26	NEIC (100%)
PKPdif	26	NEIC (96%)
PSKS	26	CLL (96%)
SCP	23	PRU (61%), BRG (39%)
Smg	23	SIGU (100%)
(PcP)	21	CLL (100%)
MSN	21	HEL (100%)
PKPM	21	BELR (100%)
pScP	18	IDC (78%), NEIC (22%)
LV	18	CLL (100%)
PnPn	18	HYB (50%), OMAN (17%), BUD (17%), SYO (17%)
SDIFF	18	BRG (78%), LPA (22%)
PKPBC	18	PRU (100%)

Table 12.2: *(continued)*

Reported Phase	Total	Agencies reporting
XSKS	17	PRU (100%)
SgSg	17	BYKL (100%)
PPM	17	BELR (88%), MOLD (12%)
SKKKS	16	BELR (94%)
PX	16	WAR (100%)
PCS	16	PRU (50%), NDI (44%)
SPP	16	MOS (50%), BELR (31%), WAR (12%)
Pmg	15	SIGU (100%)
PPlp	15	CLL (100%)
PA	15	JSN (100%)
PN5	14	THR (79%), HYB (21%)
PPPP	13	CLL (100%)
SKSp	13	BRA (100%)
SKIKP	12	LPA (100%)
PKPc	11	WAR (100%)
(pPKiKP)	11	CLL (100%)
PSPS	11	CLL (100%)
PKPPKPab	11	BUD (100%)
sPn	11	SKHL (91%)
PKSdf	11	CLL (100%)
M	10	MOLD (90%)
sg	10	BUD (100%)
pPg	9	SKHL (100%)
sPKPab	9	VIE (78%), CLL (22%)
AMPG	9	SJA (100%)
I	9	NSSC (33%), BER (33%), LSZ (22%), CSEM (11%)
AMSG	9	SJA (100%)
XM	9	MOLD (100%)
sPg	9	SKHL (89%), BUD (11%)
e	8	WAR (100%)
(SSS)	8	CLL (100%)
PPPrev	8	CLL (100%)
SN5	8	HYB (100%)
sPdiff	8	LJU (25%), BUD (25%), HYB (12%), VIE (12%), IDC (12%), SYO (12%)
PKPdiff	8	CLL (100%)
(S)	8	CLL (100%)
Li	8	MOLD (100%)
PP(2)	7	LPA (86%), CLL (14%)
SS(2)	7	LPA (100%)
SKIKS	7	LPA (100%)
P4KP	7	IDC (57%), NEIC (43%)
TT	7	NEIC (100%)
(PKiKP)	7	CLL (100%)
(Sg)	6	CLL (100%)
LH	6	CLL (100%)
PKIKS	6	LPA (100%)
SX	6	WAR (100%)
sSdiff	6	CLL (100%)
pg	5	BUD (100%)
MPN	5	HEL (100%)
SnSn	5	HYB (100%)
pP(2)	5	CLL (100%)
PKPlp	5	CLL (100%)
PSS	5	CLL (100%)
(PG)	5	BRG (100%)
SSS(2)	5	LPA (100%)
SMZ	5	BJI (100%)
aKPKbc	4	UCC (100%)
pn	4	ISN (75%), BUD (25%)
APKPbc	4	UCC (100%)
(Pg)	4	CLL (100%)
PKSab	4	LJU (100%)
(SSSS)	4	CLL (100%)
sSSS	4	CLL (100%)
(PKP)	4	CLL (50%), BRG (25%), BJI (25%)
P'P'bc	4	PPT (100%)
(PPS)	4	CLL (100%)

Table 12.2: *(continued)*

Reported Phase	Total	Agencies reporting
sPS	4	CLL (100%)
tx	4	IDC (100%)
sn	4	BUD (75%), ISN (25%)
Sglp	4	CLL (100%)
PKKSdf	4	NEIC (100%)
sPb	4	BUD (100%)
(Pn)	4	CLL (100%)
SN6	4	HYB (100%)
(PPP)	3	CLL (100%)
Px	3	WAR (100%)
H	3	IDC (100%)
R	3	LDG (100%)
SKKPab	3	HYB (33%), NEIC (33%), IDC (33%)
SKPa	3	NAO (100%)
del	3	KLM (100%)
PKKS	3	BRG (33%), PRU (33%), IDC (33%)
SKKSdf	3	NEIC (100%)
pPKKPbc	3	CLL (67%), IDC (33%)
sPPP	3	CLL (100%)
(PKPdf)	3	CLL (100%)
pPKP1	3	BELR (100%)
pPDIF	3	BRA (100%)
Slp	3	CLL (100%)
PKSbc	3	CLL (100%)
ml	3	OMAN (100%)
LgX	3	CSEM (100%)
sP(2)	3	LPA (67%), CLL (33%)
PKIKPM	2	BELR (100%)
PPP(2)	2	LPA (100%)
pPDIFF	2	BRG (100%)
Lg2	2	MOLD (100%)
LmV(360	2	CLL (100%)
(SG)	2	BRG (100%)
sSKS	2	HYB (100%)
sPPS	2	CLL (100%)
sPKP1	2	BELR (100%)
PN6	2	HYB (100%)
PKP1M	2	BELR (100%)
CS	2	NDI (100%)
PGDS	2	NDI (100%)
PGN	2	HEL (50%), NDI (50%)
(sPKPab)	2	CLL (100%)
PPmax	2	CLL (100%)
(SN)	2	BRG (100%)
PC	2	BER (100%)
PKKSbc	2	CLL (100%)
P7KP	2	IDC (100%)
(Sn)	2	CLL (100%)
(SKKSac)	2	CLL (100%)
pSKPbc	2	CLL (100%)
PNCN	2	NDI (100%)
pPKS	2	LPA (100%)
O	2	BRG (50%), ECX (50%)
pZP	1	SYO (100%)
(PKKS)	1	CLL (100%)
sPKKPab	1	CLL (100%)
(SKKPbc)	1	CLL (100%)
PKPPKPPK	1	CLL (100%)
pPKPAB	1	HYB (100%)
PDN	1	NDI (100%)
(PKKPab)	1	CLL (100%)
Pnd	1	WAR (100%)
PXA	1	WAR (100%)
(pPKPbc)	1	CLL (100%)
(SSP)	1	CLL (100%)
pPKPPKPd	1	CLL (100%)
PKPmax	1	CLL (100%)

Table 12.2: *(continued)*

Reported Phase	Total	Agencies reporting
PKPPKPbc	1	BUD (100%)
(PKKP)	1	CLL (100%)
(PS)	1	CLL (100%)
sPKKPbc	1	CLL (100%)
Lg1	1	MOLD (100%)
PCN	1	NDI (100%)
PPPPrev	1	CLL (100%)
PSP	1	MOLD (100%)
PGS	1	NDI (100%)
pPKPdiff	1	CLL (100%)
PXB	1	WAR (100%)
UNK	1	MDD (100%)
(PKS)	1	CLL (100%)
-Mb	1	SVSA (100%)
PN7	1	HYB (100%)
SSP	1	CLL (100%)
PFIF	1	BRG (100%)
SSSmax	1	CLL (100%)
(sSSS)	1	CLL (100%)
PNDN	1	NDI (100%)
sS(2)	1	LPA (100%)
LRM1	1	BELR (100%)
SKPPKPdf	1	CLL (100%)
P'Pdf	1	BUD (100%)
(Pdif)	1	CLL (100%)
pPPlp	1	CLL (100%)
SKPPKPbc	1	CLL (100%)
pSKS	1	SOME (100%)
Pnmax	1	CLL (100%)
KSP	1	BELR (100%)
pPmax	1	CLL (100%)
sPSKS	1	CLL (100%)
sPcP	1	CLL (100%)
PKPSE	1	NDI (100%)
sSSSS	1	CLL (100%)
pPS	1	CLL (100%)
(SPk)	1	CLL (100%)
PDS	1	NDI (100%)
SK	1	BRG (100%)
(LmV)	1	CLL (100%)
(sPS)	1	CLL (100%)
SKSSKSac	1	CLL (100%)
PPPS	1	DBN (100%)
(SKKSdf)	1	CLL (100%)
pPPS	1	CLL (100%)
S'S'df	1	HYB (100%)
IVmBBB	1	BER (100%)
SSrev	1	CLL (100%)
eSm	1	SKHL (100%)
pPPP	1	CLL (100%)
s	1	LPA (100%)
S(2)	1	CLL (100%)
PPKbc	1	INMG (100%)
pPSKS	1	CLL (100%)
(sPdif)	1	CLL (100%)
(PKPab)	1	CLL (100%)
(pPKPab)	1	CLL (100%)
Pxd	1	WAR (100%)
WpP	1	SYO (100%)
(pPP)	1	CLL (100%)
sPdidd	1	HYB (100%)
SSmax	1	CLL (100%)
PKPbc(2)	1	CLL (100%)
PKKPf	1	BUD (100%)
sSKKSacr	1	CLL (100%)
(PKPdif)	1	CLL (100%)
PPk	1	CLL (100%)

Table 12.2: *(continued)*

Reported Phase	Total	Agencies reporting
sSKKPdf	1	CLL (100%)
SKKSacr	1	CLL (100%)
Pmlp	1	CLL (100%)
SKPb	1	NAO (100%)
P5KPbc	1	IDC (100%)
pPIFF	1	BRG (100%)
Pl	1	CLL (100%)
-ML	1	INMG (100%)
pPKSdf	1	CLL (100%)
PKPabmax	1	CLL (100%)
Pn(2)	1	CLL (100%)
Pdifflp	1	CLL (100%)
(SP)	1	CLL (100%)
PKPP	1	NDI (100%)
Pcp	1	SYO (100%)
SSSSmax	1	CLL (100%)
S'S'ac	1	LJU (100%)

Table 12.3: *Reporters of amplitude data*

Agency	Number of reported amplitudes	Number of amplitudes in ISC located events	Number used for ISC mb	Number used for ISC MS
IDC	528638	492338	241251	43659
NEIC	381829	381200	286860	59533
MOS	280151	236220	123432	26998
CSEM	170642	31337	7398	0
BJI	124167	116572	21578	33093
WEL	75982	12361	0	0
DJA	74176	49230	14694	0
ATH	69837	10376	0	0
MDD	60666	8815	1	0
NNC	53594	15433	84	0
SOME	50536	15532	1868	0
ROM	50234	4576	0	0
BKK	33125	28766	15898	0
THE	26944	6550	0	0
RSNC	23474	2835	0	0
DMN	18488	17861	1040	0
VIE	17219	14270	7484	0
INMG	14294	6182	2780	0
TEH	13915	6360	0	0
HEL	13434	389	0	0
NSSC	12543	4589	0	0
YARS	12531	254	0	0
PPT	12177	10503	1359	0
LDG	12051	3452	2	0
GUC	11081	3723	3	0
PRU	10877	6899	0	1894
SKHL	7535	6202	0	0
SJA	7193	2128	26	0
BER	7052	3695	1870	262
PDG	6648	4616	0	0
PRE	6111	520	0	0
WBNET	6019	0	0	0
MAN	5955	2513	0	0
BRG	5580	3986	1317	0
CLL	5194	4661	1104	336
NDI	4791	3851	1785	218
NAO	4640	4532	3541	0
BYKL	4480	2694	0	0
LJU	4274	431	117	0
OTT	4124	294	0	0
DNK	4044	3666	2820	0
HYB	3606	3565	1689	0
SVSA	3366	352	221	0
BGS	3142	2645	1404	721

Table 12.3: *Continued.*

Agency	Number of reported amplitudes	Number of amplitudes in ISC located events	Number used for ISC mb	Number used for ISC MS
ZUR	3137	516	0	0
ECX	2958	910	0	0
DHMR	2404	496	21	0
SIO	1922	1919	1139	0
SKO	1875	437	0	0
UCC	1603	1455	1127	0
LIT	1454	1413	1227	0
BELR	1245	1186	0	520
KNET	1160	376	0	0
LIC	1140	1062	508	0
IGIL	1049	465	79	187
MOLD	881	503	114	0
DBN	854	570	372	0
THR	828	821	0	0
OBM	445	271	0	0
CASC	419	262	0	0
HLW	372	178	0	0
NERS	340	106	0	0
SIGU	256	35	0	0
WAR	235	235	1	193
BGR	211	130	0	0
PLV	173	169	0	0
SCB	173	153	0	0
IASPEI	18	10	0	0
SSNC	14	12	0	0
LPA	9	6	0	0
ISN	5	2	0	0
AZER	2	2	0	0
LSZ	1	0	0	0

13

Glossary of ISC Terminology

- Agency/ISC data contributor

  An academic or government institute, seismological organisation or company, geological/meteorological survey, station operator or author that reports or contributed data in the past to the ISC or one of its predecessors. Agencies may contribute data to the ISC directly, or indirectly through other ISC data contributors.

- Agency code

  A unique, maximum eight-character code for a data reporting agency (e.g. NEIC, GFZ, BUD) or author (e.g. ISC, EHB, IASPEI). Often the agency code is the commonly used acronym of the reporting institute.

- Arrival

  A phase pick at a station is characterised by a phase name and an arrival time.

- Associated phase

  Associated phase arrival or amplitude measurements represent a collection of observations belonging to (i.e. generated by) an event. The complete set of observations are associated to the prime hypocentre.

- Azimuthal gap/Secondary azimuthal gap

  The azimuthal gap for an event is defined as the largest angle between two stations with defining phases when the stations are ordered by their event-to-station azimuths. The secondary azimuthal gap is the largest azimuthal gap a single station closes.

- BAAS

  Seismological bulletins published by the British Association for the Advancement of Science (1913-1917) under the leadership of H.H. Turner. These bulletins are the predecessors of the ISS Bulletins and include reports from stations distributed worldwide.

- Bulletin

  An ordered list of event hypocentres, uncertainties, focal mechanisms, network magnitudes, as well as phase arrival and amplitude observations associated to each event. An event bulletin may list all the reported hypocentres for an event. The convention in the ISC Bulletin is that the preferred (prime) hypocentre appears last in the list of reported hypocentres for an event.

- Catalogue

  An ordered list of event hypocentres, uncertainties and magnitudes. An event catalogue typically lists only the preferred (prime) hypocentres and network magnitudes.

- CoSOI/IASPEI

  Commission on Seismological Observation and Interpretation, a commission of IASPEI that prepares and discusses international standards and procedures in seismological observation and interpretation.

- Defining/Non-defining phase

  A defining phase is used in the location of the event (time-defining) or in the calculation of the network magnitude (magnitude-defining). Non-defining phases are not used in the calculations because they suffer from large residuals or could not be identified.

- Direct/Indirect report

  A data report sent (e-mailed) directly to the ISC, or indirectly through another ISC data contributor.

- Duplicates

  Nearly identical phase arrival time data reported by one or more agencies for the same station. Duplicates may be created by agencies reporting observations from other agencies, or several agencies independently analysing the waveforms from the same station.

- Event

  A natural (e.g. earthquake, landslide, asteroid impact) or anthropogenic (e.g. explosion) phenomenon that generates seismic waves and its source can be identified by an event location algorithm.

- Grouping

  The ISC algorithm that organises reported hypocentres into groups of events. Phases associated to any of the reported hypocentres will also be associated to the preferred (prime) hypocentre. The grouping algorithm also attempts to associate phases that were reported without an accompanying hypocentre to events.

- Ground Truth

  An event with a hypocentre known to certain accuracy at a high confidence level. For instance, GT0 stands for events with exactly known location, depth and origin time (typically explosions); GT5 stands for events with their epicentre known to 5 km accuracy at the 95% confidence level, while their depth and origin time may be known with less accuracy.

- Ground Truth database

  On behalf of IASPEI, the ISC hosts and maintains the IASPEI Reference Event List, a bulletin of ground truth events.

- IASPEI

  International Association of Seismology and Physics of the Earth Interior, www.iaspei.org.

- International Registry of Seismograph Stations (IR)

  Registry of seismographic stations, jointly run by the ISC and the World Data Center for Seismology, Denver (NEIC). The registry provides and maintains unique five-letter codes for stations participating in the international parametric and waveform data exchange.

- ISC Bulletin

  The comprehensive bulletin of the seismicity of the Earth stored in the ISC database and accessible through the ISC website. The bulletin contains both natural and anthropogenic events. Currently the ISC Bulletin spans more than 50 years (1960-to date) and it is constantly extended by adding both recent and past data. Eventually the ISC Bulletin will contain all instrumentally recorded events since 1900.

- ISC Governing Council

  According to the ISC Working Statutes the Governing Council is the governing body of the ISC, comprising one representative for each ISC Member.

- ISC-located events

  A subset of the events selected for ISC review are located by the ISC. The rules for selecting an event for location are described in Section 3.3.4; ISC-located events are denoted by the author ISC.

- ISC Member

  An academic or government institute, seismological organisation or company, geological/meteorological survey, station operator, national/international scientific organisation that contribute to the ISC budget by paying membership fees. ISC members have voting rights in the ISC Governing Council.

- ISC-reviewed events

  A subset of the events reported to the ISC are selected for ISC analyst review. These events may or may not be located by the ISC. The rules for selecting an event for review are described in Section 3.3.3. Non-reviewed events are explicitly marked in the ISC Bulletin by the comment following the prime hypocentre "Event not reviewed by the ISC".

- ISF

  International Seismic Format (www.isc.ac.uk/standards/isf). A standard bulletin format approved by IASPEI. The ISC Bulletin is presented in this format at the ISC website.

- ISS

  International Seismological Summary (1918-1963). These bulletins are the predecessors of the ISC Bulletin and represent the major source of instrumental seismological data before the digital era. The ISS contains regionally and teleseismically recorded events from several hundreds of globally distributed stations.

- Network magnitude

The event magnitude reported by an agency or computed by the ISC locator. An agency can report several network magnitudes for the same event and also several values for the same magnitude type. The network magnitude obtained with the ISC locator is defined as the median of station magnitudes of the same magnitude type.

- Phase

  A maximum eight-character code for a seismic, infrasonic, or hydroacoustic phase. During the ISC processing, reported phases are mapped to standard IASPEI phase names. Amplitude measurements are identified by specific phase names to facilitate the computation of body-wave and surface-wave magnitudes.

- Prime hypocentre

  The preferred hypocentre solution for an event from a list of hypocentres reported by various agencies or calculated by the ISC.

- Reading

  Parametric data that are associated to a single event and reported by a single agency from a single station. A reading typically includes one or more phase names, arrival time and/or amplitude/period measurements.

- Report/Data report

  All data that are reported to the ISC are parsed and stored in the ISC database. These may include event bulletins, focal mechanisms, moment tensor solutions, macroseismic descriptions and other event comments, as well as phase arrival data that are not associated to events. Every single report sent to the ISC can be traced back in the ISC database via its unique report identifier.

- Shide Circulars

  Collections of station reports for large earthquakes occurring in the period 1899-1912. These reports were compiled through the efforts of J. Milne. The reports are mainly for stations of the British Empire equipped with Milne seismographs. After Milne's death, the Shide Circulars were replaced by the Seismological Bulletins of the BAAS.

- Station code

  A unique, maximum six-character code for a station. The ISC Bulletin contains data exclusively from stations registered in the International Registry of Seismograph Stations.

14

Acknowledgements

We thank John Ristau of GNS, New Zealand and Ryota Hino of Tohoku University, Japan for kindly accepting our invitation and submitting articles for this issue of the Summary.

We are also grateful to all the developers of the Generic Mapping Tools (GMT) suite of software (Wessel and Smith, 1998), used extensively here in producing the graphical figures.

Finally, we thank the ISC Member Institutions, Data Contributors, Funding Agencies (including NSF Award EAR-0949072) and Sponsors for supporting the ISC long-term operations.

References

Adams, R. D., A. A. Hughes, and D. M. McGregor (1982), Analysis procedures at the International Seismological Centre, *Physics of the Earth and Planetary Interiors*, *30*, 85–93.

Amante, C., and B. W. Eakins (2009), ETOPO1 1 arc-minute global relief model: procedures, data sources and analysis, *NOAA Technical Memorandum NESDIS NGDC-24*, NOAA.

Balfour, N., R. Baldwin, and A. Bird (2008), Magnitude calculations in Antelope 4.10, *Analysis Group Note of Geological Survey of Canada*, pp. 1–13.

Bennett, T. J., V. Oancea, B. W. Barker, Y.-L. Kung, M. Bahavar, B. C. Kohl, J. . Murphy, and I. K. Bondár (2010), The nuclear explosion database NEDB: a new database and web site for accessing nuclear explosion source information and waveforms, *Seismological Research Letters*, *81*, doi:10.1785/gssrl.81.1.12.

Bisztricsany, E. A. (1958), A new method for the determination of the magnitude of earthquakes, *Geofiz. Kozl*, pp. 69–76.

Bolt, B. A. (1960), The revision of earthquake epicentres, focal depths and origin time using a high-speed computer, *Geophysical Journal of the Royal Astronomical Society*, *3*, 434–440.

Bondár, I., and K. McLaughlin (2009a), A new ground truth data set for seismic studies, *Seismological Research Letters*, *80*, 465–472.

Bondár, I., and K. McLaughlin (2009b), Seismic location bias and uncertainty in the presence of correlated and non-Gaussian travel-time errors, *Bulletin of the Seismological Society of America*, *99*, 172–193.

Bondár, I., and D. Storchak (2011), Improved location procedures at the International Seismological Centre, *Geophysical Journal International*, *186*, 1220–1244.

Bondár, I., E. R. Engdahl, X. Yang, H. A. A. Ghalib, A. Hofstetter, V. Kirchenko, R. Wagner, I. Gupta, G. Ekström, E. Bergman, H. Israelsson, and K. McLaughlin (2004), Collection of a reference event set for regional and teleseismic location calibration, *Bulletin of the Seismological Society of America*, *94*, 1528–1545.

Bondár, I., E. Bergman, E. R. Engdahl, B. Kohl, Y.-L. Kung, and K. McLaughlin (2008), A hybrid multiple event location technique to obtain ground truth event locations, *Geophysical Journal International*, *175*, doi:10.1111/j.1365,246X.2008.03,867x.

Bormann, P., and J. W. Dewey (2012), The new iaspei standards for determining magnitudes from digital data and their relation to classical magnitudes, is 3.3, *New Manual of Seismological Observatory Practice 2 (NMSOP-2), P. Bormann (Ed.)*, pp. 1–44, doi:10.2312/GFZ.NMSOP-2_IS_3.3,10.2312/GFZ.NMSOP-2, `http://nmsop.gfz-postsdam.de`.

Bormann, P., and J. Saul (2008), The new IASPEI standard broadband magnitude mB, *Seism. Res. Lett*, *79*(5), 698–705.

Bormann, P., R. Liu, X. Ren, R. Gutdeutsch, D. Kaiser, and S. Castellaro (2007), Chinese national network magnitudes, their relation to NEIC magnitudes and recommendations for new IASPEI magnitude standards, *Bulletin of the Seismological Society of America*, *97*(1B), 114–127, doi:10.1785/012006007835.

Bormann, P., R. Liu, Z. Xu, R. Ren, and S. Wendt (2009), First application of the new IASPEI teleseismic magnitude standards to data of the China National Seismographic Network, *Bulletin of the Seismological Society of America*, *99*, 1868–1891, doi:10.1785/0120080010.

Chang, A. C., R. H. Shumway, R. R. Blandford, and B. W. Barker (1983), Two methods to improve location estimates - preliminary results, *Bulletin of the Seismological Society of America*, *73*, 281–295.

Choy, G. L., and J. L. Boatwright (1995), Global patterns of readiated seismic energy and apparent stress, *J. Geophys. Res.*, *100*(B9), 18,205–18,228.

Dziewonski, A. M., and F. Gilbert (1976), The effect of small, aspherical perturbations on travel times and a re-examination of the correction for ellipticity, *Geophysical Journal of the Royal Astronomical Society*, *44*, 7–17.

Dziewonski, A. M., T.-A. Chou, and J. H. Woodhouse (1981), Determination of earthquake source parameters from waveform data for studies of global and regional seismicity, *J. Geophys. Res.*, *86*, 2825–2852.

Engdahl, E. R., and R. H. Gunst (1966), Use of a high speed computer for the preliminary determination of earthquake hypocentres, *Bulletin of the Seismological Society of America*, *56*, 325–336.

Engdahl, E. R., and A. Villaseñor (2002), Global seismicity: 1900-1999, *International Handbook of Earthquake Engineering and Seismology, International Geophysics series*, *81A*, 665–690.

Engdahl, E. R., R. van der Hilst, and R. Buland (1998), Global teleseismic earthquake relocation with improved travel times and procedures for depth determination, *Bulletin of the Seismological Society of America*, *88*, 722–743.

Flinn, E. A., and E. R. Engdahl (1965), Proposed basis for geographical and seismic regionalization, *Reviews of Geophysics*, *3*(1), 123–149.

Flinn, E. A., E. R. Engdahl, and A. R. Hill (1974), Seismic and geographical regionalization, *Bulletin of the Seismological Society of America*, *64*, 771–993.

Gutenberg, B. (1945a), Amplitudes of P, PP and S and magnitude of shallow earthquakes, *Bulletin of the Seismological Society of America*, *35*, 57–69.

Gutenberg, B. (1945b), Magnitude determination of deep-focus earthquakes, *Bulletin of the Seismological Society of America*, *35*, 117–130.

Gutenberg, B. (1945c), Amplitudes of surface waves and magnitudes of shallow earthquakes, *Bulletin of the Seismological Society of America*, *35*, 3–12.

Gutenberg, B., and C. F. Richter (1956), Magnitude and Energy of earthquakes, *Ann. Geof.*, *9*, 1–5.

Hutton, L. K., and D. M. Boore (1987), The ML scale in southern California, *Bulletin of the Seismological Society of America*, *77*, 2074–2094.

IASPEI (2005), Summary of magnitude working group recommendations on standard procedures for determining earthquake magnitudes from digital data, `http://www.iaspei.org/commissions/CSOI.html#wgmm,http://www.iaspei.org/commissions/CSOI/summary_of_WG_recommendations_2005.pdf`.

IASPEI (2013), Summary of magnitude working group recommendations on standard procedures for determining earthquake magnitudes from digital data, `http://www.iaspei.org/commissions/CSOI/Summary_of_WG_recommendations_20130327.pdf`.

IDC (1999), IDC processing of seismic, hydroacoustic and infrasonic data, *IDC Documentation*.

Jeffreys, H., and K. E. Bullen (1940), *Seismological Tables*, British Association for the Advancement of Science.

Kanamori, H. (1977), The energy release in great earthquakes, *J. Geophys. Res.*, *82*, 2981–2987.

Kennett, B. L. N. (2006), Non-linear methods for event location in a global context, *Physics of the Earth and Planetary Interiors*, *158*, 45–64.

Kennett, B. L. N., E. R. Engdahl, and R. Buland (1995), Constraints on seismic velocities in the Earth from traveltimes, *Geophysical Journal International*, *122*, 108–124.

Kennett, B. L. N., E. R. Engdahl, and R. Buland (1996), Ellipticity corrections for seismic phases, *Geophysical Journal International*, *127*, 40–48.

Lee, W. H. K., R. Bennet, and K. Meagher (1972), A method of estimating magnitude of local earthquakes from signal duration, *U.S. Geol. Surv.*, Open-File Rep.

Murphy, J. R., and B. W. Barker (2006), Improved focal-depth determination through automated identication of the seismic depth phases pP and sP, *Bulletin of the Seismological Society of America*, *96*, 1213–1229.

NMSOP-2 (2012), *New Manual of Seismological Observatory Practice (NMSOP-2)*, IASPEI, GFZ, German Research Centre for Geosciences, Potsdam, doi:10.2312/GFZ.NMSOP-2, `http://nmsop.gfz-potsdam.de`, urn:nbn:de:kobv:b103-NMSOP-2.

Nuttli, O. W. (1973), Seismic wave attenuation and magnitude relations for eastern North America, *J. Geophys. Res.*, *78*, 876–885.

Richter, C. F. (1935), An instrumental earthquake magnitude scale, *Bulletin of the Seismological Society of America*, *25*, 1–32.

Ringdal, F. (1976), Maximum-likelihood estimation of seismic magnitude, *Bulletin of the Seismological Society of America*, *66*(3), 789–802.

Sambridge, M. (1999), Geophysical inversion with a neighbourhood algorithm, *Geophysical Journal International*, *138*, 479–494.

Sambridge, M., and B. L. N. Kennett (2001), Seismic event location: non-linear inversion using a neighbourhood algorithm, *Pure and Applied Geophysics*, *158*, 241–257.

Storchak, D. A., J. Schweitzer, and P. Bormann (2003), The IASPEI standard seismic phases list, *Seismological Research Letters*, *74*(6), 761–772.

Storchak, D. A., J. Schweitzer, and P. Bormann (2011), Seismic phase names: IASPEI standard, in *Encyclopedia of Solid Earth Geophysics*, edited by H. Gupta, pp. 1162–1173, Springer.

Tsuboi, C. (1954), Determination of the Gutenberg-Richter's magnitude of earthquakes occurring in and near Japan, *Zisin (J. Seism. Soc. Japan), Ser. II*(7), 185–193.

Tsuboi, S., K. Abe, K. Takano, and Y. Yamanaka (1995), Rapid determination of Mw from broadband P waveforms, *Bulletin of the Seismological Society of America*, *85*(2), 606–613.

Uhrhammer, R. A., and E. R. Collins (1990), Synthesis of Wood-Anderson Seismograms from Broadband Digital Records, *Bulletin of the Seismological Society of America*, *80*(3), 702–716.

Vaněk, J., A. Zapotek, V. Karnik, N. V. Kondorskaya, Y. V. Riznichenko, E. F. Savarensky, S. L. Solov'yov, and N. V. Shebalin (1962), Standardization of magnitude scales, *Izvestiya Akad. SSSR., Ser. Geofiz.*(2), 153–158, pages 108–111 in the English translation.

Villaseñor, A., and E. R. Engdahl (2005), A digital hypocenter catalog for the International Seismological Summary, *Seismological Research Letters*, *76*, 554–559.

Villaseñor, A., and E. R. Engdahl (2007), Systematic relocation of early instrumental seismicity: Earthquakes in the International Seismological Summary for 1960–1963, *Bulletin of the Seismological Society of America*, *97*, 1820–1832.

Woessner, J., and S. Wiemer (2005), Assessing the quality of earthquake catalogues: estimating the magnitude of completeness and its uncertainty, *Bulletin of the Seismological Society of America*, *95*(2), doi:10/1785/012040,007.

Young, J. B., B. W. Presgrave, H. Aichele, D. A. Wiens, and E. A. Flinn (1996), The Flinn-Engdahl regionalisation scheme: the 1995 revision, *Physics of the Earth and Planetary Interiors*, *96*, 223–297.

WHITE PAPER

COMPLETE INTEGRATED AFTERSHOCK SYSTEM PROVIDES QUICK AND EASY SOLUTION FOR RAPID AFTERSHOCK DEPLOYMENT

LEONID ZIMAKOV

TRIMBLE INFRASTRUCTURE, PLANO, TEXAS, USA

INTRODUCTION

Rapid aftershock mobilization plays an essential role in the understanding of both focal mechanism and rupture propagation caused by strong earthquakes. A quick assessment of the data provides a unique opportunity to study the dynamics of the entire earthquake process in-situ. Aftershock study also provides practical information for local authorities regarding post-earthquake activity, which is very important in order to conduct the necessary actions for public safety in the area affected by a strong earthquake.

Due to a relatively short aftershock activity period (several weeks to several months), it is critical to rapidly deploy emergency personnel to the affected area in order to minimize the time required to estimate the extent and amplitude of strong shaking from aftershock events.

A dense array of seismic stations consisting of high resolution seismic recorders with short period seismometers and accelerometers is required in order to reduce the time needed to detect an event and provide high resolution maps of ground accelerations across the affected earthquake region. Therefore, the rapid aftershock mobilization of seismic equipment should comply with the following critical requirements:

- Lightweight and small in size
- Integrated design with minimal or no external peripheral equipment
- Very low power consumption
- Minimal or no field programming
- Easy and quick data download in the field
- Low maintenance

WHAT DOES THE 160-03 OFFER?

The REF TEK High Resolution Aftershock System, Model 160-03, is a self-contained, fully integrated Aftershock System providing the customer with simple and quick deployment during aftershock emergency mobilization. The 160-03, six channel recorder, contains three major components integrated in one case:

- 24-bit resolution low power ADC with CPU and lid interconnect boards;
- power source; and
- three component 2 Hz sensors (two horizontals and one vertical and a triaxial +/-4g MEMS accelerometer.

Figure 1: REF TEK 160-03 High Resolution Aftershock System

Figure 2: Inside the case of the REF TEK 160-03 High Resolution Aftershock System

The self-contained rechargeable battery pack provides power autonomy for up to 7 days during continuous data acquisition at 200 sps on three weak motion and three triggered strong motion recording channels. For longer power autonomy, the 160-03 Aftershock System battery pack can be charged from an external source (solar power system). To download recorded data the customer has two options:

- Connect a laptop to the 160-03 and the data is then automatically uploaded; or
- Connect the REF TEK Wi-Fi Serial Adaptor to upload data to the REF TEK iFSC Controller.

The 160-03 configuration is fixed based on a configuration file stored in the system, so no external command/control interface is required for parameter setup in the field. For visual control of the system performance in the field, the 160-03 has a built-in LED display which indicates the system's recording status, as well as a hot swappable USB drive and battery status. As an added customer convenience, four 160-03 systems can be housed in a small, lightweight, watertight rolling case that will keep the recorders safe during transport. The ease of having an all-in-one aftershock system also provides the customer flexibility in sending the equipment to the affected region via a more cost effective way as the equipment/carrying case can easily be checked on both domestic and international commercial flights.

160-03 SPECIFICATIONS

Model	160-03 (Part No. 97124-00)
Mechanical	
Size: Weight: Watertight Integrity:	6” (15.2cm) high x 8.63” (21.9cm) diameter 11.7 lbs. (5.3 kg) IP67
Environmental	
Operating Temp.:	-30°C to +60°C
Storage Temp.:	-40°C to +70°C
Power	
Average Power:	<400 mW
A/D Convertor	
Type:	Delta-Sigma Modulation, 24-bit output resolution
Dynamic Range:	>138 dB@100 sps
Channels:	6
Input Impedance:	Matched to sensors
Sample Rates:	200 sps default; 100, 250, 500 sps optional
Seismometer	
Type:	Moving coil / mass
Natural Frequency:	2 Hz
Accelerometer	
Type:	± 4g
Frequency Response:	DC – 45 Hz
Damping:	0.7 to critical
Data Storage	
Type:	USB Flash
User Interface	
Type:	LED array consisting of 16 LED display recording status, USB drive status, battery voltage, etc.
Power Control:	Magnetic switch to turn on both power and acquisition

Table 1: 160-03 Specifications

CONTACT US

Phone: +1 (214) 440 1265

Email: sales@reftek.com